IJCESEN

International

Journal of

Computational and

Experimental

Science and

ENgineering

Founder-Editor-in-Chief : Prof.Dr. İskender AKKURT

Indexing/Abstracting Databases

ULAKBİM

TRDİZİN

INDEX COPERNICUS

INTERNATIONAL

A S O S indeks

GENERAL IMPACT FACTOR

Universal Digital Object Information

ISIFI — INTERNATIONAL SERVICES FOR IMPACT FACTOR AND INDEXING

Google Scholar

ISI ISI ISI ISI ISI ISI ISI ISI

INTERNATIONAL Scientific Indexing

DRJI

publons

Cosmos

SIS

J-Gate

WorldCat®

ESJI www.ESJIndex.org

Eurasian Scientific Journal Index

JIF JIFACTOR

CiteFactor Academic Scientific Journals

Academic Resource Index ResearchBib

Scientific Journal Impact Factor

TOGETHER WE REACH THE GOAL

Table of Contents

Thermoluminescence Dosimeters Holder Cassette Design and 3D Printing

Duygu TUNÇMAN[1],*, Fahrettin Fatih KESMEZACAR[2], Osman GÜNAY[3], Nami YEYİN [4], Özge DEMİR [5], Mustafa DEMİR[6], Baki AKKUŞ[7]

[1]Istanbul University, Science Faculty, Physics Department, 34134, Istanbul-Turkey
* Corresponding Author : **Email:** duygutuncman@gmail.com - **ORCID:** 0000-0002-0929-0441

[2]Istanbul University – Cerrahpasa, Vocational School of Health Services, Medical Imag. Tech. Program, Istanbul-Turkey
Email: okesmezacar@hotmail.com - **ORCID:** 0000-0001-5110-1184

[3] Yıldız Technical University, Faculty of Electrical & Electronics, Biomedical Engineering, 34220, Istanbul – Turkey.
Email: ogunay@yildiz.edu.tr - **ORCID:** 0000-0003-0760-554X

[4] Department of Nuclear Medicine, Cerrahpasa Faculty of Medicine, Istanbul University-Cerrahpasa, Istanbul, Turkey
Email: namiyeyin@gmail.com **- ORCID:** 0000-0003-0262-4020

[5] Istanbul University – Cerrahpasa, Faculty of Engineering, Department of Chemical Engineering, Department of Unit Operations and Thermodynamics, 34315, Istanbul – Turkey.
Email: ozge.demir@iuc.edu.tr - **ORCID:** 0000-0002-0342-5915

[6] Department of Nuclear Medicine, Cerrahpasa Faculty of Medicine, Istanbul University-Cerrahpasa, Istanbul, Turkey
Email: demirm@istanbul.edu.tr - **ORCID:** 0000-0002-9813-1628

[7]Istanbul University, Science Faculty, Physics Department, 34134, Istanbul-Turkey
E-mail: akkus@istanbul.edu.tr - **ORCID:** 0000-0002-9533-7671

Abstract:

3-*dimensional* (3D) printing technology has been used in many fields and has taken a significant place in several applications. The ease of production, cheap cost, being able to produce the product most suitable for your needs, and easy accessibility of the 3D printer have enabled it to be used in many areas. This study emerged from the need for an apparatus to place thermoluminescence dosimeters (TLDs) during the calibration of TLDs to be used to determine organ doses in fluoroscopy applications. In the study, the TLD holder cassette that was specially designed in the SolidWorks program was printed from PLA material using the fused deposition modelling (FDM) technique with Creality Ender 3 S1 printer. With this 3D TLD holder cassette that was designed and printed in accordance with the needs, we aimed to show the usability of the 3D printing technique in almost every field of applied sciences.

1. Introduction

In recent years, there are many technologies available that make it possible to obtain a prototype of a designed product in a relatively short time. Among the variety of additive technologies (such as fused deposition modeling (FDM) and others), some are accessible to a wide range of users due to their simplicity and relative inexpensiveness [1,2]. The interest in 3D printing technology is increasing in almost every sub-branch in the fields of Health and Medicine. When it comes to 3D printing, the first thing that comes to mind is the general areas where this technique is used and the products known to be produced. The study is important in terms of emphasizing that 3D printing produces products suitable for the purpose. Various devices are used to detect the presence of ionizing radiation that cannot be detected by human sense organs and to measure its level. Thermoluminescent dosimeters (TLD) are routinely used for dose measurements due to their small size (Fig. 1), tissue equivalence, and high sensitivity [3]. TLD is a layer of solid crystals. After the ionizing radiation interacts with the crystal, the crystal is heated and the trapped electrons in the crystal emit a visible light photon with an energy equivalent to the energy of ionizing radiation. The emitted light photons are counted by means of photomultiplier tubes. Thus, the amount of radiation reaching the dosimeter is determined [4]. Before TLDs can measure doses, they must be prepared by going through a number of processes [5].

Figure 1. *Types of TLD dosimeters*

All dosimeters must be annealed under the manufacturer's instructions before making radiation measurements to standardize their sensitivity and natural background. Pre-irradiation annealing is especially important in order to eliminate the thermoluminescent radiation left over from previous irradiations, create thermoluminescence sensitivity, and eliminate unstable low-temperature radiation peaks. After annealing, it must be calibrated with a monoenergetic radiation source such as a gamma ray. For sensitive irradiation of TLDs, cassette holders suitable for TLD size are usually produced from hard-plexiglass or polymethylmethacrylate (PMMA) materials [6,7]. TLD irradiation apparatuses are produced by cutting in desired dimensions in special cutting machines. As an alternative to this conventional production technique, TLD irradiation and storage TLD holder cassette can be produced in accordance with the intended use of 3D printing technology. Apart from the ease of use of the TLD holder cassette, the choice of material before printing is important in terms of the backscattering of radiation during irradiation. Because TLDs are very sensitive dosimeters, it is necessary to minimize adverse environmental conditions during calibration in order to get the most accurate result from measurements.

This study arose from the need for an apparatus in which TLDs can be placed for dose measurements. In this sense, this study is aimed to introduce the 3D printing technique of a TLD holder cassette with 100 slots (10x10).

2. Material and Methods

The 3D printing process, which allows the transition from direct design to production, consists of the steps described below. In this study, the 3D model was created using the SolidWorks program (Fig. 2).
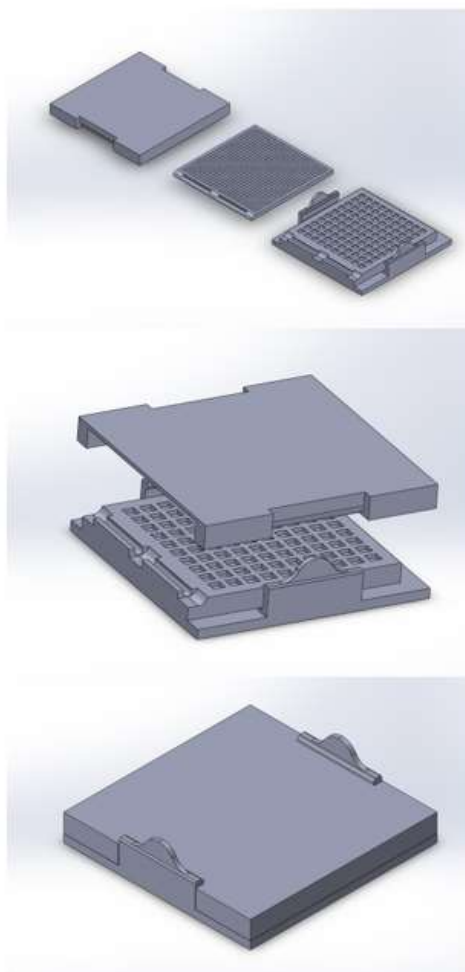
Figure 2. *Design of the TLD holder cassette in the SolidWorks 3D program*

TLD holder cassette is designed to consist of three basic parts as shown in Fig. 3. A top cover was designed to keep TLDs stable during irradiation (Fig. 3-A). Furthermore, the top cover is locked thanks to its latch structure on the side and ensures that the TLDs in the apparatus remain stable during irradiation. The intermediate plate that is shown in Fig. 3-B is produced for direct irradiation of TLDs even without a cover. There are 100 slots in the lower plate (Fig. 3-C). The slots shown in Fig. 3 - Detail A are designed to place TLDs in the apparatus (Fig. 3).

In order to take the output of the drawn model from the 3D printer, it is exported as a Standard Triangle Language (STL) file that the Ultimaker Cura software program will detect (Fig. 4). The TLD holder cassette was planned at a %30 infill ratio. Designed modes that are obtained as an STL file to slice software are divided into layers. After specifying the required variables such as fill, printing speed, and printing temperature with Ultimaker Cura, g. code extension output to 3D printer transferred.
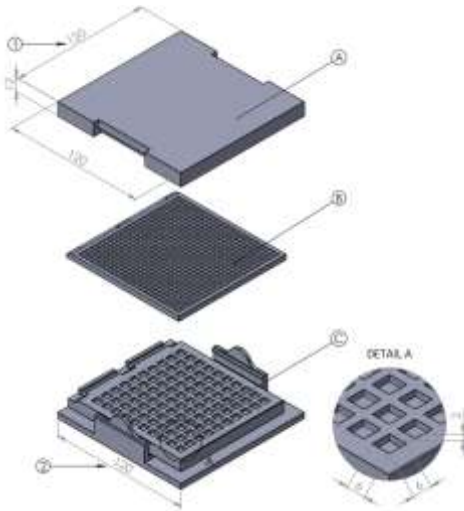
Figure 3. *The scaled version of the TLD holder cassette in the design program*

Figure 5. *Creality Ender 3 S1 printer*

Table 1. *Creality Ender 3 S1 printer product parameters*

Molding Technology	FDM
Printer Size	487x453x622 mm
Build Size	220 x 220 x 270 mm
Package Size	540 x 510x 260 mm
Supported Filaments	PLA/TPU/ PETG/ABS
Nozzle Diameter	0.4 mm
Maximum Nozzle Temperature	260°C
Printing Speed	Maximum 160mm /s
Maximum Heatbed Temperature	100°C

The technical features of the Creality Ender 3 S1 3D printer that is used for printing are given in table 1 [8]. Material selection is important since the produced TLD holder cassette will be used in radiation irradiation. Porima PLA (Polylactic acid) filament was used in this study. Because this material has much better mechanical properties than materials such as polyurethane, polypropylene and plastic. Therefore, it is the most preferred filament type. PLA filament parameters are given in table 2

Figure 4. *The image of the TLD holder cassette in the Ultimaker Cura program*

3. Results and Discussions

Creality Ender 3 S1 printer was used for the output of the 3D model (Fig. 5). FDM technique was used while printing the TLD holder cassette.

[9]. Fig. 6 shows the 3D printing of the model created for the TLDs.

Table 2. Technical properties of PLA material

Density	1.24 g/cm^3
Coefficient of Thermal Expansion	68μm/m-°C
Tensile Strength	65 MPa
Maximum Operating Temperature	52 °C
Nozzle	200 – 230 °C
Bed	60- 75 °C

Figure 6. *A printed version of the TLD holder cassette*

When the printed material is examined visually, it is seen that it is exactly compatible with the designed model. Fig. 6 shows TLDs placed in the printing TLD holder for irradiation.

As shown in detail A in Fig. 2, each slot is manufactured in accordance with the TLD size. Chip-type TLDs are embedded in Fig. 5. However, the TLD holder cassette is also suitable for the placement of rod and powder-type TLDs.

In Fig. 6, markings on the plates are placed to orient them during the calibration of the TLDs. The printed TLD holder cassette has been used and tested in the calibration of TLDs.

There are many publications in the literature on the use of 3D printing applications in different fields and for specific purposes. When time and cost calculations are made, products produced with 3D printing are more advantageous.

One of the most common areas where 3D printing technologies are used for professional purposes in the production of functional parts is the biomedical sector.

In the literature, there are TLD holder apparatus made from various materials used during the storage and irradiation of TLDs. In Toossi et. al study, TLDs were set in a PMMA plate, which had slots for putting TLDs [10]. In Suleiman et.al study, the PMMA slab was used to accommodate the TLD chips in an array of slots 10x10 [6]. In Aksözen et. al study, TLDs were calibrated on a 30 cm x 30 cm rigid plexiglass holder cassette [11].

In our study, PLA material, which is a 3D printer material, was used for the TLD cassette holder, unlike the materials in the literature. The production processes of cassette holders that were produced with plexiglass and PMMA materials are more time-consuming and costly than 3D printing. Thanks to 3D design and printing technology, it can be used for calibration and storing TLDs by creating holes on the cassette holder according to the TLD type to be used. At the same time, the loss of TLDs can be prevented by producing a top cover for the cassette holder exactly as in our study.

4. Conclusions

3D design and printing technology have a wide range of applications in the health sector, from patient-specific designs to special production of device parts. Thanks to its 3D printing technique, easy design, fast production, and low cost solves the problems or deficiencies. In this study, for TLD irradiation, an apparatus has been designed to be used in calibration and readings of TLD dosimeters and it has been proven that it can be printed with 3D printing technique.

Author Statements:

- **Ethical approval:** The conducted research is not related to either human or animal use.
- **Conflict of interest:** The authors declare that they have no known competing financial interests or personal relationships that could have

appeared to influence the work reported in this paper

- **Data availability statement:** The data that support the findings of this study are available on request from the corresponding author. The data are not publicly available due to privacy or ethical restrictions.

References

[1] Sürmen, H. K. (2019). Eklemeli İmalat (3b Baski): Teknolojiler Ve Uygulamalar. *Uludağ Üniversitesi Mühendislik Fakültesi Dergisi*. 24 (2): 373-392 . DOI: 10.17482/uumfd.519147.

[2] Ecker, J.V., Kracalik, M., Hild, S., & Haider, A. (2017). 3D- Material Extrusion – Printing with Biopolymers: A Review. *Chemical and Materials Engineering*. 5(4): 83-96.

[3] Aksözen, M. T., Yaray, K., Menteş, S., Gündoğ, M., Eroğlu, C.(2012). "Calibration of Gamma Rays With LiF Thermoluminescence Dosimeters". *Türk Onkoloji Dergisi*, 27(1): 24-28.

[4] Dönmez, S. (2017). Radyasyon Tespiti ve Ölçümü. *Nucl Med Semin*.3:172-177.

[5] McKinlay, AF.(1981). *Thermoluminescence dosimetry-medical physics handbook*; 5. Çeviri: Aypar A, Akın E. Medikal fizik kitapları 5. Termolüminesans dozimetri. Adam Hilger Ltd; s. 57-123.

[6] D'Avinio, V., Caruso, M., Arrichiello, C.et. al. (2020). *Il Nuovo Cimento*.43 C:142. DOI 10.1393/ncc/i2020-20142-0.

[7] Suleiman, A. Theodorou,K., Vlychou, M. et al. (2007). "Radiation dose measurement and risk estimation for paediatric patients undergoing micturating cystourethrography". *The British Journal of Radiology*, 80:731-737. https://doi.org/10.1259/bjr/16010686

[8] Creality Ender 3 S1 3D printer technical features, https://www.porima3d.com/

[9] Porima PLA Filament technical features, https://www.porima3d.com/

[10] Bahreyni Toossi, MT., Vejdani Noghreiyan, A., Gholamhosseinian H. (2018). "Assessment of the Effects of Radiation Type and Energy on the Calibration of TLD-100". *Iran J Med Phys*., 15:140-145. 10.22038/ijmp.2017.26744.1275.

[11] Aksözen, MT, Yaray, K., Menteş, S. vd. (2012). "LiF termolüminesans dozimetrelerin gama ışınları ile Kalibrasyonu". *Türk Onkoloji Dergisi*, 1;24-28. doi: 10.5505/tjoncol.2012.714

Research Article
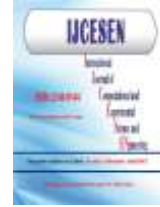
A Novel Deep Learning Model for Pain Intensity Evaluation

Mahmut Emin ÇELİK [1]*

[1]Electrical Electronics Engineering Department, Faculty of Engineering, Gazi University, Ankara, Turkey
* **Corresponding Author** : **Email:** mahmutemincelik@gazi.edu.tr - **ORCID:** 0000-0002-1766-5514

Abstract:

Pain assessment is a critical component of healthcare, influencing effective pain management, individualized care, identification of underlying issues, and patient satisfaction. However, the subjectivity and limitations of self-reported assessments have led to disparities in pain evaluation, particularly in vulnerable populations such as children, the elderly, individuals with cognitive impairments, and those with mental health conditions. Recent advances in technology and artificial intelligence (AI) have paved the way for innovative solutions in pain intensity evaluation.This paper presents a novel deep learning model to automatically classify pain intensity levels and compares them with six state-of-the-art deep learning classification models - ResNet-50, VGG-19, EfficientNet, DenseNets, Inception, and Xception- using the UNBC-McMaster Shoulder Pain Expression Archive Database for training. Transfer learning is employed to optimize model efficiency and minimize the need for extensive labeled data. Model evaluations are conducted based on accuracy, precision, recall, and F1 score. The proposed model, ZNet, showed superior performance of 95.4%, 64.4% and 63.4%, 63.7% for accuracy, precision, recall and F1-score respectively. Furthermore, this study addresses the challenge of accurately evaluating pain intensity in patients who cannot communicate verbally or face language barriers. By harnessing AI technology and facial expression analysis methods, we aim to provide an objective, reliable, and precise pain assessment methodology. Automated artificial based solutions enhance the reliability of pain evaluations, and holds promise for improving decision-making in pain management and treatment processes, ultimately enhancing patients' quality of life.

1. Introduction

Pain assessment is the process of evaluating and measuring an individual's pain experience to understand its nature, severity, and impact on their well-being. It is an essential component of healthcare, as it helps healthcare providers and clinicians make informed decisions regarding pain management and treatment. It is critically needed for the following reasons:

- Effective Pain Management: Accurate pain assessment is crucial for providing appropriate pain relief. It helps healthcare professionals determine the most suitable interventions, medications, or therapies to alleviate pain and improve the patient's comfort and quality of life.
- Individualized Care: Pain experiences can vary greatly from person to person. Pain assessment allows healthcare providers to tailor their approach to each patient's unique needs,

ensuring that treatment plans are individualized and effective.

- Identification of Underlying Issues: Pain can be a symptom of an underlying medical condition. By assessing pain comprehensively, healthcare providers can identify potential causes that may require further investigation and treatment.
- Patient Satisfaction: Adequate pain management and communication about pain contribute to higher levels of patient satisfaction with their healthcare experience.

There is a notable absence of an effective and dependable method for the objective quantification of an individual's pain experience. Healthcare professionals and organizations predominantly depend on a patient's self-reported assessment to ascertain the severity of pain; however, these approaches may exhibit limitations and potential inaccuracies. On the other hand, there are several

disadvantaged groups of patients that pain intensity evaluation is of great importance due to the impossibility of communication [1,2]. The first group is children and the elderly. Vulnerable populations like children and the elderly may experience disparities in pain assessment. Young children may have difficulty communicating their pain, while older adults may have their pain dismissed as a natural part of aging. The other is individuals with cognitive impairments. People with cognitive impairments, such as dementia or intellectual disabilities, may have difficulty expressing their pain or may not be taken seriously when they do communicate their pain. This can lead to underassessment and undertreatment. Lastly, individuals with mental health conditions may experience disparities in pain assessment. Pain complaints in these individuals can sometimes be attributed to their psychiatric condition, and their physical pain may be overlooked or undertreated. In recent years, advances in technology, along with multidisciplinary studies in medicine and engineering, have enabled the development of various approaches to understand and manage pain. The use of AI techniques for pain intensity evaluation contributes to the more effective assessment of patients and the creation of appropriate treatment plans [1-4]. Artificial intelligence (AI) plays a pioneering role in various fields of research including medicine. It has a wide range of applications providing a crucial support in medical and dental diagnosis and treatment processes [5-7]. Table 1 presents previous works using deep learning. AI-based automated solutions are now needed to reduce the subjectivity of existing methods that often rely on subjective and inconsistent reports from patients or clinicians due to lack of measurements and different conceptualizations. The present study aims:

- to develop a novel deep learning model for pain intensity evaluation that can automatically
- detect the pain level using facial expressions with 4 different levels.
- to compare the proposed model with the state of art six different deep learning classification models.

The publicly available dataset, UNBC-McMaster Shoulder Pain Expression Archive Database, is used for training the models. The transfer learning concept has been applied to leverage pre-existing knowledge, reduce the need for massive amounts of labeled data, and improve the efficiency of model training. Deep learning models are evaluated by accuracy, precision, recall and F1 score.

Table 1. Comparison of previous studies with details

Reference	Purpose	Dataset	Method	Results
Weitz et al [1]	Distinguishing expressions of pain from emotions such as happiness and disgust using facial expressions	Pain Intensity 3: 12,006 Pain Intensity 4: 12,006 Disgust: 24,075 Happiness: 24,075	VGG-Face LRP (Layer-wise Relevance Propagation)	Pain: Precision: 0.62 Recall: 0.69 F1-score: 0.66 Disgust: Precision: 0.70 Recall: 0.73 F1-score: 0.71 Happiness: Precision: 0.67 Recall: 0.57 F1-score: 0.62
Prabal Datta et al [18]	Assisting physicians in non-verbal identification of pain using facial images for uncommunicative patients or during surgery	UNBC: 10852 frames DISFA: 39182 frames	DarkNet19	UNBC-McMaster Acc: 95.57% UAR: 95.59% UAP: 95.79% Average F1: 95.67% MCC: 94.14% CK: 93.93% GM: 95.58% DISFA Acc: 96.06% UAR: 96.04% UAP: 96.16% Average F1: 96.08% MCC: 94.78% CK: 94.74% GM: 96.03%
Zakia Hammal and Jeffrey F. Cohn [19]	To reliably measure pain intensity Pain assessment and management	16,657	AAM (Active Appearance Model): are used to extrac the canonical appearence of the face (CAPP) Log Normal Filters SVM (for classification)	Mean CR: 97% Mean PR: 96.75% Mean F1-score: 93.5%
Fontaine et al	Pain intensity evaluation for especially non- communicating people in clinical condition	2810	ResNet- 18	Accuracy: 32% - 53%

This work contributed to the existing technology as follows:

- it proposes a new deep learning model, namely ZNet
- it compares proposed model with existing 6 classification models
- it provides superior performance with transfer learning
- it promises for improved decision-making
- it comprehensively discusses current limitations towards clinical integration.

2. Material and Methods

The facial expressions are based on the Prkachin and Solomon Pain Intensity (PSPI) metric that relies on the Facial Action Coding System (FACS) and is widely used for manual pain assessment [8]. The UNBC-McMaster Shoulder Pain Expression Archive Database is publicly available, and it is used for training the models [8]. The UNBC-McMaster database has been classified according to the PSPI metric, resulting in 16 different levels. To facilitate the analysis and balance the data, we performed class merging inspired by previous works, resulting in 4 classes [4,9,10]. Each class includes PSPI0, PSPI1-2, PSPI3-4, and PSPI4+ respectively. Each class, namely, class0, class1-2, class3-4 and class4+ has 40,029, 5,260, 2,214 and 895 frames respectively. Figure 1 demonstrates example images from the dataset for each class. Data is divided into training, validation and test set with the ratio of 70%, 20% and 10%. Additionally, a preprocessing step normalized and resized images to 128x128 pixels to get more stable training process. The state of art 6 different deep learning classification models is used to classify pain intensity using facial expressions. Namely, ResNet-50, VGG-19, EfficientNet, DenseNets, Inception, and Xception were implemented [11-16]. Additionally, a novel custom-designed deep learning model is proposed for the same problem. Model performances are evaluated by widely used evaluation metrics that might be considered as a standard for the classification tasks. Accuracy, Precision, Recall, and F1-score are employed to determine classification ability of the models. Briefly, accuracy metric measures the model's correct classification rate, while precision and recall metrics assess how the model classifies positive and negative classes. The F1-score combines precision and recall metrics to measure the overall performance of the model. These metrics serve as essential tools to understand how effective the models are in real-world applications and to enhance their performance. Figure 2 shows the flowchart of the deep learning application.

Figure 1. *Example images for each class form the dataset*
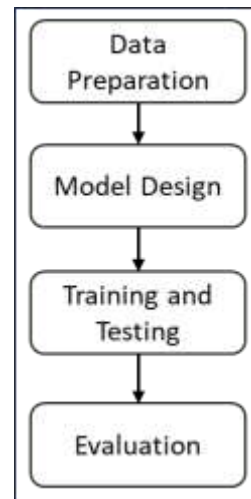
Figure 2. *Flowchart of the application*

2.1 Proposed Model: ZNet

ZNet model is inspired by the UNet architecture. The model architecture can be explained as follows. Figure 3 presents model architecture.

The ZNet model consists of double convolutional blocks, max-pooling layers, and Z-point merging layers for feature extraction and learning.

The configuration of the model is as follows:

•Input Layer: The model takes color images as input (n_channels=3).

•Double Convolutional Blocks (DoubleConv): Each DoubleConv block comprises two consecutive convolutional layers, batch normalization, and ReLU activation functions. These blocks serve as the basic building blocks for learning and feature extraction.

•Max Pooling Layers (MaxPoolLayer): Max pooling layers are used in the Znet model to reduce the size of feature maps. These layers significantly decrease the computation cost and the number of learnable parameters.

•Z-point Merging Layers (Zpoint): Zpoint layers are employed to merge feature maps with different dimensions. This allows the model to combine both low-level and high-level features for better feature extraction.

•Batch Normalization Layers: Batch normalization is a technique that accelerates the training of the network and reduces the risk of overfitting. In the ZNet model, batch normalization layers are used to stabilize the model's performance.

•Classification Layer (classifierPart): The classification layer at the output of the ZNet model is used for pain level classification. This layer flattens the feature maps and uses fully connected layers to predict the pain level.
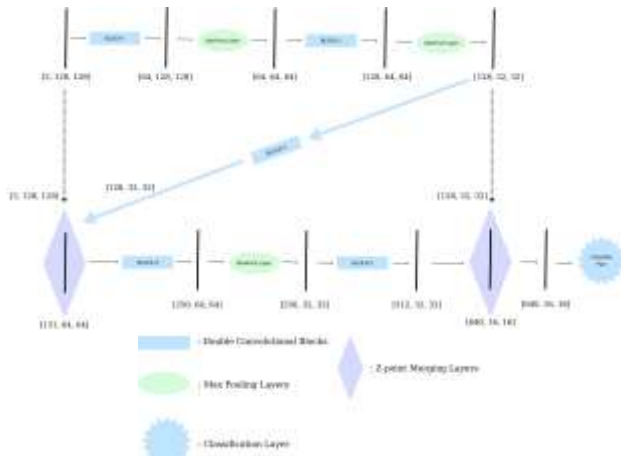
Figure 3. ZNet architecture representation

It is aimed to enhance model's performance by using skip connections to directly transmit low-level features to high-level features. These connections allow our model to transfer the knowledge of low-level features to more complex and meaningful features in the high-level layers. Skipped connections are a widely used technique, especially in models like UNet, and they often yield good results in segmentation and image processing tasks. Low-level features usually contain more basic and local information, while high-level features represent more abstract and comprehensive information. Therefore, skipped connections contribute to the model's ability to generalize better. However, each connection passing through each layer adds to the increase in the number of parameters. This is an important consideration in model training and performance evaluation [17]. Using skipped connections too frequently can lead to overfitting and unnecessary growth of weight

matrices. Hence, it is needed to carefully determine the skip connections and reduce them when necessary. This way, we can achieve good performance while keeping the number of parameters under control, making the model training more effective.

3. Results and Discussions

Model performances are obtained and presented as follows. The confusion matrix for each model, Inception, Xception, Densenet, EfficientNet, Znet, ResNet-50, and VGG-19, are used to get evaluation metrics. Inception achieved a validation accuracy of 88.4% but struggled with precision and recall, scoring 48.9% and 45.5% respectively. The F1-score of 46.4% indicates a moderate balance between precision and recall. On the test set, Inception achieved a decent general accuracy of 87.7%, but the accuracy for certain classes (class1-2, class3-4, and class4+) was significantly lower. The Xception demonstrated better results than Inception, with a validation accuracy of 95.3% and higher precision and recall scores of 49.7% and 48.4% respectively. However, the F1-score remained relatively low at 48.9%. On the test set, Xception performed well overall with a general accuracy of 95.4%. However, particularly class3-4 and class4+ provided lower rates. The Densenet achieved a validation accuracy of 92.2% with balanced precision and recall scores of 59.3% and 57.3% respectively. The F1-score of 58.0% indicates a satisfactory balance. On the test set, Densenet demonstrated a good general accuracy of 91.9%, but similar to other models, it faced challenges with several other class accuracies. The EfficientNet achieved a validation accuracy of 89.4% with relatively low precision and recall scores of 48.8% and 45.9% respectively. The F1-score was 46.7%, indicating a need for better improvement in handling class imbalances. On the test set, EfficientNet showed a general accuracy of 89.5%. ResNet-50 achieved a validation accuracy of 92.0% with precision and recall scores of 42.8% and 40.8% respectively, resulting in an F1-score of 41.6%. On the test set, ResNet-50 demonstrated an overall accuracy of 91.6%, with better performance for class0 but lower accuracy for other classes. VGG-19 achieved a validation accuracy of 91.9% with balanced precision and recall scores of 66.4% and 64.1% respectively, leading to an F1-score of 64.8%. On the test set, VGG-19 showed high accuracy for class0 but decreased with several class accuracies, especially for class1-2 and class3-4. ZNet, a novel model inspired by skip connections and Unet architecture, demonstrated remarkable performance. It achieved a validation accuracy of 95.4%, with precision and recall scores of 64.4% and 63.4%,

respectively, resulting in an F1-score of 63.7%. The model exhibited a strong balance between precision and recall. On the test set, ZNet excelled in classifying minority classes (class1-2, class3-4, and class4+), achieving an accuracy of 85.2%, 85.5%, and 69.7% respectively. The overall test accuracy of 96.5% showcases ZNet's capability to achieve superior performance in real-world applications.

Overall, the proposed model achieves superior and successful results. In real-life tests conducted on the test dataset, we can observe that the ZNet model achieved better results compared to other models in terms of both class-specific and overall accuracy values, as shown in Table 2.

Table 2. Class-based performance of the models for testing

Model	Accuracy (%)				
	Class 0 (PSPI$_0$)	Class 1-2 (PSPI$_{1-2}$)	Class 3-4 (PSPI$_{3-4}$)	Class4 + (PSPI$_{4+}$)	Average
Densenet	98.13	67.30	51.13	59.55	91.92
Efficient Net	97.93	55.70	37.10	40.45	89.50
Inception	97.95	40.87	35.29	33.71	87.70
ResNet-50	96.75	65.97	70.14	61.80	91.55
VGG-19	**99.35**	55.89	57.01	53.93	91.86
Xception	97.48	**90.87**	*79.74*	*65.17*	*95.35*
ZNet	*99.20*	*85.17*	**85.52**	**69.66**	**96.51**

Automated pain level evaluation research using modern artificial intelligence technologies has an increasing trend in medical informatics. This work explores the applicability and performance of various deep learning models for pain level classification using facial expressions. Results indicate that the proposed model in addition to other deep learning models can successfully predict pain level classes with high performance. The proposed model yielded superior performance for three out of four classes in the dataset. Deep learning models have shown promising results in accurately categorizing pain intensity levels. However, it is important to acknowledge that the accuracy of these models may vary depending on the dataset, the choice of architecture, and the quality of the input data. Transitioning from research to practical clinical applications requires careful consideration. The integration of deep learning models into healthcare settings demands robust validation, collaboration with medical professionals, and adherence to regulatory guidelines. Additionally, the development of user-friendly interfaces for healthcare providers is essential to facilitate

adoption. Previous studies including intensity level classification using deep learning are investigated for comparison purposes. Table 2 lists previous studies based on their purpose, dataset size, method and results reported. Weitz et al applied a deep learning model to distinguish pain expressions from emotions such as happiness and disgust using facial expressions [1]. Prabal Datta et al used DarkNet19 to assist physicians in non-verbal identification of pain using facial images for uncommunicative patients or during surgery [18]. Zakia Hammal et al used SVM for classification to reliably measure pain intensity pain assessment and management [19]. Fontaine et al applied ResNet-18 classification model to facial expressions of patients taken in clinical conditions, then compared them with the findings of nurses related to pain level of the patients [2]. There are several limitations, firstly the lack of a wide balanced public dataset of facial expressions. Previous studies have not used significant open datasets, making it difficult to compare the performance of deep learning models. In order to apply the developed models, it is necessary to use large, balanced datasets that have been identified by doctors. In the open-source dataset used in this study, the number of categories was reduced from 16 to 4 to ensure balance between classes as applied in previous studies, but a more balanced dataset is ideally an important requirement for clinical integration. Data privacy and ethical concerns should be considered, which may limit the ability to prepare and share a large multi-centered data set.

4. Conclusions

The application of deep learning techniques for the evaluation of pain intensity levels represents a significant advancement in the field of healthcare and pain management. Deep learning models have demonstrated their effectiveness in categorizing pain intensity levels. In conclusion, the use of deep learning for pain intensity level evaluation is a promising development with the potential to revolutionize pain management and improve the lives of countless individuals. As researchers and healthcare providers continue to work on refining and implementing these technologies.

Author Statements:

- **Ethical approval:** The conducted research is not related to either human or animal use.
- **Conflict of interest:** The authors declare that they have no known competing financial interests or personal relationships that could have

appeared to influence the work reported in this paper

References

[1]. Weitz, K., Hassan, T., Schmid, U., & Garbas, J. U. (2019). Deep-learned faces of pain and emotions: Elucidating the differences of facial expressions with the help of explainable AI methods. *tm-Technisches Messen,* 86(7-8); 404-412. DOI: 10.1515/teme-2019-0024.

[2]. Fontaine, D., Vielzeuf, V., Genestier, P., Limeux, P., Santucci-Sivilotto, S., Mory, E., ... & DEFI study group. (2022). Artificial intelligence to evaluate postoperative pain based on facial expression recognition. *European Journal of Pain*, 26(6); 1282-1291. DOI: 10.1002/ejp.1948.

[3]. Hasan, M. K., Ahsan, G. M. T., Ahamed, S. I., Love, R., & Salim, R. (2016). Pain level detection from facial image captured by smartphone. *Journal of Information Processing*, 24(4); 598-608. DOI: 10.2197/ipsjjip.24.598.

[4]. Barua, P. D., Baygin, N., Dogan, S., Baygin, M., Arunkumar, N., Fujita, H., ... & Acharya, U. R. (2022). Automated detection of pain levels using deep feature extraction from shutter blinds-based dynamic-sized horizontal patches with facial images. *Scientific reports,* 12(1); 17297. DOI: 10.1038/s41598-022-21380-4.

[5]. Çelik, B., & Çelik, M. E. (2023). Root Dilaceration Using Deep Learning: A Diagnostic Approach. *Applied Sciences,* 13(14); 8260. DOI: 10.3390/app13148260.

[6]. Wang, R., Lei, T., Cui, R., Zhang, B., Meng, H., & Nandi, A. K. (2022). Medical image segmentation using deep learning: A survey. *IET Image Processing*, 16(5); 1243-1267. DOI: 10.1049/ipr2.12419.

[7]. Çelik, B., & Çelik, M. E. (2022). Automated detection of dental restorations using deep learning on panoramic radiographs. *Dentomaxillofacial Radiology*, 51(8); 20220244. DOI: 10.1259/dmfr.20220244.

[8]. Lucey, P., Cohn, J. F., Prkachin, K. M., Solomon, P. E., & Matthews, I. (2011, March). Painful data: The UNBC-McMaster shoulder pain expression archive database. In 2011 IEEE International Conference on Automatic Face & Gesture Recognition (FG) (pp. 57-64). IEEE. DOI: 10.1109/FG.2011.5771462.

[9]. Bargshady, G., Zhou, X., Deo, R. C., Soar, J., Whittaker, F., & Wang, H. (2020). Enhanced deep learning algorithm development to detect pain intensity from facial expression images. *Expert Systems with Applications*, 149; 113305. DOI: 10.1016/j.eswa.2020.113305.

[10]. Nguyen, D. C., Pham, Q. V., Pathirana, P. N., Ding, M., Seneviratne, A., Lin, Z., ... & Hwang, W. J. (2022). Federated learning for smart healthcare: A survey. *ACM Computing Surveys (CSUR)*, 55(3); 1-37. DOI: 10.48550/arXiv.2111.08834.

[11]. He, K., Zhang, X., Ren, S., & Sun, J. (2016). Deep residual learning for image recognition. In Proceedings of the IEEE conference on computer vision and pattern recognition (pp. 770-778). DOI: 10.48550/arXiv.1512.03385.

[12]. Simonyan, K., & Zisserman, A. (2014). Very deep convolutional networks for large-scale image recognition. arXiv preprint arXiv:1409.1556. DOI: 10.48550/arXiv.1409.1556.

[13]. Tan, M., & Le, Q. (2019, May). Efficientnet: Rethinking model scaling for convolutional neural networks. In International conference on machine learning (pp. 6105-6114). PMLR. DOI: 10.48550/arXiv.1905.11946.

[14]. Huang, G., Liu, Z., Van Der Maaten, L., & Weinberger, K. Q. (2017). Densely connected convolutional networks. In Proceedings of the IEEE conference on computer vision and pattern recognition (pp. 4700-4708). DOI: 10.48550/arXiv.1608.06993.

[15]. Szegedy, C., Liu, W., Jia, Y., Sermanet, P., Reed, S., Anguelov, D., ... & Rabinovich, A. (2015). Going deeper with convolutions. In Proceedings of the IEEE conference on computer vision and pattern recognition (pp. 1-9). DOI: 10.48550/arXiv.1409.4842.

[16]. Chollet, F. (2017). Xception: Deep learning with depthwise separable convolutions. In Proceedings of the IEEE conference on computer vision and pattern recognition (pp. 1251-1258). DOI: 10.1109/CVPR.2017.195.

[17]. Erol, T., & Sarikaya, D. (2022). PlutoNet: An Efficient Polyp Segmentation Network with Modified Partial Decoder and Decoder Consistency Training. *arXiv preprint arXiv*:2204.03652. DOI: 10.48550/arXiv.2204.03652.

[18]. Barua, P. D., Baygin, N., Dogan, S., Baygin, M., Arunkumar, N., Fujita, H., ... & Acharya, U. R. (2022). Automated detection of pain levels using deep feature extraction from shutter blinds-based dynamic-sized horizontal patches with facial images. Scientific reports, 12(1), 17297. DOI: 10.1038/s41598-022-21380-4.

[19]. Hammal, Z., & Cohn, J. F. (2012, October). Automatic detection of pain intensity. In Proceedings of the 14th ACM international conference on Multimodal interaction (pp. 47-52). DOI: 10.1145/2388676.2388688.

Research Article
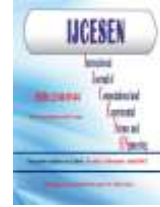
Possibility of Using Eggshell in Industry

Günnur PEŞMEN*

Afyon Kocatepe Üniversity, Laborant Veterinary Health Programme, 32200, Afyonkarahisar/Turkey
* **Corresponding Author** : **Email:** gpesmen@aku.edu.tr - **ORCID:** 0000-0002-9164-6629

Abstract:

The amount of eggshells (chicken, duck, ostrich, turkey, goose, and quail eggs) that go to waste every year around the world is frightening. Eggshells are foods with high nutritional value that should not go to waste. Chicken egg shells, which contain significant amounts of calcium and minerals, end up in landfills without further processing. As a by-product, it creates an important problem for producers both economically and ecologically. The purpose of this review is to summarize the results of various research articles on eggshell and to provide a reference for subsequent studies in this field and to expand the usage areas of eggshell. Numerous studies have shown that eggshells are an important material, a currently unused calcium store. Finding ways to use eggshells for nutritional and non-nutritional purposes not only reduces waste but also provides several economic benefits. A total of 83 sources were used in the review. In the compilation study, the studies on saving the eggshell from the waste position and transforming it into a material with high added value are summarized. It is a reference in studies to be conducted on alternative uses of eggshell.

1. Introduction

In proportion to the high consumption of eggs in the world, a huge amount of waste eggshell is generated. Eggshell has the opportunity to be reused in various fields due to its valuable organic and inorganic components, and studies on this subject have increased in recent years [1]. Eggshells reached a worldwide production of 7.8 million tons in 2018 [2]. While approximately 10% of eggshells can be used in the feed industry in Turkey, the remaining 90% goes to waste. This means that 120,000 tons of eggshells are thrown away unused annually [3]. It is important to evaluate waste materials in the production of some useful products and also to follow the 3R sustainability concept (reduce, reuse, and recycle) [4]. The main components of eggshell are carbonates, sulfates and phosphates of calcium and magnesium, and organic matter. The density of the egg shell is about 2.53 g/cm3. The main components of eggshell are calcium carbonate (94%) (380 mg Ca per gram), organic matter (4%), calcium phosphate 1% and magnesium carbonate (1%) [1;5] Ajala et al. [6], eggshell characterization Ca: 2300.33 ± 3.80, Mg; 850.00 ± 1.24, Na; 33.83 ± 0.72, N; 17.06 ± 1.04, Fe; 1.4 ± 0.03, Zn; 0.99 ± 0.04 and Cu; as 0.063 ± 0.01 mg/L, 0.95 ± 0.89 moisture,

45.29 ± 0.06, ash; 1.40 ± 0.25, crude protein; 0.37 ± 0.06, lipid; 4.38 ± 0.32, crude fiber; 47.63 ± 0.32 (%), carbohydrate and caloric value it was found to be 811 ± 12.71 (cal/g). The shell makes up 9-12 percent of the total weight of an egg and there are about 8,000 microscopic pores in the eggshell [7; 8]. Unlike commercial activated carbon, the pore size of eggshell is about 10 times higher. The measured pH values of eggshell and commercial activated carbon are 9.49 and 5.76, respectively [9].

Among the toxic gases released into the atmosphere during the decomposition process of the eggshell are ammonia (NH3) and hydrogen sulfide (H2S). Proper management of these wastes can reduce the risk of microbiological problems and the costs of their disposal into the environment and provide a better source of CaCO3 than limestone mined from non-renewable sources [10].

After removing the membranes from egg shells, drying, grinding, and sieving, it is possible to obtain calcium carbonate. The purity of the obtained calcium carbonate is about 93.7% [11]. Ayawanna et al. [12] reported that glass-ceramic implants produced from eggshells have good chemical stability in the biological environment (in vitro). Biomaterials are materials used in the human body to perform the functions of living tissues that have

lost their function [13]. Egg shells are biodegradable and biocompatible. When used in biomedical materials, it is possible to obtain fillers or biologically neutral implants for bones and implants. Shells can be a valuable source of hydroxyapatite, especially in biomedical applications [14;15]. Yönetken et al. [16] produced composite material using a powder metallurgy technique with titanium, boron carbide, and eggshell powders, which is one of the indispensable elements of biomaterials, and demonstrated the alternative use of eggshell. Yönetken et al. [17] reported that the composite obtained by adding eggshell powder to Ti-Titanium-based intermetallic compounds would be suitable for cutting or scratching tools used in the soil industry. Bilici et al. [18] and Yönetken et al. [19] reported that the hardness and ultrasonic wave speeds of the material produced increased by using certain amounts of eggshell powder in ceramic-metal composites. Jannet et al. [20] reported that an aluminum alloy (AA2024) composite containing 7% eggshell powder has properties that make it suitable for high tensile and compression applications in the automobile and aerospace industries. Akgürbüz and Uysal [21] determined that the composites obtained by using eggshell, sewage sludge, and meerschaum provided sufficient mechanical properties (tensile strength, modulus of elasticity in tensile, bending strength, modulus of elasticity in bending, elongation at break and impact resistance). Skórczewska et al. [15] successfully produced poly(vinyl chloride) composites with significantly improved thermal stability by using waste eggshell as a natural filler in poly(vinyl chloride) composites [15].

In recent years, the human population and anthropogenic activities have increased and the need to develop an efficient gas sensor has arisen [22]. Ammonia (NH3) is a poisonous gas and its threshold concentration is 25 ppm [23]. Therefore, the development of an NH3 gas sensor is of great importance due to its various applications in many industries such as food, automotive, chemical, and pharmaceutical [22]. A simple, cost-effective, and novel chemical sensor for ammonia (NH3) gas detection has been developed from polyaniline (PANI)/eggshell (ES) composites. Norsham et al. [22] found that PANI/ES biocomposites exhibit excellent selectivity towards NH3 gas even in the presence of other gases such as acetone, ethanol, and hexane.

The pores in the eggshell indicate that they can also be used as effective adsorbents. In the last decade, eggshell has been used in wastewater treatment to remove organic and inorganic hazardous substances [5]. Heavy metals slow down metabolic reactions and are toxic to living organisms. Lee et al. [24]

reported that calcined eggshell had the highest P adsorption in an aqueous solution. Researchers have stated that eggshell can be used as a P-binding absorbent and P-adsorbed calcined eggshells can be used as a potential P fertilizer, thus allowing P to circulate from water to soil [24]. One of the compounds used to absorb heavy metals in water is activated carbon. Activated carbon is the most widely used adsorbent and is used in drinking water treatment, solvent recovery, decolorization, metal mining processes, and various domestic applications. Activated carbon has disadvantages such as regeneration costs and less neutralization of acids [25; 26]. In eggshells, CaCO3 is a polar adsorbent that can be used not only as an absorber for heavy metals but also for neutralizing acids in water [27; 27]. The adsorption process takes place in the pores or in certain parts of the particles [29]. Eggshell can be developed in nanoporous form using sodium hypochlorite and hydrochloric acid [30]. Setiawan et al.[30] stated that duck egg shell had a better ability to absorb metal and neutralize acid than chicken and quail egg shells to reduce heavy metal and acidity in water. They also reported that the nanoporous eggshell had a better ability to absorb metals and neutralize acids compared to activated carbon. Ajala et al. [6] revealed the presence of the correct ratio of carbon and oxygen in the eggshell as a good alternative adsorbent for the removal of heavy metals and dyes from aqueous solutions.

Kamgang-Syapnjeu et al. [31] used eggshell in the production of a new ceramic membrane for the removal of pathogenic microorganisms in water and reported that the obtained ceramic membrane had the ability to retain 90% of E. coli bacteria and could be used for a preliminary water treatment. Ok et al. [32] reported that eggshell wastes can be used as an alternative to CaCO3 for the immobilization of heavy metals in polluted soils.

Recently, in removing heavy metal ions from industrial wastes, conventional metal ion removal methods have become ineffective in removing metal ions below 1 mg/kg concentration. Therefore, there was a need for other methods that could be effective at low concentrations [33]. It has been determined that eggshells have a biosorption capacity two times higher than activated carbon in the absorption of Cr (III) ions from aqueous solutions [34]. According to Kim et al. [9], eggshells are an effective bioadsorbent in removing heavy metals such as Pb2+, Cd2+, and Cr3+ from water. Muhaisen et al. [35] reported that cadmium was significantly adsorbed by eggshells. According to Somaia et al. [36], copper (II) ions in aqueous solutions can be removed from eggshell nanoparticles significantly more quickly than from untreated eggshell. Fluoride is a dangerous pollutant that must be removed during

water treatment to provide water suitable for consumption [37]. Lee et al. [24] reported that eggshells are highly efficient adsorbents that can replace bone charcoal and activated alumina for fluoride removal in water as adsorbent, and that their adsorption capacity can be improved by heat treatment. The presence of various functional groups and high carbon content in eggshell make it a potential material for adsorbent to remove heavy metals and dyes in wastewater treatment [6]. Eggshell is a low-cost adsorbent to remove cobalt $(CO+2)$ and lithium $(Li+)$ ions from polluted soils [38].

Biodiesel is an environmentally friendly fuel and a good alternative to fossil fuels. Wei et al. [39] found that eggshell could be used as a 98% efficient solid catalyst in biodiesel synthesis, Chavan et al. [40], on the other hand, 90% efficiency in biodiesel production from Jatropha curcas oil using calcium oxide prepared from eggshell as a catalyst, Navajas et al. [41], on the other hand, obtained 100% yield from edible oil. Cho and Seo [42] reported that calcined quail egg shells showed better catalytic activity than chicken egg shells. Çetin [43], Rashid et al. [44] reported that eggshells, which are used as heterogeneous catalysts, reach high yields in the green fuel production reaction, are environmentally friendly, and reduce catalyst costs. Ayoola et al. [45] revealed that duck eggshells can lead to the production of high quantity and quality CaO catalysts. The pores in the eggshell have made it suitable for the use of heterogeneous catalysts in biodiesel production [6].

Stainless steel is one of the most widely used metals in many industries because it forms a protective film on its surface that prevents the metal from reacting with corrosive environments such as sulfuric acid [46]. Sanni et al. [46] revealed that eggshell powder can be used as a corrosion inhibitor on stainless steel. Ultraviolet (UV) light has harmful effects on synthetic polymers and biopolymers such as leather, hair, and wood [47]. These materials absorb UV, triggering photolytic and photooxidative reactions, causing photodegradation and permanent loss of beneficial physical, mechanical, and optical properties [48]. While many materials used today contain UV-protective additives, they are not always effective and durable, can be expensive, and their natural extraction or synthetic production can be harmful to the environment. Lippens et al. [48] used untreated egg shells to provide UV protection to polystyrene and nylon and compared them with TiO2 UV protective additive. The eggshell used in the study provided effective and durable protection to nylon and polystyrene. Nylon protected with eggshell showed slower photo-oxidative rates

compared to nylon protected with embedded TiO2 particles [48].

Due to the high CaCO3 content in eggshells, Binici et al. [49] found that the radiation permeability of composites with eggshell added significantly decreased. These composites could be used as radiation-scavenging flooring and partition walls in areas with radioactive devices.

Nath et al. [50] determined that the antibacterial activity of pure CaO obtained from egg shells at 900 °C against E. coli was quite effective in the preparation of antibacterial composites. The mechanism behind the antibacterial activity is due to the generation of superoxide (O2-) radicals from the CaO surface, reacting with hydrogen and oxygen to produce ROS (reactive oxygen species) in the system. ROS damaged the bacterial cell colony through several mechanisms [51; 50].

Cement production requires a significant amount of energy and produces a significant amount of CO2 [52; 53]. It was observed that the use of calcined eggshell powder at low replacement rates (5%) increased the compressive strength of cement-based materials [53; 54]. Teara et al. [55] reported that 35% fly ash and eggshell and cement substitute in concrete production improved the compressive strength and durability of concrete compared to conventional concrete, Hamada et al. [56], the eggshell powder could be used to improve concrete properties and reduce cement production, Bhartiya and Dubey [57] stated that 10% substituted egg instead of cement, Adogla et al. [58] reported that 30% of eggshell powder significantly improved the density, compressive strength and durability properties of laterite bricks. Since the eggshell has a specific gravity that varies between 0.85 and 2.66, which is lighter than cement, it is lighter than normal concrete and can be used in structures that require lightweight concrete. The different effects of eggshell powder on cement and concrete are due to surface morphology, CaO content and particle size [57].

In their study, Razzaq and Yousif [59] added eggshell powder at the rate of 3, 5, 7, 10 and 15% by weight of asphalt. As a consequence of the testing, the flash point improved with increased additive ratio despite a large loss in penetration value and a significant rise in viscosity. Temperature has strengthened the resistance to persistent deformation. It has been reported that the addition of eggshell to asphalt can be used as an asphalt binder material because it reduces high temperature deformation and rutting damage of asphalt pavement.

The stabilization of the soil is done to improve certain properties of the soil (plasticity index, gradation, etc.) by adding expensive additives such

as lime, cement, and bitumen. Since the chemical composition of the eggshell powder is similar to that of lime, it can be a good alternative to industrial lime as a stabilizing material [60]. In a study using eggshell powder as a stabilizing material to increase the strength of floors, it was concluded that a floor containing 6% eggshell powder was the optimum combination. It was concluded that eggshell powder could improve the performance of clay in terms of plasticity index, compression properties, and strength aspects [60].

Vilarinho et al. [61] developed eco-ceramic wall tiles using bio-calcium carbonate from eggshell as a raw material. Eggshell (0, 25, 50, 75, and 100 wt%) was used instead of limestone in the study. Through the characterization of the samples, the properties of biocalcium carbonate with the same granulometry were within industrial limits. Therefore, the study has proven that limestone can be completely replaced by eggshell in the production of eco-ceramic wall tiles. Reintroducing the eggshell to the ceramics industry contributes to a real industrial symbiosis as well as a circular economy [61].

Tutus et al. [62] in the study where precipitated calcium carbonate and eggshell calcium carbonate mixtures were used in the production of wallpaper, they reported that water-resistant opaque papers were obtained as a result of reducing the spaces between the fibers by using eggshells [62].

The use of pH modifiers in mining and related industries is very important because certain reactions require certain pH to occur. Also, without the required pH, some undesirable chemical reaction byproducts can occur which tend to make the atmosphere unsafe. The calcined eggshell increased the pH of a solution with a native pH of 9.71 to 12.44 [63]. Technologies used in acid mine drainage have many limitations in terms of high capital cost, large volumes of sludge production, operational sensitivity, and applicability for active treatment only [64; 65; 66; 67]. Calugari et al. [64] reported that thermally activated eggshells are effective in acid mine drainage neutralization and processing of heavy metals in acid mine drainage in cold climates, and can be used in active or passive solution methods, post-closure, and restoration, barrier and drainage processes. Choi and Lee [67] found that the combined use of calcined eggshells and microalgae to remove heavy metals from acid mine drainage (AMD) and simultaneously increase biomass productivity, removal percentage of Fe, Cu, Zn, Mn, As, and Cd from acid mine drainage wastewater is 99.47 to 100%.

Fernandes et al. [68] used eggshells in the production of foam glass and proved to be a good alternative to conventional foaming agents such as $CaCO_3$, $MgCO_3$, or SiC used in foam glass production. In addition, eggshells have advantages such as being a waste material, potentially cost-effective, contributing to the cleaning of the environment, and saving energy by releasing gas at low temperatures (700oC) [68].

Due to the fact that polyurethanes can have different properties depending on the type and composition of the components that make them up; They are valuable engineering materials used in many fields, especially in the automobile, adhesive, furniture, paint, construction, and cooling sectors [69]. Victor et al. [70] reported that eggshells have a higher flexibility and ability to resist deformation as a filler in the production of flexible polyurethane foam. These features are the most needed features in foam mattresses. Erdem et al.[69] reported that rigid polyurethane foams with 7% eggshell powder additives may be the most likely structure to be recommended for many applications. Egg shells have good strength and tensile strength to strengthen the mechanical stability of polymer matrices [70].

Minakshi et al. [71] reported that the eggshell can be used for energy storage, the shape of the electrochemical curves obtained in the study is similar to that of the commercially available activated carbon electrode, and the $CaCO_3$ obtained from the eggshells can be used as an electrode in Li-ion capacitors. Abdi et al. [72] studied 1% and 2% eggshell powder, eggshell ash, acid-activated eggshell powder, acid-activated eggshell ash, and commercial bleaching earth for bleaching neutralized soybean oil. Due to its high efficiency in removing unwanted components (pigments, iron, copper, oxidation products, and free oil) and environmental protection against acid pollution, eggshell powder can be used as an adsorbent and can be considered as a good alternative for bleaching edible oils, according to the study [72]. The application of organic fertilizers provides valuable nutrients to the plants and not only improves the physical and chemical condition but also increases the crop yield and reduces the use of chemical fertilizers [73]. Eggshell is an enriched source of calcium, essential for plant growth [74]. In agriculture, potassium is called potash, which is used as fertilizer. The combination of potassium and calcium in eggshell can make it a suitable raw material for fertilizer production [6]. Biswas et al. [74] reported that the combination of eggshell, chicken feather hydrolyzed protein, and vermicompost (100:10:3 ratio) increased the agronomic parameters of the capsicum plant approximately four-fold compared to its chemical counterpart. In addition, the combination used increased the yield parameters of the crops by enriching the soil with both micro and macronutrients [75].

Eggshell and Chlorella Vulgaris algae increased the Ca content of tomatoes as well as minerals such as B, K, Mg, and Zn in soilless agriculture [76]. Holmes et al. [76] reported that ground eggshells proved to be an effective liming material in the region with acidic surface soil and were applicable for soil pH correction. Laohavisuti et al. [77] obtained low and high-purity calcium carbonate from eggshell to produce dicalcium phosphate, monocalcium phosphate, and tricalcium phosphate for the fertilizer, mineral feed, and food additive industries. The study showed that eggshell can be used in the fertilizer, animal feed and food additive industries that require very large quantities [77]. It contains high amounts of bioavailable calcium, such as egg shells, shellfish, bones, and fish scales. The eggshell is easy to separate from the protein part, namely the yolk and albumen. Considering the separation of muscle and other protein masses from the bones and the removal of the proteinaceous portion from fish scales and shellfish shells, it takes more time and less efficient separation processes [78]. Although oyster shells contain some toxic elements such as Pb, Al, Hg and Cd, egg shells do not contain such toxic elements. Eggshell calcium has good solubility [79] and $CaCO_3$ extraction from eggshells is relatively inexpensive, physically feasible, and efficient compared to other sources [78]. In rat studies, calcium from eggshell powder was discovered to have a high bioavailability compared to commercially available $CaCO_3$ [79]. Zerek [81] reported that the ash content and calcium mineral content of cookies containing 3%, 6%, and 9% eggshell powder increased with increasing eggshell powder. As a result of the microbiological evaluation of sterilized egg shells, total mesophilic aerobic bacteria (TMAB), mold-yeast, Salmonella spp. were not detected. Hassan [82] reported a significant difference in calcium (Ca) content and Ca bioavailability in biscuits made from wheat flour with eggshell powder additives. On the other hand, Perez et al. [83] developed functional yogurt that was purified from pathogenic microorganisms from micro powders obtained from egg shells and suitable for human consumption. The calcium content of eggshell-added yogurt was found to be twice as much as normal yogurt. Eggshells are an inexpensive and readily available source of calcium that can be prepared at home, provided that appropriate precautions are taken (Salmonella), leaving no major contaminants behind.

2. Conclusions

Eggshell waste generation is growing rapidly and will continue to increase. Instead of destroying the eggshells, which create an important environmental problem, it should be aimed to use them in appropriate areas, and at the same time to improve their reuse capabilities. The positive results obtained from the studies support the perspective of the zero waste operation to produce material recycling, waste management, sustainable development, and value-added products in the future. When waste is evaluated, it will have an economic contribution as it will be transformed into high value-added materials. Literature studies have shown that eggshells are an important bio-waste in providing the transition from garbage to value-added products. By organizing the collection of eggshells from industrial egg uses, food factories, poultry farms, and bakeries, they can become fully usable raw materials for many of the above-mentioned applications.

Author Statements:

References

[1] Mittal, A., Teotia, M., Soni, R.K., Mittal, J. (2016). Applications of egg shell and egg shell membrane as adsorbents. *Journal of Molecular Liquids.* 223: 376–387. DOI: 10.1016/j.molliq.2016.08.065

[2] Aina, S.T., Du Plessis, B.J., Mjimba, V, Brink H.G. (2022). From Waste to Best Valorization and Upcycling of Chicken Eggshells. *Waste Management.* Edition1st Edition.

[3] Tok, A. (2017). Geleneksel ve Atık Takviyeli Metal Matrisli Kompozitlerin Mekanik ve Fiziksel Özelliklerinin İncelenmesi. Bartın Üniversitesi Fen Bilimleri Enstitüsü. Master's Thesis.

[4] Mishra, G. and Pathak, N. (2017). Strength And Durability Study On Standard Concrete With Partial Replacement of Cement and Sand Using Egg Shell Powder and Earthenware Aggregates For Sustainable

Construction. *International Journal for Research & Development in Technology.* 8:6.

[5] Nakano, T., Ikawa, N.I., Ozimek, L. (2003). Chemical composition of chicken eggshell and shell membranes. *Poult. Sci.* 82.510–514. DOI: 10.1093/ps/82.3.510

[6] Ajala, E.O., Eletta, O.A.A., Ajala, M.A., Oyeniyi S.K. (2018). Characterization and Evaluation of Chicken Eggshell for Use as a Bio-Resource. *Arid Zone Journal of Engineering, Technology and Environment.* 14(1):26-40.

[7] Sharma, S., Netula, N. (2018). Experimental Investigation of Partial Replacement of Opc (43 Grade) Cement By Egg Shell Powder For M-35 Concrete Grade. *Jetır.* 5(9).

[8] Bongiorno, L., "Green, Greener, Greenest", A Perigee Book, 2008.

[9] Kim, D., Hwang, S.J., Kim, Y., Ho, Jeong, C., Hong, Y.P., and Ryoo, K.S. (2019). Removal of Heavy Metals from Water Using Chicken Egg Shell Powder as a Bio-Adsorbent. *Bull. Korean Chem. Soc.* 40. 1156–1161. DOI: 10.1002/bkcs.11884

[10] Huang, L,M., Chen, C,H., Wen, T,C. (2006). Development and characterization of flexible electrochromic devices based on polyaniline and poly(3,4-ethylenedioxythiophene)-poly(styrene sulfonic acid). *Electrochim. Acta.* 51:26. 5858-5863. DOI: 10.1016/j.electacta.2006.03.031

[11] Killi, U. (2017). Production of Writing Paper from Waste Office Papers and Waste Eggshells. Kahramanmaraş Sütçü İmam University. Faculty of Forest. Master Thesis. 2017.

[12] Ayawanna, J., Kingnoi, N., Laorodphan, N.A. (2019). Feasibility study of egg shell-derived porous glass–ceramic orbital implants. *Materials Letters.* 241; 39–42. DOI: 10.1016/j.matlet.2019.01.040

[13] Alkaya, A., Şereflişan, H., Duysak, Ö. (2019). Biyomateryal Kaynakları Ve Kullanım Alanları. *1. International Conference on Environment, Technology and Managemet (ICETEM).* 27-29 June 2019. Niğde

[14] Shafiei, S., Omidi, M., Nasehi, F., Golzar, H., Mohammadrezaei, D., Rezai, Rad, M., Khojasteh, A. (2019). Egg Shell-Derived Calcium Phosphate/Carbon Dot Nanofibrous Scaffolds for Bone Tissue Engineering: Fabrication and Characterization. *Mater. Sci. Eng.* 100, 564–575. DOI: 10.1016/j.msec.2019.03.003

[15] Skórczewska, K., Lewandowski, K., Szewczykowski, P., Wilczewski, S., Szulc, J., Stopa, P., and Nowakowska, P. (2022). Waste Eggshells as a Natural Filler for the Poly(Vinyl Chloride) Composites. *Polymers.* 14, 4372. DOI: 10.3390/polym14204372

[16] Yönetken, A., Erol, A., Peşmen, G. (2022). Characterization of egg shell powder-doped ceramic–metal composites. *Open Chemistry.* 20: 716–724. DOI: 10.1515/chem-2022-0175

[17] Yönetken, A., Peşmen, G., Erol, A. (2020). Production and Characterization of Ti-10Cr-3,33Co-3,33Egg Shell Composite Materials Using By Powder

Metallurgy. *International Journal of Engineering Research and Development.* UMAGD. 12(1), 158-165. DOI: 10.29137/umagd.474031.

[18] Bilici, V.O., Peşmen, G., Yönetken, A., and Erol, A., (2023). Effect of variation of egg-shell particulate reinforcement on ultrasonic pulse velocity, attenuation, and hardness prediction in ceramic-metal composites. *Thermal Science* 27: 4B, 3179-3188. DOI: 10.2298/TSCI2304179B

[19] Yönetken, A., Erol, A., Yakar, A., Peşmen, G. (2016). Investigation of Ceramic-Metal Composites Producedby Electroless Ni Plating of AlN- Astaloy Cr-M. *World Academy of Science. Engineering and Technology International Journal of Chemical, Molecular, Nuclear, Materials and Metallurgical Engineering* Vol:10, No:3.

[20] Jannet, S., Raja, R., Rajesh, Ruban, S., Khosla, S., Sasikumar, U., Sai, N.B, Teja, P.M. (2021). Effect of egg shell powder on the mechanical and microstructure properties of AA 2024 metal matrix composite. *Materials Today:* Proceedings 44. 135–140. DOI: 10.1016/j.matpr.2020.08.546.

[21] Akgürbüz, İ., Uysal, Y. (2019). Arıtma Çamuru, Lüle Taşı (Sepiyolit) ve Yumurta Kabuğu Atıklarının Polimer Kompozit Plaka Üretiminde Değerlendirilmesi. *KSU J Eng Sci,* 22.

[22] Norsham, I.N.M., Baharin, S.N.A., Raoov, M., Shahabuddin, S., Jakmunee, J., Sambasevam, K.P. (2020). Optimization of waste quail eggshells as biocomposites for polyaniline in ammonia gas detection. *Polym Eng Sci.* 60:3170–3182. DOI: 10.1002/pen.25545

[23] Mustapa R, Mansor Z.I.A, Sambasevam K.P. J. Phys. Sci. 2018. 29, 9.

[24] Lee, J.I., Hong, S.H., Lee, C.G., Park, S.J. (2021). Fluoride removal by thermally treated egg shells with high adsorption capacity, low cost, and easy acquisition. *Environmental Science and Pollution Research.* 28:35887–35901. DOI: 10.1007/s11356-021-13284-z.

[25] Enniya, I., Rghioui, L., Jourani, A. (2018). Adsorption of hexavalent chromium in aqueous solution on activated carbon prepared from apple peels. *Sustain. Chem. Pharm.* 7, 9–16. DOI: 10.1016/j.scp.2017.11.003.

[26] Fedyukevich, V.A., Vorob'ev-Desyatovskii, N.V. (2016). Advantages and disadvantages of various kinds of adsorbents used in industrial extraction of [Au(CN)2]– anions from cyanide solutions and pulps. *Russ. J. Appl. Chem.* 89, 577–582.

[27] Hammarstrom, J.M., Sibrell, P.L., Belkin, H.E. (2003). Characterization of limestone reacted with acid-mine drainage in a pulsed limestone bed treatment system at the Friendship Hill National historical site. *Appl. Geochem.* 2003. 18, 1705–1721. DOI: 10.1016/S0883-2927(03)00105-7.

[28] Suzuki, S. (2002). Black tea adsorption on calcium carbonate: a new application to chalk powder for brown powder materials. *Colloids Surf. Physicochem. Eng.Asp.* 202, 81–91. DOI: 10.1016/S0927-7757(01)01063-9.

[29] Pettinato, M., Chakraborty, S., Arafat, H.A., Calabro, V. (2015). Eggshell: a green adsorbent for

heavy metal removal in an MBR system. *Ecotoxicol. Environ. Saf., Green. Technol. Environ. Pollut. Control Prev. (Part 1)* 2015.121, 57–62. DOI: 10.1016/j.ecoenv.2015.05.046.

[30] Setiawan, B.D., Rizqi, O., Brilianti, O.F., Wasito, H. (2018). Nanoporous of waste avian eggshell to reduce heavy metal and acidity in water. *Sustainable Chemistry and Pharmacy*. 10: 163–167. DOI: 10.1016/j.scp.2018.10.002.

[31] Kamgang-Syapnjeua, P., Njoyaa, D., Kamseub, E., Cornette de Saint Cyrc L., Marcano-Zerpac, A., Balmec, S., Bechelanyc, M., Soussan, L. (2020). Elaboration of a new ceramic membrane support from Cameroonian claysi coconut husks and eggshells: Application for Escherichia coli bacteria retention. *Applied Clay Science* 198:105836.

[32] Ok, Y.S., Lee, S.S., Jeon, W.T., Oh, S.E., Usman A.R.A., Moon D.H. (2011). Application of eggshell waste for the immobilization of cadmium and lead in a contaminated soil. *Environ. Geochem. Health.* 33(1 Suppl.), 31e39. DOI: 10.1007/s10653-010-9362-2.

[33] Bailey, S., Olin, T.R., Dean, M.A. (1999). A review of potentially low-cost sorbents for heavy metals. *Water Res.* 3(11)2469–2479. DOI: 10.1016/S0043-1354(98)00475-8.

[34] Chojnacka, K. (2005). Biosorption of Cr(III) ions by eggshells. *Journal of Hazardous Materials.* B121. 167–173. https://doi.org/10.1016/j.jhazmat.2005.02.004.

[35] Muhaisen, L.F., Muhaisen, F.F., Abdulkareem, Z.M. (2019). Egg Shell as Natural Sorbent To Remove Cadmıum Ions From Sımulated Wastewater. *Journal of Engineering And Sustainable Development.* 23(06). DOI: 10.31272/jeasd.23.6.12.

[35] Somaia, G., Mohammad, Sahar, M., Ahmed & Mayyada M. H. El-Sayed. (2022). Removal of copper (II) ions by eco-friendly raw eggshells and nano-sized eggshells: a comparative study. *Chemical Engineering Communications.* 209:1, 83-95. DOI: 10.1080/00986445.2020.1835875.

[37] Li, Y., Zhang, P., Du, Q., Peng, X., Liu, T., Wang, Z., Xia, Y., Zhang, W., Wang, K., Zhu, H., Wu, D. (2011). Adsorption of fluoride from aqueous solution by graphene. *J Colloid Interface Sci.* 363(1):348–354. DOI: 10.1016/j.jcis.2011.07.032.

[38] Abbas, M.N., Israa, M. Al-T., Hasan, M.B., Al-Madhhachi, A.T. (2021). Chemical removal of cobalt and lithium in contaminated soils using promoted white eggshells with different catalysts. *South African Journal of Chemical Engineering*. 35. 23–32. DOI: 10.1016/j.sajce.2020.11.002.

[39] Wei, Z., Xu, C., Li, B. (2009). Application of waste eggshell as low-cost solid catalyst for biodiesel production. *Bioresour. Technol.* 100, 2883e2885. DOI: 10.1016/j.biortech.2008.12.039.

[40] Chavan, S.B., Kumbhar, R.R., Madhu, D., Singh, B., Sharma, Y.C. (2015). Synthesis of biodiesel from Jatropha curcas oil using waste eggshell and study of its fuel properties. *RSC Adv.* 5, 63596e63604. DOI: 10.1039/C5RA06937H.

[41] Navajas, A., Issariyakul, T., Arzamendi, G., Gandía, L.M., Dalai, A.K. (2013). Development of eggshell derived catalyst for transesterification of used cooking oil for biodiesel production. *Asia Pac. J. Chem. Eng.* 8, 742e748. DOI: 10.1002/apj.1715.

[42] Cho, Y.B., Seo, G. (2010). High activity of acid-treated quail eggshell catalysts in the transesterification of palm oil with methanol. *Bioresour. Technol.* 101, 8515e8519. DOI: 10.1016/j.biortech.2010.06.082.

[43] Çetin, G.N. (2018). Doğal CaO Kaynaklarının Biyodizel Üretiminde Katalizör Olarak Kullanılmasının İncelenmesi. Kocaeli Üniversitesi Fen Bilimleri Enstitüsü. Master's Thesis.

[44] Rashid, I.M., Atiya, M.A., Hameed, B.H. (2017). Production of Biodiesel from Waste Cooking Oil using CaO-Egg Shell WasteDerived Heterogeneous Catalyst. *International Journal of Science and Research (IJSR).* 6(11). DOI: 10.21275/ART20177723.

[45] Ayoola, A.A., Raji, A.O., Babalola, A. (2021). The use of Waste Duck Eggshells for Sustainable Energy Production. IOP Conf. Series: *Earth and Environmental Science.* 655. 012051.

[46] Sanni, O., Popoola, A.P.I., Fayomi, O.S.I. (2018). Electrochemical Analysis of Austenitic Stainless Steel (Type 904) Corrosion Using Egg Shell Powder in Sulphuric Acid Solution. *Technologies and Materials for Renewable Energy, Environment and Sustainability,* TMREES18. DOI: 10.1016/j.egypro.2018.11.227.

[47] Andrady, A.L., Hamid, S.H., Hu, X., Torikai, A. (1998). Effects of increased solar ultraviolet radiation on materials. *J. Photochem. Photobiol. B.* 46, 96–103. DOI: 10.1016/S1011-1344(98)00188-2.

[48] Lippens, D.F., Nallapaneni, A., and Shawkey, M.D. (2017). Exploring the Use of Unprocessed Waste Chicken Eggshells for UV-Protective Applications. *Sustainability.* 9, 232; DOI:10.3390/su9020232.

[49] Binici, H., Temiz, H., Sevinç, A.H., Eken, M., Küçükönder, A., Ergül, T. (2013). Atık Pil Kömürü ve Yumurta Kabuğunun Radyasyon Tutucu Materyal Olarak Üretimde Kullanılması. *KSU Journal of Engineering Sciences.* 16(1).

[50] Nath, D., Jangid, K., Susaniya, A., Kumar, R., Vaish, R. (2021). Eggshell derived CaO-Portland cement antibacterial composites. *Composites Part C: Open Access* 5. 100123. DOI:10.1016/j.jcomc.2021.100123.

[51] Kumar, S., Sharma, M., Kumar, A., Powar, S., Vaish, R. (2019). Rapid bacterial disinfection using low frequency piezocatalysis effect. *J. Ind. Eng. Chem.* 77. 355–364, DOI: 10.1016/j.jiec.2019.04.058.

[52] Khan, M., Ali, M. (2019). Improvement in concrete behavior with fly ash, silica-fume and coconut fibres. *Constr. Build. Mater.* 203. 174–187. DOI: 10.1016/j.conbuildmat.2019.01.103.

[53] Alsharari, F., Khan, K., Amin, M.N., Ahmad, W., Khan, U., Mutnbak, M., Houda, M., Yosri, A.M. (2022). Sustainable use of waste eggshells in cementitious materials: An experimental and modeling-based study. *Case Studies in Construction Materials.* 17: e01620. DOI: 10.1016/j.cscm.2022.e01620.

[54] Mokhtar, M., Long, T.B., Rahman, N.S.A., Kassim, S. (2022). Utilisation of Eggshells Powder in Construction of Concrete. *Multidisciplinary Applied Research and Innovation.* 3(1). 183-192. DOI:10.30880/mari.2022.03.01.023

[55] Teara, A., Doh, I., Chin, S.C., Ding, Y.C., Wong, J. and Jiang, X.X. (2019). Investigation on the durability of use fly ash and eggshells powder to replace the cement in concrete productions. *IOP Conf. Series: Earth and Environmental Science* 244: 012025. DOI: 10.1088/1755-1315/244/1/012025.

[56] Hamada, H.M., Tayeh, B.A., Al – Attar, A., Yahaya, F.M., Muthusamy, K., Humada, A.M. (2020). The present state of the use of eggshell powder in concrete: A review. *Journal of Building Engineering.* 32: 101583. DOI:10.1016/j.jobe.2020.101583.

[57] Bhartiya, A., and Dubey, M. (2018). Replacement of Cement Wıth Coconut Shell Ash and Egg Shell Powder For Preparation of Fresh Concrete. *International Research Journal of Engineering and Technology (IRJET).* 05(06).

[58] Adogla, F., Yalley, P.P.K., Arkoh, M. (2016). Improving Compressed Laterite Bricks using Powdered Eggshells. *The International Journal of Engineering And Science (IJES).* 5(4);65-70.

[59] Razzaq, A.K. and Yousif, R.A. (2017). Sustainability of HMA by Using of Egg Shell Powder. *International Conference on Sustainable Futures.* ICSF Kingdom of Bahrain.

[60] Soundara, B. and Vilasini, P.P. (2015). Effect of Egg Shell Powder on the Properties of Clay. 50th Indian Geotechnical Conference. 17th–19th December 2015, Pune, Maharashtra, India.

[61] Vilarinho, I.S., Filippi, E., Seabra, M.P. (2020). Development of eco-ceramic wall tiles with bio-CaCO3 from eggshells waste. *Open Ceramics.* 9: 100220. DOI:10.1016/j.oceram.2022.100220.

[62] Tutuş, A., Özdemir, A., Bozkurt, F., Erkan, S., Birbilen, Y., Çiçekler, M. (2018). Evaluation of Egg Shells in Wallpaper Production. 1. International Technological Sciences and Design Symposium. 27-29 June 2018 - Giresun/Turkey.

[63] Commey, A., and Mensah, M. (2019). An Experimental Study on the Use of Eggshell Powder as a pH Modifier: Production of Lime from Eggshells. *International Journal of Innovative Science and Research Technology.* 4(9).

[64] Calugaru, I.L., Etteieb, S., Magdouli, S., Brar, K.K. (2022). Efficiency of thermally activated eggshells for acid mine drainage treatment in cold climate. *Journal of Environmental Science and Health, Part A,* 57:2, 81-91. DOI:10.1080/10934529.2022.2027699.

[65] Akcil, A., Koldas, S. (2006). Acid Mine Drainage (AMD): Causes, Treatment and Case Studies. *J. Clean. Prod.* 14, 1139–1145. DOI:10.1016/j.jclepro.2004.09.006.

[66] Yadollahi, A., Abdollahi, H., Ardejani, F.D., Mirmohammadi, M., Magdouli, S. (2021). Bio-Oxidation Behavior of Pyrite, Marcasite, Pyrrhotite, and Arsenopyrite by Sulfur- and Iron-Oxidizing Acidophiles. Bioresour. Technol. Rep. 15, 100699. DOI:/10.1016/j.biteb.2021.100699.

[67] Choi, H.J. and Lee, S.M. (2015). Heavy metal removal from acid mine drainage by calcined eggshell and microalgae hybrid system. *Environmental Science and Pollution Research.* 22, 13404–13411. DOI: 10.1007/s11356-015-4623-3.

[68] Fernandes, H.R., Andreola, F., Barbieri, L., Lancellotti, I., Pascual, M.J., Ferreira, J.M.F. (2013). The use of egg shells to produce Cathode Ray Tube (CRT) glass foams. *Ceramics International* 39: 9071–9078. DOI:10.1016/j.ceramint.2013.05.002

[69] Erdem, M., Akdoğan, E., Üreyen, M.E., Uysal, O., Kaya, M., Irmak, C. (2018). Yumurta Kabuğu Tozu Katkılanmış Sert Poliüretan Köpükler: Termal İletkenlik, Basma Mukavemeti ve Yanma Davranışlarının İncelenmesi. *Isı Bilimi ve Tekniği Dergisi.* 38(1)83-93.

[70] Victor, E.I., Louis, I.C., Alfred, N.O., Ozioma, U.N. (2019). Use of Chicken Eggshells as Fillers in Flexible Polyurethane Foam Production. *International Journal of Industrial Engineering.* 3(1):1-6.

[71] Minakshi, M., Visbal, H., Mitchell, D.R.G., Fichtner, M. (2018). Bio-waste chicken eggshells to store energy. *Dalton Trans.* 47, 16828-16834. DOI:10.1039/C8DT03252A.

[72] Abdi, E., Gharachorloo, M., Ghavami M. Investigation of using egg shell powder for bleaching of soybean oil. (2021) *LWT.* 140. 110859. DOI:10.1016/j.lwt.2021.110859.

[73] Andhare, A.A., Shinde, R.S., Deshmukh, A.J. (2019). Banana peel, duckweed and egg shell: cheap sources of organic fertilizer. *Int J of Green Herbal Chem.* 8(1):055-060.

[74] Biswas, I., Mitra, D., Mitra, D., Chattaraj, S., Senapati, A., Chakraborty, A., Basak, G., Mohapatra, P.K.D. (2022). Application of egg shell with fortified vermicompost in Capsicum cultiva-tion: A strategy in waste management. *International Journal of Recycling of Organic Waste in Agriculture.* 11: 451-461. DOI:10.30486/ijrowa.2022.1940565.1338.

[75] Ertürk, H. (2021). Growth of tomato plantlets in soilless culture, enriched with egg shell waste and algae. *International Journal of Science and Research Archive.* 03(02), 161–167.

[76] Holmes, J.D., Sawyer, J.E., Kassel, P., and Ruiz, Diaz D. (2011). Using ground eggshells as a liming material in corn and soybean production. Online. *Crop Management.* DOI:10.1094/CM-2011-1129-01-RS.

[77] Laohavisuti, N., Boonchom, B., Boonmee, B., Chaiseeda, K., Seesanong, S. (2022). Simple recycling of biowaste eggshells to various calcium phosphates for specific industries. www.nature.com/scientificreports. Erişim tarihi: 23.11.2022.

[78] Singh, A., Kelkar, N., Natarajan, K., Selvaraj, S. (2021). Review on the extraction of calcium supplements from eggshells to combat waste generation and chronic calcium deficiency. *Environmental Science and Pollution Research.* 28:46985–46998. DOI:10.1007/s11356-021-15158-w.

[79] Waheed, M., Butta, M.S., Shehzada, A., Adzahanc, N.M., Shabbira, M.A., Suleriad, H.A.R., Aadila. R.M.

(2019). Eggshell calcium: A cheap alternative to expensive supplements. *Trends in Food Science & Technology.* 91:219–230. DOI: 10.1016/j.tifs.2019.07.021.

[80] Świątkiewicz, S., Arczewska-Wlosek, A., Krawczyk, J., Puchala, M., & Józefiak, D. (2015). Effects on performance and egg shell quality of particle size of calcium sources in laying hens' diet with different Ca concentrations. *Archives of Animal Breeding*. 58(1), 301–307. DOI:10.5194/aab-58-301-2015.

[81] Zerek, E. (2021). Yumurta Kabuğu Tozu Eklenmiş Kurabiyelerin Bazı Besinsel ve Kalite Özelliklerinin Belirlenmesi. İstanbul Medipol Üniversitesi, Sağlık Bilimleri Enstitüsü, Master's Thesis. 2021.

[82] Hassan, N.M.M. (2015). Chicken Eggshell Powder as Dietary Calcium Source in Biscuits World. *Journal of Dairy & Food Sciences* 10 (2): 199-206. DOI: 10.5829/idosi.wjdfs.2015.10.2.1152

[83] Pérez, G., Guzman, J., Duran, K., Ramos, J., Acha, V. (2018). Use of Egg Shells in Food Fortification. *Revista Ciencia, Tecnología E Innovación*. 16 (18) 29-38.

Research Article

e-Commerce Return Processes and Data Analysis in Logistics

Ahmet DAGLI[1], Serap Özhan DOGAN[2]*

[1]Ceva Ceva Logistics R&D Department İstanbul-Turkiye
Email: ahmet.dagli@cevalogistics.com **- ORCID:** 0009-0005-0643-8358

[2]İstanbul Beykent University, İstanbul-Turkiye
* **Corresponding Author Email:** serapdogan@beykent.edu.tr **- ORCID:** 0000-0001-5210-1549

Article Info:

Abstract:

E-commerce data transfers within the framework of logistics; It is a process that involves the transfer of products, customers, purchase reservations, return reservations and other data from an e-commerce platform (online/web) or store to logistics platforms. In this study, one of the largest transportation companies in the world is analyzed using case study method, which is one of the qualitative research methods. The study is not built on generalization, but on understanding the situation. The fact that the portal and existing applications can work together and provide data flow has contributed positively to the quality of existing processes. The "return intake form" solution found in returns added value to the corporate identity of the company and provided customer satisfaction. With the integrated E-Archive feature, it offers solutions to customers in terms of problems and data flow. The limitations of the study are that it deals with the online applications of a company and understands the situation through this. In order to make generalizations about the researched subject, other companies operating in the same sector and using similar platforms should be examined and the scope of the study should be expanded.

1. Introduction

Information and communication technologies, especially the Internet and the World Wide Web (www), have caused changes in almost every aspect of our lives, from education to health, entertainment to communication, social life to business life, and have gained an important place in our lives [1].

Today, developments related to technology are taken seriously by businesses in many areas. Thanks to the applications that we encounter as electronic commerce and expressed as e-logistics with its special name in the field of logistics, accurate and timely information sharing and simultaneous satisfaction of customer expectations are provided and this situation affects the competitiveness level of businesses. The use of technology in the international supply chain has led logistics service providers to focus more on information technologies in storage, transportation and distribution activities and to achieve a more competitive structure in the global sense [2].

Electronic Data Interchange (EDI) can be defined as systems that are significantly used in logistics operations that provide information and document exchange with the parties of the enterprises in accordance with certain standards. At the same time, the first area of use of the EDI system was the logistics sector [3]. One of the benefits of EDI starts with the integration of businesses into the e-commerce system. In businesses that use this system efficiently, purchasing processes gain speed, transaction times are shortened, inventory management is facilitated and the quality of the services provided is increased. At the same time, it provides convenience for consumers to take quick action with suppliers and place automatic orders [4].

With the advancement of technological systems and the widespread use of the internet, companies have developed digital platforms such as web services and online portals that offer solutions for many purposes, such as internal solutions and offering them to customers. Thanks to these platforms, logistics

companies can provide customers with a fast and efficient service, which can be considered as a decisive and distinguishing factor in customers' choice of carrier. Transmission of customer orders, which is considered a key point within the framework of logistics processes, at the right time and in a way that satisfies the customer; It is extremely important to manage the delivery process with the right strategies and procedures [5].

Returns management is also very important in logistics processes for e-commerce businesses. Returns management plays a critical role in increasing customer satisfaction and minimizing potential problems. Therefore, businesses should strive to make their returns processes as fast and smooth as possible. To optimize these processes, businesses can use special logistics solutions for their returns or develop digital platforms and applications to make returns processes as simple as possible. E-commerce businesses must also take returns management into account in their logistics processes.

Logistics companies are working to create an effective returns-issue management system for their businesses. These systems use technologies such as data analysis techniques, specialized logistics solutions, digital platforms and applications in the return processes. The problem support system is of great importance to increase customer satisfaction and improve the efficiency of businesses.

An illustration of the functioning of the problem support system is presented in Figure 1.

Figure 1. Problem support system

Data transfer can be done manually, but this method is very time and effort consuming. Accordingly,

there is a high probability of error. For this reason, many e-commerce platforms provide automatic data transfer using a software interface called API (Application Programming Interface). This allows data to be synchronized and updated automatically. Integrations between the customer and the Logistics company can be referred to as logistics data transfer solutions. Logistics data transfer solutions greatly help to manage internal and external processes more efficiently.

The volume of e-commerce has been growing rapidly in our country and in the world in recent years. Due to the developing sales strategies, sellers have their products shipped from different warehouses and suppliers. For this reason, deliveries, delivery points and return points of the products to be returned are dynamically changing and multiplying in this context.

Damage or loss of some of the products during shipment will cause the delivery to turn into a return. The seller company may not accept the damage and deficiencies and may demand the cost of the product from the logistics company. Determining the return of the products to be delivered in the warehouses and branches, processing this information into the system, ensuring that the products waiting to be returned at the buyer are reflected in the system in a short time will save time and space in the operation.

2. Analysis Method and Process

The aim here is to reveal how the theoretical concepts of e-logistics and customer portal are applied in the sectoral sense, to collect, analyze and interpret the results from a systematic perspective. The company examined within the scope of the study is one of the large enterprises providing major transportation services in the world and all findings are kept confidential within the framework of corporate policies and all findings are stated without giving the name of the company.

In this study, it examined how the systematic data tracking, solutions and processes of delivery orders and return orders created from e-commerce customers to the logistics company are managed. While conducting this examination, the case analysis method, which is one of the qualitative research methods, was used.

On the basis of the results obtained in the studies, it is based on understanding the situation, not generalization.

2. Data Collection

While collecting the data, an interview was conducted with a responsible person from the project management who deals with all partial and e-commerce processes of the company. The interviews lasted 240 minutes on different days. In addition, a responsible person from the company's operational development team was interviewed to obtain information on customer satisfaction with the work done. During the interviews, interpretative and clarification questions were asked to gather information about the operation within the scope of e-commerce and returns.

The data collection process was constructed by interpreting the customer portals, staff portals and information transferred to customers on interaction and data transfers. In addition to the data, the company website, news in the press and numerical statistics were used. During the interview, information was obtained about the company's e-commerce infrastructure, return systems and solutions.

The company provides many logistics services and warehousing services operating in different sectors. It can work with different channels as B2B (Business To Business), B2C (Business To Customer) and C2C Consumer To Consumer.

3. E-Commerce Customer Data Transfer Systems of the Company

In the first step, the company offers 2 different solution methods for creating, updating and deleting purchase reservations (purchase reservation) from e-commerce customers.

The first one is the web-based TMS Customer portal that the company has created for small, medium-sized customers or customers who do not want to establish integration. The customer can access the portal with a user name and password created separately for each customer. Then, they can create purchase reservations individually and in bulk with Microsoft Excel in this portal. (Receiver address,

sender address, piece and desi information, etc.) It is possible to receive the common barcodes of the orders created by the customer through the TMS Customer portal through the system. The barcode contains the origin branch, destination branch, consignee address, order number and reference numbers, delivery note number and barcode of the carrier company belonging to the order. The data belonging to the reservation list prepared by the customer is transferred by giving approval. The data of the orders are transferred to the e-commerce purchase pool system. Since the portal can be presented to the contracted customer in a short time, this speed creates satisfaction on the customer side. According to the information obtained, this data transfer model is a frequently preferred method by customers. This is because it is easy to use and provides effective results.

The second channel provided by the company for the creation, updating, retrieval and deletion of tag information for future purchase reservations from e-commerce customers is the data transfer model using the e-commerce integration service (E-Com API) created by the company. The web user and web user password information that can provide data flow to the system are transmitted to the customer together with the system access URLs. Information about the order is received from the customer in XML or JSON format. (Receiver address, sender address, piece and desi information, etc.) Orders and updates received through the integration are transferred to the company's e-commerce purchase pool system. In this method, the customer can transmit and update their reservations to the carrier company in a faster and safer way. Label information is also received through the integration to create a common barcode.

4. Company's Data Acquisition and Management

E-commerce sellers may sometimes give the products from their warehouses to the carrier, or they may request purchases to be made from the location of their own suppliers. If the suppliers are large-scale, they label the package with a common label. In smaller suppliers, barcoding may not be done. For suppliers working with both methods, the company ensures the flow of information by documenting the purchase transaction made during the purchase with

a signed purchase form and scanning it with a mobile device in order to make purchases healthy. The signed documents are archived in the branches. The readings use Android APK (Android Package Kit) software called "IOD" developed by the company. The data of the order, which cannot be received due to various reasons, is instantly transferred to the systems.

"IOD application has been developed to realize the receipt of cargo from the supplier and delivery to the recipient in operational business processes." (Google Play Store)

- The company carries out the purchase and planning management of the purchase reservations coming from 2 channels to the e-commerce purchase pool in its internal structure with a web application called "E-commerce Portal". For access to the e-commerce portal created for company personnel, they can access the portal with the username and password created by admin users. Each user can only perform transactions belonging to the authorized branch. Orders falling into the pool are separated on this screen on the basis of branch and listed on the basis of branch for users. The operations performed by the user afterwards are listed and explained below.
- Purchase planning; The branch creates routes for purchase and the orders to be purchased from the customers booked on the route are selected. The first step of planning is done.
- Receiving plan Approval; The plan is checked and approved.
- Purchase form printing; The purchase form of the customer-based purchase reservation for the purchase reservations belonging to the plan is received as PDF. If there is a return (from the end consumer to the seller) order in the plan, a "Return Receipt Form" is issued. On the Return Receipt form, there are sections on the recipient and sender information, as well as sections indicating that the return order received was received from the consumer with or without damage. For customers who request Digital Archive, the return receipt form can be stored in the digital archive in case of any dispute between the seller and the buyer. There is also a barcode on the return purchase form for digital archive scanning.

- Purchase operations; Check-out preparations are made for the reservations that are planned and the forms are printed. Suppliers who cannot print labels are identified and barcodes are printed on the e-commerce portal purchase transfer screen for the orders belonging to the relevant supplier and given to the courier. The courier sets off for the route, collects the products, makes labeling and closes the plan by entering the reading and order status of the plan with the IOD application. The operator controls through the e-commerce portal and ensures that the data belonging to the plan is transferred to the distribution systems.
- Data reaches the company distribution application, shipment is tracked from here.

5. Problem Support System

The company uses a separate module, the "Problem Support System" (SDS), to communicate customer requests to customer service and return purchase reservations to operations teams. SDS is an application integrated with the Company's distribution program, designed to create and track "Work Orders" and manage the "Return Work Order" process when problems related to an order need to be investigated and action needs to be taken. In case of any problem in cargo supply, operators create a "Work Order" by entering "Transfer" on the cargo information. The customer service officer examines the problem and takes action, the action taken is entered into the system and the operation is directed. If the relevant cargo is not accepted by the customer for any reason, the delivery type "undeliverable/return" is entered in the distribution program. In order to reflect the recharging to the sender company and for systematic tracking, a "Baby ATF" is created, in the new ATF, the recipient information is now the address that sent the cargo in the first place.

If the cargo is delivered to the recipient and the customer later wants to return the cargo; usually marketplace companies transmit this information as a return pickup reservation via E-com API services. Customers who do not have integration forward this information as a list to customer service, and customer service uses the bulk upload feature in the SDS system to bulk upload the return purchase reservations to the system with Microsoft Excel. The

list is displayed on the SDS system, checked and approved. The purchase reservations belonging to the uploaded data are automatically transferred to the e-commerce purchase pool by the system. In the e-commerce portal, it falls on the "Purchase Planning" screen of the relevant branch screen and the branch makes the purchase by planning.

Data transfers of purchase appointments from data transfer channels and the Problem Support System to the e-commerce purchase pool and data transfers from the e-commerce portal to the distribution application are shown in Figure 2.
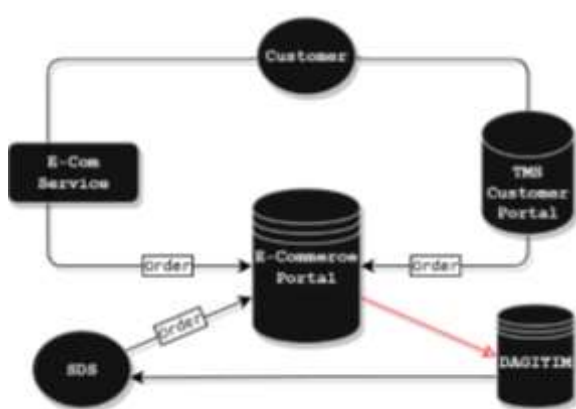

***Figure 2**. E-commerce Delivery and Returns Data Flow*

5. Performance Evaluation

The evaluation of the company is determined by taking into account the annual occurrence percentage of purchase reservations created by e-commerce customers on the company's e-commerce portal. These rates include all channels (E-com API, TMS Customer, SDS). The company obliges all branches to make purchases in all e-commerce processes and expects branches to successfully respond to reservations.

Among the company's performance evaluation criteria, e-commerce purchase reservation numbers are evaluated with "on-time purchase performance", which is evaluated with titles such as on-time purchase, late purchase, late (still not received), and expected purchase. The Company is managed in a corporate structure based on a domestic and international organization chart. Certain regions and branches have been established in Turkey. In

addition to the "On-Time Purchase Performance", the performance of branches and regions is measured by continuously monitoring the deficits in deliveries to be made. With the performance data received from regions and branches, the company measures the delivery success rate and compares it with other regions and branches.

5. Conclusion and Recommendations

The answers received during the interviews with the company were categorized. The relevant answers are organized under headings in the article. The company is continuously improving its technological development with the improvements it has made in the past, implemented in the current process and planned for the future. In addition to the company's own internal software, it outsources in different areas and utilizes its own experience as well as different business experiences. All the distances covered globally and locally are reflected positively on operations and customer satisfaction. As mentioned in the article, e-commerce portal development brings order and speed to operations. Integrations with the customer have reduced operator error margins and made the overall performance and flow traceable. With the reports on the portal, the company has become able to respond faster to the customer.

The fact that the portal and existing applications can work together and provide data flow has contributed positively to the quality of existing processes. The "return intake form" solution found in returns added value to the corporate identity of the company and provided customer satisfaction. With the integrated E-Archive feature, it offers solutions to customers in terms of problems and data flow. The company has adapted to the rapidly developing e-commerce and contributed to continuity by providing fast solutions. Thanks to the functionality brought by different integrations and portals, it was able to carry out the data coming from different customers in different ways in a single data flow. The company's solutions increased employee performance in internal processes and enabled more transparent processes and the ability to share information simultaneously.

Case studies are studies that contribute to understanding what to focus on in future research. However, the limitations of the study are that it deals

with the online practices of a company and understands the situation through this. In order to make generalizations about the researched subject, other companies operating in the same sector and using similar platforms should be examined and the scope of the study should be expanded. This situation will bring future studies to the agenda where the results of this study will shed light after the study. In this context, considering that this study was carried out with a logistics service provider, it will be important to conduct a similar study with the companies receiving logistics services and to reveal the mutual advantages and disadvantages.

Author Statements:

- **Ethical approval:** The conducted research is not related to either human or animal use.
- **Conflict of interest:** The authors declare that they have no known competing financial interests or personal relationships that could have appeared to influence the work reported in this paper
- **Acknowledgement:** The authors declare that they have nobody or no-company to acknowledge.
- **Author contributions:** The authors declare that they have equal right on this paper.
- **Funding information:** The authors declare that there is no funding to be acknowledged.
- **Data availability statement:** The data that support the findings of this study are available on request from the corresponding author. The data are not publicly available due to privacy or ethical restrictions.

References

[1] Ali Acilar; E-TİCARETTE TÜRKİYE NE DURUMDA; *Press Academia Procedia;* 2016, Cilt: 2 Sayı: 1 Sayfa 281 – 288.
[2] İsmail Karayün, Nagihan Uca (2018). E-Lojistik Kapsamında Çevrimiçi Müşteri Portallarının Yük Operasyonlarına Etkisinin Değerlendirilmesi: Vaka Analizi; Pazarlama İçgörüsü Üzerine Çalışmalar-somi. 2(1):46-56.
[3] Naim Sevinç; Tedarik Zinciri Yönetiminde Bilgi teknolojilerinin Kullanılması ve Önemi; *Trakya Üniversitesi Sosyal Bilimler Enstitüsü Yüksek Lisans Tezi;* 2008.
[4] Volkan Akyön; *İnternet ve E-Ticaret; Öneri Dergisi.* 2 (12):211 – 217.
[5] Haldun Soydal (2006). Küçük ve Orta Büyüklükteki İşletmelerde E-Ticaret; *Selçuk Üniversitesi Sosyal Bilimler Enstitüsü Dergisi* 15:539 - 552
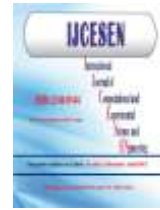
The Characterization of Welded AA 5005 Alloy with AA 5356 Filler Metals According to Slow Welding Rate Using by MIG Welding Technique

Günhan BAYRAK[1], Hüseyin MÜŞTAK[2*]

[1]Sakarya University of Applied Science, Arifiye Vocational School, 54580, Sakarya-Türkiye,
Email: gunhanb@subu.edu.tr - **ORCID:** 0000-0002-3837-0459

[2]ASAŞ Aluminyum Tic. A.Ş, 54400, Sakarya-Türkiye
Corresponding Email : huseyin.mustak@asastr.com - **ORCID:** 0000-0002-5109-2684

Article Info:

Abstract:

In the present study, AA 5005 cold rolled plate was used for welding application with AA 5356 filler materials using MIG welding process. Slow (780 mm/min) welding rate was applied for weld joint of the plate. After the welding operation, NDT tests (Visual Test, Liquid Penetrant Test, Radiography Test) and X ray Diffraction analyzes were applied to the welded plates for proving the weld quality and determination of the phases in the weld beat during the solidification of the weld pool. Then, microstructural color metallography technique was used for the investigations of grain size distribution of the weld joint and heat affected zone and base metal. Vickers microhardness tests applied on the cross-section of the weld joint together with HAZ and base metal. In addition these, tensile tests were realized for the determination of the mechanical properties of the welded cold worked AA 5005 alloy with AA5356.

1. Introduction

Aluminium AA 5005 alloy is a versatile and widely used aluminium-magnesium alloy known for its excellent corrosion resistance and formability. It belongs to the AA 5xxx series of aluminium alloys, which are non-precipitation hardenable and characterized by their high strength-to-weight ratio [1]. The presence of magnesium as the primary alloying element enhances the alloy's strength and weldability. Aluminium AA 5005 finds extensive application in various industries, including automotive, marine, and architectural sectors, where its corrosion resistance makes it ideal for outdoor and marine environments. This is why these alloys are called as marine alloys at the same time. Additionally, the alloy is favoured for its ease of fabrication, making it a popular choice for a wide range of structural and decorative applications [1,2]. MIG welding, also known as Gas Metal Arc Welding (GMAW), is a widely used and preferred welding process for Aluminium alloys because of its efficiency and versatility. MIG welding of aluminium alloys realized by a consumable electrode wire made of Aluminium or Aluminium alloys. The welding arc is formed between the electrode and the work-piece, with an externally supplied shielding gas, typically argon or a mixture of argon and helium, protecting the molten pool from atmospheric contamination [3]. MIG welding of Aluminium offers several advantages, including high welding speeds, good weld quality, and minimal post-weld clean up [4]. However, Aluminium's high thermal conductivity requires precise control of welding parameters to achieve proper fusion and prevent potential defects like porosity. With proper technique and parameter adjustment, MIG welding is an effective method for joining Aluminium components across a wide range of industries [3,5].

Welding rate in MIG welding for Aluminium alloys is a critical parameter that can significantly impact the welding process and the quality of the resulting welds. Welding rates, generally defined as travel speeds of the welding torch, can offer several advantages and challenges when working with Aluminium alloys [6,7]. Aluminium alloys have a relatively high thermal conductivity, meaning they dissipate heat quickly. By reducing the welding speed, welders can focus more heat on the joint, allowing for better penetration and fusion of the metal which will avoid lack of fusion. This can result

in stronger and more reliable welds, particularly in thicker sections or when welding dissimilar Aluminium alloys [5,8]. Slow rated welding also comes with potential risks that welders must be mindful of. One significant risk is the potential for excessive heat input and prolonged exposure to the weld pool. Slow welding rates can lead to higher heat concentration, causing the Aluminium to become more susceptible to distortion, warping, and burn-through and porosity. Welders must carefully manage the travel speed and adjust other welding parameters to avoid these issues and maintain optimal heat control [9,11].

The other side effect of slow welding speed can be undercut defect. Undercut is a common welding defect where the weld metal does not completely fill the joint, resulting in a groove or depression along the weld joint's edges. One of the factors that can contribute to the occurrence of undercut is the welding speed. Slow welding speeds can cause undercut faults due to the prolonged exposure of the weld metal to excessive heat. When the welding speed is slow, the heat input becomes higher, and the weld pool remains in a molten state for an extended period. The prolonged molten state of the weld pool can lead to excessive melting of the base metal at the edges of the joint. As a result, the molten metal flows away from the edges, causing a groove or depression, which is the undercut [10,11]. In the literature, it is observed that AA 4346 additive material is often preferred when welding AA 5005 alloys [12], however the mechanical properties of which is lower than that of the weld joint of the alloys with AA 5356 filler material.

The main goal of this study was to investigate the weldability, hardness and tensile properties and microstructural investigations of weld joints of marine AA 5005 alloy at low welding speed by using AA 5356 filler material.

2. Material and Methods

2.1 Preparing the samples and welding

AA 5005 aluminum alloy plates which are used in this study of which chemical composition and mechanical properties are shown in Table 1 and Table 2, respectively.

Table 1. Chemical composition of AA 5005 alloy

Si [%]	Fe [%]	Cu [%]	Mn [%]	Mg [%]	Zn [%]	Ti [%]	Cr [%]
0,1490	0,4042	0,0078	0,0299	0,5136	0,0067	-	0,0021

Table 2. Mechanical properties of AA 5005 alloy plate

Sample Direction °	Yield strength %0,2, MPa	Tensile strength, MPa	Elongation A_{50}, %
90	160	174	9
90	160	173	8,3
0	147	165	7,6
0	147	166	8,5

MIG welding was employed as the welding process, and Safra brand AA 5356 filler wire was utilized for the welding operation. Chemical composition and mechanical properties of filler wire are shown in Table 3 and Table 4, respectively.

Table 3. Chemical composition of filler wire

Si [%]	Fe [%]	Cu [%]	Mn [%]	Mg [%]	Zn [%]	Ti [%]	Cr [%]
0,25	0,40	0,10	0,05-0,2	4,5-5,5	0,10	0,15	0,1-0,3

Table 4. Mechanical properties of filler wire

ER5356 Mechanical Properties	
Yield Strength, MPa	>110
Elongation, %	17
Tensile Strength, MPa	240

The size of the starting test plate was 300 mm x 150 mm x 3mm. Before commencing the welding, meticulous cleaning of all plates was conducted with acetone to ensure a pristine surface free from contaminants. The prepared plates were then securely positioned and clamped in a welding fixture to ensure stable welding conditions. Fronius Transpuls Synergic 4000 robotic MIG welding machine was used for the precise and consistent welds, at pulse synergie mode. The welding process was carried out at a deliberately slow rate of 780 mm/min to explore its effects on the resulting weld joint and properties.

2.2 Non-Destructive tests

Visual control of weld seams is a critical aspect of the welding process, and it is conducted in accordance with the guidelines outlined in the EN ISO 13018 standard. This inspection method involves carefully examining the weld beat and

surrounding areas to detect any surface defects, discontinuities, or irregularities that could potentially compromise the integrity of the weld joint. Control criteria can be seen in Figure 1. Before control, weld beat was cleaned with a wire brush after then, the visual control of the weld beat was performed under 160 lux lighting conditions.
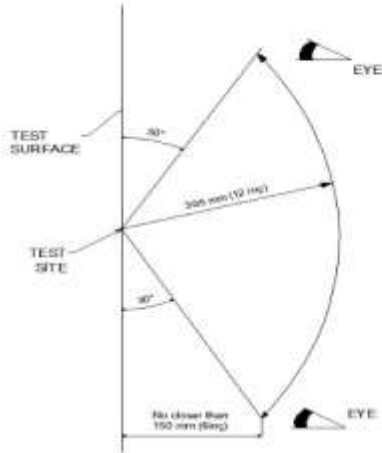

***Figure 1.** TS EN ISO 10042 control criteria*

The penetrant test for welding seams was performed. The liquid penetrant method was utilized, and a penetrant liquid was applied to the surface of the weld seam and allowed to dwell for the specified time. The excess penetrant was then removed, and a developer was applied to draw out any indications of surface-breaking defects. The developer rendered the indications visible, and the weld seams were carefully examined for any potential cracks, porosity, or lack of fusion. The penetrant test proved to be an effective non-destructive testing method in detecting surface discontinuities, ensuring the quality and integrity of the welded components and structures.

Radiographic inspection is shown as the most important inspection method used to test the quality and reliability of welded joints among non-destructive testing methods. Therefore, in our study, radiographic examination was performed to detect potential internal defects or discontinuities in the weld seams. As part of this test, weld seams were exposed to X-rays by an ICM X-ray device with specific parameters as 150 kV tube voltages, 5 mA tube current. Then, X-ray films were taken and the weld seam area was carefully examined.

The weld zone was characterized by XRD analysis (Rigaku D/Max which has a wavelength of 1.54056 Å with a Cu Kα radiation.

2.3 Destructive tests

After grinding the weld seam, a tensile strength test was carried out for the welded parts. Welded parts are meticulously prepared in accordance with ASTM E-8 standard and ground to ensure homogeneity. The samples obtained in this way were subjected to tensile strength test using Zwick Roell Z050 Tensile Test Machine (Figure 2). The test speed was 10 mm/min and the load was 50 kgf. By recording the data obtained during the experiment, it was checked whether the welded joint is within the range of tensile strength values recommended in the literature.
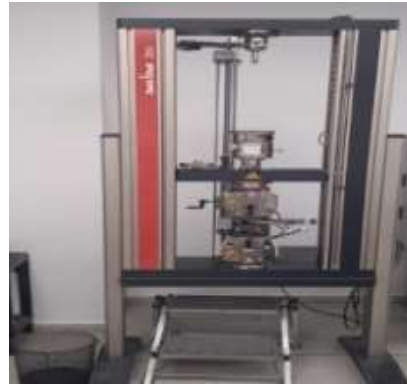
***Figure 2**: Zwick Roell Z050 Tensile Test Machine*

Tensile test specimen dimensions is shown on the Figure 3.
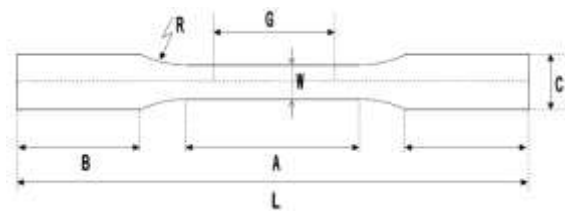
STANDART	STANDART
G = 50,00 ± 0,10 mm	A = 57 mm (min.)
W = 12,50 ± 0,05 mm	B = 50 mm
R = 12,5 mm (min.)	C = 20 mm
L = 200 mm (min.)	

***Figure 3**: Tensile test specimen and its dimensions*

by going through cutting, grinding and polishing stages, and then their microstructures were examined

using by optical microscope and electron microscopy.

The macro test provides valuable information about the size, shape and general characteristics of the weld, helping to identify visible defects or irregularities. The macro testing using the NIKON SM2 allowed the samples to be examined on a larger scale to evaluate their overall appearance and macro structure.

After welding AA 5005 alloy with AA 5356 additional wire, microstructure examination tests of weld zone, HAZ and base metal were performed using NIKON Eclipse MA200 microscope. This test method provides valuable information about grain structure, phase distribution, and possible defects or irregularities present in welds.

Grain size analysis was carried out using Zeiss Scope A1 and grain sizes were measured by the intersection method. The samples were carefully observed and analysed with a Zeiss Scope A1 microscope and detailed examination of the grain structure was provided. Quantitative data on average grain sizes in the material were obtained by using the intersection method to measure grain sizes. This non-destructive testing approach helps to comprehensively evaluate the grain size distribution and its effect on the mechanical properties of the material.

The samples were examined using the ZEISS EVO MA15 scanning electron microscope. Changes in the microstructure and phase size distributions of the source transition zone were studied in the BSE image material contrast mode.

Hardness measurements were carried out on the samples using the Zwick Roell ZHV 10 microhardness tester, in which sequential measurements were taken at 500 micron intervals starting from the base metal, according to the ASTM- E92 standard. In these measurements, applied loads and dwell times are 10 grf and of 15s, respectively. In this way, a Microhardness Contour diagram was obtained using by Minitab 19 software.

3. Results and Discussions

The visual test results of the weld bead were examined and it was found that it complies with the

TS EN ISO 10042 B criteria. During visual inspection, the weld bead and surrounding areas are carefully inspected for visible defects, discontinuities or irregularities. Inspection revealed that the weld piece displayed a satisfactory appearance with no signs of significant defects that could compromise its quality or structural integrity. The weld joint was observed to be well formed and free of any visible cracks, lack of melting or porosity.

The penetration test results of the weld bead were examined; < 3 mm surface porosity has been seen on the bead. This porosity had been occurred due to slow welding speed [9]. Porosity can be seen at Figure 4. But according to the TS EN ISO 23277 Level II standard, this scaled porosity is allowed. The penetration test involved inspecting the weld bead for any indications of incomplete fusion or penetration. The examination revealed that the weld bead exhibited satisfactory fusion and penetration, meeting the requirements specified in the TS EN ISO 23277 Level II standard. There were no indications of incomplete fusion or lack of penetration, indicating that the welding process was performed effectively, and the weld joint had achieved the desired level of fusion and penetration.

Figure 4: *Penetration Test*

In the radiography test conducted in this study, porosities were identified, similar to the observations in the penetration test. Similar to the findings of Zhan et al., it was observed that low welding speeds can lead to porosity formation. Some porosity formation was also observed at 780 mm/min welding speed. [15]. X-ray can be seen at Figure 5.
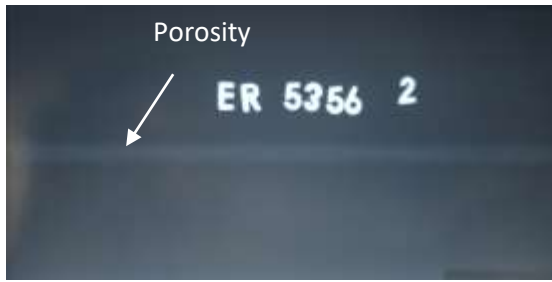
Figure 5: X-Ray of weld seam

The tensile test results, in accordance with TS EN ISO 15614-2 standard, met the condition of equal to or above "0" (Original condition; H_0) for the tensile strength. During the test, the test part was broken apart from the heat-affected zone (HAZ) (Figure 6). The yield strength was measured at 88 MPa, and the tensile strength recorded at 110 MPa (Table 5), the tensile strength minimum requirement of "0" condition tensile strength, which is set at 100 MPa. The successful outcome of the tensile test demonstrates the weld joint's excellent mechanical properties, as it withstood the applied tensile forces well above the minimum threshold. These results affirm the weld's reliability and structural integrity, meeting the stringent criteria outlined by the TS EN ISO 15614-2 standard.

Figure 6: Sample after tensile test.

Table 5: Mechanical properties after welding

Tensile Strength (MPa)	Yield Strength (MPa)
110	88

The macro test image (Figure 7) revealed the formation of a weld bead with a width of 4.90 mm and a depth of 3.44 mm. The height of the weld bead was measured to be 1.83 mm. These measurements indicate the dimensions and overall appearance of the weld bead on a larger scale.
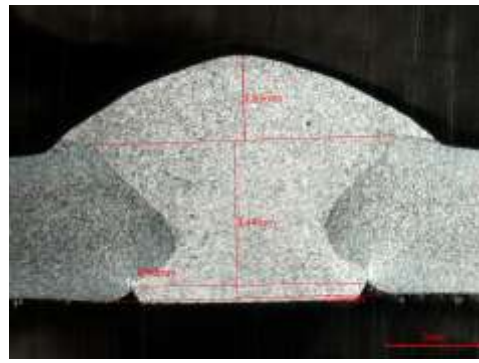

Figure 7: Macro image of welding

The micro test results revealed significant findings along the transition from fiber grains to recrystallization and regrowth grains. The examination displayed distinct microstructural changes, illustrating the transformation from initial fiber-like grains to newly recrystallized grains (Figure 8). Additionally, the presence of regrowth grains was evident, indicating the material's response to the welding thermal influence during welding. The differentiation of grain types from the base metal to the HAZ and fusion zone has significant implications for the mechanical properties and overall performance of the weld joint. The finer grain structure in the HAZ can lead to enhanced mechanical strength and improved resistance to certain forms of corrosion. On the other hand, the coarser grain structure in the fusion zone may result in reduced mechanical properties, such as lower tensile strength and increased susceptibility to brittle [13].
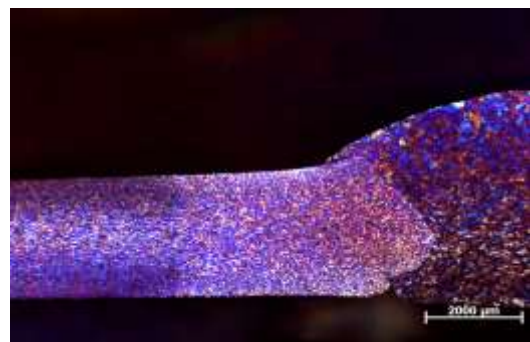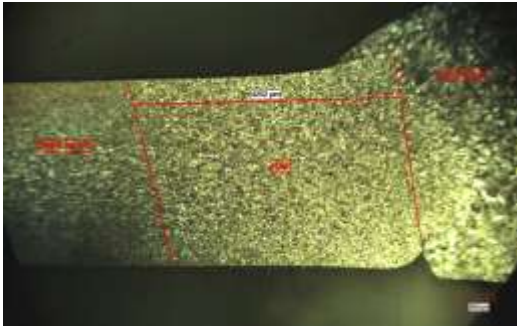

Figure 8: Transition of grains

Figure 9: HAZ measurement

HAZ length was measured as 4252 microns (Figure 9).Grain size measurement using the intercept method revealed distinct differences between the heat-affected zone (HAZ) and the fusion zone. The HAZ exhibited an average grain size of 33.99 µm, indicating a finer microstructure compared to the fusion zone. In contrast, the fusion zone displayed a larger average grain size of 68.94 µm (Figure 10 and 11), suggesting coarser grains within this region.
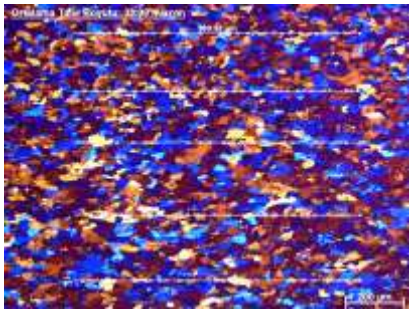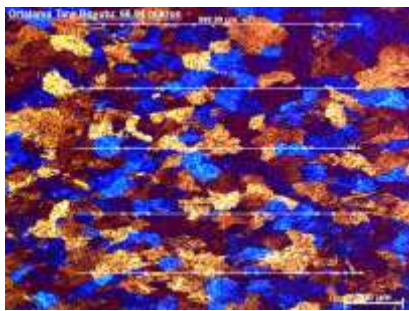

Figure 10: HAZ grain size measurement

Figure 11: Fusion zone grain size measurement

The SEM analysis revealed the presence of small and numerous white contrasted particles in the microstructure. Additionally, black contrasted areas were observed, indicating the formation of porous regions in the weld metal. The effect of heat input during the welding process resulted in the occurrence of coarse and large-sized intermetallic

phases within the welding zone. These findings provide valuable insights into the microstructural characteristics of the weld, shedding light on the distribution of particles and porosity, as well as the impact of heat on the formation of intermetallic phases. During the welding process, hydrogen can be introduced into the molten weld pool from various sources, such as moisture, contaminants, or the electrode coating. As the weld solidifies, the hydrogen can become trapped within the metal structure, forming hydrogen gas bubbles. These gas bubbles are responsible for the observed black contrast in the micrographs. The slow welding speed plays a crucial role in the hydrogen entrapment phenomenon. When the welding speed is slow, the solidification of the weld metal occurs at a slower rate. This extended solidification time provides more opportunities for the hydrogen atoms to diffuse and become trapped within the microstructure, leading to the formation of the black contrasted particles [14]. SEM image can be seen at Figure 12. Especially white parts took place grain boundaries and, in the grains are intermetallic phase (Al_3Mg_2) together with α-matrix phase (constituent gray parts). M.Bilgin et.al explained that the Al-Mg alloys includes Al_3Mg_2 and $Al_{12}Mg_{17}$ intermetallic phases in the welding zone and matrix (Figure 13) [16].
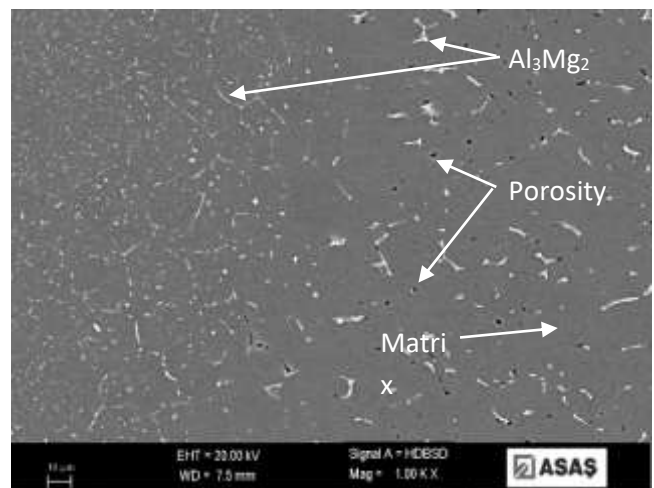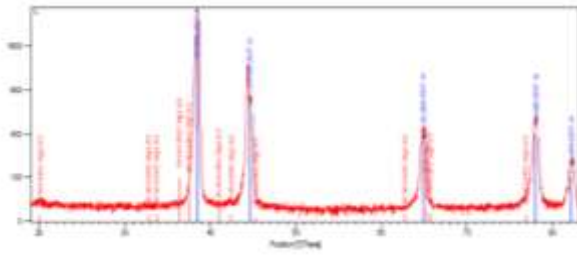

Figure 12: SEM image at BSE mode

Figure 13:. XRD analysis of the weld zone

The hardness test results showed findings as the measurements transitioned from the base metal to the recrystallized heat-affected zone (HAZ) region. During this transition, the hardness values were observed to decrease. Although, in the weld bead characterized by grain growth, a notable increase in hardness up to 100 HV was observed, because of the including higher alloying elements including filler materials composition. These results highlight the significant influence of microstructural changes on the material's hardness properties within different regions of the weld joint. Microhardness Contour Graphic can be seen at Figure 14.
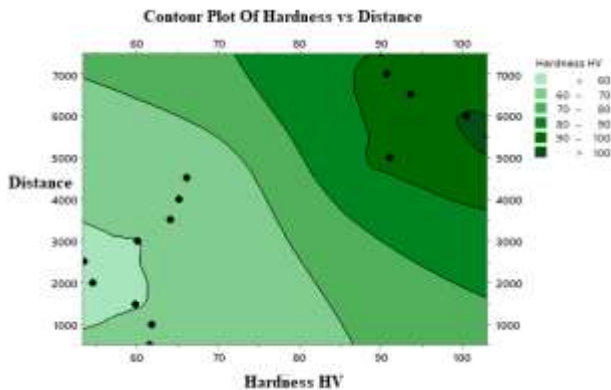

Figure 14: Microhardness Contour diagram

4. Conclusion
Based on the experimental results ;

1. The welding conducted at 780 mm/min welding speed was deemed suitable in terms of mechanical properties. However, during the radiographic and metallographic examinations, certain drawbacks were observed due to the low welding speed, resulting in high heat input. Grain size of heat-affected zone (HAZ) and the fusion zone are 33.99 µm and 68.94 µm, respectively.

2. AA 5005 alloy welded with AA 5356 exhibits that yield strength and tensile strength were 88 MPa and 110 MPa, respectively.

3. In comparison to the HAZ region, the weld bead contained significantly larger grains, with evident grain coarsening within the welding. The hardness was observed to decrease as it transitioned from the base metal to the HAZ region, while an increase in hardness was observed during the transition from the HAZ region to the weld bead. This can be attributed to the superior mechanical properties of the used 5356 filler wire compared to the 5005 alloy.

Overall, these findings provide valuable insights into the microstructural changes and mechanical properties of the welded joints, contributing to a comprehensive understanding of the welding process and the implications on the weld's performance and quality.

Author Statements:

- **Ethical approval:** The conducted research is not related to either human or animal use.
- **Conflict of interest:** The authors declare that they have no known competing financial interests or personal relationships that could have appeared to influence the work reported in this paper
- **Acknowledgement:** The authors declare that they have nobody or no-company to acknowledge.
- **Author contributions:** The authors declare that they have equal right on this paper.
- **Funding information:** The authors declare that there is no funding to be acknowledged.
- **Data availability statement:** The data that support the findings of this study are available on request from the corresponding author. The data are not publicly available due to privacy or ethical restrictions.

References

[1]Davis, J. R. (Ed.). (1999). Corrosion of aluminum and aluminum alloys. Asm International.

[2]. Quebbou, Z., Chafi, M., & Omari, L. E. H. (2021). Corrosion resistance of 5005 aluminum alloy by anodizing treatment in a mixture of phosphoric and boric acids. *Materials Today: Proceedings*, 37; 3854-3859.

[3]. Kaluç, E., & Taban, E. (2004). EN AW-5083-H321 Alüminyum alaşımının MIG, TIG ve sürtünen eleman ile birleştirme (FSW) kaynaklı bağlantılarının mekanik ve mikroyapısal özellikleri. *Mühendis ve Makina,* 46 (541); 40-51

[4]. Hooda, A., Dhingra, A., & Sharma, S. (2012). Optimization of MIG welding process parameters to predict maximum yield strength in AISI 1040. *International journal of Mechanical engineering and Robotics research*, 1(3); 203-213.

[5] Praveen, P., & Yarlagadda, P. K. D. V. (2005). Meeting challenges in welding of aluminum alloys through pulse gas metal arc welding. *Journal of Materials Processing Technology*, 164; 1106-1112.

[6] Mishra, B., Panda, R. R., & Mohanta, D. K. (2014). Metal Inert Gas (MIG) welding parameters optimization. *International Journal of Multidisciplinary and Current Research*, 2(1); 637-639.

[7] Olson, D. L., Dixon, R. D., & Liby, A. L. (Eds.). (2012). Welding: theory and practice. Elsevier.

[8] Wang, J., Feng, J. C., & Wang, Y. X. (2008). Microstructure of Al–Mg dissimilar weld made by cold metal transfer MIG welding. *Materials Science and Technology*, 24(7); 827-831.

[9] Çevik, B., & Koç, M. J. K. M. (2019). The effects of welding speed on the microstructure and mechanical properties of marine-grade aluminium (AA5754) alloy joined using MIG welding. *Metallic Materials/Kovové Materiály*, 57(5).

[10] Bhatt, D. A., & Mehta, H. R. (2015). Analyzing Effects of Weld Parameters for Increasing the Strength of Welded Joint on Mild Steel Material by Using the MIG Welding Process. Dimension, 300(300mm), 10mm.

[11] Himarosa, R. A., Rahman, M. B. N., Adi, R. K., Putra, L. A., & Nugroho, S. W. (2022). Effect of MIG Welding Speed Butt-Joint on Physical and Mechanical Properties of Materials AA 5083. *Materials Today: Proceedings*, 66, 3101-3106.

[12] EDITION, F. Arc Welding of Nonferrous Metals, Pg 16.

[13] Meseguer-Valdenebro, J. L., Martínez-Conesa, E., & Portoles, A. (2022). Influence of welding parameters on grain size, HAZ and degree of dilution of 6063-T5 alloy: optimization through the Taguchi method of the GMAW process. *The International Journal of Advanced Manufacturing Technology*, 120(9-10); 6515-6529.

[14] Atabaki, M. M., Yazdian, N., & Kovacevic, R. (2016). Partial penetration laser-based welding of aluminum alloy (AA 5083-H32). *Optik,* 127(16); 6782-6804.

[15] Zhan, X., Zhao, Y., Liu, Z., Gao, Q., & Bu, H. (2018). Microstructure and porosity characteristics of 5A06 aluminum alloy joints using laser-MIG hybrid welding. *Journal of Manufacturing Processes,* 35; 437-445.

[16] Bilgin, m., karabulut, ş., & özdemir, A. (2017). Alüminyum Magnezyum Alaşımlarının Sürtünme Karıştırma Kaynağı İle Kaynak Edilebilirliğinin Değerlendirilmesi. *Gazi University Journal of Science Part C: Design and Technology,* 5(2); 191-209.

Research Article

Determining the Relationship of Awareness of Radioactivity and Radiation Protection with the Level of Education in Turkey

Ramazan MANAV

Isparta University of Applied Sciences, Vocational School of Technical Sciences, Nuclear Technology and Radiation Safety Program, 32200, Isparta-Turkey
* **Corresponding Author** : **Email:** ramazanmanav@isparta.edu.tr - **ORCID:** 0000-0002-3666-6125

Abstract:

In this study, it was aimed to determine the level of awareness of Turkish society about radiation and the level of knowledge about radiation protection, and the relationship between the knowledge and education levels. A 22-item questionnaire was prepared for the participation of individuals who did not receive any academic training in the field of radiation. The prepared questionnaire was published on the web and 737 participants answered the questions. The answers of participants were evaluated using the SPSS 26 program. Relationship analyzes were made with the Pearson chi-square test on the data obtained from the questionnaire, and the data with a p value less than 0.05 were considered statistically significant. It was determined that the participants were aware of artificial and technological radiation sources, while their awareness about natural ionizing radiation sources was not at a sufficient level. The participants stated that they are aware of the effects of technological developments and the devices used in health institutions and also they trust the radiation workers working in the radiation fields. In addition it was determined that Turkish people had a low level of awareness of radioactivity and radiation protection information.

1. Introduction

Radiation affects us in every aspect of our life since the beginning of our world and is necessary for the continuation of our lives. Radioactive elements in the soil and cosmic rays from the sun are the fundamental elements of the world ecosystem. These sources described as natural radioactive elements, are necessary for the life-cycle of our ecosystem. However, radiation can negatively affect the body according to the level of exposure. People are exposed to radiation from cosmic rays originating from the sun and elements such as potassium-40, carbon-14, and radium can be affected in the body [1, 2]. With the development of technology, there is an increase in non-ionising (electromagnetic origin) and ionising (particle origin) radiation sources. Ionising radiation is used for scientific studies, diagnostic and surgical techniques, food industry, industrial establishments, and the health sector [3]. Technological developments are indispensable for our lives, especially in the field of health. Therefore, the exposure levels of artificial radiation that affect

our ecosystem and people are increasing. Increased exposure can cause instantaneous cell structure change in biological organisms or mutations of genetic material. Furthermore, radiation can cause structural disorders in future generations from inheritance and can promote the formation of cancer cells [4]. For this reason, it is important to be aware of and protect from radiation, which has now become integral in our lives because of technology. In this study, a survey was conducted to determine the awareness level of Turkish people about radiation and their level of knowledge of radiation protection.

2. Materials and methods

Within the scope of the study, a 22-item questionnaire was prepared for participants who were also screened to determine those who had received training in the field of radiation. Ethics approval was obtained from Isparta University of Applied Sciences Ethics Committee on 01/09/2022 (E-96714346-050.99-45454). In order to obtain the

demographic characteristics of the participants, three questions regarding sex, age, and educational status were asked. To measure participant awareness of radiation and radio production, 19 questions with basic information about radiation, were presented to the participants. The 22-item questionnaire was presented to the participants online and was answered by 737 participants.

The data obtained from the participants were evaluated using the SPSS 26 software. Correlation analyses were performed with the Pearson chi-square test and data with a p value less than 0.05 were considered statistically significant. The data of the study were evaluated in terms of the significance of the relationship between radioactivity and radiation protection and the education level of Turkish participants.

3. Results and discussion

737 participants were evaluated for this study. 9.5% of the participants were under 19 years old, 12.1% were 20-29 years old, 25% were 30-39 years old, 33.6% were 40-49 years old, 13.5% were 50-59 years old, and 6.3% over the 60 years old. It was determined that 25.9% of participants had high school education, 20.3% had an associate degree, 43.9% had bachelor's degree, and 9.9% had a MSc or PhD degree.

Participants were asked to give a yes or no answer in agreement or disagreement to the statement: "Some of the devices we use daily, such as mobile phones, televisions, and computers also emit radiation to the environment". 96.3% of participants with a high school education, 97.3% with an associate degree, 99.1% with a bachelor's degree, and 95.8% with either a MSc or PhD degree answered yes. For this question, the difference between the answers and the level of education were found to be statistically significant (p=0.014).

The percentages of answers given by the participants to the question: "I have knowledge about radiation protection methods", are given in table 1 and the variation between of participants with different education levels was statistically significant (p=0.015). The percentages of the answers given by the participants to the multiple-choice question: "Which of the following is the competent institution dealing with the developments and precautions regarding radiation in Turkey?" are given in table 2. A high degree of statistical significance was found between the awareness of the official institution dealing with radiation in Turkey and the education level of the participants (p=0.000). 24.4% of the participants answered yes to the

Table 1. *Percentages of participant answers to the question: "I have knowledge about radiation protection methods"*

	Yes	**No**	**No idea**
High school	42.0%	42.6%	15.4%
Associate degree	50.7%	29.1%	20.3%
Bachelor's degree	56.6%	30.6%	12.8%
MSc or PhD degree	45.8%	34.7%	19.4%
Total	50.5%	33.8%	15.7%

p=0.015.

question: "The radiation we take into our body with food and drinks causes internal irradiation in our body", and a statistically significant relationship could not be obtained with the level of education (p=0.264).

The majority of the participants (85%) answered yes in agreement to the statement: "Radiation is harmful to living things", and stated that they are aware of the harm of radiation to human health. It was determined by statistical analysis that this awareness was significantly related to education level (p=0.017). To the question: "Radiation is harmful only for pregnant women", the majority of participants answered no and the minimum percentage of this question (88.9%) were given by high school degree participants. No statistical significance was found for this question with education level (p=0.195)

51.0% of the participants answered yes in agreement to the statement: "The dosage of artificial radiation we are exposed to from medical applications and from nuclear sources is higher than the dosage we are exposed to from natural sources including cosmic radiation". It was found that the answers given were related to the level of education (p=0.000). The percentages of the answers given by the participants to the statement: "Our body needs some radiation for vital activities", are given in table 3. Also, 75.5% of the participants stated that they do not need radiation for vital activities. When the answers given were evaluated statistically, no significant difference was found between education levels (p=0.282).

To the statement: "Radon gas, which is a natural radiation source, is a source of ionizing radiation that accompanies us at every stage of our lives", 30.3% of participants answered yes, and there is a meaningful relationship with education levels (p=0.255). 77.8% of participants selected the medical waste symbol correctly (p=0.813) and 91.6% chose the radiation symbol correctly. It was determined that the awareness of the symbol was not significant with the education level.

Table 2. *Percentage of answers given by the participants to the question: Which of the following is the competent institution dealing with the developments and precautions regarding radiation in Turkey?*

	TBMM Grand National Assembly of TURKEY	TAEK Turkish Atomic Energy Authority	TUİK Turkish Statistical Institute	Ministry of Health	No idea
High school	4.3%	24.6%	3.2%	26.2%	41.7%
Associate degree	0.7%	22.6%	2.1%	34.9%	39.7%
Bachelor's degree	0.6%	37.0%	1.9%	24.1%	36.4%
MSc or PhD degree	0.0%	50.0%	0.0%	16.7%	33.3%
Total	1.5%	32.2%	2.1%	26.1%	38.1%

p=0.000

In addition, 94.0% answered yes to the question: "When I see the signs indicating radiation areas in health institutions, I can understand that the area is a radiation area", which was significant between the awareness of field marks in health institutions and the level of education (p=0.043).

Table 3. *Response percentages of the participants to the statement: "Our body needs some radiation for vital activities"*

	Yes	No	No idea
High school	23.9%	31.9%	44.1%
Associate degree	21.6%	38.5%	39.9%
Bachelor's degree	25.3%	38.4%	36.3%
MSc or PhD degree	28.2%	43.7%	28.2%
Total	24.5%	37.3%	38.2%

p=0.282

71.6% of participants correctly responded that the devices used in the health sector for medical imaging and treatment are an important source of radiation and can cause diseases such as cancer in later years of life (p=0.091). Also, 41.0% of participants answered correctly that these devices emit radiation even when turned off (p=0.102). There was no significant relationship between the participants' views about radiation emitting devices used for examination and treatment in health institutions and their education levels.

In this study, the majority of the participants (97.7%, p=0.014) stated that they were aware of the fact that technological developments increased the amount of radiation, and to the question " Which institution is responsible for radiation-related controls is Turkey?", 32.2% of the participants correctly suggested TAEK.

75.2% of the participants answered yes in agreement to the statement: "The radiation dosage that the human body can be exposed to decreases when moving away from the radiation source ", and a significant difference was found between damage caused by the distance from the radiation source and the level of education (p=0.000). In addition, 77.6% of the participants answered yes in agreement to the statement: "The amount of radiation damage to human health depends on the duration of exposure", but there was no significant relationship between the duration of exposure and damage and education level (p=0.291).

Some questions were prepared to determine the knowledge and attitudes about medical radiation-emitting devices used in health institutions, and the consequences for people working with these devices (table 4). 85.0% of the participants who had not received any radiation related training stated that radiation was harmful to living organisms, while 50.5% stated that they had sufficient knowledge about radiation protection. Paolicchi et al. (2016) showed with the participation of those working in the field of radiation, that 90.0% stated that they did not show the necessary sensitivity in taking radiological precautions [5]. While 24.5% (p=0.282) of participants thought that people receive low levels of radiation for vital activities, 37.5% (p=0.264) thought that people are exposed to radiation by internal irradiation from food intake. Dönmez et al. (2021) generated a survey for radiation workers and found that 85.6% of radiation workers correctly agreed to the statement that exposure to a small amount of radiation is healthy [3]. 77.8% (p=0.813) and 91.6% (p=0.133) of participants correctly identified medical waste and radiation symbols, respectively. Jafri et al., (2022) in their study of radiation workers found that 96.7% of participants had correct awareness of the radiation symbol [6]. In our study, 94.0% of the participants (p=0.043) stated that they could understand the radiation field from markers found in health institutions. 75.2% of the participants (p=0.000) agreed to the statement: " The radiation dosage that the human body can be exposed to decreases when moving away from the radiation source". Futhermore, 77.6% of the participants (p=0.291) answered correctly that the duration of exposure to radiation increases the effect of radiation. Dönmez et al. (2021) reported that 72.2% of radiation workers gave the correct answer to a similar question [3].

Table 4. *Response percentages and p value about the participants' knowledge and attitudes towards devices and the effects to staff in health institutions*

	Yes	No	No idea	p
I think that the most used x-ray method in diagnostic imaging examinations may increase the risk of developing cancer in the future.	71.6%	9.1%	19.2%	0.091
We are exposed to radiation without having an examination that involves a radiation-emitting device.	75.7%	8.6%	15.8%	0.041
Although radiation devices are switched off, they still emit radiation into the environment.	41.0%	26.5%	32.6%	0.102
I take care to use the following protection tools (such as lead apron, neck collar, gonad protector ...) while having an X-ray.	32.8%	67.2%	-	0.794
I trust the information of radiology units in health institutions about radiation protection and patient dose.	45.6%	54.4%	-	0.268

32.8% of participants stated that they took care to use protective measures such as lead aprons while having x-rays, and this was not related to their education level (p=0.794). Güden et al. (2012) found that 22.5% of radiation workers used protective measures such as lead aprons for themselves, 97.8% used a shielded cabin, and 15.7% allowed patients to use protective measures [7,8]. Conversely, 45.6% of participants in our study stated that they trust radiation workers in health institutions, and no significant relationship was found between this trust and education levels (p=0.268).

4. Conclusions

In this study, we determined that the awareness about radiation and radioprotection of individuals who did not receive any training about radiation or who did not work in these fields, was at a moderate level. Participants stated that they are aware of the effects of radiation-emitting technological developments and devices used in health institutions and that they moderately trust radiation workers. However, participants were not informed enough about natural radioactivity and radioactive elements. Therefore, Turkish people had a low level of awareness of radioactivity and radiation protection. In addition, no significant relationship was found between the low level of awareness and the level of education. As a result, in order to increase the level of knowledge and awareness about radiation in Turkish people, it would be beneficial to attract the attention of people with adverts or posters through social media, health institutions, educational institutions, and so on.

Author Statements:

References

[1] White, S. C., & Pharoah, M. J. (2018). White and Pharoah's Oral Radiology: *Principles and Interpretation*. Elsevier Health Sciences.
[2] Başaran, M., & Bozdemir, E. (2021). Diş Hekimliği Öğrencileri ve Uzmanlık Öğrencilerinin Radyasyondan Korunma ve Radyasyonun Biyolojik Etkileri Hakkındaki Farkındalığının Değerlendirilmesi. *Düzce Üniversitesi Sağlık Bilimleri Enstitüsü Dergisi*, *11*(2); 165-170.

[3] Dönmez, A., Türk A., Bacak, A., & Şentürk, Ö. Sağlık Çalışanlarının İyonize Radyasyon ve Radyoaktif Maddelerden Korunmaya Yönelik Bilgilerinin Belirlenmesi. *Gümüşhane Üniversitesi Sağlık Bilimleri Dergisi*, *10*(4); 876-882.

[4] Coşkun, Ö. (2011). İyonize radyasyonun biyolojik etkileri. *Teknik Bilimler Dergisi*, *1*(2); 13-17.

[5] Paolicchi, F., Miniati, F., Bastiani, L., Faggioni, L., Ciaramella, A., Creonti, I., ... & Caramella, D. (2016). Assessment of radiation protection awareness and knowledge about radiological examination doses among Italian radiographers. *Insights into imaging*, *7*(2); 233-242.

[6] Jafri, M. A., Farrukh, S., Zafar, R., & Ilyas, N. (2022). A survey on radiation protection awareness at various hospitals in Karachi, Pakistan. *Heliyon*, *8*(11); e11236

[7] Mudun, A. (2009). Meme Kanserinde İntraoperatif Gama Prob Kullanımında Radyasyon Güvenliği. Meme Sagligi Dergisi/Journal of Breast Health, 5(3); 115-118.

[8] Güden, E., Öksüzkaya, A., Balcı, E., Tuna R., Borlu, A., & Çetinkara, K. (2012). Radyoloji çalışanlarının radyasyon güvenliğine ilişkin bilgi, tutum ve davranışı. *Sağlıkta Performans ve Kalite Dergisi*, *3*(1); 29-45.

Research Article
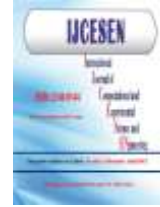
Classification of Histopathological Images in Automatic Detection of Breast Cancer with Deep Learning Approach

Yasin KIRELLİ[1*], Gizem AYDIN[2]

[1]Kütahya Dumlupınar University, Management Information Systems Department, Kütahya-Türkiye
* Corresponding Author: Email: yasin.kirelli@dpu.edu.tr – **ORCID:** 0000-0002-3605-8621

[2] Ereteam, İstanbul-Türkiye
Email: gaydin@ereteam.com – **ORCID:** 0000-0001-6353-0648

Abstract:

Convolutional neural networks have emerged as an essential tool for image classification and object detection. In the health field, these tools are a crucial factor in saving time and minimizing the margin of error for the health system and employees. Breast cancer is the most common type of cancer in women worldwide. In many cases, it can threaten human life, resulting in death. Although methods have been developed for the early diagnosis of this health problem, its support with digital systems remains incomplete. In diagnosis, histopathological images are examined with microscope methods. In cases where the number of pathologies is insufficient, delay problems may occur and the error rate increases in manual controls. The study aims to design a deep-learning object detection method for the pre-detection of breast cancer. The publicly published BreaKHis dataset is used as the dataset. Model results that generated with VGG16, InceptionV3 and ResNet50 deep learning architectures have been compared. The highest accuracy rate have been obtained with the proposed model as 85%. Accuracy, AUC, precision, recall, F-score performance metrics have been analysed for each model. A decision support system screen design has been created using the proposed model weight file. With the study, the computer-assisted clinical support system makes clinicians' life more manageable and recommends early diagnosis.

1. Introduction

With the development of artificial intelligence day by day, image classification problems have become a popular topic. It is expected to make people's lives easier with machine learning methods used in many areas in our daily life. In recent years, machine learning techniques have been used in cancer detection [1]. In order to prevent human errors, it has become more important to move machine learning processes to automated processes. Various ML-based methods have been presented to contribute to early diagnosis in computer-aided diagnosis systems, and their reliability and effectiveness have been proven [2,3]. Deep learning has had great success in medical image diagnostics. Convolutional networks perform better in medical image analysis than other machine learning techniques. However,

large amounts of labelled data are needed for these networks to be effective [4,5].

Breast cancer is the most common type of cancer in women and the highest risk of death in the world. A report by the American Cancer Society shows that breast cancer accounts for an estimated 31% of new cancer cases in women [6]. In 2012, it was observed that approximately 12% of newly diagnosed cancer patients were women, but it has now been found that it is rarely seen in men. The most effective and essential way to prevent this situation is the early diagnosis of cancer [5,7]. Three different models, frequently preferred in the literature, have been used in the study. The user interface is designed with a proposed VGG16-based model with high accuracy. Performance metrics obtained from the models have been evaluated with AUC metrics and a confusion matrix.

2. Artificial intelligence (ai) studies in breast cancer

2.1. Breast Cancer

Breast cancer is a disease caused by cell mutations. It usually begins in the breast tissue but may rarely occur in the chest wall, breastbone, or lungs. Breast cancer, a malignant tumour that can be seen in both men and women, is the most common type of cancer affecting many women worldwide [13]. In addition, side effects during the treatment can affect the quality of life. Therefore, regular screening and early diagnosis are important in the fight against breast cancer [14].

According to statistics, breast cancer is one of the leading causes of cancer-related deaths in women. According to the World Health Organization, approximately 2.3 million women worldwide were diagnosed with breast cancer in 2020, and about 685,000 women died [14]. However, with regular screening tests and early detection, death rates from breast cancer can be reduced. According to the National Cancer Institute, diagnosing breast cancer in its early stages increases treatment options and control of the disease. Therefore, regular screening tests are essential for diagnosing breast cancer, especially in high-risk individuals (e.g., those with a family history) [13]. Breast cancer treatment may include different approaches such as surgery, chemotherapy, radiotherapy, and hormone therapy. However, treatment options are determined by the patient's age, general health, stage of the disease, and other factors. Breast cancer treatment can also cause various side effects, so it's crucial for patients to follow their treatment plan and consult their doctor to manage side effects. In conclusion, breast cancer is a significant health problem, and regular screening tests and early diagnosis are vital for treatment and maintenance of quality of life [15].

2.2. Early Detection of Breast Cancer

Early detection of breast cancer is vital as it is the most common type in women. Early breast cancer diagnosis involves detecting cancer cells before they multiply rapidly [16]. Thanks to early diagnosis, the progression of the disease is prevented by diagnosing cancer in treatable stages. Breast examination, mammography, and other imaging tests detect breast cancer early in women [17].

Women can monitor themselves by checking themselves regularly, but self-examination in this way is not enough. It is imperative to have regular screening tests. Traditional methods for the early diagnosis of this cancer take a long time and do not always give accurate results [18]. Therefore, automated machine learning systems are needed for breast cancer prediction.

2.3. Use of Artificial Intelligence in Breast Cancer Diagnosis

Artificial intelligence has been used widely in breast cancer diagnosis in recent years. Artificial intelligence and its deep learning subfield are practical tools for analysing and interpreting breast cancer data. This technology can help to obtain faster and more accurate results in screening tests, cancer diagnosis, and treatment processes. Artificial intelligence is accepted to automatically recognize and diagnose tumour lesions by quickly learning the image data with correctly labelled data [19]. In this way, it is expected to alleviate the workload of doctors to a great extent [20].

Mammography images create large datasets and artificial intelligence technologies such as machine learning and AI networks can be used to analyse these data. These technologies are also used to detect early stages of cancer in screening tests, which can help make treatment more successful [21]. In addition, predicting the risk of cancer spreading by AI tools. For example, an artificial intelligence algorithm that considers many factors such as tumour size, type, extent of spread, personal and family history, and genetic factors can predict a patient's risk of cancer progression. This can help make treatment more effective and personalized [22]. Related studies and AI methods that used in the subject are shown comparatively in the Table 1.

3. Materials and Methods

3.1. BreakHis Dataset

BreakHis is a database called Breast Cancer Histopathological Image Classification. Different size factors are used in this database as Table 2. It consists of 9,109 microscopic breast tumour images obtained from 82 patients.

Table 1. Literature review on the subject

Author	Data Size	Method	Result - AUC
Farjana Parvin, Md. Al Mehedi Hasan[4]	2013	VGG-16 LeNet-5 AlexNet ResNet-50 Inception-v1	%86 %50 %85 %50 %94
Xujuan Zhou, Yuefeng Li v.d.[8]	10389	GoogleNet SVM The Proposed Model	%54 %78 %84
Karthiga R, Narasimhan K[9]	300	Linear SVM Quadratic SVM Fine Gaussian SVM Weighted KNN Fine KNN	%93 %92 %91 %90 %90
Zhan Xiang, Zhang Ting v.d.[10]	4960	AlexNet	%83
Mahesh Gour, Sweta Jain, T.Sunil Kumar[11]	2013	AlexNet GoogleNet VGG16	%84 %83 %83
Karan Gupta, Nidhi Chawla[12]	1617	VGG16 VGG19 Xception ResNet50	%82 %83 %78 %84

- Size factors of images include 40X, 100X, 200X, and 400X.
- These images contain a total of 2,480 samples, both benign and malignant.
- The features of the images are represented by 700X460 pixels, 3-channel RGB color space, and each channel has 8 bits of depth.
- The format of the images is PNG [23].

Table 2. BreakHis image sets and features

Magnification	Benign	Malignant	Total
40X	652	1,370	1,995
100X	644	1,437	2,081
200X	623	1,390	2,013
400X	588	1,232	1,820
Total of Images	2,480	5,429	7,909

The image below is image of some examples in the BreakHis dataset. The upper row shows benign tumours of different sizes, and the lower row shows malignant tumours of various sizes as Figure 1.
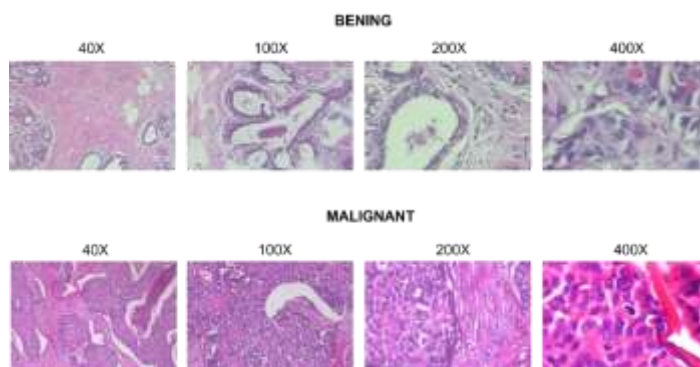

Figure 1. BreakHis image set samples

- 800 images from the BreakHis image database have been used in the model.
- Of these, 640 images have been used as a training set and 160 as a test dataset.
- Training and test data sets are separated by 80% - 20%, respectively.
- Within the training and test data, 200x images have been used in the dataset.

3.2. Proposed VGG Based Model

VGG16 is a CNN architecture introduced in 2014 by Karen Simonyan and Andrew Zisserman in their article titled Very Deep Convolutional Networks for Large-Scale Image Recognition [24]. There are two forms of the VGG Neural Network model. These are the VGG16 and VGG19 models. VGG16 is a 16-layer neural network and is one of the most popular deep learning architectures, not counting the maximum pooling and softmax layers. VGG19 is a slightly deeper version of VGG16 and consists of 19 layers. The Keras library includes pre-trained models VGG16 and VGG19 for both Theano and TensorFlow backends. These models have pre-trained weights for use in tasks such as image classification and are frequently preferred for transfer learning [25]. The VGG16 architecture is as Figure 2.

- VGG16 uses only 3x3 size filters in convolutional and pooling layers. These filters perform convolution by acting on the input data at 3x3 size and then downscaling it to a 2x2 layer for pooling.
- Convolutional layers use 3x3 filters in VGG16. This small kernel size is used to create feature maps that are more complex and can generalize better.
- VGG16 has 1x1 convolution layers to transform the input linearly. These layers perform dimensional transformations by changing the input data channels without interacting with each other.

- In convolutional layers of the network, the step size is 1 pixel. This helps preserve spatial resolution because filters are applied to each pixel, thus helping to maintain detail.
- ReLU (Rectified Linear Unit) activation function is used in all hidden layers of VGG16. ReLU adds non-linearity by directly passing positive inputs while reducing negative inputs to zero.
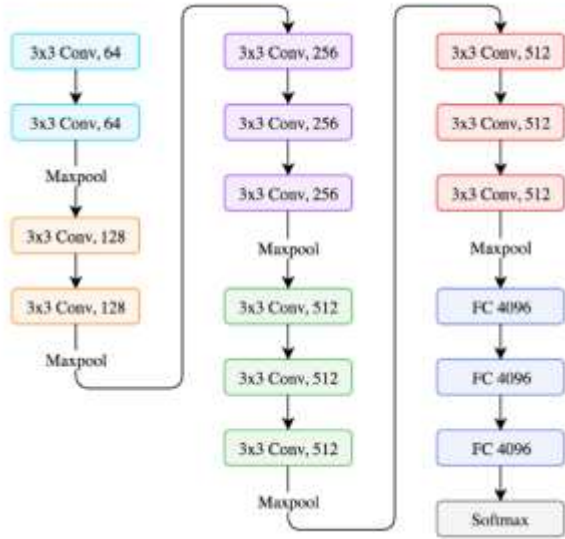

Figure 2. *VGG16 Architecture [25]*

The model has been developed using Python language and Keras deep learning library. As shown in Figure 3, the Vgg16 model architecture is the first layer and offers a relearning model with a previously learned model. As shown in the figure, the number of parameters at 14 million in the Vgg16 layer starts with a previously pre-trained parameter number.
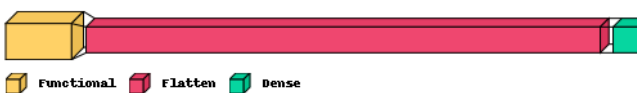

Figure 3. *Proposed VGG16 based architecture*

The result of a 70-epoch training cycle is shown in accuracy and loss graphs with training and validation curves. According to the charts, it is seen in the graph that the accuracy rate is 85% on average, and it performs successful classification as shown Figure 4.
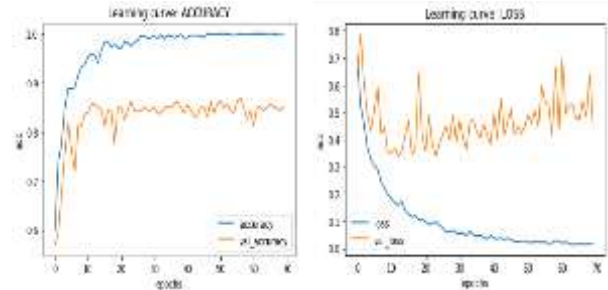

Figure 4. *Proposed model accuracy and loss chart*

Accuracy, precision, recall, and f1 score values according to the general and individual metrics of the classification metrics are given in the table. According to the metrics, a satisfactory classification has been achieved with 85% accuracy. According to the classification metrics of the separate classes, a classification rate has been obtained as more successful than benign, with a success rate of 86% and 83% for malignant as shown Table 3.

Table 3. *Performance metrics of proposed model*

	Accuracy	Precision	Recall	F1-Score
General	0.850	0.858	0.850	0.849
Class 'benign'	-	0.912	0.775	0.838
Class 'malignant'	-	0.804	0.925	0.860

As another metric in the classification performance obtained with the test data set, the ROC curve is given in the image below. The upward trend of the curve indicates a successful classification efficiency with an AUC ratio of 0.93 as shown Figure 5.

3.3. ResNet50 Architecture Model

ResNet-50 is a 50-layer convolutional neural network and backbone architecture used in computer
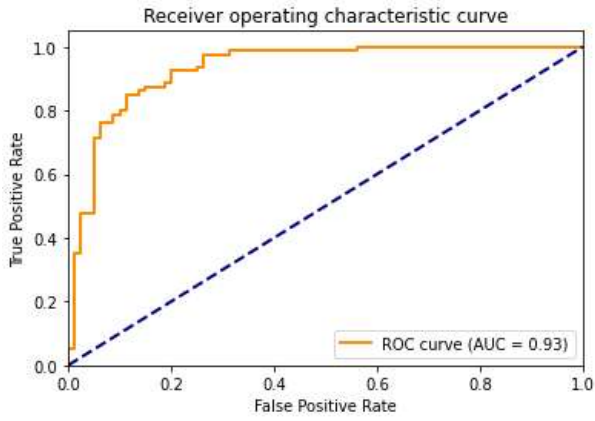
Figure 5. Proposed model ROC Curve

vision tasks. ResNet introduced an innovation in training deep neural networks, making it possible to train networks with more than 150 layers. This innovative neural network was first introduced in 2015 by Kaiming He et al. in a paper titled "Deep Residual Learning for Image Recognition." A significant problem convolutional neural networks face is the "vanishing gradient problem." In this problem, the gradient values decrease significantly during backpropagation, and the weights hardly change; ResNet uses the "skip connection" feature to overcome this problem and architecture, as shown in Figure 6 [26-28].
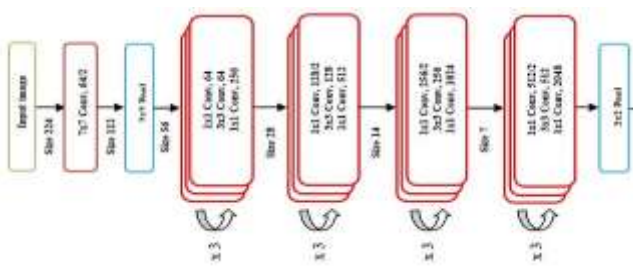

Figure 6. ResNet50 architecture

The result of a 70-epoch training cycle is shown in accuracy and loss graphs with training and validation curves. According to the charts, it is seen in the graph that the accuracy rate is 73% on average, and the ROC curve, as another metric in the classification performance obtained with the test data set, is given in the image below with an AUC ratio of 0.79 as shown Figure 7 and Figure 8. According to the classification metrics of the separate classes, a classification rate has been obtained as more successful than benign, with a success rate of 84% and 67% for malignant as shown Table 4.
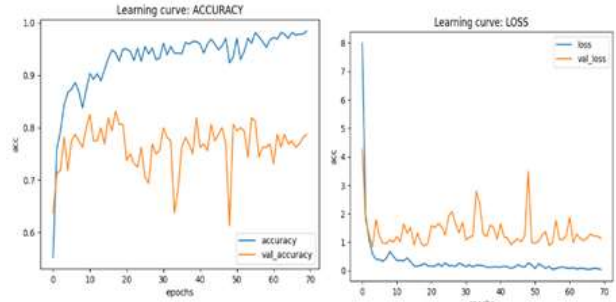
Figure 7. ResNet50 model accuracy and loss chart

Table 4. Performance metrics of ResNet50 model

	Accuracy	Precision	Recall	F1-Score
General	0.731	0.761	0.731	0.723
Class 'benign'	-	0.849	0.562	0.677
Class 'malignant'	-	0.673	0.900	0.770
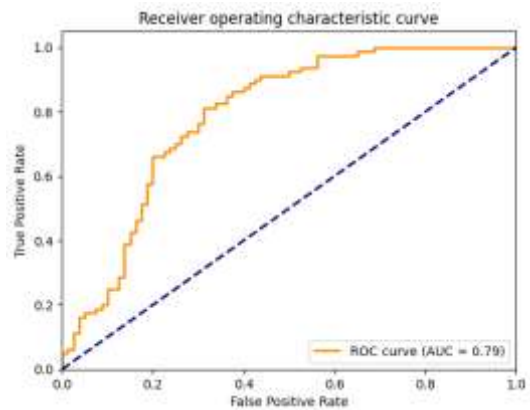
Figure 8. ResNet50 model ROC Curve

3.4. InceptionV3 Architecture Model

InceptionV3 is a convolutional neural network model for image classification developed by Google and released in 2015. InceptionV3 is an improved version of the InceptionV1 model introduced in 2014 as GoogLeNet, and the components of the Inception V3 model are shown in the Figure 9. InceptionV3 includes architectural improvements over the V1 version and includes:

Factored convolutions: This technique helps reduce computational complexity and improve performance by splitting a single large convolution into multiple smaller convolutions.

Asymmetric convolutions: This technique helps capture features of different scales and orientations using various filter sizes in other channels.

Auxiliary classifiers: These classifiers are added to the intermediate layers of the network to help improve gradient flow and regularization.

Efficient grid dimension reduction: This technique combines maximum pooling and convolutional layers to reduce the spatial dimensions of feature maps, which helps minimize computational load while preserving crucial spatial information. These architectural improvements have helped Inception V3 achieve state-of-the-art results on various image classification benchmarks. For example, Inception V3 has reached a top 5 error rate of 23.1% in the ImageNet Large Scale Visual Recognition Challenge (ILSVRC) 2015 [29-33].
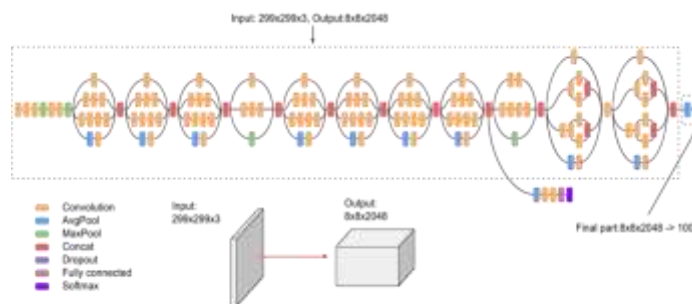
Figure 9. *InceptionV3 architecture*
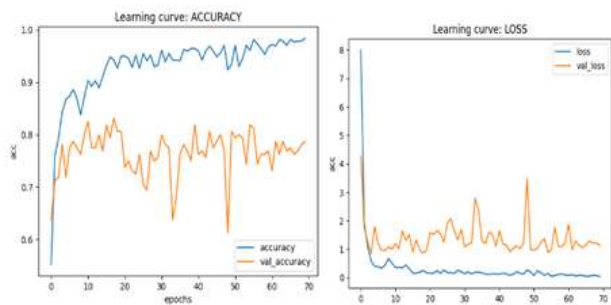
Figure 10. *InceptionV3 model accuracy and loss chart*

According to the graphs, it is seen in the chart that the accuracy rate is 78% on average, and the ROC curve, as another metric in the classification performance obtained with the test data set, is given in the image below with an AUC ratio of 0.86 as shown Figure 10 and Figure 11. Accuracy, precision, recall, and f1 score values according to the general and individual metrics of the classification metrics are given in the table. It has been observed that with 78% accuracy according to the metrics. According to the classification metrics of the separate classes

Table 5. *Performance metrics of InceptionV3 model*

	Accuracy	Precision	Recall	F1-Score
General	0.787	0.788	0.787	0.787
Class 'benign'	-	0.774	0.812	0.793
Class 'malignant'	-	0.803	0.762	0.782
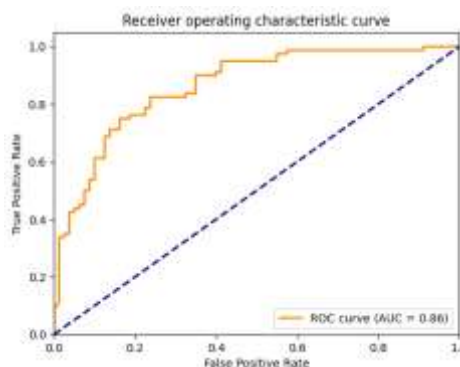
Figure 11. *InceptionV3 model ROC curve*

a classification rate has been obtained as more successful than benign as shwon Table 5. A screen for the end user has been developed using the Python Tkinter library. The Keras weight file has been obtained due to the application's model training. The flowchart shows that the weight file of the presented model that provides the most successful classification among the three models has been selected as shown Figure 12. Thus, as shown in the screenshots as Figure 13, as a result of a fast classification, the classification process from the selected image takes less than one second. It creates a decision support system for physicians. In future studies, it has shed light on using different layered model architectures to increase the classification success.

4. Results

In this study proposed vgg-based deep learning method has been developed to classify histopathological images of breast cancer. The presented model has achieved successful results in the classification of pathological images, and accordingly, it shows that it can be an essential help to doctors in clinical applications. The results obtained with the presented model emphasize the

Figure 12. *Clinical decision support system workflow chart*

Figure 13. *User interface and sample result screens*

importance of making a quick and accurate decision to diagnose the disease and provide a decision support system with the interface created. With the proposed model, the result presented as the study output, false positive or false negative classification in pathological classification, can help reduce the 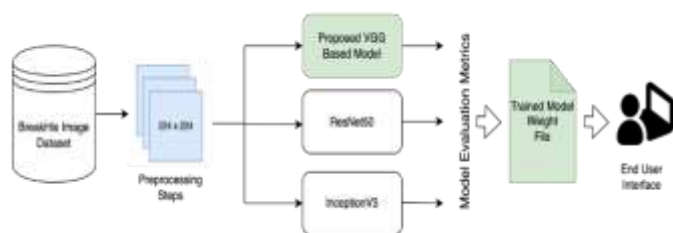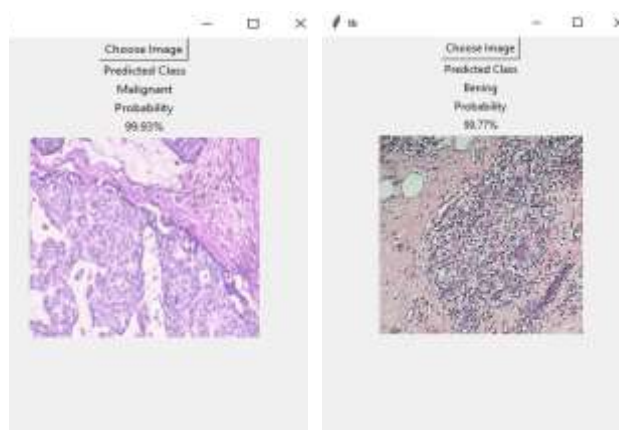effects and make the treatment process more effective. In addition, the high sensitivity obtained as a result of the presented model classification can reduce the risk of exposure of patients and physicians to the workload of patients and physicians when potentially invasive interventions are not needed. In conclusion, this study demonstrated the potential of using deep learning techniques, user interfaces, and practical applications to diagnose breast cancer. The developed VGG-based model offers high accuracy and sensitivity, close to 90 percent, which can be used as a reliable tool to classify histopathological images. This study may contribute to the further development of artificial intelligence-based methods for disease diagnosis with histopathological images by inspiring future research.

Author Statements:

- **Ethical approval:** The conducted research is not related to either human or animal use.

- **Conflict of interest:** The authors declare that they have no known competing financial interests or personal relationships that could have appeared to influence the work reported in this paper

- **Acknowledgement:** The authors declare that they have nobody or no-company to acknowledge.

- **Author contributions:** The authors declare that they have equal right on this paper.

- **Funding information:** The authors declare that there is no funding to be acknowledged.

- **Data availability statement:** The data that support the findings of this study are available on request from the corresponding author. The data are not publicly available due to privacy or ethical restrictions.

References

[1] Abdar, M., Zomorodi-Moghadam, M., Zhou, X., Gururajan, R., Tao, X., Barua, P. D., & Gururajan, R. (2020). A new nested ensemble technique for automated diagnosis of breast cancer, *Pattern Recognition Letters*, vol. 132, pp. 123–131, doi: 10.1016/j.patrec.2018.11.004.

[2] Liu, M., Hu, L., Tang, Y., Wang, C., He, Y., Zeng, C., ... & Huo, W. (2022). A Deep Learning Method for Breast Cancer Classification in the Pathology Images, IEEE *Journal of Biomedical Health Informatics*, vol. 26, no. 10, pp. 5025–5032, doi: 10.1109/JBHI.2022.3187765.

[3] Nahid, A. A., & Kong, Y. (2017). Involvement of machine learning for breast cancer image classification: a survey. *Computational and mathematical methods in medicine*, 2017., doi: 10.1155/2017/3781951.

[4] Parvin, F., & Hasan, M. A. M. (2020, June). A comparative study of different types of convolutional neural networks for breast cancer histopathological image classification. In 2020 *IEEE Region 10 Symposium (TENSYMP)* (pp. 945-948), doi: 10.1109/TENSYMP50017.2020.9230787.

[5] Jiang, Y., Chen, L., Zhang, H., & Xiao, X. (2019). Breast cancer histopathological image classification using convolutional neural networks with small SE-ResNet module. *PloS one*, 14(3), e0214587, doi: 10.1371/journal.pone.0214587.

[6] Giaquinto, A. N., Miller, K. D., Tossas, K. Y., Winn, R. A., Jemal, A., & Siegel, R. L. (2022). Cancer statistics for African American/black people 2022. *CA: a cancer journal for clinicians*, 72(3), 202-229, doi: 10.3322/caac.21718.

[7] Kakde, A., Arora, N., & Sharma, D. (2019). A comparative study of different types of cnn and highway cnn techniques. *Global Journal of Engineering Science and Research Management*, 6(4), 18-31, doi: 10.5281/zenodo.2639265.

[8] Zhou, X., Li, Y., Gururajan, R., Bargshady, G., Tao, X., Venkataraman, R., ... & Kondalsamy-Chennakesavan, S. (2020, November). A new deep convolutional neural network model for automated breast Cancer detection. In 2020 *7th International Conference on Behavioural and Social Computing (BESC)* (pp. 1-4), doi: 10.1109/BESC51023.2020.9348322.

[9] Karthiga, R., & Narasimhan, K. (2018, March). Automated diagnosis of breast cancer using wavelet based entropy features. In 2018 *Second international conference on electronics, communication and aerospace technology (ICECA)* (pp. 274-279), doi: 10.1109/ICECA.2018.8474739.

[10] Xiang, Z., Ting, Z., Weiyan, F., & Cong, L. (2019, June). Breast cancer diagnosis from histopathological image based on deep learning. In 2019 *Chinese Control And Decision Conference (CCDC)* (pp. 4616-4619), doi: 10.1109/CCDC.2019.8833431.

[11] Gour, M., Jain, S., & Sunil Kumar, T. (2020). Residual learning based CNN for breast cancer histopathological image classification. *International Journal of Imaging Systems and Technology*, 30(3), 621-635, doi: 10.1002/ima.22403.

[12] Gupta, K., & Chawla, N. (2020). Analysis of histopathological images for prediction of breast cancer using traditional classifiers with pre-trained CNN. *Procedia Computer Science*, 167, 878-889, doi: 10.1016/j.procs.2020.03.427.

[13] "Breast Cancer Treatment," National Cancer Instıtute, 2023. https://www.cancer.gov/types/breast/patient/breast-treatment-pdq.

[14] "Breast Cancer," World Health Organization, 2021. https://www.who.int/news-room/fact-sheets/detail/breast-cancer.

[15] DeSantis, C. E., Bray, F., Ferlay, J., Lortet-Tieulent, J., Anderson, B. O., & Jemal, A. (2015). International variation in female breast cancer incidence and mortality rates. *Cancer epidemiology, biomarkers & prevention*, 24(10), 1495-1506, doi: 10.1158/1055-9965.EPI-15-0535.

[16] Anderson, B. O., Braun, S., Lim, S., Smith, R. A., Taplin, S., & Thomas, D. B. (2003). Early detection of breast cancer in countries with limited resources. *The breast journal,* 9, S51-S59, doi: 10.1046/j.1524-4741.9.s2.4.x.

[17] Kösters, J. P., Gøtzsche, P. C., & Cochrane Breast Cancer Group. (1996). Regular self-examination or clinical examination for early detection of breast cancer. *Cochrane Database of Systematic Reviews*, 2010(1)., doi: 10.1002/14651858.CD003373.

[18] Spanhol, F. A., Oliveira, L. S., Petitjean, C., & Heutte, L. (2016, July). Breast cancer histopathological image classification using convolutional neural networks. In 2016 *international joint conference on neural networks (IJCNN)* (pp. 2560-2567), doi: 10.1109/IJCNN.2016.7727519.

[19] Zheng, D., He, X., & Jing, J. (2023). Overview of artificial intelligence in breast cancer medical imaging. *Journal of Clinical Medicine,* 12(2), 419, doi: 10.3390/jcm12020419.

[20] Evans, K. K., Birdwell, R. L., & Wolfe, J. M. (2013). If you don't find it often, you often don't find it: why some cancers are missed in breast cancer screening. *PloS one*, 8(5), e64366., doi: 10.1371/journal.pone.0064366.

[21] Cheng, J. Z., Ni, D., Chou, Y. H., Qin, J., Tiu, C. M., Chang, Y. C., ... & Chen, C. M. (2016). Computer-aided diagnosis with deep learning architecture: applications to breast lesions in US images and pulmonary nodules in CT scans. *Scientific reports*, 6(1), 24454.

[22] Esteva, A., Kuprel, B., Novoa, R. et al. Dermatologist-level classification of skin cancer with deep neural networks. *Nature*, 115–118 (2017). https://doi.org/10.1038/nature21056.

[23] Spanhol, F. A., Oliveira, L. S., Petitjean, C., & Heutte, L. (2015). A dataset for breast cancer histopathological image classification. *Ieee transactions on biomedical engineering*, 63(7), 1455-1462, doi: 10.1109/TBME.2015.2496264.

[24] Simonyan, K., & Zisserman, A. (2014). Very deep convolutional networks for large-scale image recognition. *arXiv preprint arXiv:1409.1556*.

[25] Sewak, M., Karim, M. R., & Pujari, P. (2018). *Practical convolutional neural networks: implement advanced deep learning models using Python.* Packt Publishing Ltd.

[26] ERDEM, E., & AYDİN, T. (2021). Göğüs Kanseri Histopatolojik Görüntü Sınıflandırması. *Bilişim Teknolojileri Dergisi,* 14(1), 87-94, doi: 10.17671/gazibtd.746673.

[27] A. Rastogi, "ResNet50." https://blog.devgenius.io/resnet50-6b42934db431.

[28] S. Mukherjee, "The Annotated ResNet-50." https://towardsdatascience.com/the-annotated-resnet-50-a6c536034758.

[29] Al Husaini, M. A. S., Habaebi, M. H., Gunawan, T. S., Islam, M. R., & Hameed, S. A. (2021, June). Automatic breast cancer detection using inception V3 in thermography. In 2021 *8th International Conference on Computer and Communication Engineering (ICCCE)* (pp. 255-258), doi: 10.1109/ICCCE50029.2021.9467231.

[30] Cao, J., Yan, M., Jia, Y., Tian, X., & Zhang, Z. (2021). Application of a modified Inception-v3 model in the dynasty-based classification of ancient murals. *EURASIP Journal on Advances in Signal Processing,* 2021(1), 1-25., doi: 10.1186/s13634-021-00740-8.

[31] Mujahid, M., Rustam, F., Álvarez, R., Luis Vidal Mazón, J., Díez, I. D. L. T., & Ashraf, I. (2022). Pneumonia classification from X-ray images with inception-V3 and convolutional neural network. *Diagnostics*, 12(5), 1280, doi: 10.3390/diagnostics12051280.

[32] Mednikov, Y., Nehemia, S., Zheng, B., Benzaquen, O., & Lederman, D. (2018, July). Transfer representation learning using Inception-V3 for the detection of masses in mammography. In 2018 *40th Annual International Conference of the IEEE Engineering in Medicine and Biology Society (EMBC)* (pp. 2587-2590). IEEE., doi: 10.1109/EMBC.2018.8512750.

[33] Liu, Z., Yang, C., Huang, J., Liu, S., Zhuo, Y., & Lu, X. (2021). Deep learning framework based on integration of S-Mask R-CNN and Inception-v3 for ultrasound image-aided diagnosis of prostate cancer. *Future Generation Computer Systems,* 114, 358-367, doi: 10.1016/j.future.2020.08.015.

Research Article

Collider signature of $e^+e^- \to H^+H^-$ in the Scotogenic model

Nagat A. Elmahdy[1], Asmaa Al-Mellah[2]*, Hakan Akyıldırım[3]

[1]Basic Science Department, Modern Academy for Engineering and Technology, Cairo-Egypt
Email: nagat_elmahdy@yahoo.com **- ORCID:** 0000-0002-6152-5842

[2]Süleyman Demirel University, Faculty of Arts & Sciences, Physics Department, 32200, Isparta-Türkiye
Corresponding Author: **Email:** asmaa.almellah@gmail.com **ORCID:** 0000-0003-3975-3504

[3]Süleyman Demirel University, Faculty of Arts & Sciences, Physics Department, 32200, Isparta-Türkiye
Email: hakanakyildirim@sdu.edu.tr **- ORCID:** 0000-0001-5723-958X

Abstract:

We investigate the process $e^+e^- \to H^+H^-$ in the framework of the scotogenic model. The process receives different contributions arising from tree-level diagrams mediated by photon exchange, Z boson exchange and from the exchange of new singlet right-handed fermions $N_{1,2,3}$. We estimate the size of each contribution and the total cross section of the process after applying all dominant constraints on the parameters of the model. We show that the dominant contribution to the cross section originate from the new singlet right-handed fermions $N_{1,2,3}$. Additionally, we show the dependency of the cross section on the centre of mass energy for set of benchmark points of the parameter space of the model respecting the strong obtained bounds. These predictions can be tested in future e^+e^- colliders and hence can test the validity of the model or setting further strong constraints on the model.

1. Introduction

The necessity of the presence of New Physics (NP) beyond the standard model (SM) is a consequence of the lack of mechanism to generate neutrino masses in the SM in addition to the absence of Dark Matter (DM) candidate in the SM. Other reasons include the non-inclusion of the gravity in the framework of the SM and the baryon number asymmetry of the Universe that cannot be explained in the SM.

One of the well-known NP beyond the SM is the scotogenic model proposed by Ma in 2006 [1]. The scotogenic Model provides a mechanism for the generation of small neutrino masses favoured by experimental searches. Not only this, but the model also providing a DM candidate that can be any one of the new fermionic or scalar particles proposed by the model. Explicitly, the DM candidate can be a component of (η, N_i), η is a new scalar doublet, or can be the lightest one of the three singlet Majorana

fermions $N_{1,2,3}$[1]. These are the extra new particles added to the particle content of the SM. It should be noted that a Z_2 symmetry is imposed in the model under which all SM particles are even while the new extra particles are odd under this symmetry. In Table 1, we list the quantum numbers of these new extra particles.

Table 1: Quantum numbers of the new extra particles.

	N_k	η
SU(2)$_L$	1	1
U(1)$_Y$	0	0
Z$_2$	-1	-1

In Ref. [2], the process $e^+e^- \to H^+H^- \to \ell^+\ell'^- \not{E}$ was studied for possible collider signatures. With the progress in the last decade related to neutrino oscillation experiments and different bounds on neutrino masses from some cosmological observations, one can update the previously imposed constraints obtained in that reference. Moreover,

other observations like dark matter relic density measurement have been updated in the last years and thus it turns to be important to include this measurement in the analysis of the model for further possible strong constraints on the model.

Having updated constraints allows us to give correct predictions of the cross section of the process $e^+e^- \longrightarrow H^+H^-$ for which no analysis and predictions were given in Ref. [2]. In fact, our concern about studying the cross section of the process $e^+e^- \longrightarrow H^+H^-$ only as the produced H^+H^- pair can decay to many final states with different combinations of particles. One common effect for all such decay modes is the size of the cross section of $e^+e^- \longrightarrow H^+H^-$. Hence, analysis of this cross section turns to be important. In this study, we do this analysis and investigate the different individual contributions to the cross section that originate from Z, photon and the new singlet fermions proposed by the scotogenic model.

2. The scotogenic model

The scotogenic model extends the scalar sector of the SM by adding extra scalar doublet denoted by η. Thus, the Lagrangian describing the scalar sector of the scotogenic model can be written as

$$\mathcal{L} = (\mathcal{D}^\mu\Phi)^\dagger\mathcal{D}_\mu\Phi + (\mathcal{D}^\mu\eta)^\dagger\mathcal{D}_\mu\eta - \mathcal{V} \qquad (1)$$

where Φ is the SM Higgs doublet, $\mathcal{D}^\mu$ denotes the covariant derivative including the SM gauge fields and the scalar potential $\mathcal{V}$ has the form [1]

$$\mathcal{V} = \mu_1^2\Phi^\dagger\Phi + \mu_2^2\eta^\dagger\eta + \frac{1}{2}\lambda_1(\Phi^\dagger\Phi)^2 + \frac{1}{2}\lambda_2(\eta^\dagger\eta)^2$$
$$+\lambda_3(\Phi^\dagger\Phi)(\eta^\dagger\eta) + \lambda_4(\Phi^\dagger\eta)(\eta^\dagger\Phi)$$
$$+\frac{1}{2}\lambda_5\left[(\Phi^\dagger\eta)^2 + (\eta^\dagger\Phi)^2\right]$$

Upon electroweak symmetry breaking, we can write

$$\Phi = \begin{pmatrix} 0 \\ \frac{1}{\sqrt{2}}(h+v) \end{pmatrix}, \quad \eta = \begin{pmatrix} H^+ \\ \frac{1}{\sqrt{2}}(\mathcal{S}+i\mathcal{P}) \end{pmatrix} \qquad (2)$$

where h stands for the physical Higgs boson and v represents the vacuum expectation value (VEV) of Φ. One of the consequences of the Z_2 symmetry is that the VEV of η is zero. The scalar particles masses are given as $m_S^2 = m_\mathcal{P}^2 + \lambda_5 v^2 = \mu_2^2 + \frac{1}{2}(\lambda_3 + \lambda_4 + \lambda_5)v^2$ and $m_H^2 = \mu_2^2 + \frac{1}{2}\lambda_3 v^2$ [2]. In the limit of

very small λ_5 [3], $|\lambda_5| \ll |\lambda_3 + \lambda_4|$, one finds that, $m_S^2 \simeq m_\mathcal{P}^2$.

The masses and interactions of the new singlet Majorana fermions, N_k, can be inferred from the following Lagrangian

$$\mathcal{L}_N = -\frac{1}{2}M_k\overline{N_k^c}P_RN_k +$$
$$\mathcal{Y}_{rk}\left[\bar{\ell}_rH^- - \frac{1}{\sqrt{2}}\bar{\nu}_r(S-i\mathcal{P})\right]P_RN_k + \text{H.c.,} \qquad (3)$$

with $\ell_{1,2,3} = e, \mu, \tau$, $\mathcal{Y}_{rk}$ and M_k denote the Yukawa couplings and masses of N_k, and the superscript c refers to the charge conjugation of the field. In the above equation, we have $P_R = \frac{1}{2}(1+\gamma_5)$ and $k, r = 1,2,3$. The interactions of $H^\pm$ with photon A, and Z boson relevant to our process can be obtained from the Lagrangian $\mathcal{L}_H^\pm$ that can be expressed as

$$\mathcal{L}_H^\pm \supset ie(H^+\partial^\rho H^- - H^-\partial^\rho H^+)A_\rho$$
$$+ \frac{g}{2c_w}[i(1-2s_w^2)(H^+\partial^\rho H^-$$
$$- H^-\partial^\rho H^+)]Z_\rho$$
$$(4)$$

where $e = gs_w$ is the electromagnetic charge, $c_w = \cos\theta_w$ and $s_w = \sin\theta_w$ with θ_w being the Weinberg angle.

2.1 Neutrino masses generation

Due to the imposed Z_2 symmetry, neutrinos masses cannot exist at the tree level in the scotogenic model. This is not the case at one loop level where neutrinos masses can be generated through S, $\mathcal{P}$, and N_k mediating the loop. The mass eigenvalues of the light neutrinos m_i can be obtained using the loop generated quantity [1]

$$\Lambda_k = \frac{\lambda_5 v^2}{16\pi^2 M_k}\left[\frac{M_k^2}{m_0^2-M_k^2} + \frac{2M_k^4 ln(M_k/m_0)}{(m_0^2-M_k^2)^2}\right] \qquad (5)$$

Here $m_0 = \frac{1}{2}(m_S + m_\mathcal{P}) \simeq m_S \simeq m_\mathcal{P}$. The neutrino mass matrix then becomes

$$\mathcal{M}_v = Y\,\text{diag}(\Lambda_1, \Lambda_2, \Lambda_3)Y^T, \qquad (6)$$

which can be diagonalized using

$$\text{diag}(m_1, m_2, m_3) = \mathcal{U}^\dagger\mathcal{M}_v\mathcal{U}^*, \qquad (7)$$

The unitary matrix U denotes the well-known Pontecorvo-Maki-Nakagawa-Sakata (PMNS) matrix. In our study we use the PDG parametrization [4] $\mathcal{U} = \tilde{u}\,\text{diag}(e^{i\alpha_1/2}, e^{i\alpha_2/2}, 1)$, where $\alpha_{1,2}$ denoting

the Majorana CP-violation phases and the matrix $\tilde{u}$ is expressed in terms of $c_{mn} = \cos\theta_{mn} \geq 0$, $s_{mn} = \sin\theta_{mn} \geq 0$ and a Dirac phase δ. The expression of the matrix $\tilde{u}$ can be found in Eq. (10) in Ref. [5]. Analytic solutions for Eqs. (7) yield [2]

$$Y_{e1} = \frac{-c_{12}c_{13}Y_1}{c_{12}c_{23}s_{13}e^{i\delta} - s_{12}s_{23}},$$
$$Y_{e2} = \frac{-s_{12}c_{13}Y_2}{s_{12}c_{23}s_{13}e^{i\delta} + c_{12}s_{23}},$$

$$Y_{\mu 1} = \frac{(c_{12}s_{23}s_{13}e^{i\delta} + s_{12}c_{23})Y_1}{c_{12}c_{23}s_{13}e^{i\delta} - s_{12}s_{23}}, \quad Y_{\mu 3} = \frac{s_{23}Y_3}{c_{23}},$$

$$Y_{e3} = \frac{s_{13}Y_3}{c_{23}c_{13}e^{i\delta}}, \quad Y_{\mu 2} = \frac{(s_{12}s_{23}s_{13}e^{i\delta} - c_{12}c_{23})Y_2}{s_{12}c_{23}s_{13}e^{i\delta} + c_{12}s_{23}},$$
$$Y_{\tau k} = Y_k \,, \tag{8}$$

which correspond to the light neutrino mass eigenvalues [2]

$$m_1 = \frac{\Lambda_1 Y_{e1}^2 e^{-i\alpha_1}}{c_{12}^2 c_{13}^2}, m_2 = \frac{\Lambda_2 Y_{e2}^2 e^{-i\alpha_2}}{s_{12}^2 c_{13}^2}, m_3 = \frac{\Lambda_3 Y_3^2}{c_{13}^2 c_{23}^2} \tag{9}$$

The Majorana CP-violation phases can be calculated with the help of the following relations.

$$\alpha_1 = \arg(\Lambda_1 Y_{e1}^2), \alpha_2 = \arg(\Lambda_2 Y_{e2}^2), \arg(\Lambda_3 Y_3^2) = 0 \tag{10}$$

2.2 Dark Matter

The scotogenic model enlarges particle contents of the fermionic and scalar sectors of the SM through introducing the new particles $N_{1,2,3}$ and $S, P, H^{\pm}$ respectively. These new particles are odd under Z_2 symmetry and hence the lightest one among them will be stable and can be a DM candidate.

In our study we consider the familiar scenario in which N_1 is the DM particle and the second lightest particle N_2 is degenerate in mass with N_1. This scenario is favored as it ensures the ability of satisfying simultaneously the constraints from the DM relic density and the Branching ratio (BR) of the lepton flavour violation process $\mu \to e\gamma$.

The relic density can be expressed in terms of the present DM density relative to its critical value, denoted by Ω, and the Hubble parameter, denoted by $\hat{h}$, as $\Omega\hat{h}^2$. Theoretically, it can be estimated from the relation [3, 6]

$$\Omega\hat{h}^2 = \frac{1.07 \times 10^9 x_f \, GeV^{-1}}{\sqrt{g_*} m_{P1}[a_{eff} + 3(b_{eff} - a_{eff}/4)/x_f]}$$

$$x_f = \ln \frac{0.191(a_{eff} + 6b_{eff}/x_f)M_1 m_{P1}}{\sqrt{g_* x_f}} \tag{11}$$

here g_* is the number of relativistic degrees of freedom below the freeze-out temperature $T_f = M_1/x_f$ and $m_{P1} = 1.22 \times 10^{19}$ GeV is the Planck mass. The expressions of a_{eff} and b_{eff} can be inferred from the expansion of the coannihilation rate $\sigma_{eff} v_{rel} = a_{eff} + b_{eff} v_{rel}^2$ where the expansion is performed in terms of the relative speed of the annihilating particles in their center-of-mass frame denoted by v_{rel} and $\sigma_{eff} = \frac{1}{4}(\sigma_{11} + \sigma_{12} + \sigma_{21} + \sigma_{22})$. The expression of σ_{ij}, for $i, j = 1, 2$, can be obtained from the relation.

$$\sigma_{ij} = \sigma_{N_i N_j \to \ell_i^- \ell_j^+} + \sigma_{N_i N_j \to v_i v_j} \tag{12}$$

Above cross sections were computed in Refs. [7, 2] and each arises from the t and u channels tree-level diagrams mediated by the exchange of $H^{\pm}$ and (S, P) depending on whether the final states are charged leptons or neutral neutrinos.

In our analysis of the resultant constraint, from the measured value of the DM relic density, on the parameter space of the model under concern we consider the case that the DM and the new scalar particles are not degenerate in mass to avoid the contributions of the coannihilation processes of the scalars to the relic density.

2.3 $e^+(p_+)e^-(p_-) \longrightarrow H^+H^-$

In the scotogenic model under the study in this work, the amplitude of the process $e^+(p_+)e^-(p_-) \to H^+H^-$ receive contributions from the tree-level diagrams mediated by the exchange of photon (γ), Z and $N_{1,2,3}$ diagrams. In the limit of massless $e^{\pm}$, the resulting cross section is given as [2]

$$\sigma_{e^+e^- \to H^+H^-} = \frac{\pi\alpha^2\beta^3}{3s} + \frac{\alpha}{12}\frac{(g_L^2 + g_L g_R)\beta^3}{s - m_Z^2} +$$

$$\frac{(g_L^4 + g_L^2 g_R^2)\beta^3 s}{96\pi(s - m_Z^2)^2} + \sum_k \frac{|y_{1k}|^4}{64\pi s}\left(\omega_k \ln\frac{\omega_k + \beta}{\omega_k - \beta} - 2\beta\right) +$$

$$\left[\frac{\alpha}{16s} + \frac{g_L^2}{64\pi(s - m_Z^2)}\right]\sum_k |y_{1k}|^2 \left[(\omega_k^2 - \beta^2)\ln\frac{\omega_k + \beta}{\omega_k - \beta} - \right.$$

$$\left. 2\beta\omega_k\right] + \sum_{j,k>j} \frac{|y_{1j}y_{1k}|^2}{64\pi s}\left(\frac{\omega_j^2 - \beta^2}{\omega_j - \omega_k}\ln\frac{\omega_j + \beta}{\omega_j - \beta} + \right.$$

$$\left. \frac{\omega_k^2 - \beta^2}{\omega_k - \omega_j}\ln\frac{\omega_k + \beta}{\omega_k - \beta} - 2\beta\right) \tag{13}$$

here $j, k = 1, 2, 3$, $s = (p_+ + p_-)^2$, $\alpha = \frac{e^2}{4\pi}$, $\beta = \sqrt{1 - \frac{4m_H^2}{s}}$ and $\omega_k = 1 + \frac{2M_k^2}{s} - \frac{2m_H^2}{s} > \beta$. In the numerical analysis, we employ the effective values $\alpha = 1/128$, $g = 0.6517$, and $s_w^2 = 0.23146$ [4].

2.4 Constraints

In our study, we adopt the normal ordering (NO) of neutrino masses. The mixing angles, the Dirac phase, $\left|\Delta m_{31}^2\right|$ and $\left|\Delta m_{21}^2\right|$ can be determined from various measurements. In our numerical evaluation, we employ the results of the fit to the global data on neutrino oscillations carried out in Ref. [8]. Using the results of the fit allows us to impose the constraint $32.0 < Rm \equiv \frac{\left|\Delta m_{31}^2\right|}{\Delta m_{21}^2} < 36.0$ on the parameter space based on the 90% CL ranges of the data. On the other hand, the CMB temperature, polarization and lensing measurements from the Planck satellite, BAO observations, $H(z)$ information and Supernovae Ia data constraint result in the stringent 2σ upper limit $\sum m_i < 0.12$eV. Possible constraints can be derived from Neutrinoless double beta decay experiments. The resulted constraint reads $|\langle m \rangle_{ee}| < 0.06 - 0.2$eV at the 95% confidence level [9, 10, 11] where $\langle m \rangle_{ee}$ is defined as $\langle m \rangle_{ee} = m_1 \mathcal{U}_{e1}^2 + m_2 \mathcal{U}_{e2}^2 + m_3 \mathcal{U}_{e3}^2$.

The Yukawa interactions including the charged Higgs $H^\pm$ listed in Eq. (3) can generate one loop-level diagrams that contribute to the lepton flavour violation (LFV) processes. A detailed discussion of these process can be found in Ref. [12]. Currently, the experimental upper bounds on the branching ratios of a class of these processes are $BR(\mu \to e\gamma) < 4.2 \times 10^{-13}$ [13], $BR(\tau \to e\gamma) < 3.3 \times 10^{-8}$ [14], and $BR(\tau \to \mu\gamma) < 4.4 \times 10^{-8}$ [14] with the most stringent constraint come from $BR(\mu \to e\gamma)$. The expressions of the branching ratios of these LFV processes in the framework of the scotogenic model can be found in Ref. [12]. On the other hand, the flavour-diagonal counterpart of the aforementioned LFV processes can modify the anomalous magnetic moment, a_{ℓ_i}, as [15]

$$\Delta a_{\ell_i} = \frac{-m_{\ell_i}^2}{16\pi^2 m_H^2} \sum_k |Y_{ik}|^2 \mathcal{F}(M_k^2/m_H^2) \qquad (14)$$

It turns out that, the anomalous magnetic moment of the muon yields a stronger bound compared to the

others, electron and tau, on the scotogenic parameter space. The difference between the SM prediction and the currently experimental value of a_μ reads $a_\mu^{exp} - a_\mu^{SM} = (2.51 \pm 0.59) \times 10^{-9}$ [16].

Direct detection of DM through the interaction of N_1 with nucleons, resulting from the Higgs exchange at the one-loop level, was discussed in Ref. [17]. To avoid the stringent constraints from direct detection [18, 19], we can follow Ref. [17, 20] and take $\lambda_{3,4} = 0.01$. This has a consequence that $m_o \simeq m_{H^\pm} + \frac{1}{2}\lambda_4 v^2 \simeq m_{H^\pm} + 350 \, GeV$. One should remark that the strong bounds from the direct detection were not taken into account in Refs. [2]. In this study we take these bounds into account and employ the latest neutrino oscillation data obtained as a result of the global analysis presented in Ref. [8]. In the next section, we will present our results and will give our analysis and discussion of these results. To do this, we first set the mixing angles $\theta_{12,23,13}$ and the Dirac phase δ to their central values obtained in the fit to the global data on neutrino oscillations performed in Ref. [8]. In the second step, we perform a scan over the parameter space of the model namely, the masses of the new scalars m_H, m_o and the new singlet fermions $N_{1,2,3}$ and the input parameters $Y_{1,2,3}$ appearing in the Yukawa couplings listed above in Eq. (8). For light dark matter masses $M_1 < 100 \, GeV$, lepton flavor violation [21] and direct search at LHC [22, 23] mostly exclude the parameter space. Concerning the scalar masses, using the data on W and Z widths and the null results of direct searches for new particles at e^+e^- colliders we have the following upper bounds on the scalar masses [24, 25, 26]

$$m_{H^\pm} + m_{S,\mathcal{P}} > m_{W^\pm}, \; m_{H^\pm} > 70 \, GeV, m_S + m_{\mathcal{P}} > m_Z \qquad (15)$$

One should remark that there are constrains on the charged Higgs mass from the $B \to \tau\nu$, $B \to s\gamma$ and from the direct measurements of the charged Higgs decays at the LHC. In our analysis, we take into account all these constraints.

3. Results and Discussions

We start our analysis by showing the allowed regions in the parameter space of the scotogenic

model upon applying the most stringent constraints individually and then simultaneously.
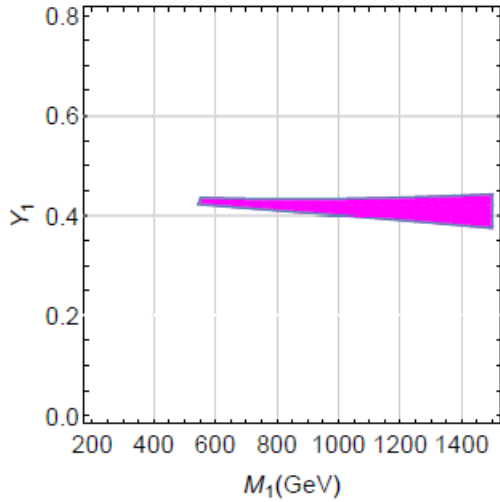

Figure 1. *Region in magenta colour is allowed by* $\mu \rightarrow e\gamma$ *constraint for the parameters* $M_2 = M_1$, $M_3 = M_1 + 380\ GeV$, $m_H = M_1 + 400\ GeV$, $Y_2 = 0.49$ *and* $Y_3 = 0.66$.

In Fig.1, the region in magenta colour is allowed by $\mu \rightarrow e\gamma$ constraint where we fixed the other parameters as $M_2 = M_1$, $M_3 = M_1 + 380\ GeV$, $m_H = M_1 + 400\ GeV$, $Y_2 = 0.49$ and $Y_3 = 0.66$. Clearly from the figure that, satisfying $\mu \rightarrow e\gamma$ constraint requires large charged Higgs mass and also large $N_{1,2,3}$ masses.
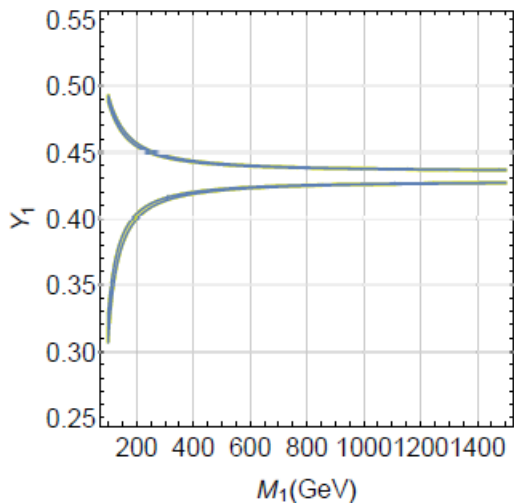

Figure 2. *Allowed regions after imposing* $\frac{|\Delta m_{31}^2|}{\Delta m_{21}^2}$ *constraints for the choice of the parameters as* $M_2 = M_1$, $M_3 = M_1 + 380\ GeV$, $m_o = M_1 + 750\ GeV$, $Y_2 = 0.49$ *and* $Y_3 = 0.66$.

In Fig.2, we display the allowed regions after taking into account the imposed $\frac{|\Delta m_{31}^2|}{\Delta m_{21}^2}$ constraint. In the

figure we set the parameters as $M_2 = M_1$, $M_3 = M_1 + 380\ GeV$, $m_o = M_1 + 750\ GeV$, $Y_2 = 0.49$ and $Y_3 = 0.66$. The colored regions in the $M_1 - Y_1$ plane satisfy the desired constraint.

We turn now to display the allowed region in the $M_1 - Y_1$ plane by the DM relic density $\Omega \hat{h}^2$ constraints. Our result is presented in Fig.3 for the set of the parameters $M_2 = M_1$, $M_3 = M_1 + 380\ GeV$, $m_H = M_1 + 400\ GeV$, $m_o = M_1 + 750\ GeV$, $Y_2 = 0.49$ and $Y_3 = 0.66$. As can be seen from the figure that, large values of DM masses M_1 require large values of the parameter Y_1 to satisfy the constraint. This requirement is not favored by the other constraints discussed above. It should be noted that, in the previous figures presented above we discussed the effect of each individual constraint on the parameter space. However, the parameter space must be subjected to all strong constraints at the same time. Consequently, in Fig.4, we show our results for the allowed region in the $M_1 - Y_1$ plane by the dominant constraints arising from $\mu \rightarrow e\gamma$, $\frac{|\Delta m_{31}^2|}{\Delta m_{21}^2}$, and $\Omega \hat{h}^2$. The green colour region in the figure simultaneously satisfies all these constraints simultaneously. We deduce from this region that; it is possible to have points satisfying all constraints for masses of the new particles in the model with masses close to or higher than 1 TeV. Moreover, we can use this region to obtain set of benchmark points that satisfy the imposed constraints on the parameter space of the model and hence can give a prediction of the model to the cross section of $\sigma_{e^+e^- \rightarrow H^+H^-}$ which can be tested in future colliders.
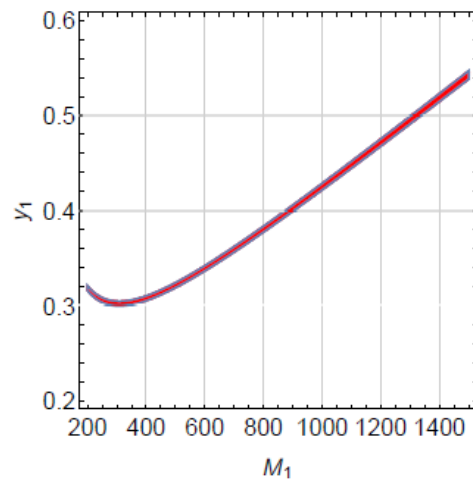

Figure 3. *Allowed regions in the* $M_1 - Y_1$ *plane by* $\Omega \hat{h}^2$ *constraints for the parameters* $M_2 = M_1$, $M_3 = M_1 + 380\ GeV$, $m_H = M_1 + 400\ GeV$, $m_o = M_1 + 750\ GeV$, $Y_2 = 0.49$ *and* $Y_3 = 0.66$.

Figure 4. *Allowed regions in the $M_1 - Y_1$ plane by $\mu \to e\gamma$, $\frac{|\Delta m^2_{31}|}{\Delta m^2_{21}}$, $\Omega\hat{h}^2$ constraints for the parameters $M_2 = M_1$, $M_3 = M_1 + 380$ GeV, $m_H = M_1 + 400$ GeV, $m_o = M_1 + 750$ GeV, $Y_2 = 0.49$ and $Y_3 = 0.66$.*
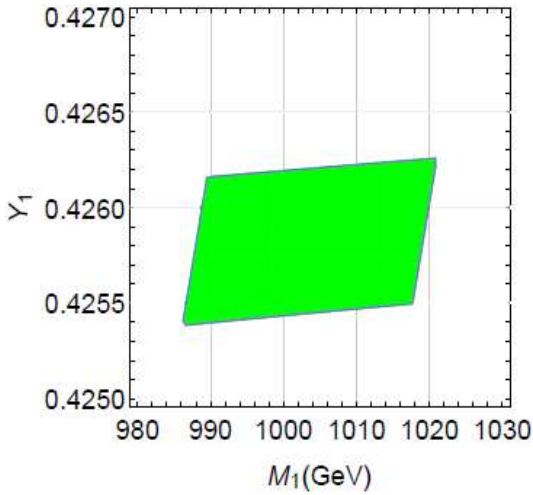
In Fig.5, we show our results for the individual contributions of Z, photon and new singlet fermions $N_{1,2,3}$ to the cross section of $\sigma_{e^+e^- \to H^+H^-}$ as a function of the centre of mass energy $\sqrt{s}$ in red, orange and magenta colors respectively. The plots in the figure correspond to the one of the allowed benchmark points of the parameter space namely $M_1 = 1005$ GeV, $M_2 \simeq M_1 = 1005.0000035$ GeV, $M_3 = 1385$ GeV, $m_H = 1405$ GeV, $Y_1 = 0.4258$, $Y_2 = 0.49$ and $Y_3 = 0.66$. Clearly from the figure that Z contribution to the cross section is the least one while contributions from the new singlet fermions $N_{1,2,3}$ are the dominant ones. It should be noted from the figure that we extended the center of mass energies to higher values and that the prospective ILC has an upper limit of 1 TeV and the CLIC has an upper limit to 3 TeV. Our objective, doing so, is to cover large ranges of energies that can be tested in any future collider with much higher center of mass energies than ILC and CLIC.

Finally, in Fig.6, we show our results for the total cross section of $\sigma_{e^+e^- \to H^+H^-}$ as a function of the centre of mass energy $\sqrt{s}$ in red, orange and magenta colors respectively. As above, the figure correspond to the one of the allowed benchmark points of the parameter space namely $M_1 = 1005$ GeV, $M_2 \simeq M_1 = 1005.0000035$ GeV, $M_3 = 1385$ GeV, $m_H = 1405$ GeV, $Y_1 = 0.4258$, $Y_2 = 0.49$ and

$Y_3 = 0.66$. As can be seen from the figure that, the cross section increases with increasing the centre of mass energy till it reach to its beak and then starting to decrease with increasing the centre of mass energy.
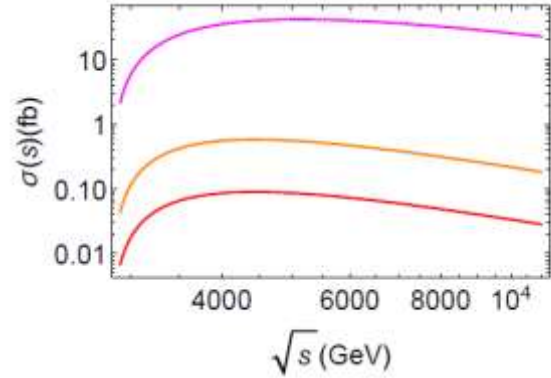

Figure 5. *Z, photon, and new singlet fermions $N_{1,2,3}$ individual contributions to the cross section of $\sigma_{e^+e^- \to H^+H^-}$ in red, orange, and magenta colours respectively. The plots correspond to the allowed parameters $M_1 = 1005$ GeV, $M_2 \simeq M_1 = 1005.0000035$ GeV, $M_3 = 1385$ GeV, $m_H = 1405$ GeV, $Y_1 = 0.4258$, $Y_2 = 0.49$ and $Y_3 = 0.66$.*
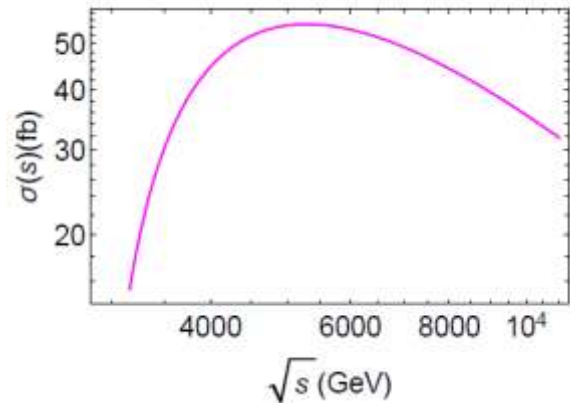
Figure 6. *Total cross section $\sigma_{e^+e^- \to H^+H^-}$. The plots correspond to the allowed parameters $M_1 = 1005$ GeV, $M_2 \simeq M_1 = 1005.0000035$ GeV, $M_3 = 1385$ GeV, $m_H = 1405$ GeV, $Y_1 = 0.4258$, $Y_2 = 0.49$ and $Y_3 = 0.66$.*

4. Conclusions

In this work we have studied the process $e^+e^- \to H^+H^-$ in the Scotogenic model. The different contributions to the amplitude of the process originate from tree-level diagrams mediated by photon, Z boson and from the right-handed fermions $N_{1,2,3}$. We have studied the processes that can impose strong constraints on the parameter space relevant to the process $e^+e^- \to H^+H^-$. Moreover, we have estimated the size of the individual contributions of each of photon, Z boson and the

right-handed fermions $N_{1,2,3}$ to the cross section of $e^+e^- \rightarrow H^+H^-$ after taking into account all stringent constraints on the parameters of the model.

We have shown that the main contribution to the cross section arise from the new singlet right-handed fermions $N_{1,2,3}$. Finally, we have shown the dependency of the cross section on the centre of mass energy for set of benchmark points of the parameter space of the model respecting the strong obtained bounds. Future e^+e^- colliders will search for the process $e^+e^- \rightarrow H^+H^-$ and thus can test our predictions for either setting more stringent constraints or verifying these predictions.

Author Statements:

- **Ethical approval:** The conducted research is not related to either human or animal use.
- **Conflict of interest:** The authors declare that they have no known competing financial interests or personal relationships that could have appeared to influence the work reported in this paper
- **Acknowledgement:** The authors declare that they have nobody or no-company to acknowledge.
- **Author contributions:** The authors declare that they have equal right on this paper.
- **Funding information:** The authors declare that there is no funding to be acknowledged.
- **Data availability statement:** The data that support the findings of this study are available on request from the corresponding author. The data are not publicly available due to privacy or ethical restrictions.

References

[1] E. Ma. (2006). Verifiable radiative seesaw mechanism of neutrino mass and dark matter. *Physical Review D.* 73: 077301. DOI:10.1103/PhysRevD.73.077301.

[2] S. Y. Ho & J. Tandean. (2014). Probing ScotogenicEffects in Colliders. *Physical Review. D.* 89:114025. DOI: 10.1103/PhysRevD.89.114025.

[3] J. Kubo, E. Ma & D. Suematsu. (2006). Cold Dark Matter, Radiative Neutrino Mass, μ→e, and Neutrino less Double β Decay. *Physical Letter B.* 642:18-23. DOI: 10.1016/j.physletb.2006.08.085.

[4] J. Beringer et al., (2012). Review of Particle Physics (RPP). *Physical Review D.* 86:010001. DOI:i:10.1103/PhysRevD.86.010001.

[5] G. Faisel, S. Y. Ho & J. Tandean, (2014). Exploring X-ray lines as scotogenic signals. *Physics Letters B.* 738:380-385. DOI:10.1016/j.physletb.2014.09.063.

[6] G. Jungman, M. Kamionkowski, & K. Griest, (1996). Supersymmetric dark matter. *Physics Reports.* 267(5–6): 195-373. DOI:10.1016/0370-1573(95)00058-5.

[7] S. Y. Ho & J. Tandean, (2013). Probing Scotogenic effects in Higgs Boson Decays. *Physical Review D.* 87:095015. DOI:10.1103/PhysRevD.87.095015.

[8] P. F. de Salas et al., (2021). 2020 global reassessment of the neutrino oscillation picture. *Journal of High Energy Physics.* 02:071. DOI:10.1007/JHEP02(2021)071.

[9] G. Anton et al., (2019). Search for Neutrino less Double-β Decay with the Complete EXO-200 Dataset. *Physical. Review Letter.* 123(16): 161802. DOI:10.1103/PhysRevLett.123.161802.

[10] A. Gando et al., (2016). Search for Majorana Neutrinos near the Inverted Mass Hierarchy Region with KamLAND-Zen. *Physical Review Letter.* 117(8): 082503. DOI:10.1103/PhysRevLett.117.082503.

[11] M. Agostini et al., (2020). Final Results of GERDA on the Search for Neutrino less Double-β Decay. *Physical Review Letter.* 125(25): 252502. DOI:10.1103/PhysRevLett.125.252502.

[12] T. Toma & A. Vicente. (2014). Lepton flavour violation in the scotogenic model. *Journal of High Energy Physics.* 2014(1):1-27. DOI:https://doi.org/10.48550/arXiv.1312.2840.

[13] A. M. Baldini et al., (2016). Search for the lepton flavour violating decay → with the full dataset of the MEG experiment. *European Physics J. C.* 76(8):434. DOI: 10.1140/epjc/s10052-016-4271-x.

[14] B. Aubert et al., (2010). Searches for Lepton Flavor Violation in the Decays →γ and →γ. *Physical Review Letter.* 104:021802. DOI:10.1103/PhysRevLett.104.021802.

[15] E. Ma & M. Raidal. (2001). Neutrino mass, muon anomalous magnetic moment, and lepton flavor non conservation. *Physical Review Letter.* 87:011802. DOI: 10.1103/PhysRevLett.87.011802.

[16] T. Aoyama, et al., (2020). The anomalous magneticmoment of the muon in the Standard Model. *Physics Report* 887:1-166. DOI:10.1016/j.physrep.2020.07.006.

[17] A. Ibarra, C. E. Yaguna & O. Zapata. (2016). Direct Detection of Fermion Dark Matter in the Radiative Seesaw *Model. Physical Review D.* 93(3): 035012.DOI:10.1103/PhysRevD.93.035012.

[18] E. Aprile et al., (2018). Dark Matter Search Results from a One Ton-Year Exposure of XENON1T. *Physical Review Letter.* 121(11): 111302. DOI: 10.1103/PhysRevLett.121.111302.

[19] Y. Meng et al., (2021). Dark Matter Search Results from the PandaX-4T Commissioning Run. *Physical Review Letter.* 127(26): 261802. DOI:10.1103/PhysRevLett.127.261802.

[20] Jiao Liu et al. (2022). Unraveling the Scotogenic model at muon collider. *Journal of High Energy Physics.* 12(57):001-034

[21] A. Vicente & C. E. Yaguna. (2015). Probing the scotogenic model with lepton flavor violating

processes. *Journal of High Energy Physics*. 2015(2):144-150. DOI: 10.1007/JHEP02(2015)144.

[22] G. Aad et al., (2020). Searches for electroweak production of supersymmetric particles with compressed mass spectra in =13 TeV pp collisions with the ATLAS detector. *Physical Review D.* 101(5): 052005. DOI: 10.1103/PhysRevD.101.052005.

[23] A. M. Sirunyan et al., (2021). Search for supersymmetry in final states with two oppositely charged same-flavor leptons and missing transverse momentum in proton-proton collisions at =13 TeV. *Journal of High Energy Physics.* 04:123. DOI:10.1007/JHEP04(2021)123.

[24] A. Arhrib, R. Benbrik, & N. Gaur. (2012). H→ in Inert Higgs Doublet Model. *Physical Review D.* 85:095021. DOI: 10.1103/PhysRevD.85.095021.

[25] Q.H. Cao, E. Ma, & G. Rajasekaran. (2007). Observing the Dark Scalar Doublet and its Impact on the Standard-Model Higgs Boson at Colliders. *Physical Review D.* 76:095011. DOI: 10.1103/PhysRevD.76.095011.

[26] Dolle, Ethan M. and Su, Shufang. (2022) Inert dark matter, *Physical Review D.* 5(80): 1550-2368. DOI:10.1103/physrevd.80.055012.
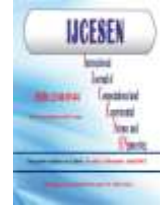
The Effect of Marble Powder Additive at Different Ratios on the Radiation Absorption Parameters of Barite Based Concretes

Yasemin SAVAŞ[1], Boğaçhan BAŞARAN[2], Betül ÇETİN[3*]

[1]Amasya University, Institute of Science, Physics Department, 05100, Amasya-Turkey
Email: yasmin35333@gmail.com- **ORCID:** 0009-0008-6028-2501

[2]Amasya University, Vocational School of Technical Sciences, Construction Department, 05100, Amasya-Turkey
Email: bogachan.basaran@amasya.edu.tr- **ORCID:** 0000-0002-5289-8436

[3]Amasya University, Science and Arts Faculty, Physics Department, 05100, Amasya-Turkey
* Corresponding Author: Email: betulcetin3205@gmail.com**- ORCID:** 0000-0001-9129-2421

Abstract:

This article contains the results of an experimental study to investigate the radiation shielding effect as a result of adding crushed marble powder at different rates to barite-based concretes. The mixtures of the produced concretes were calculated according to TS 802. In 1st group concretes formed by 9x9x9 cm sized cube samples, cement and aggregate ratio were kept constant and marble and barite ratios were changed. In the 2nd group concretes, the cement and barite ratio were kept constant and the marble and aggregate ratios were changed. The linear attenuation coefficients have been measured at 1773 and 1332 keV for samples using a gamma spectrometer that contains a 3"x3" NaI (Tl) detector and connected to Multi-Channel Analyzer (MCA). Also, the correlation between linear attenuation coefficients and marble doped % for the photon energies was calculated and R^2 was found to be 0.90 and above for all samples. In addition, these results have been used to calculate the half value layer (HVL) and mean free path (mfp) parameters. This study shows that the added of crushed marble powder contributes positively to the radiation absorption properties of barite added to concrete.

1. Introduction

With the use of natural stones as building and decoration materials, natural stone production has gained importance. Marble is also an important natural stones used for decoration purposes. Turkey possesses nearly 40 percent of the world's marble reserves, totalling 13.9 billion tons, with 5.2 billion tons [1]. The buildings are constructed mainly from concrete containing cement, water and aggregates. Two main factors have to be taken into account when constructing buildings: one is earthquake resistance, and the other is radiation resistance [2]. Therefore, the development of different shielding materials is important for radiation protection and concrete strength. In the production of concrete, different materials and methods are used in studies on the strength and durability of concrete. One of these materials is a marble powder. Marble powder fills the existing voids in the concrete by creating a filling effect in

concrete mixtures, which positively affects the compressive strength of concrete [3, 4]. Marble powder consists of the smallest-sized marble granules formed during the cutting of blocks and slabs in marble processing plants. Due to the use of water in the marble cutting process, marble powders are transported to the settling pools together with water. Marble powder deposited in the pools is then taken to the waste sites. Marble powders are either precipitated using a sedimentation method or released directly into the field. It is a known fact that wastes that cannot be non-recycled cause problems for the environment. Therefore, in order to reduce environmental pollution, it will be useful to evaluate marble powders in different industrial areas [5].

In the studies on the use of marble wastes in concrete production [6-8]; it is stated that the pressure resistance will increase when the ratio of

fine material in concrete production is changed with marble powder.

However, there are no come across studies investigating the radiation shielding properties of barite-based concretes produced using different amounts of waste marble powder in the literature.

For this reason, in this study, investigated radiation shielding properties of marble powder doped barite-based concretes. The shielding measurements have been performed via a gamma spectrometer in the Radioactive Research Laboratory of Amasya University, Sciences and Arts Faculty. The concretes have been produced in the Structural Material Laboratory of Vocational School of Technical Sciences at Amasya University.

2. Material and Methods
2.1. Sample Preparations

Mixing calculations of all concrete samples were made for minimum C30 / 37 class concrete design using TS 802 [9] standard. CEM IV B (P) 32.5N pozzolanic cement was used in various dosages in concrete samples due to its easy regional availability. The largest aggregate grain diameter was 16mm. The grain diameter distributions and specific weights of the aggregates used in the study are presented in Table 1. Also, the W/C ratios of all mixtures have kept as 0.54 and the consistency of the mixtures was adjusted by using super plasticizer additive (0.50-1.50% of cement weight). Within the scope of the study, the produced concrete samples, the amount of material in the mixture calculation of these samples and their proportions are presented in Table 2. Concrete mixtures were prepared in proportion given in Table 1 as 3 for each series of concrete. The samples have placed in 9x9x9 cm specially prepared concrete molds in two stages

using a vibrator (Fig.1). Produced concretes have kept at least 28 days under the cure conditions pecified in EN 12390-2 [10] standard.
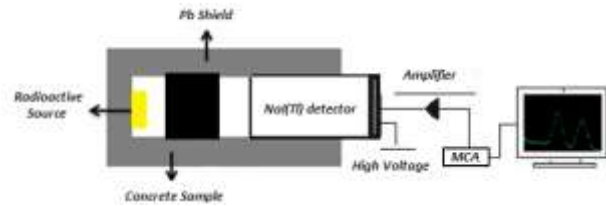

Figure 1. Concrete molds

Figure 2. The schematic view of gamma-ray spectroscopy system

2.2. Experimental procedures

The LAC was determined by using marble powder doped concrete samples prepared as 9x9x9 cm size cubic for 1773 and 1332 keV energy values which were produced by Co-60 radioactive sources. The shielding measurements have been performed using a gamma-ray spectrometer with 3"x3" NaI (Tl) detector in the Radioactive Research Laboratory of Amasya University Science & Arts Faculty. The system contains a 3"x3" NaI (Tl) detector coupled to a digital spectrum analyzer (DSPEC LF) which was connected to the Multi-Channel Analyzer (MCA) provided by ORTEC hardware controlled by MAESTRO-32 software [11] (Fig. 2).

The LAC is calculated using the Beer-Lambert equation:

$$\mu = \frac{1}{x} In(\frac{N_0}{N})$$

Table 1. Particle diameters distribution and physical properties in aggregates

Sample Type	Sieve Analysis (% Passed)								Unit Volume Mass (kg/m³)
	16	9.5	8	4	2	1	0.5	0.25	
Crushed Stone	100	67	37	0	0	0	0	0	2680
Crushing Sand	100	100	100	97	69	41	27	18	2680
Barite	98	69	47	1	1	1	1	0	4050
Thin Barite	100	100	100	83	44	14	6	3	4050
Marble Powder	100	100	100	100	100	100	100	100	2700

Table 2. *Amounts and ratios of material used in 1 m³ concrete mixture*

| Sample Name | Cement Dosage (kg) | Aggregate (% volume) (kg) | | | Water (kg) | Unit Volume Mass (kg/m³) |
		Marble powder	Crushed stone Aggregate	Barite		
16-CIV500-M0-A30-B70	500	0 (0)	30 (446)	70 (1572)	270	2790
16-CIV500-M4-A30-B66		4 (60)		66 (1482)	270	2762
16-CIV500-M8-A30-B62		8 (120)		62 (1392)	270	2735
16-CIV500-M12-A30-B58		12 (180)		58 (1302)	270	2705
16-CIV500-M0-A70-B30	500	0 (0)	70 (1040)	30 (674)	270	2486
16-CIV500-M4-A66-B30		4 (60)	66 (981)		270	2489
16-CIV500-M8-A62-B30		8 (120)	62 (921)		270	2492
16-CIV500-M12-A58-B30		12 (180)	58 (862)		270	2492

Table 3. *Amounts and ratios of Material Used in 1 m³ Concrete Mixture for the 1ˢᵗ group*

| Sample Name | Cement Dosage (kg) | Aggregate (% volume) (kg) | | | Water (kg) | Unit Volume Mass (kg/m³) |
		Marble powder	Crushed stone Aggregate	Barite		
16	500	0 (0)	30 (446)	70 (1572)	270	2790
17		4 (60)		66 (1482)	270	2762
18		8 (120)		62 (1392)	270	2735
22		12 (180)		58 (1302)	270	2705

Table 4. *Amounts and ratios of Material Used in 1 m³ Concrete Mixture for the 2ⁿᵈ group*

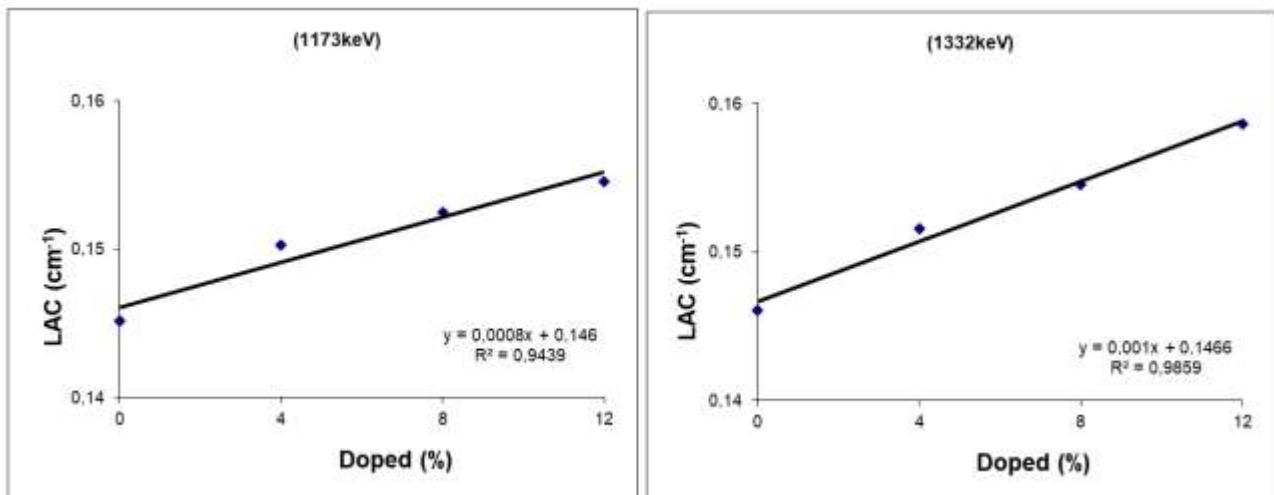| Sample Name | Cement Dosage (kg) | Aggregate (% volume) (kg) | | | Water (kg) | Unit Volume Mass (kg/m³) |
		Marble powder	Crushed stone Aggregate	Barite		
19	500	0 (0)	70 (1040)	30 (674)	270	2486
20		4 (60)	66 (981)		270	2489
21		8 (120)	62 (921)		270	2492
23		12 (180)	58 (862)		270	2492

Figure 3. *Variation of linear attenuation coefficient with energy for 1ˢᵗ group samples*
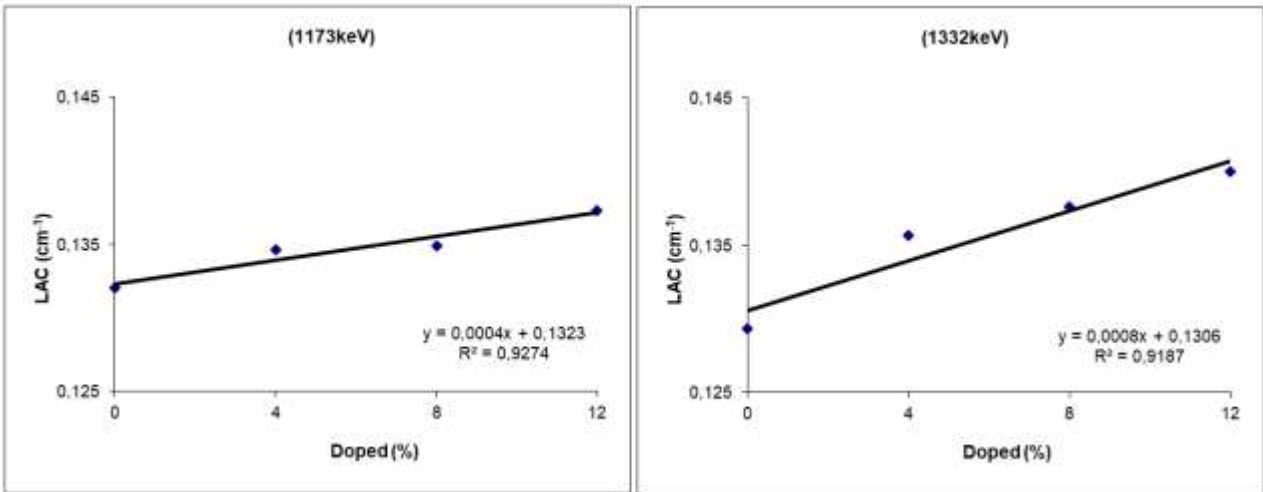
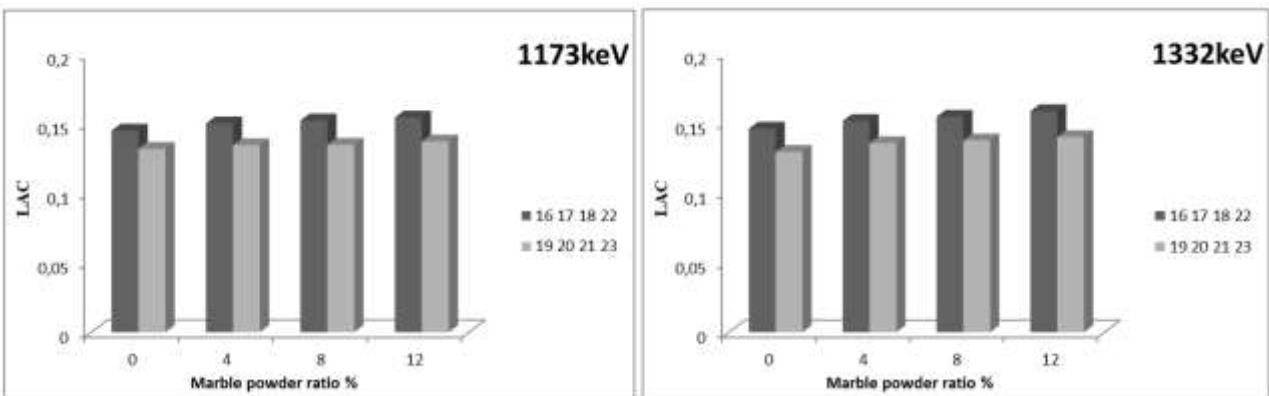**Figure 4.** *Variation of LAC with energy for 2nd group samples*

Figure 5. *Comparison of LAC with marble powder ratio for all samples*
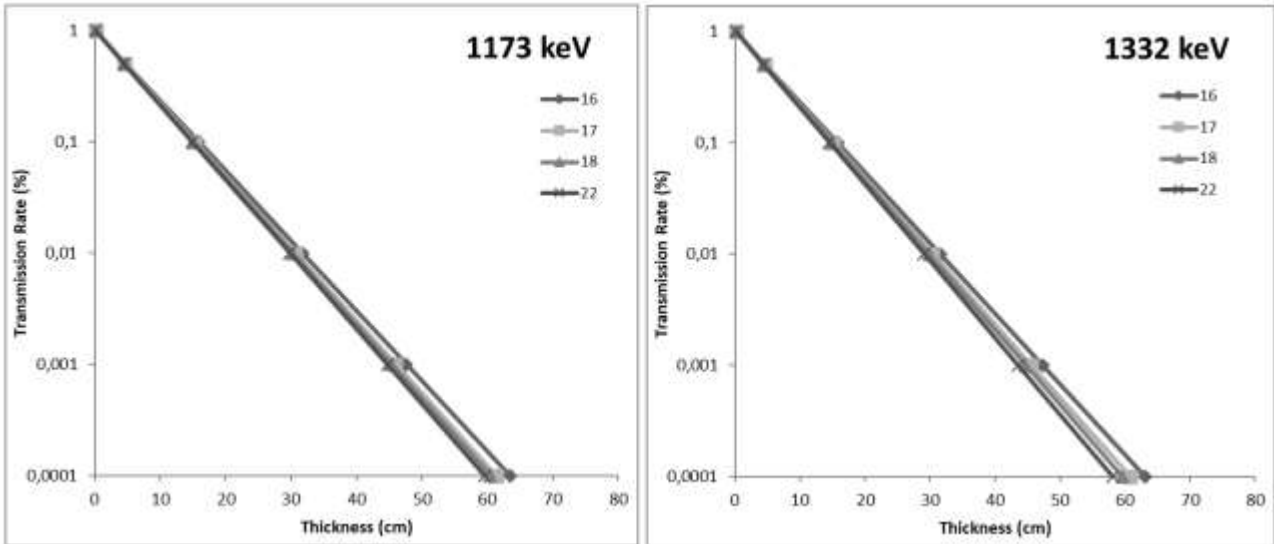

Figure 6. *The transmission rate of the samples as a function of concrete thickness for 1st group samples*
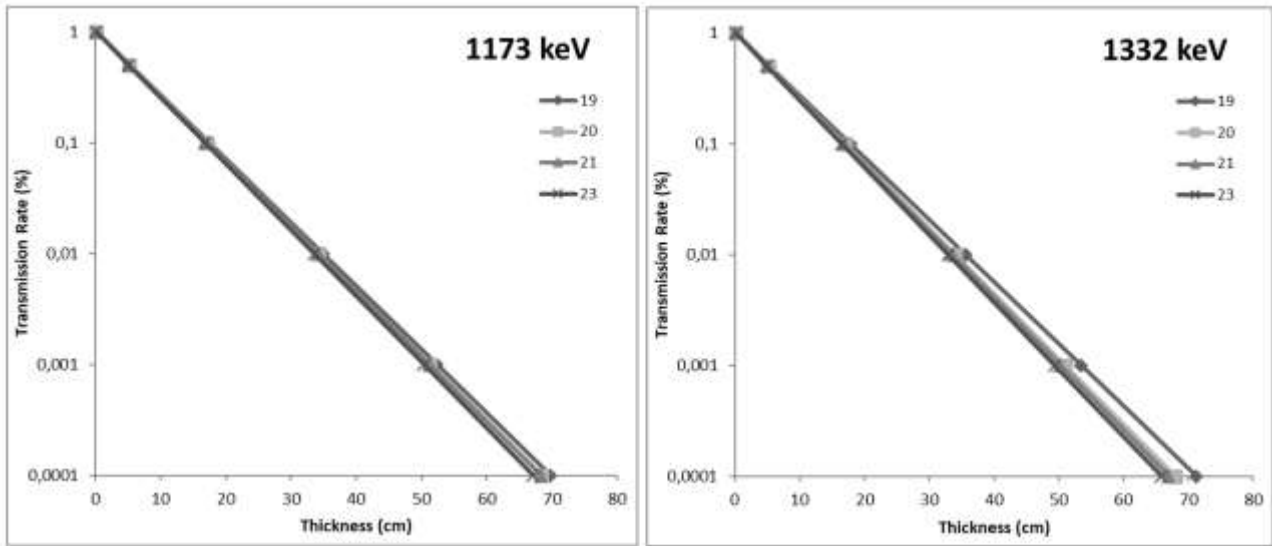
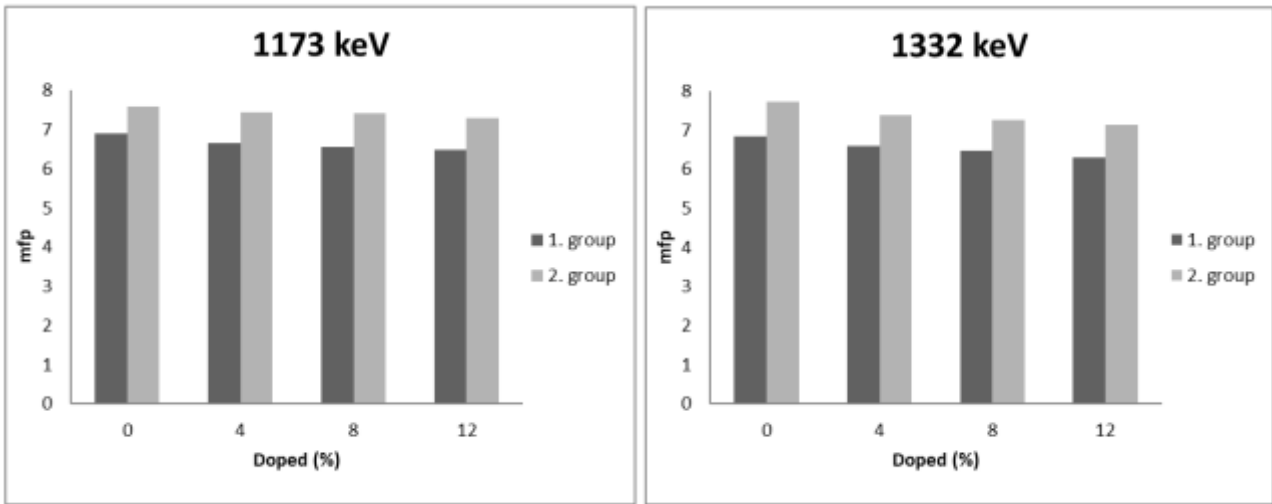***Figure 7.*** *The transmission rate of the samples as a function of concrete thickness for 2ⁿᵈ group samples*

Figure 8. *Mean free path- Marble powder ratio % changes measured for 1ˢᵗ and 2ⁿᵈ group samples*

where μ is the linear attenuation coefficient, x is the concrete samples thickness, N_0 and N are the net count before attenuation and after attenuation.

Eight groups of concrete were prepared to test the contribution of marble doped barite-based concretes to protect against gamma-rays. Each concrete was prepared with different amounts of marble powder, barite, cement and aggregates (Table 3 and Table 4).

3. Results and Discussions

Figure 3 and Figure 4 shows the LAC calculated for the concrete samples in the 1173 and 1332 keV gamma energies using ⁶⁰Co radioactive sources. The LAC values measured for *1ˢᵗ and 2ⁿᵈ group* are

given in Figure 5 comparatively. The shielding properties of concrete which high ratio barite in marble powder doped concrete samples are higher than the high ratio aggregate. In high ratio barite doped samples, the increased shielding property against the decreasing barite rate is the result of increased marble powder.

The thickness of any given material with the half the incoming radiation intensity has been attenuated is referred to as the half-value layer (HVL). The HVL is defined as units of distance (cm). Similar to the attenuation coefficient depends on the photon energy [12, 13].
The following relations are given for the values of HVL.

$$HVL = \frac{In2}{\mu}$$

The calculated half value layer (HVL) values have been displayed in Fig. 6 and Figure 7.

It can be seen from this figure that larger thickness of materials is required to stop the photons of higher energy.

The mean free path is the average distance between two consecutive photon interactions in the sample and was obtained from the following equation:

$$mfp = \frac{1}{\mu}$$

The obtained results has been displayed in figure 8 where it is plotted mfp as a function of doped rate for gamma ray energies.

4. Conclusions

According to these results obtained in the study, the shielding properties of the concrete samples with high barite content in the marble powder added concrete samples are higher than the concrete samples with high aggregate content. In high ratio barite doped samples, the increased shielding property against the decreasing barite rate is the result of increased marble powder. As a result of this study shows that the added of marble powder contributes positively to the properties of barite and aggregate added to concrete.

Author Statements:

- **Ethical approval:** The conducted research is not related to either human or animal use.
- **Conflict of interest:** The authors declare that they have no known competing financial interests or personal relationships that could have appeared to influence the work reported in this paper
- **Acknowledgement:** This study includes the results of the MSc Thesis conducted by Yasemin Savaş under supervision of Prof. Dr. Betul Cetin.
- **Author contributions:** The authors declare that they have equal right on this paper.
- **Funding information:** The authors declare that there is no funding to be acknowledged.
- **Data availability statement:** The data that support the findings of this study are available on request from the corresponding author. The data are not publicly available due to privacy or ethical restrictions.

References

[1] Çetin, T. (2003). Marble Potential, Production and Export of Turkey. *Gazi Üniversitesi Gazi Eğitim Fakültesi Dergisi,* 23 (3), 243-256.
[2] Akkurt, I., Basyigit, C., Kılıncaslan, S., Mavi, B., (2005). The shielding of g-rays by concretes produced with barite. *Progress in Nuclear Energy*, 46, 1-11.
[3] Demir, T. & Alyamaç, K. E. (2022). Investigation of the Use of Marble Powder in Production of High Strength Concretes. *Open Journal of Nano,* 7 (1) , 18-25. DOI: 10.56171/ojn.1034691
[4] Ashish, D. K. (2019). Concrete made with waste marble powder and supplementary cementitious material for sustainable development. *J. Clean. Prod.,* 211, 716–729.
[5] Terzi, S. & Karaşahin, M. (2003). Mermer Toz Atıklarının Asfalt Betonu Karışımında Filler Malzemesi Olarak Kullanımı . *Teknik Dergi* , 14 (67).
[6] Gülan, L., Yıldız, S. & Keleştemur, O. (2016). Atık Mermer Tozu ve Cam Lif Katkılı Betonun Mekanik ve Fiziksel Özellikleri Üzerine Karbonatlaşmanın Etkisi. *Fırat Üniversitesi Mühendislik Bilimleri Dergisi*, 28 (2), 189-200.
[7] Yazicioğlu, S. & Kara, C. (2017). Effects of Using Waste Marble Dust in Concrete to Carbonation. *Journal of Polytechnic*, 20 (2), 369-376.
[8] Şenol, A. F. & Karakurt, C. (2023, February 18-21). Atık Mermer Tozunun Çimento Harçlarının Dayanım Özelliklerine Etkisi, 1st International Conference on Frontiers in Academic Research, Konya, Turkey https://www.icfarconf.com/
[9] Türk Standartları Enstitüsü (TSE). (2016). TS 802 Beton Karışım Tasarımı Hesap Esasları. Ankara.
[10] EN 12390-2:2009 (2009). Testing hardened concrete - Part 2: Making and curing specimens for strength tests.
[11] Çetin, B., Oner, F., Akkurt, I., (2016). Determination of Natural Radioactivity And Associated Radiological Hazard In Excavation Field In Turkey (Oluz Höyük). *Acta Physica Polonica* A, 130(1), 475-478.
[12] Mavi, B., (2012). Experimental investigation of γ-ray attenuation coefficients for granites. *Annals of Nuclear Energy*, 44, 22-25.
[13] Akkurt, I.,Akyıldırım, H., Mavi, B., Kılıncaslan, S., Basyigit, C., (2010). Photon attenuation coefficients of concrete includes barite in different rate, *Annals of Nuclear Energy,* 37, 910-914.
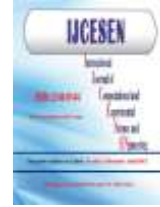
Exergetic Analyses of Hypersonic Flows

Esra Nur TOPAL[1], Rabi KARAALİ[2]*

[1]*Bayburt University, Mechanical Engineering Department M.S., Merkez, Bayburt, Turkey.*
Email: nuresratpl066@gmail.com - **ORCID:** *0000-0002-8201-4232*

[2]**Bayburt University, Engineering Fac., Department of Mechanical Eng., Merkez, Bayburt, Turkey.*
*Corresponding Author**: **Email:** rabikar@gmail.com - **ORCID:** 0000-0002-2193-3411

Abstract:

Hypersonic devices and vehicles and hypersonic flows are very important and competitive advanced technology in science and in the World. Hypersonic technology is rapidly spreading and turning into competition in developed countries, especially in space studies and defense industry. This technology is vital for developed countries. Because of shock waves emerging in hypersonic devices during hypersonic flow, the energy and exergy destructions they cause are the most important difficulties, obstacles and problems which arise in this vital technology. To overcome these problems and difficulties, to prevent or reduce or minimize energy and exergy destruction, aerodynamic analysis and energy and exergy analysis methods are applied. The data and the results that can be guiding and useful for the calculations and the design have been obtained. In this study optimal design and optimum calculations ways of the energy and exergy destructions of hypersonic devices and instruments are discussed. It is obtained and shown that how much exergy destruction and entropy production occurs at which altitude and hypersonic velocities and also at which oblique shock angles.

1. Introduction

Flows above $5 < Ma$ are called hypersonic flows, flows between $1 < Ma < 5$ are called supersonic and flows less than $Ma < 1$ are called subsonic flows. Hypersonic devices and vehicles and hypersonic flows are very important advanced technology topics in space studies, in science, and defense industry. In developed countries this technology is rapidly turning into technological competition and becoming widespread. During hypersonic flow of a vehicle thin shock layers over the body of the vehicle occurs and called oblique shock. Besides these during hypersonic flow in the region of a shock detachment point an entropy layer occurs and then continues to flow downstream. Strong vorticities in this entropy layer that mostly cause analytical problems in the calculations and also, through the boundary layer viscous interaction of the mass flow is another important problem. Besides these problems extreme temperatures may occur in the hypersonic boundary layers and on the nose zone. The ionization might happen in the dissociation of the air molecules under these extreme temperatures [1, 2, 3].

Shock waves emerging in hypersonic flow and devices and the energy and exergy destructions they create are the most important obstacles and difficulties that arise in this technology. To reduce or to prevent or to minimize energy and exergy destruction in hypersonic vehicles lots of experiments have done in laboratories and in atmosphere. Some very important empiric equations and relations are found and applied to develop hypersonic devices.

Moorhouse [2, 3], and also Bejan [4, 5], have investigated and studied on this topic and proposed the second law of thermodynamics and exergy-based methods for analyses of the hypersonic vehicles. They obtained and showed that will allow better analyses and more complete systems integration.

In this study aerodynamic analysis, energy and exergy analyses methods are applied. Results and data that can be useful and guiding in the design have been obtained. Some optimal design methods of hypersonic instruments and devices are discussed and investigated. It is obtained and shown how much entropy production and exergy destruction occurs at which oblique shock angles and/or at which hypersonic velocities and altitudes.

2. Material and Methods

Hypersonic vehicles and flows are taken as materials in this study. As in figure 1 the optimal cruise scramjet hypersonic vehicles representation is given as examples for hypersonic vehicles. Energy analysis is done by using the equations;

$$\dot{Q}_{CV} - \dot{W}_{CV} + \sum_{in} \dot{m}_{in}\left(h_{in} + \frac{V_{in}^2}{2} + gz_{in}\right) - \sum_{out} \dot{m}_{out}\left(h_{out} + \frac{V_{out}^2}{2} + gz_{out}\right) = 0 \qquad (1)$$

$\dot{W}_{CV}$ and $\dot{Q}_{CV}$ are the work and the heat energy, m is mass, h is enthalpy, z is altitude and v is speed. The law of conservation of mass in steady state is written as [6, 7].
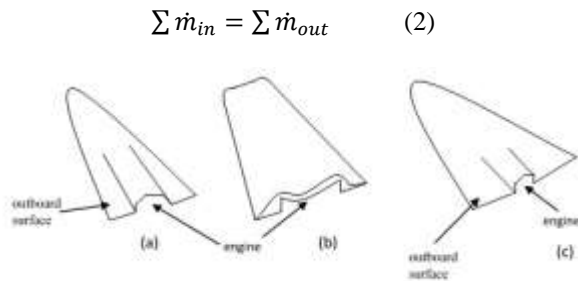
$$\sum \dot{m}_{in} = \sum \dot{m}_{out} \qquad (2)$$

Figure 1. *The optimal cruise scramjet hypersonic vehicles schematic views.*

Exergy can be obtained if equilibrium with the environment is achieved at the end of a reversible process and it is the theoretical maximum amount of useful work. Chemical and physical exergy are the two components of it. For the perfect gas mixtures physical exergy for mixed substances can be written in molar terms as;

$$e_{phy} = (\bar{h} - \bar{h}_0)_{mix} - T_0.(s - s_0)_{mix} = \sum_i x_i \left[\int_{T_0}^{T} \bar{c}_{p0i}(T)dT - T_0.\left(\int_{T_0}^{T} \frac{\bar{c}_{p0i}(T)}{T}dT - \bar{R}\ln\frac{P_i}{P_0}\right)\right] (3)$$

In the equations, P is pressure, T is temperature, s is entropy, and x is molar rate. The maximum useful work which is achieved when a substance in the reference state becomes thermodynamic equilibrium in terms of chemical composition with its surroundings called chemical exergy [8, 9]. The chemical exergy of gas mixtures;

$$\bar{e}_{chem,mix} = \sum_i x_i.\bar{e}_{chem,i} + \bar{R}.T_0.\sum_i x_i.\ln x_i \qquad (4)$$

And, the total exergy of control mass or a flow is;

$$\bar{E} = \bar{E}_{phy} + \bar{E}_{chem} \qquad (5)$$

Exergy equation for open systems is;

$$\sum_i \dot{m}_i h_i - \sum_i T_0 S_i - \sum_j \dot{m}_j h_j + \sum_j T_0 S_j + \sum \dot{Q}_k - \sum \dot{Q}_k \frac{T_0}{T_k} - \dot{W} = \dot{E}_{loss} \qquad (6)$$

In Figure 2 oblique shock diagram is given, and in Figure 3 a) Shock angle versus deflection angle, and b) propulsion sub-system components are given. Mach number can be written as;

$$Ma = \frac{V}{c} = \frac{V}{\sqrt{kRT}} \qquad (7)$$

The speed of sound is c;

$$Ma_{1n} = Ma_1.\sin\beta \qquad (8)$$

$$Ma_{1t} = Ma_1.\cos\beta \qquad (9)$$

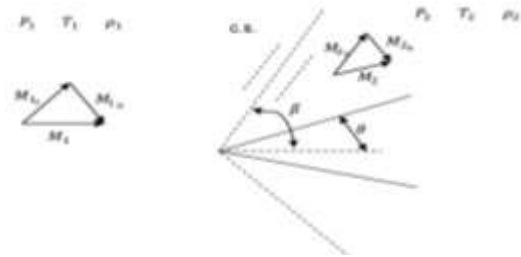$$Ma_{2n} = Ma_2.\sin(\beta - \alpha) \qquad (10)$$
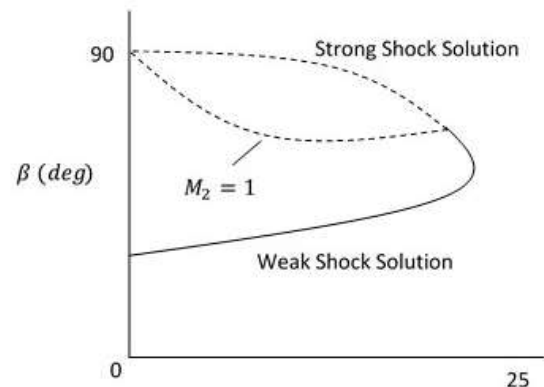

Figure 2. *Oblique shock diagram*

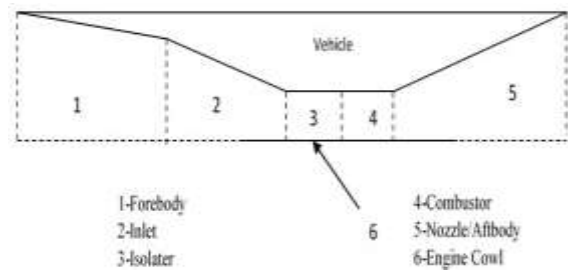**Figure 3.** *Shock angle versus deflection angle*

Figure 4. *Propulsion sub-system components.*

$$Ma_{2t} = Ma_2.\cos(\beta - \alpha) \qquad (11)$$

$$\tan\alpha = 2\cot\beta.\frac{Ma_1^2.\sin^2\beta - 1}{Ma_1^2.(k + \cos^2 2\beta) + 2} \qquad (12)$$

Since the angle α and Ma_1 are known, iteratively β strong shock angles and β weak shock angles can be calculated and other unknowns can be found by using this. The ratio of specific heats is k and k=1.4 is taken for air.

$$Ma_{2n} = \frac{Ma_{1n}^2 + 2/(k-1)}{Ma_{1n}^2 \cdot \frac{2.k}{k-1} - 1} \qquad (13)$$

Pressure and temperature rates are;

$$\frac{P_2}{P_1} = \frac{k.Ma_{1n}^2 + 1}{k.Ma_{2n}^2 + 1} \qquad (14)$$

$$\frac{T_2}{T_1} = \frac{(\frac{k-1}{2})Ma_{1n}^2 + 1}{(\frac{k-1}{2})Ma_{2n}^2 + 1} \qquad (15)$$

The equation of the irreversible entropy is;

$$s_{irr} = s_2 - s_1 = c_p.\ln\left(\frac{T_2}{T_1}\right) - R\ln\left(\frac{P_2}{P_1}\right) \qquad (16)$$

The exergy destruction is;

$$I_{irr} = \dot{m}T_0(s_2 - s_1) \qquad (17)$$

3. Results and Discussions

In Table 1, the results of the calculations for weak shock angle, P_2/P_1, Ma_1, T_2/T_1, Ma_2, ρ_1, ρ_2/ρ_1, $\dot{m}$, V, s_{irr}, and I_{irr} values for $Ma_1=5$ and for 2000 meters altitude, are given. Here the calculations are made for T1=250 K, Ma=5, and P1=1000 Pa. The altitude is defined as $H_{altitude}$= 2000 meters, and the speed of sound is taken for this altitude as c=332.5329 m/s, and ρ_1 is calculated as ρ_1 =1.00499 kg/m^3 for the Table 1 and Figure 4. As it can be seen that, increasing turn angle increases weak shock angles. Increasing turn angle also increases entropy and exergy destruction of the supersonic and hypersonic vehicles or systems. In Figure 5, variation of the entropy generation with turn angles in degrees (weak shock) for different Mach numbers for 2000 meters altitude are given. As can be seen that, increasing Mach number increases the entropy generation of the supersonic and hypersonic vehicles or the systems. For low Mach numbers these increases are low. However, for high Mach numbers these increases are very high. Also increasing turn angles in degrees (weak shock) increases the entropy generation. For low turn angles in degrees these increases are low. However, for high angles in degrees the entropy generation increases are very high. In Figure 6, variation of the entropy generation with turn angles in degrees (strong shock) for different Mach numbers for 2000 meters altitude are given. As can be seen that, increasing Mach number increases the entropy generation of the supersonic and hypersonic

Table 1. *The calculation results of the weak shock angle, P_2/P_1, Ma_1, T_2/T_1, Ma_2, ρ_2/ρ_1, V, ρ_1, $\dot{m}$, s_{irr}, and I_{irr} values for 2000 meters altitude and for $Ma_1=5$ ($V=1662.7$ m/s, $\rho_1=1.005$ kg/m³ and $\dot{m}= \rho_1 VA=1671$ kg/s ($A=1m^2$)).*

Turn angle α^0	weak shock angle β^0	Ma_2	P_2/P_1	T_2/T_1	ρ_2/ρ_1	$s_{irr}=s_2-s_1$ (kJ/kgK)	$I_{irr}=\dot{m}T_\zeta$ (s_2-s_1) (kW)
2	12.85	4.79	1.277	1.0727	1.190	0.354	148
4	14.30	4.59	1.613	1.15	1.403	3.25	1356
6	15.87	4.39	2.016	1.234	1.634	10.1	4215
8	17.57	4.20	2.491	1.326	1.878	21.9	9165
10	19.38	3.99	3.044	1.429	2.13	39.3	16408
12	21.28	3.80	3.676	1.543	2.383	62.3	26014
14	23.29	3.60	4.392	1.67	2.632	90.7	37884
16	25.38	3.40	5.191	1.807	2.872	121.9	50947
18	27.55	3.21	6.073	1.958	3.101	157.6	65826
20	29.80	3.02	7.037	2.123	3.315	196.6	82130
22	32.13	2.84	8.084	2.299	3.515	237.2	99102
24	34.54	2.65	9.210	2.490	3.699	279.6	116809
26	37.04	2.48	10.41	2.693	3.868	323.1	134959
28	39.63	2.30	11.70	2.909	4.023	367.2	153404
30	42.34	2.13	13.07	3.138	4.164	400.1	167124
32	45.19	1.97	14.52	3.38	4.294	456.2	190559
34	48.24	1.80	16.06	3.639	4.413	501.3	209430

Figure 5. *Variation of the entropy generation with turn angles in degrees (weak shock) for different Mach numbers for 2000 meters altitude.*
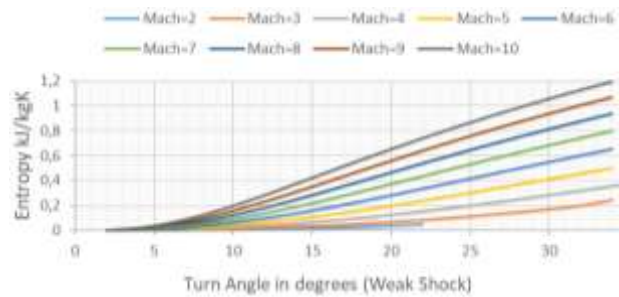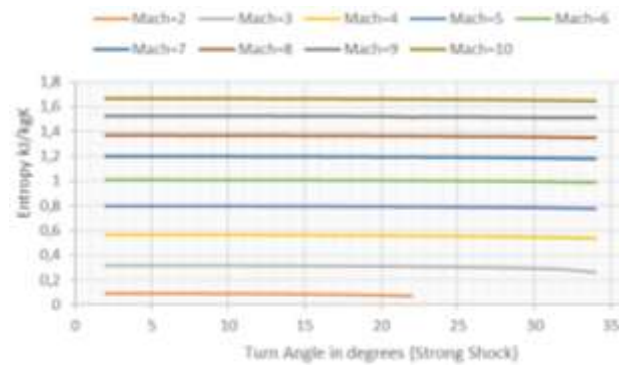

Figure 6. *Variation of the entropy generation with turn angles in degrees (strong shock) for different Mach numbers for 2000 meters altitude.*

vehicles or the systems. For low Mach numbers these increases are low. However, for high Mach numbers these increases are very high. As can be seen that, increasing turn angles in degrees (strong

shock) do not make any effect on the entropy generation which almost stay constant.

For the weak shock angle, the calculation results, in Table 2, for Ma_1, T_2/T_1, Ma_2, P_2/P_1, $\dot{m}$, ρ_2/ρ_1, ρ_1, V, s_{irr}, and I_{irr} values for $Ma_1=5$ altitude and for 24000 meters, are given. The calculations are made for P1=1000 Pa, Ma=5, and T1=250 K.

Table 2. *The calculation results for weak shock angle, Ma_2, P_2/P_1, T_2/T_1, ρ_2/ρ_1, $\dot{m}$, s_{irr}, and I_{irr} values for 24000 meters altitude ($\rho_1=0.0412$ kg/m³, V=1488.92 m/s, $\dot{m}=\rho_1 VA=61.39$ kg/s, (A=1m²) and $Ma_1=5$).*

| Turn angle α^0	weak shock angle β^0	Ma_2	P_2/P_1	T_2/T_1	ρ_2/ρ_1	$s_{irr}=s_2-s_1$ (kJ/kgK)	$I_{irr}=\dot{m}T_ç(s_2-s_1)$ (kW)
2	12.85	4.79	1.277	1.073	1.190	0.354	5.4
4	14.30	4.59	1.613	1.15	1.402	3.247	49.8
6	15.87	4.39	2.016	1.234	1.633	10.09	154.8
8	17.57	4.19	2.491	1.326	1.878	21.94	336.7
10	19.38	3.99	3.044	1.429	2.13	39.28	602.8
12	21.28	3.80	3.676	1.543	2.383	62.27	955.7
14	23.29	3.60	4.392	1.67	2.632	90.69	1391.8
16	25.38	3.40	5.191	1.807	2.872	121.96	1871.7
18	27.55	3.21	6.073	1.958	3.101	157.58	2418.4
20	29.80	3.02	7.037	2.123	3.315	196.61	3017.3
22	32.13	2.84	8.084	2.299	3.515	237.23	3640.9
24	34.54	2.65	9.210	2.490	3.699	279.62	4291.4
26	37.04	2.48	10.416	2.693	3.868	323.07	4958.3
28	39.63	2.30	11.701	2.909	4.023	367.22	5635.9
30	42.34	2.13	13.067	3.138	4.164	400.07	6140.0
32	45.19	1.97	14.516	3.38	4.294	456.17	7001.0
34	48.24	1.80	16.061	3.639	4.413	501.34	7694.3
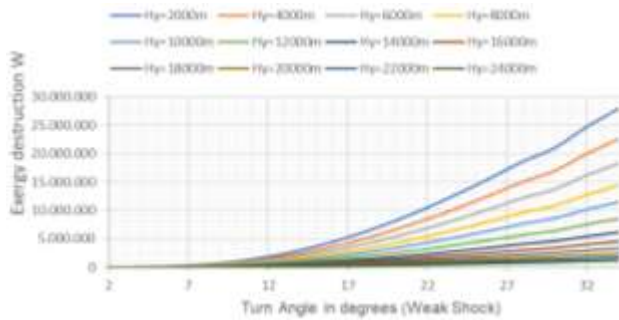
Figure 7. *Variation of the exergy destruction with turn angles in degrees (weak shock) for Ma=5 and different altitudes.*

The altitude is taken as $H_{altitude}=24000$ meters and the speed of sound is taken for this altitude as c=297.784 m/sec, and ρ_1 is calculated as $\rho_1=0.04123$ kg/m^3, for the Figure 7 and Table 2. It can be seen that, increasing in turn angle values increases weak shock angles and that also means increasing turn angle also increases entropy and exergy destruction of the supersonic and hypersonic vehicles or systems.

In Figure 7, variation of the exergy destruction with turn angles in degrees (weak shock) for Ma=5 and different altitudes are given. As can be seen that,

increasing altitudes decreases the exergy destruction of the supersonic and hypersonic vehicles or the systems. For low altitudes these increases are very high. However, for high altitudes these increases are very low. Also increasing turn angles in degrees (weak shock) increases the exergy destruction. For low turn angles in degrees these increases are low. However, for high angles in degrees the exergy destruction increases are very high for low altitudes. The density of the air is very effective on the entropy generation and on the exergy destruction. In Figure 8, variation of the exergy destruction with turn angles in degrees (strong shock) for Ma=5 and different altitudes are given. As can be seen that, increasing altitudes decreases the exergy destruction of the supersonic and hypersonic vehicles or the systems. For low altitudes these increases are very high. However, for high altitudes these increases are very low. As can be seen that, increasing turn angles in degrees (strong shock) do not make any effect on the entropy generation and on the exergy destruction which almost stay constant.
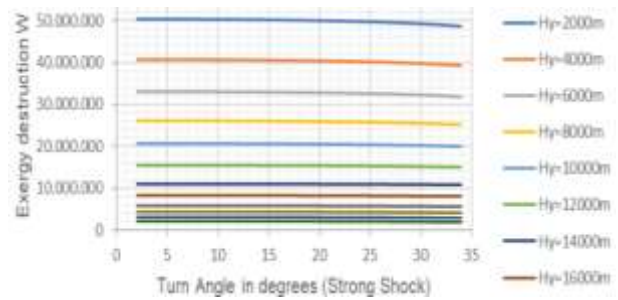

Figure 8. *Variation of the exergy destruction with turn angles in degrees (strong shock) for Ma=5 and different altitudes.*

It can be seen that; higher Mach means higher exergy destruction and higher altitudes means lower exergy destruction for the weak shock and the strong shock. Increasing turn angles in degrees for the strong shock do not make any effect on the entropy generation and on the exergy destruction which almost stay constant. Increasing turn angles in degrees for the weak shock makes rapidly increases on the entropy generation and on the exergy destruction. To decrease entropy generations of the supersonic and hypersonic vehicles or the systems, gradual compression method for the flow is very effective. In Figure 9, gradual compression of flow is given schematically. In Table 3 gradual compression results for 10^0 of turn angle are given. As can be seen that for 10^0 of turn angle the entropy generation is about 39 kJ/kgK. When 10^0 of turn angle is made as $10^0=5^0+5^0+0^0$ the entropy generation is about 13.3 kJ/kgK. When 10^0 of turn angle is made as $10^0=3^0+7^0+0^0$ the entropy
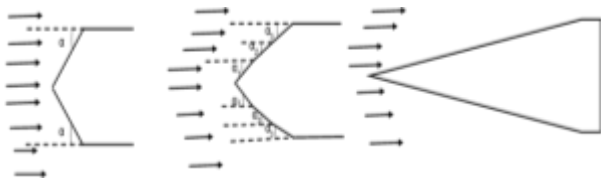
Figure 9. Gradual compression of flow

generation is about 17.8 kJ/kgK. The best solution $10^0=1^0+1^0+1^0+1^0+1^0+1^0+1^0+1^0+1^0+1^0$ seems to be **case8** as calculated its' total entropy 0.214 kJ/kgK.

Table 3. Gradual compression results for 10^0 of turn angle.

Case	$\alpha 1 + \alpha 2 + \cdots$	S_{irr} (kJ/kgK)
1	10	39.2793
2	3+7	17.8171
3	5+5	13.3394
4	4+6	13.3394
5	3+3+4	6.8489
6	2+4+4	6.8489
7	2+2+2+2+2	1.77
8	1+1+1+1+1+1+1+1+1+1	0.214

The designers of supersonic and hypersonic vehicles prefer empirically to gradually compression or contour surfaces. However, no matter how perfect the gradual compression or contour surfaces, oblique shock cannot be avoided. It is possible to provide some of its energy and exergy only by reducing the entropy production of the supersonic and hypersonic vehicles or the systems.

4. Conclusions

Hypersonic devices and vehicles and hypersonic flows are very important advanced technology which are rapidly turning into technological competition and becoming widespread in science and in the World. Hypersonic technology in developed countries, especially in space studies and defense industry, is vital for developed countries. In hypersonic flow and devices shock waves cause the energy and exergy destructions and they create the most important problems, obstacles and difficulties in calculations in this advanced technology which is very new.

In this study aerodynamic analysis and energy and exergy analysis methods have been applied. The results and data that can be guiding and useful in the design are investigated. For hypersonic devices and instruments optimal design ways of are discussed and investigated. It is concluded that higher Mach numbers causes higher exergy destruction and higher altitudes decreases the exergy destruction for the strong shock and the weak shock. For the strong shock increasing turn angles in degrees do not make any effect on the exergy destruction and on the entropy generation that almost stay constant. For the weak shock increasing turn angles in degrees causes rapidly increases on the exergy destruction and on the entropy generation. To decrease entropy generations of the supersonic and hypersonic vehicles or the systems, gradual compression method for the flow is very effective.

The designers of supersonic and hypersonic vehicles prefer empirically to gradually compression or contour surfaces. However, no matter how perfect the gradual compression or contour surfaces, oblique shock cannot be avoided. By reducing the entropy production of the supersonic and hypersonic systems or the vehicles some of its energy and exergy can be provided.

Author Statements:

References

[1] Keven, A., Karaali, R. (2015). Investigation of an Alternative Fuel for Diesel Engines. *Acta Physica Polonica A*, 128(2B);282 – 286. DOI:10.12693/APhysPolA.128.B-282

[2] Keven, A., Karaali, R. (2022). Analysis of Some Tribological Properties of Hazelnut Oil in Gasoline engines. *Erzincan University Journal of Science and Technology.* 15;75–83. DOI:10.18185/erzifbed.1199745

[3] Keven, A., Öner, C. (2023.) Emission and Lubrication Performance of Hazelnut Oil as A Lubricant. *International Journal of Computational and Experimental Science and Engineering,* 9;219 – 224. DOI: 10.22399/ijcesen.1321604

[4] Atasbak, M., Karaali, R., Keven, A. (2022). Exergy analyses of two and three stage cryogenic cycles. *Applied Rheology,* 32;194 – 204.

DOI:10.1515/arh-2022-0134

[5]Keven, A. (2023). Exergy Analyses of Vehicles Air Conditioning Systems for Different Refrigerants. *International Journal of Computational and Experimental Science and Engineering,* 9; 20 – 28. DOI: 10.22399/ijcesen.1258770

[6]Keven, A. (2023). Performance analyses of detonation engine cogeneration cycles. *Open Chemistry,* 21;1 – 9. DOI: 10.1515/chem-2022-0313.

[7]Keven, A. (2023). Exergetic performance analyses of three different cogeneration plants. *Open Chemistry,* 21;1 – 13. DOI: 10.1515/chem-2022-0295.

[8]Karaali, R., Keven, A. (2022). Performance Analysis of Air Fuel Heating Effects on Cogeneration cycles. *European Journal of Science and Technology*, 43;91 – 96. DOI: 10.31590/ejosat.1199414

[9]Karaali, R., Keven, A. (2022). Exergy Analysis of Inlet Air Absorption Cooling Effects on Basic Cogeneration Systems. *European Journal of Science and Technology.* 43;97 – 103.
DOI: 10.31590/ejosat.1199382

[10]Karaali R., Keven, A. (2022). Evaluation of four different cogeneration cycles by using some criteria. *Applied Rheology*, 32;122 – 137.
DOI: 10.1515/arh-2022-0128

[11]Anderson, Jr.J.D. (2001). *Fundamentals of Aerodynamics*. 3rd Edition, McGraw-Hill, New York.

[12]Moorhouse, D. J., and Suchomel, C.F. (2001). Exergy Methods Applied to the Hypersonic Vehicle Challenge. *AIAA Paper* No. 2001-3063.

[13]Moorhouse, D.J. (2003). Proposed System-Level Multidisciplinary Analysis Technique Based on Exergy Methods. *Journal of Aircraft*. Vol. 40, No. 1.

[14]Bejan, A. (2000). Architecture From Exergy-Based Global Optimization: Tree-Shaped Flows and Energy Systems for Aircraft. *AIAA Paper* No. 2000-4855.

[15]Dincer, I., Rosen, M.A. (2007). *EXERGY, energy, environment and sustainable development*, 1sted. Elsevier Ltd.

[16]Bejan, A. (2003). Constructal Theory: Tree-Shaped Flows and Energy Systems for Aircraft. *Journal of Aircraft*. Vol. 40, No. 1.

[17]Çengel, Y., Boles, M.A. (2001). *Thermodynamics: an engineering approach.* McGraw-Hill.

[18]Bejan, A. (1996). *Entropy Generation Minimization: The Method of Thermodynamic Optimization of Finite-Sized Systems and Finite-Time Processes*. CRC Press Inc. Boca Raton FL.

[19]Bejan, A., Tsatsaronis, G., Moran, M. (1996). *Thermal design and optimization*. Wiley Pub, New York.

Research Article
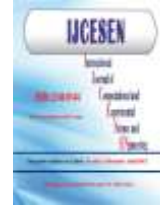
Investigation of Shielding Parameters of Fast Neutrons for Some Chemotherapy Drugs by Different Calculation Methods

Turan Şahmaran[1], *, Taylan TUĞRUL[2]

[1]Kırıkhan Vocational School, Hatay Mustafa Kemal University, Hatay, Turkey.
*Corresponding Author: Email: tsahmaran@gmail.com - **ORCID**: 0000-0003-3708-6162

[2] Department of Radiation Oncology, Medicine Faculty of Van Yüzüncü Yıl University, Van, Turkey
Email: taylantugrul@gmail.com - **ORCID**: 0000-0002-0557-1334

Abstract:

In this study, we investigated the neutron attenuation properties of twelve different chemotherapy drugs utilizing various computational techniques. The computed fast neutron effective removal cross-section (Σ_R, cm^{-1}) results were compared with empirical formulas, Monte Carlo simulation data obtained from MCNP, MRCsC, and Phy-X/PSD computer program results. Additionally, within each calculation method, the half-value layer (HVL) and the mean free path (λ) values were determined. Our calculations revealed that, when compared to water and paraffin, Gemcitabine, Etoposide, Vincristine, and Doxorubicin exhibited the highest Σ_R values, while Oxaliplatin exhibited the lowest Σ_R value. Understanding and determining the radiation properties of drugs, especially in treatment methods involving radiation, will provide an advantage for both patients and clinical personnel.

1. Introduction

The shielding of fast neutrons holds critical significance in nuclear engineering and radiation protection due to the inherent risks posed by these high-energy particles, generated in nuclear reactions and reactors, to human health and the environment. Effective shielding and the choice of shielding materials are of paramount importance to mitigate these risks. Free neutrons can significantly alter the microstructural properties of a material through elastic or inelastic collisions, nuclear transformations, or ionizations [1,2]. Furthermore, neutrons occurring within biological matter can indirectly cause double-strand breaks in DNA molecules, resulting in cell mutations and fatalities [3]. The effects of neutrons in both living and inanimate materials necessitate a thorough evaluation of radiation shielding. Fast neutrons, typically characterized by energies exceeding 1 MeV, emerge as fundamental components of nuclear reactions. The efficacy of materials in shielding against these neutrons is quantified through the concept of attenuation [4]. Neutron attenuation is calculated using various parameters such as macroscopic effective removal cross-section and macroscopic thermal neutron cross-section [5,6]. ΣR is a fundamental quantity used for predicting neutron shielding. Furthermore, it measures potential for energy reduction of fast neutrons through elastic and inelastic collisions within the material [7]. ΣR is considered as a material property and can be calculated for various protective environments such as alloys [8], ceramics [9], glasses [10], polymers [11], natural minerals [12], as well as rocks, construction, and building materials [13-15]. Neutron shielding materials generally consist of low atomic number elements with high scattering cross-sections that effectively slow down or thermalize incoming neutrons. In practice, small neutron sources are shielded with materials like polyethylene or paraffin, while larger sources necessitate concrete or large water pools/tanks for effective shielding. Cancer treatment often necessitates a combination of modalities, including surgery, chemotherapy, and radiotherapy, depending on the cancer type and stage. One of these treatment methods is chemoradiotherapy, where both chemotherapy and radiotherapy are administered together. After receiving chemotherapy drugs, the patient undergoes radiotherapy and is directly exposed to radiation. Therefore, it is of great importance to investigate the

interaction between these drugs and radiation [16]. In this study, the ΣR parameters were theoretically calculated for twelve different chemotherapy drugs with varying densities and chemical compositions. The calculated results were compared with empirical formulas, Monte Carlo simulation data obtained from Monte Carlo N-Particle (MCNP, version 5), and results derived from MRCsC and Phy-X/PSD computer programs. Additionally, the half-value layer (HVL) and the mean free path (λ) values were determined for chemotherapy drugs using each of the different calculation methods. This study represents one of the few investigations on ΣR concerning chemotherapy drugs.

2. Materials and methods

2.1 Theoretical calculation

The total microscopic cross-section of neutrons (σt) represents the probability of interaction with the traversed medium. This total microscopic cross-section is the sum of the microscopic scattering cross-section (σs) and the absorption cross-section (σa). The calculation of the total macroscopic cross-section is expressed in Equation 1.

$$\sigma_t = \sigma_s + \sigma_a \qquad (1)$$

A practical method for determining the intensity of neutrons involves obtaining the number of neutrons per unit area or flow rate [17]. The decay of neutrons within a material can be likened to the Lambert-Beer Law, which is commonly used for the absorption of photons. The formula for neutron decay intensity is presented in equation 2 [18,19].

$$I = I_0^{-(\Sigma_t x)} \qquad (2)$$

In this equation, I_0 represents the initial neutron density, while I denotes the neutron density passing through the attenuator thickness (x, cm). Σt represents the total macroscopic cross-section. ΣR is the probability of a fast or fission-energy neutron undergoing its first collision. Empirical approaches are used to obtain mass removal cross-section (ΣR/ρ, cm²/g) values for certain elements lacking experimental data. Since chemotherapy drugs are composed of multiple elements, calculating ΣR requires the use of the ΣR/ρ rule for constituent elements. One of the empirical models is detailed in equations 3 and 4 [20].

$$\sum_{R/\rho} = 0.190 \, Z^{-0.743} \, Z \leq 8$$

$$\sum_{R/\rho} = 0.125 \, Z^{-0.565} \, Z > 8 \qquad (4)$$

Generally, protective materials are composed of chemical compounds or mixtures. The macroscopic removal cross-sections are computed from the ΣR values of the constituent elements and are presented equation 5 [5, 21-23].

$$\Sigma_R = \sum_i \rho_i \, (\Sigma_R/\rho)i \qquad (5)$$

In this equation, ρ_i, ρ and $(\Sigma_R/\rho)i$ represent the partial density of the first component (g/cm³), the density, and the mass removal cross-section, respectively. The formula for partial density is provided in Equation 6.

$$\rho_i = \sum_i w_i \rho_s \qquad (6)$$

Here, w_i and ρ_s represent the weight fraction of the ith component (element or compound) and the total density of the material, respectively. The half-value layer (HVL) expresses the thickness of the material that reduces incoming neutron radiation by half. HVL can be calculated for neutrons using equation 7 [24,25].

$$HVL = \frac{ln2}{\Sigma R} \qquad (7)$$

The mean free path (λ) is defined as the distance traveled by neutrons within the interaction materials and can be computed using equation 8 [25,26].

$$\lambda = \frac{1}{\Sigma R} \qquad (8)$$

The MRCsC and Phy-X/PSD program

The user-friendly software "MRCsC," comprises a front-end and back-end processor, an analytical model, and an integrated database. It has been meticulously developed as an efficient tool for radiation shielding design. MRCsC is engineered to provide reliable predictions of the macroscopic effective removal cross-section of fast neutrons for various materials [27]. An accessible web-based software tool called Photon Shielding and Dosimetry (PSD) has been developed to simplify the computation of dosimetry and shielding-related parameters. This software is able to generate comprehensive data on shielding parameters covering the continuous energy range in different energy ranges [28].

3. Results and Discussion

The Σ_R values of twelve different chemotherapy drugs have been computed by using the theoretical

Table 1. Chemical properties of chemotherapy drugs

Molecule	Chemical formula	Mol. weight (g/mole)	ρ (g/cm³)
Cisplatin	$PtCl_2H_6N_2$	300.04	3.74
Methotrexate	$C_{20}H_{22}N_8O_5$	454.44	1.50
Oxaliplatin	$C_8H_{14}N_2O_4Pt$	397.29	1.01
Ifosfamide	$C_7H_{15}Cl_2N_2O_2P$	261.09	1.35
Gemcitabine	$C_9H_{11}F_2N_3O_4$	263.20	1.83
Fluorouracil	$C_4H_3FN_2O_2$	130.08	1.51
Pemetrexed	$C_{20}H_{19}N_5Na_2O_6$	471.37	1.02
Etoposide	$C_{29}H_{32}O_{13}$	588.56	1.61
Vincristine	$C_{46}H_{56}N_4O_{10}$	824.96	1.43
Tamoxifen	$C_{32}H_{37}NO_8$	563.64	1.00
Paclitaxel	$C_{47}H_{51}NO_{14}$	853.90	1.42
Doxorubicin	$C_{27}H_{29}NO_{11}$	543.51	1.60

Table 2. Elemental composition of twelve different chemotherapy drugs [29]

Molecule	H	C	N	O	Cl	Pt	P	F	Na
Cisplatin	0.0201		0.0933		0.2363	0.6501			
Methotrexate	0.0487	0.5286	0.2465	0.1760					
Oxaliplatin	0.0355	0.2418	0.0705	0.1610		0.4910			
Ifosfamide	0.0579	0.3220	0.1072	0.1225	0.2715		0.118		
Gemcitabine	0.0421	0.4107	0.1596	0.2431				0.1443	
Fluorouracil	0.0232	0.3693	0.2153	0.2459				0.1460	
Pemetrexed	0.0406	0.5096	0.1485	0.2036					0.0975
Etoposide	0.0548	0.5918		0.3533					
Vincristine	0.0684	0.6697	0.0679	0.1939					
Tamoxifen	0.0661	0.6819	0.0248	0.2270					
Paclitaxel	0.0601	0.6610	0.0164	0.2623					
Doxorubicin	0.0537	0.5966	0.0257	0.3237					

Table 3. Comparison of different chemotherapy drugs ΣR from MCNP, MRCsC, Phy-X/PSD and empirical fit

Materials	(Σ_R) cm⁻¹				PD* MRCsC- Phy-X/PSD	PD* MCNP - $\Sigma R/\rho$
	MRCsC	Phy-X/PSD	MCNP	Estimation using $\Sigma R/\rho$ of elements		
Cisplatin	0.1276	0.1090	0.1038	0.1085	14.57	4.52
Methotrexate	0.1204	0.1108	0.0953	0.1055	7.97	10.70
Oxaliplatin	0.0548	0.0480	0.0441	0.0487	12.40	10.43
Ifosfamide	0.1104	0.0955	0.0897	0.0952	13.49	6.13
Gemcitabine	0.1346	0.1244	0.1140	0.1241	7.57	8.85
Fluorouracil	0.0933	0.0865	0.0785	0.0864	7.28	10.06
Pemetrexed	0.0759	0.0698	0.0627	0.0692	8.03	10.36
Etoposide	0.1349	0.1236	0.1105	0.1238	8.37	12.03
Vincristine	0.1343	0.1221	0.1106	0.1227	9.08	10.94
Tamoxifen	0.0925	0.0841	0.0758	0.0842	9.08	11.08
Paclitaxel	0.1257	0.1143	0.1025	0.1142	9.06	11.41
Doxorubicin	0.1334	0.1222	0.1092	0.1224	8.39	12.08
H_2O	0.1103	0.1030	0.1000	0.1030	6.61	3.00
Paraffin, $C_{25}H_{52}$	0.1417	0.1223	0.1190	0.1220	13.69	2.52

*Percentage deviation

respectively. The discrepancies observed in neutron attenuation coefficients among the calculation methods are notable. MCNP consistently yielded lower coefficients compared to MRCsC, estimation and Phy-X/PSD. These variations might be attributed to the inherent assumptions and approximations each method employs. MCNP, for instance, assumes a simplified molecular structure, potentially underestimating neutron interaction probabilities compared to the more intricate representations in MRCsC, estimation and Phy-X/PSD. The molecular composition of the drugs appears to significantly impact their neutron attenuation capabilities. Oxaliplatin, with a higher Z content of, consistently exhibited lower shielding efficiency across all calculation methods. This reinforces the idea that the elemental composition and molecular structure play pivotal roles in neutron attenuation. Table 3 presents the ΣR values of chemotherapy drugs obtained using various calculation methods. In the study conducted by Hila et al. (2023), fast neutron mass removal cross-sections ($\Sigma R/\rho$, cm²/g) based on ENDF/B-VIII.0 were numerically generated using the sliced spherical shell MCNP Monte Carlo model under different neutron source spectra (^{241}Am–Be, ^{252}Cf, ^{235}U). The values in Table 3 about MCNP were obtained from this study. In this study, the ΣR values were computed using the $\Sigma R/\rho$ values obtained using Californium-252 (^{252}Cf). According to Table 3, in all calculation methods, Parafine (0.1417 cm⁻¹) has been found to be the closest to chemotherapy drugs, including Gemcitabine (0.1346 cm⁻¹), Etoposide

(0.1349 cm⁻¹), Vincristine (0.1343 cm⁻¹), and Doxorubicin (0.1334 cm⁻¹). With the exception of Tamoxifen (0.0925 cm⁻¹), Pemetrexed (0.0759 cm⁻¹), Fluorouracil (0.0933 cm⁻¹), and Oxaliplatin (0.0548 cm⁻¹), the ΣR values of all other chemotherapy drugs are higher than that of water (0.1103 cm⁻¹). In the study conducted by Aygün and Karabulut (2020), a simulation method was employed to investigate the gamma and neutron interactions of select cancer drugs. Similar to our study, they found that the Oxaliplatin has a lower ΣR value compared to other drugs. This result suggests that an increase in the content of low atomic number (Z) elements within the compound leads to an increase in the ΣR value. Furthermore, the presence of hydrogen within the compound significantly contributes to elevated ΣR values, as the $\Sigma R/\rho$ value for hydrogen is nearly double that of other elements. Consequently, compounds with higher hydrogen content exhibit increased ΣR values, a phenomenon that has been corroborated by Akyıldırım's study on basic carbohydrates (2019), focusing on fast neutron shielding parameters.

Understanding the shielding parameters of chemotherapy drugs against fast neutrons is crucial, especially in radiation therapy settings where unintended exposure can impact treatment outcomes. These findings underscore the importance of considering the molecular makeup of drugs when evaluating their potential shielding effectiveness.

Table 4. Comparison of HVL and λ results with different calculation method

Materials	(HVL)$_{MRCsC}$	(λ)$_{MRCsC}$	(HVL)$_{Phy-X}$	(λ)$_{Phy-X}$	(HVL)$_{MCNP}$	(λ)$_{MCNP}$	(HVL)$_{Zoller}$	(λ)$_{Zoller}$
Cisplatin	5.4310	7.8370	6.3577	9.1743	6.6729	9.6287	6.3833	9.2111
Methotrexate	5.7558	8.3056	6.2545	9.0253	7.2684	10.4883	6.5657	9.4743
Oxaliplatin	12.6460	18.2482	14.4375	20.8333	15.7044	22.6614	14.2123	20.5083
Ifosfamide	6.2772	9.0580	7.2565	10.4712	7.7242	11.1461	7.2777	10.5017
Gemcitabine	5.1486	7.4294	5.5707	8.0386	6.0778	8.7703	5.5698	8.0373
Fluorouracil	7.4277	10.7181	8.0116	11.5607	8.8542	12.7766	8.0132	11.5631
Pemetrexed	9.1304	13.1752	9.9284	14.3266	11.0495	15.9444	10.0104	14.4452
Etoposide	5.1371	7.4129	5.6068	8.0906	6.2686	9.0456	5.6048	8.0877
Vincristine	5.1601	7.4460	5.6757	8.1900	6.2655	9.0411	5.6736	8.1870
Tamoxifen	7.4919	10.8108	8.2402	11.8906	9.1417	13.1915	8.2433	11.8951
Paclitaxel	5.5131	7.9554	6.0630	8.7489	6.7566	9.7498	6.0635	8.7497
Doxorubicin	5.1949	7.4963	5.6710	8.1833	6.3446	9.1552	5.6744	8.1881
H$_2$O	6.2828	9.0661	6.7281	9.7087	6.9300	10.0000	6.7281	9.7087
Paraffin	4.8906	7.0571	5.6663	8.1766	5.8235	8.4033	5.6803	8.1967

Moreover, this insight might guide the design and development of new drugs optimized for both therapeutic efficacy and radiation safety. Table 4 presents the computed HVL and λ values using different calculation methods. Lower HVL and λ values indicate better neutron stopping capabilities. Paraffin (4.8906 cm) has the closest HVL values to Gemcitabine (5.1486 cm), Etoposide (5.1371 cm), Vincristine (5.1601 cm), and Doxorubicin (5.1949 cm). The highest λ values were obtained using MCNP method. According to this, the highest λ values are found for Tamoxifen (13.1915 cm), Pemetrexed (15.9444 cm), Fluorouracil (12.7766 cm), and Oxaliplatin (22.6614 cm). Greater λ values signify deeper penetration of fast neutrons for drugs with high λ values compared to those with low λ values. The variations in results across different calculation programs can be attributed to discrepancies in their data libraries and calculation models.

4. Conclusions

In this study, the attenuation properties of 12 different chemotherapy drugs, particularly when exposed to fast neutrons, which are commonly used in cancer treatments, were determined using various calculation methods. It was found that all chemotherapy drugs have a capacity for absorbing neutron radiation when compared to water and paraffin. Notably, Gemcitabine, Etoposide, Vincristine, and Doxorubicin exhibit the highest ΣR values. HVL and λ values were computed using different calculation methods, and Gemcitabine, Etoposide, Vincristine, and Doxorubicin were found to be the chemotherapy drugs closest to water and paraffin. In the study, Oxaliplatin was found to have a lower ΣR value compared to other drugs. These drugs are also administered concurrently with radiotherapy depending on the treatment method. Therefore, knowing and determining their radiation properties will provide an advantage for clinicians.
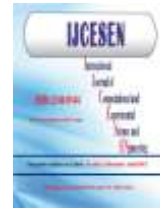
Author Statements:

References

[1] Wu, Y., & Wu, Y. (2017). Neutron irradiation and material damage. *Fusion neutronics*, 91-113.

[2] Konings, R., & Stoller, R. E. (2020). *Comprehensive nuclear materials*. Elsevier., 456–467.

[3] Biau, J., Chautard, E., Verrelle, P., & Dutreix, M. (2019). Altering DNA repair to improve radiation therapy: specific and multiple pathway targeting. *Frontiers in oncology*, 9; 1009.

[4] Akyıldırım, H. (2019). Calculation of Fast Neutron Shielding Parameters for Some Essential Carbohydrates. *Erzincan University Journal of Science and Technology*, 12(2); 1141-1148.

[5] Kaplan, M. F. (1989). Concrete radiation shielding. Longman Scientific and Technology, Longman Group UK Limited, Essex, London.

[6] Jaeger, T., & Dresner, L. (1965). Principles of radiation protection engineering, McGraw-Hill Book Company, New York.

[7] Hila, F. C., Jecong, J. F. M., Dingle, C. A. M., Asuncion-Astronomo, A. J., Balderas, C. V., Sagum, J. A., & Guillermo, N. R. D. (2023). ENDF/B-VIII. 0-based fast neutron removal cross sections database in Z= 1 to 92 generated via multi-layered spherical geometry. *Radiation Physics and Chemistry*, *206;* 110770.

[8] Perişanoğlu, U., El-Agawany, F. I., Tekin, H. O., Kavaz, E., Zakaly, H. M., Issa, S. A., ... & Rammah, Y. S. (2021). Multiple characterization of some glassy-alloys as photon and neutron shields: In-silico Monte Carlo investigation. *Materials Research Express*, 8(3); 035202.

[9] Slimani, Y., Hamad, M. K., Olarinoye, I. O., Alajerami, Y. S., Sayyed, M. I., Almessiere, M. A., & Mhareb, M. H. A. (2021). Determination of structural features of different Perovskite ceramics and investigation of ionizing radiation shielding properties. *Journal of Materials Science: Materials in Electronics*, 32; 20867-20881.

[10] Alotaibi, B. M., Abouhaswa, A. S., Sayyed, M. I., Mahmoud, K. A., Al-Yousef, H. A., Hila, F. C., & Al-Hadeethi, Y. (2021). Structural, optical, and gamma-ray shielding properties of a newly fabricated P 2 O 5– B 2 O 3–Bi 2 O 3–Li 2 O–ZrO 2 glass system. *The European Physical Journal Plus*, 136; 1-22.

[11] Vega-Carrillo, H. R., Garcia-Reyna, M. G., Sanchez-Ortiz, A., Rio, M. D., Estefania, D., & Hernandez-Adame, L. (2022). Attenuation of Γ-Rays and Fast Neutrons in Water, Alcohol, Polyethylene, Diesel and Gasoline. *Alcohol, Polyethylene, Diesel and Gasoline*.

[12] Gili, M. B. Z., & Hila, F. C. (2021). Characterization and Radiation Shielding Properties of Philippine

Natural Bentonite and Zeolite. *Philippine Journal of Science*, *150*.

[13] Perişanoğlu, U., Kavaz, E., Tekin, H. O., Armoosh, S. R., Ekinci, N., & Oltulu, M. (2020). Comparison of gamma and neutron shielding competences of Fe–Cu- and brass-added Portland cement pastes: an experimental and Monte Carlo study. *Applied Physics A*, *126;* 1-14.

[14] Yılmaz, E., Baltas, H., Kırıs, E., Ustabas, İ. L. K. E. R., Cevik, U. Ğ. U. R., & El-Khayatt, A. M. (2011). Gamma ray and neutron shielding properties of some concrete materials. *Annals of Nuclear Energy*, *38*(10); 2204-2212.

[15] Sikora, P., El-Khayatt, A. M., Saudi, H. A., Chung, S. Y., Stephan, D., & Abd Elrahman, M. (2021). Evaluation of the effects of bismuth oxide (Bi2O3) micro and nanoparticles on the mechanical, microstructural and γ-ray/neutron shielding properties of Portland cement pastes. *Construction and Building Materials*, *284*; 122758.

[16] Tuğrul, T. (2020). Investigation of mass attenuation coefficients, effective atomic numbers, and effective electron density for some molecules: study on chemotherapy drugs. *Journal of Radiation Research and Applied Sciences*, *13*(1); 758-764.

[17] Aygün, B., & Karabulut, A. (2022). Investigation of epithermal and fast neutron shielding properties of Some High Entropy Alloys Containing Ti, Hf, Nb, and Zr. *Eastern Anatolian Journal of Science*, *8*(2); 37-44.

[18] Shultis, J. K., & Faw, R. E. (2016). *Fundamentals of Nuclear Science and Engineering Third Edition*. CRC press.

[19] Martin, J. E. (2000). Physics for radiation protection. First printing.Wiley, New York.

[20] Zoller, L. K. (1964). Fast-neutron-removal cross sections. *Nucleonics (US) Ceased publication*, *22*.

[21] Glasstone, S., & Sesonske, A. (1986). Nuclear Reactor Engineering, third ed.

[22] Profio, A. E. (1979). Radiation shielding and dosimetry. Wiley, New York.

[23] Wood, J. (1982). Computational Methods in Reactor Shielding. Pergamon Press, New York.

[24] Zali, N. M., Yazid, H., & Ahmad, M. H. A. R. M. (2018). Neutron shielding behavior of thermoplastic natural rubber/boron carbide composites. In *IOP Conference Series: Materials Science and Engineering* 298(1);012018.

[25] Aygün, B., & Karabulut, A. (2020). The interaction of neutron and gamma radiation with some cancer drug effect ingredients. *Eastern Anatolian Journal of Science*, *6*(2), 35-43.

[26] Lechner, A. (2018). CERN: Particle interactions with matter. *CERN Yellow Rep. School Proc.*, *5*, 47.

[27] El-Samrah, M. G., El-Mohandes, A. M., El-Khayatt, A. M., & Chidiac, S. E. (2021). MRCsC: A user-friendly software for predicting shielding effectiveness against fast neutrons. *Radiation Physics and Chemistry*, *182*, 109356.

[28] Şakar, E., Özpolat, Ö. F., Alım, B., Sayyed, M. I., & Kurudirek, M. (2020). Phy-X/PSD: development of a user friendly online software for calculation of parameters relevant to radiation shielding and dosimetry. *Radiation Physics and Chemistry*, *166*, 108496.

[29] Berger, M. J., & Hubbell, J. H. (1987). XCOM: Photon cross sections on a personal computer (No. NBSIR-87-3597). National Bureau of Standards, Washington, DC (USA). Center for Radiation Research.

Microstructure and tensile properties of AISI 410 stainless steel welded TIG method

Adnan CALIK[1] and Nazim UCAR[2*]

[1]Isparta University of Applied Sciences, Faculty of Technology, Mechanical Engineering, 32260, Isparta, Türkiye
Email: adnancalik@isparta.edu.tr- **ORCID**: 0000-0002-2470-5051

[2]Süleyman Demirel University, Faculty of Arts and Sciences, Department of Physics, 32260, Isparta, Türkiye
* **Corresponding Author: Email**: nazimucar@sdu.edu.tr - **ORCID**: 0000-0002-0936-0382

Abstract:

In this study, the weldabilities, microstructures and tensile properties of AISI 410 stainless steel joints fabrication by tungsten inert gas (TIG) welding method were investigated. TIG welding was carried out on steels by using welding wire ER 410 (AWS A5.9) 2.8 mm in diameter. Tensile test results showed that while tensile and yield strength increased, the elongation value decreased significantly. The yield strength and tensile strength were measured as 619 and 801 MPa after welding process, respectively. In addition, the failure location occurred without any significant cross-sectional narrowing. Microstructure investigations have been carried out using optical microscopy and Scanning Electron Microscopy (SEM). The obtained results indicated that the microstructure of weld metal region had a dual phase such as martensite and ferrite.

1. Introduction

Martensitic stainless steels are obtained by adding 12% chromium and 0.12% carbon elements on a mass basis [1,2]. This group of steels can be easily heated and hardened due to their low carbon content [3]. They are generally hard and therefore brittle. Martensitic stainless steels are a class of stainless steels generally used in applications where better mechanical strength is required [4,5]. AISI 410 stainless steel is one of the most commonly used martensitic stainless steels that provide high strength and hardness with moderate corrosion resistance [6,7]. These steels can also be welded easily. In a study [8]*,* the mechanical properties and microstructures of steels joined by laser welding were characterized. Due to the heat treatment applied after welding, it was determined that the grain structure became coarser and there was a decrease in hardness and tensile strength. As a result, it was concluded that the mechanical properties were negatively affected due to the heat treatment applied after welding. Muthusamy et.al.[9] showed that the tensile strength of gas tungsten arc welded (GTAW) AISI 410 stainless steel decreased with increasing heat input and testing temperatures. In addition, it

was also found that the toughness of the welded joints corresponded to approximately 80% of the toughness of the base metal. In another study by Kim et.al.[10] on steels joined by methods of metal inert gas (MIG) welding and friction stir welding (FSW), the hardness of the MIG welded steels was the highest in the weld metal, decreased in HAZ, and rose slightly in the base metal. The weld metal had a Widmstatten structure that consisted of fine or coarse laths. On the other hand, the microstructure of welded FSW consisted of the stir zone. The stir zone had a relatively high hardness, owing to intense plastic deformation and dynamic recrystallization. These studies show that microstructure and mechanical properties are closely dependent on welding methods [11,12]. AISI 410 martensitic stainless steel is widely used in marine applications, especially for turbine blades [13,14]. In these work areas, two or more parts often need to be joined as one piece. Then, it is important to know the properties of the new material. In the literature, there have been limited studies related to welded joints of AISI 410 stainless steels. This research investigates the microstructure and some mechanical properties of welded joints of AISI 410 stainless steel by Tungsten inert gas welding *(*TIG welding).

2. Material and Methods

In this study, AISI 410 martensitic stainless steels used in this study were initially cut to dimensions of 200x50x4 mm. The chemical composition of AISI 410 martensitic stainless steel and welding wire is given in Table 1.

Table 1 Chemical composition of AISI 410 stainless steel and welding wire (in wt.%)

	AISI 410	AWS 5.9
C	0.20	0.10
Cr	13.4	13.0
Mn	1.0	0.5
Si	1.1	-
S	0.03	0.35
P	0.04	-
Fe	Bal.	Bal.

Table 2 Tensile test results of AISI 410 stainless steel

	Yield strength (MPa)	Tensile strength (MPa)	Elongation (%)
Before welding	286	504	30
After welding	619	801	7.8

TIG welding is a welding method in which the arc is formed between a non-consumable electrode and the workpiece and is protected by an inert gas atmosphere. The filler metal is delivered to the welding area manually or with an automatic system. The main application area is stainless steel, aluminum and nickel alloys. In the present study, the TIG process was performed using an INV DC TIG 200 A welding machine. In addition, AWS/ASME SFA - 5.9 (ER 410) welding wire was used, which is a martensitic stainless steel welding wire that is also used in TIG welding of stainless steels containing up to 13% chromium. Argon gas is used as the shield gas in TIG welding. Tensile processes were carried out at room temperature on welded samples prepared according to the ASTM E8: 2016 standard. The yield, tensile strength and elongation values were determined from these stress–strain curves as displayed in Table 2. On the other hand, the microstructures of the AISI 410 stainless steels joined by TIG welding were determined by optical microcope and SEM.

3. Results and Discussions

The tensile test results of welded AISI 410 stainless steel are given in Table 2. From this table, we see that the yield and tensile strength values of the welded AISI 410 stainless steel have increased significantly compared to their values before welding. However, a strong decrease in elongation value was observed. As a result, it is possible to say that the welded sample turns into a very hard but brittle structure. A similar result is also found in Kumar and Shahi' s study [15]. They obtained that the tensile strength and elongation of AISI 304 stainless steel welded by the TIG method are 657.32 MPa and 24.28 %, respectively. In another study [16], the tensile strength value for TIG welded Cr13Ni5Mo martensitic stainless steel was recorded as 910 MPa. This value is quite high. However, it should not be forgotten that the tensile properties of welded samples will change with the welding parameters. In our study, the obtained results showed that the welding process increases yield and tensile strength. But, while CrC compound formation has a negative effect on the tensile properties of AISI 304 series martensitic stainless steel welded with TIG [17], no difference was observed between the mechanical properties of AISI 316L stainless steel steels before welding and after TIG welding [18].

.

Figure 1 Photograph showing the failure location in AISI 410 stainless steel welded with TIG

Looking at the tensile test results (Fig. 1), it appears that the failure location occurred without any significant cross-sectional narrowing. This result shows us once again that the AISI 410 stainless steel welded with TIG is brittle in this study. From Table 3, we say that carbon (C) content in the weld metal region increases after the welding process. This increase can be explained by the transfer of C from the base material to the weld metal region through heat flow during the welding process. The similar results were observed in the studies of Akhatova et al. [19] and Ata et al. [20]. In addition, since the welding was done in an environment open to the atmosphere, an increase in oxygen (O) was observed in the weld metal region after welding. Besides, it is seen that chromium carbide precipitations cause a decrease in the amount of Cr in the weld metal region (Table 3). Similar thoughts are also mentioned in literature [21].

Table 3 Chemical compositions of weld metal region of AISI 410 stainless steel

Element (weight %)	Before welding	After welding
C	0.6	11.7
Si	1.7	1.06
Mn	1.14	-
P	2.3	-
S	0.3	-
Cr	11.27	7.64
Ni	4.6	-
N	1.3	-
Ti	1.0	-
O	-	13.71
Na	-	0.56
Mg	-	0.39
Al	-	0.43
Cl	-	0.4
K	-	0.68
Ca	-	1.45
Fe	52.48	55.85
Cu	-	0.87
Zn	-	5.27

The dual-phase microstructure of welded AISI 410 martensitic stainless steel consisted of the ferritic extensions in the martensitic matrix (Fig. 2). The phase transformation that occurs heterogeneously in the weld metal region is also partially visible in region heat affected zone (HAZ) (Fig. 3). Meanwhile, it is possible to say that the porosity seen in this structure originates from increasing O content during welding. It is well known that O causes porosity in the weld metal region [22].

4. Conclusions

In this study, the microstructure and tensile properties of AISI 410 martensitic stainless steel welded with the TIG method were determined. The following conclusions have been drawn from this study.

- While the yield and tensile strength values of the welded AISI 410 martensitic stainless steel have increased significantly compared to their values before welding, a strong decrease in elongation value was observed.
- Tensile failure location occurred in the weld metal region without any significant cross-sectional narrowing.
- The dual-phase microstructure of welded AISI 410 martensitic stainless steel consisted of the ferritic extensions in the martensitic matrix.

Author Statements:

- **Ethical approval:** The conducted research is not related to either human or animal use.
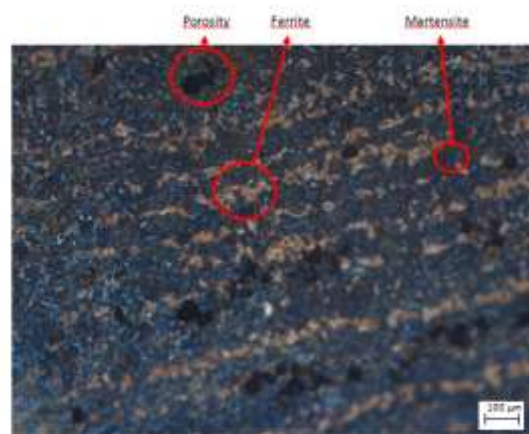

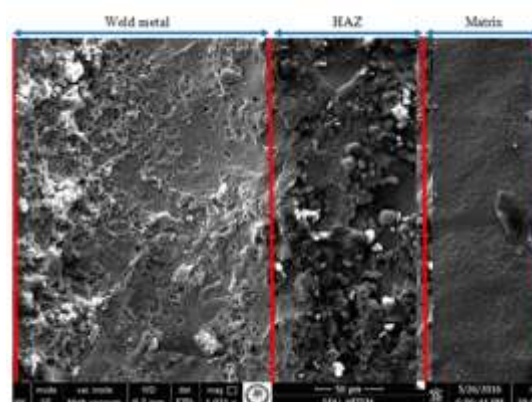*Figure 2 Optical micrograph of weld metal region of AISI 410 martensitic stainless steel*

Figure 3 SEM micrograph of AISI 410 martensitic stainless steel after welded by TIG.

- **Conflict of interest:** The authors declare that they have no known competing financial interests or personal relationships that could have appeared to influence the work reported in this paper
- **Acknowledgement:** The authors declare that they have nobody or no-company to acknowledge.
- **Author contributions:** The authors declare that they have equal right on this paper.
- **Funding information:** The authors declare that there is no funding to be acknowledged.
- **Data availability statement:** The data that support the findings of this study are available on request from the corresponding author. The data are not publicly available due to privacy or ethical restriction.

References

[1] Mahato, J. R. Handbook for Mechanical Maintenance Engineers Paperback, IK International Publishing House, 2019.

[2] Wang, Y., Sebeck, K., Tess, M., Gingrich, E., Feng, Z., Haynes, J. A., Lance, M. J., Muralidharan, G., Marchel, R., Kirste, T. and Pierce, D., (2023). Interfacial microstructure and mechanical properties of rotary inertia friction welded dissimilar 422

martensitic stainless steel to 4140 low alloy steel joints. *Materials Science and Engineering A* 885; 145607.

[3] Digges, T. G. and Rosenberg, S. I. J., Heat Treatment and Properties of Iron and Steel, National Bureau of Standards Library, Washington, 1960.

[4] Loto, C. A., Fayomia, O. S. I. and Loto, R. T., (2015). Electrochemical corrosion resistance and inhibition behaviour of martensitic stainless steel in hydrochloric acid, *Der Pharma Chemica,* 7;102-111.

[5] M. K. Howlader, Cold-forming effect on stainless steel, PhD thesis, Czech Technical University, 2015.

[6] Saravanan, G., Rahul, V., Mahatme, Reddy, G. K., Sharon, T., Suresh, G., Karthikeyan, R. and Subbiah, R., (2023). Assessment of Wear Properties on Treated AISI 410 Martensitic Stainless Steel by Annealing Process, *E3S Web of Conferences,* 391; 01108.

[7] Al-Sayed, S. R., Hussein, A. A., Nofal,A. A., Hassab Elnaby, S. I. and Elgazzar, H., (2017). Characterization of a Laser Surface-Treated Martensitic Stainless Steel, *Materials*, 10; 595.

[8] Köse, C. and Topal, C., (2020). Lazer Kaynağı İle Birleştirilen AISI 410S Ferritik Paslanmaz Çeliğin Mikroyapı ve Mekanik Özelliklerine Gerilme Giderme Isıl İşleminin Etkileri, European Journal of Science and Technology, 20; 922-931.

[9] Muthusamy, C., Karuppiah, L., Paulrajc, S., Kandasamid, D. and Kandhasamy, R., (2016). Effect of Heat Input on Mechanical and Metallurgical Properties of Gas Tungsten Arc Welded Lean Super Martensitic Stainless Steel, *Materials Research*, 19; 572-579.

[10] Kim, S. K., Jung, S. B. and Lee, D. B., (2013). Characteristics of Microstructure, Micro hardness and Oxidation of FSW and MIG Welded Steels, *Chiang Mai Journal of Science,* 40; 831-838.

[11] Tutar, M., Aydin, H. and Bayram, A., (2017). Effect of Weld Current on the Microstructure and Mechanical Properties of a Resistance Spot-Welded TWIP Steel Sheet, *Metals*, 7; 519.

[12] Tolvanen, S., Influence of welding process and alloy composition on microstructure and properties, PhD thesis, Chalmers University of Techonology, Gothenburg, Sweden 2018.

[13] Tsai, M. C., Chiou, C. S., Du, J. S. and Yang, J. R., (2002). Phase transformation in AISI 410 stainless steel, *Materials Science and Engineering A,* 332;1-10.

[14] de Paula, M. A., Ribeiro, M. V., Souza, J. V. C. and Kondo, M. Y., (2019). Analysis of the performance of coated carbide cutting tools in the machining of martensitic stainless steel AISI 410 in dry and mql conditions, *Materials Research Express*, 6, 016512.

[15] Kumar, S. and Shahi, A. S., (2011). Effect of heat input on the microstructure and mechanical properties of gas tungsten arc welded AISI 304 stainless steel joints, *Materials and Design*, 32; 3617–3623.

[16] Lu, S. P., Qin, M. P. and Dong, W. C., (2013). Highly efficient TIG welding of Cr13Ni5Mo martensitic stainless steel, *Journal of Materials Processing Technology*, 213; 229-237.

[17] Bayrak, M. A., Onar, V. and Isıtan, A., (2018). The Investigation of Microstructure and Mechanical Properties of Austenitic Stainless Steel Joints Obtained by Different Welding Methods and Different Welding Parameters, *ETSCI Conference Indexing System*, 3; 324-327.

[18] Molak, R. M., Paradowski, K., Brynk, T., Ciupinski, L., Pakiel, Z. and Kurzydlowski, K. J., (2009). Measurement of mechanical properties in a 316L stainless steel welded joint, *International Journal of Pressure Vessels and Piping*, 86; 43–47.

[19] Akhatova, A., Robaut, F., Verdier, M., Yescas, M., Roch, F., Tassini, C and Van Landeghem, H. P., (2020). Microstructural and mechanical investigation of the near fusion boundary region in thermally aged 18MND5 / Alloy 52 narrow-gap dissimilar metal weld, *Materials Science and Engineering*: A, 788; 139592.

[20] Ata, F., Calik, A and Ucar, N., (2022). Investıgatıon on the mıcrostructure and mechanıcal propertıes of astm a131 steel manufactured by dıfferent weldıng methods, *Advances ın materıals scıence,* 22; 32-40.

[21] Tehçi, T., AISI 316 serisi ostenitik paslanmaz çeliklerde kaynak parametrelerinin nufuziyete ve mekanik özelliklere etkisi, Yüksek Lisans Tezi, Sakarya Üniversitesi, 2011.

[22] Rana, H., Badheka, V., Patel, P., Patel, V., Li, W. and Andersson, J., (2021). Augmentation of weld penetration by flux assisted TIG welding and its distinct variants for oxygen free copper, *Journal of Materials Research and Technology*, 10; 138-151.

Research Article

Theoretical and Experimental Investigation of Gamma Shielding Properties of TiO₂ and PbO Coated Glasses

Arzu COŞKUN[1,2], Betül ÇETİN[3*], İbrahim YİĞİTOĞLU[4], Betül CANIMKURBEY[5]

[1]Vocational School of Health Services, Toros University, 33100, Mersin-Turkey
[2]Amasya University Institue of Science, Amasya University, 05000, Amasya-Turkey
Email:arzu.coskun@toros.edu.tr**- ORCID:** 0000-0003-4771-1558

[3]Amasya University Faculty of Arts and Sciences, Physics Department, Amasya University,05000, Amasya-Turkey
* **Corresponding Author** : **Email:**betulcetin3205@gmail.com**- ORCID:** 0000-0001-9129-2421

[4]Gaziosmanpaşa University Faculty of Arts and Sciences, Physics Department, 60000,Tokat-Turkey
Email:iyigitoglu@yahoo.com **- ORCID:** 0000-0001-9029-0897

[5] Vocational School of Health Services, Amasya University, 05000, Amasya-Turkey
Email:betul.canimkurbey@amasya.edu.tr**- ORCID:** 0000-0003-1900-3722

Abstract:

This manuscript has investigated the effect of TiO2 and PbO-coated glasses on radiation absorption properties to develop alternative materials for radiation shielding. The shielding properties of glass materials coated with oxides were calculated experimentally with a gamma spectrometer with NaI(Tl) detector and theoretically with the XCOM computer program and GATE simulation program. Within this scope, the shielding properties of TiO₂, Pb0, and Pb0 doped TiO₂ glasses at 511, 662, 1274 keV gamma energies were calculated. The results obtained showed that 50% Pb0 contribution can increase the shielding properties of TiO₂ glasses. Also, it has been observed that the experimental and theoretical results obtained are compatible with each other.

1. Introduction

Developing protective materials that are suitable to reduce the effects of increasing radiation dose is important with the development of technology. Placement of a shielding material between the radiation source and the living being is the best way to protect from radiation. Radiation protection materials are used to protect radiation workers and patients from the harmful effects of exposure to ionizing radiation, such as x-rays, gamma rays, and neutrons, which are used in many fields [1]. Due to the importance of shielding in radiation protection, studies on the development of protective materials in the nuclear field have gained momentum [1]. Radiation absorption properties of various materials have been examined by many scientific studies such as granite [2], concrete [3], historical building [4], polymer [5], steel [6], steel and iron slags [7], glasses [8-11] and marble [12].

The use of TiO₂ as a coating element for thin films is advantageous due to its photocatalytic properties, low toxicity, thermal stability, and dielectric properties [9].

In addition to experimental studies, simulation programs are important in shielding studies.

For this reason, the purpose of the development of alternative materials that can be used in radiation shielding, absorption properties of TiO₂, Pb0, and Pb0 doped TiO₂ glasses at 511, 662, 1274 keV gamma energies investigated experimentally and theoretically.

2. Material and Methods

2.1 Experimental Procedure

PbO and TiO₂ solutions were prepared using the lead (II) oxide (powder, <10 μm, Sigma Aldrich), Titanium dioxide (powder, 5 μm, Sigma Aldrich),

poly (methyl methacrylate) (PMMA, ThermoScientific), and Toluene (Merck). 1 mL of toluene was added to 60 mg of PMMA, thoroughly mixed, and kept at 50 °C for 24h to obtain a homogeneous transparent solution. A 0.5 mg sample was weighed and 2 mL of stock PMMA solution was added and mixed at 500 rpm at 50 °C for 2h.

Glass sheets were washed with isopropyl alcohol to remove metals and organic contaminants from the glass surface. Then prepared solutions were coated on a glass sheet by spin coater at 2500 rpm two times.

2.2 Theoretical Procedure

The XCOM and GATE simulations used in the study were made with the same method in the article on the effects of BiO_2 additives on the radiation absorption of PbO [1].

The linear attenuation coefficient is calculated from the Beer-Lambert's Law given by Eq.1:

$$I = I_o e^{-\mu x} \qquad [1]$$

where $\mu(LAC)$ is the linear attenuation coefficient, x is the thickness of the glass samples, I and I_0 are the net count which are the measured with and without the absorber, respectively.

The mass attenuation coefficient of a material characterizes how easily it can be penetrated by a radiation beam and it is given by Eq. 2:

$$\mu_m = \frac{\mu}{\rho} \ (cm^2 /g) \qquad [2]$$

where ρ is the density of the material [8].

The material thickness required to halve incident gamma radiation is referred to as the Half Value Layer (HVL) given by Eq.3 [9]:

$$HVL = \frac{ln2}{\mu} \ (cm) \qquad [3]$$

Mean Free Path (MFP) is the average distance the gamma-ray moves without interacting with the material, and it is given in Eq. 4 [10]:

$$MFP = \frac{1}{\mu} \ (cm) \qquad [4]$$

3. Results and Discussions

In this study, the radiation attenuation properties of glass materials obtained by coating PbO and TiO_2

nanopowders were investigated. First of all, mass absorption values were calculated in the photon energy range of 511, 662, and 1274 keV with GATE and XCOM theoretical programs. The absorption properties of the obtained glass materials were examined in a laboratory environment using a NaI(Tl) detector and point sources. Additionally, using LAC, MFP and HVL values were calculated using the Eq. 1, 3, and 4. Graphs of the theoretical and experimental LAC (μ) values given Fig.1- Fig. 3.
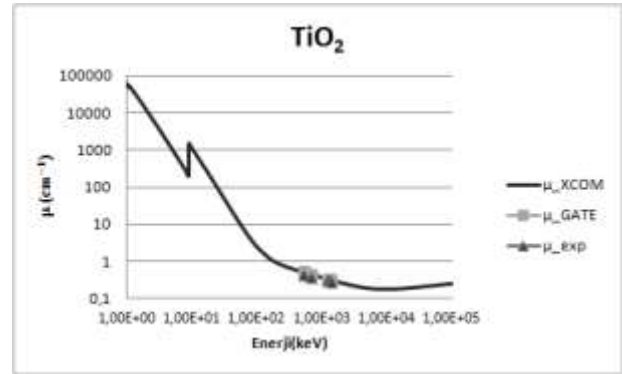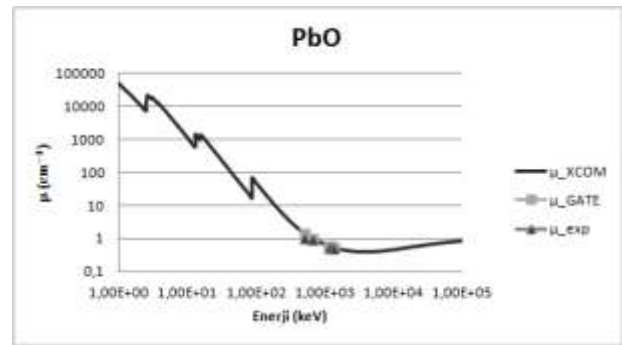

Figure 1. *LAC values of TiO_2*

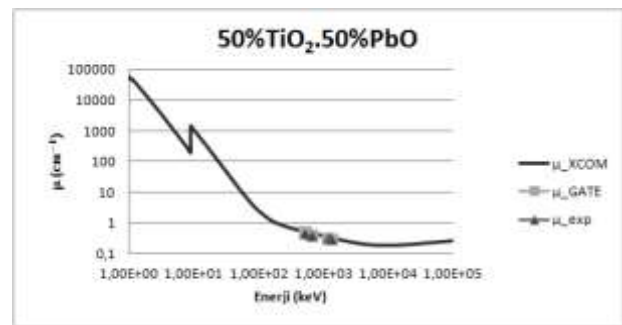***Figure 2***. *LAC values of PbO*

Figure 3.*LAC values of the mixture*

In the study, it was observed that while the absorption coefficient of PbO at 511 keV energy value was 1.44 cm⁻¹, this value decreased to 0.806 cm⁻¹ with the addition of TiO_2. It was observed that as the energy increased, it decreased from 0.55 cm⁻¹ to 0.38 cm⁻¹. The decrease in the linear absorption coefficient at 1274 keV can be considered as the emergence of the Compton effect rather than the material contribution. While the photoelectric effect

is dominant at 511 keV, the Compton effect becomes dominant as the energy increases.

The theoretical and experimental HVL and MFP graphs obtained by substituting the LAC value in Eq. 3 are as follows.
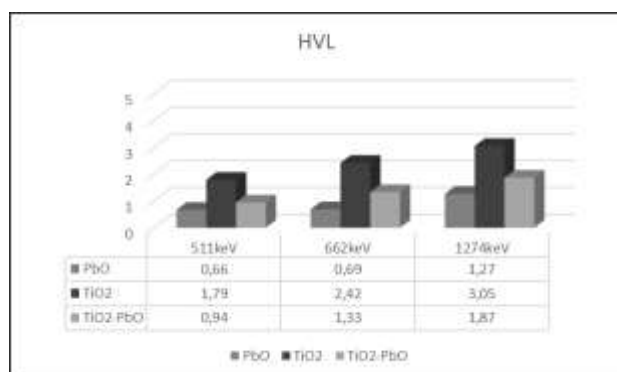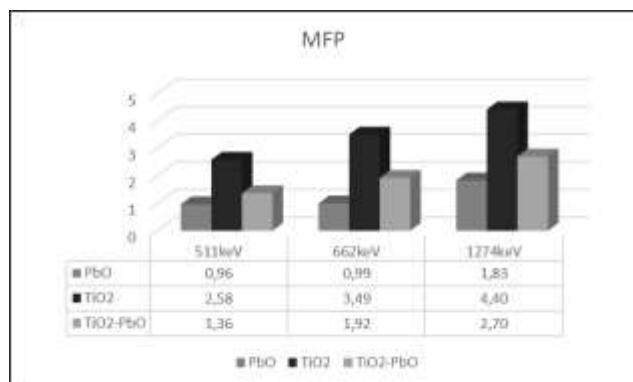

***Figure 4.** Experimental HVL values*

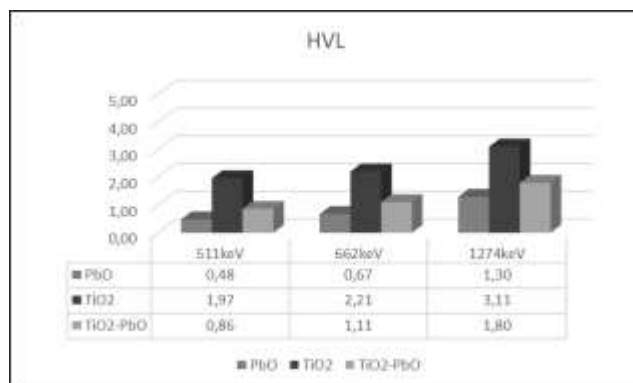
***Figure 5**. Experimental MFP values*
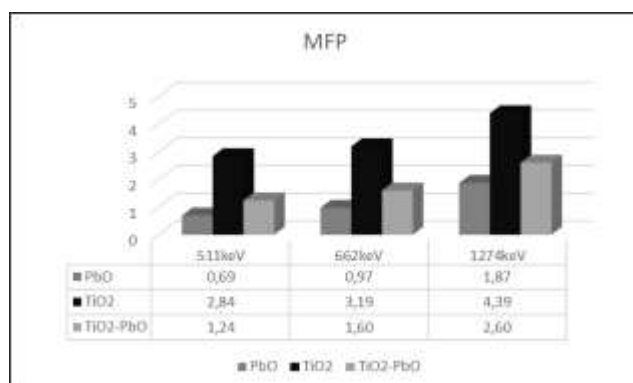

Figure 6.Theoretical HVL values*

***Figure 7.** Theoretical MFP values*

Figure 4 and Figure 5 give experimental HVL and MFP values, and Figure 6 and Figure 7 give theoretical HVL and MFP values. It is seen that the experimental values are compatible with the theoretical values.

4. Conclusions

As a result of the study, experimental and theoretical values were found to be compatible with each other. According to the absorption coefficients obtained, 50% PbO addition to TiO_2 increases the absorption properties of the prepared glass material. At the same time, a decrease in the absorption property was observed as the energy value increased. This situation is compatible with the interaction of gamma radiation with matter.

Author Statements:

- **Ethical approval:** The conducted research is not related to either human or animal use.
- **Conflict of interest:** The authors declare that they have no known competing financial interests or personal relationships that could have appeared to influence the work reported in this paper
- **Acknowledgement:** This work is supported by Amasya University Scientific Research Projects Department (BAP) under Project No. FMB-BAP-18-0315.
- **Author contributions:** The authors declare that they have equal right on this paper.
- **Funding information:** The authors declare that there is no funding to be acknowledged.
- **Data availability statement:** The data that support the findings of this study are available on request from the corresponding author. The data are not publicly available due to privacy or ethical restrictions.
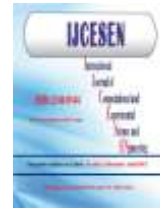
References

[1] A. Coşkun, B. Cetin, (2023). The Effect of Lead Oxide on the Change in Gamma Ray Protection Parameters of Bismuth Oxide. ,*European Journal of Science and Technology*, 47, 18-21.

[2] B. Mavi, (2012). Experimental investigation of γ-ray attenuation coefficients for granites, *Annals of Nuclear Energy*, 44, 22–25.

[3] I. Akkurt, H. Akyildirim, B. Mavi, S. Kilincarslan, C. Basyigit, (2010). Gamma-ray shielding properties of concrete including barite at different energies, *Progress in Nuclear Energy*, 52(7), 620–623.

[4] T. Singh, U. Kaur, P.S. Singh, (2010). Photon energy absorption parameters for some polymers, *Ann. Nucl. Energy*, 37(3), 422–427.

[5] O. Agar, (2018). Investigation on Gamma Radiation Shielding Behaviour of CdO–WO3–TeO2 Glasses from 0.015 to 10 MeV, *Cumhuriyet Sci. J.*, 39-4, 983-990.

[6] H. Singh, K. Singh, L. Gerward, K. Singh, H.S. Sahota, R. Nathuram, (2003). ZnO–PbO–B2O3 glasses as gamma-ray shielding materials, *Nucl. Instrum. Methods*, 207, 257–262.

[7] G. Demircan, E. F. Gurses, B. Aktas, S. Yalcin, A. Acikgoz, G. Ceyhan, M. V. Balak, (2023). Sol–gel synthesis of Si-ZnO, Ti-ZnOand Si-Ti-ZnO thin films: Impact of Si and Ti content on structural and optical properties, *Materials Today Communications*, 34 105234.

[8] K.S. Krane, W.G. Lynch, (1989). Introductory nuclear physics. *Phys. Today.* https://doi.org/ 10.1063/1.2810884.

[9] M.I. Sayyed, (2016). Bismuth modified shielding properties of zincborotellurite glasses. *J. Alloys Compd.* 688, 111–117. https://doi.org/10.1016/ j.jallcom.2016.07.153.

[10] V.P. Singh, N.M. Badiger, J. Kaewkhao, (2014). Radiation shielding competence of silicate and borate heavy metal oxide glasses: comparative study. *J. Non-Cryst. Solids* 404, 167–173. https://doi.org/ 10.1016/ *J.JNONCRYSOL*.2014.08.003.

[11] A. Coşkun, B. Cetin, (2023). The Effect of Lead Oxide on the Change in Gamma Ray Protection Parameters of Bismuth Oxide. *European Journal of Science and Technology Special Issue 47, pp. 18-21.* DOI:10.31590/ejosat. 1234613

[12] Y. Savaş, B. Başaran, B. Cetin, (2023). The Effect of Marble Powder Additive at Different Ratios on the Radiation Absorption Parameters of Barite Based Concretes. *International Journal of Computational and Experimental Science and ENgineering (IJCESEN) 9 (4) 376-38.*DOI:10.22399/ijcesen. 1322248

Research Article

Design and Analysis of the Housing of Ball Screw's Nut with Generative Design Method

Mustafa Rasit TURGUT[1]*, Selim HARTOMACIOGLU[2]

[1]Marmara University, Institute of Science and Technology, Dep. of Mechanical Engineering, Istanbul-Turkey
* **Corresponding Author** : **Email:** ms.rasitturgut@gmail.com - **ORCID:** 0000-0003-1128-7919

[2]Marmara University, 34722, Istanbul-Turkey
Email: : selimh@marmara.edu.tr **- ORCID:** 0000-0002-4541-4894

Abstract:

Product design is highly developed with different CAD software and design tools. It is convenient to generate innovative design models with the development of design tools. One of the creative design tools is generative design, which has become an interesting solution for many industries recently. In this study, it is aimed to generate the optimum design of the housing of a ball screw's nut, which is a part of the z axis of a woodworking cnc router by the Generative Design (GD) tool in terms of strength, weight, manufacturing process, manufacturing cost, and manufacturing duration with the Fused Deposition Modeling (FDM) process on Autodesk Fusion 360 software. The generated model's mechanical properties have been compared to the one produced by a traditional method.

1. Introduction

An AI tool is a software application that uses artificial intelligence algorithms to perform specific tasks, analyze data and solve problems. AI tools can be used in a variety of industries such as finance, education, manufacturing, etc. One of the artificial intelligence tools is generative design (GD), which is one of the upcoming design tools allowing the users set up design goals into the GD tool including parameters such as preserved and obstacle geometries, load and safety requirements, materials, manufacturing methods, cost constraints. The software generate and evaluate tens or hundreds of potential designs according to a set of criteria. Generated models can be manufactured by 2, 2.5, 3 and 5 axes milling process, die casting, additive manufacturing (AM) process or an unrestricted manufacturing process according to the manufacturing method selected. AM is gaining popularity and gradually used in almost every industry. GD solutions are mostly adapted to additive manufacturing method.

GD process was first introduced by Frazer in the 1970s, given that it has been quoted from Krish[1]. In 1989, GD was further studied with the release of

parametric CAD tools [2]. In 1997, Bentley and Wakefield [3] have had contribution for development and optimization of the first generation of GD systems based on genetic algorithms. Then, some representative GD methods like cellular automata, L-systems, and swarm systems were developed [4]. GD has gained superior reputation and has been widely studied and used in various fields [5], since the rapid development and popularization of a new period of intelligent automation technology and optimization algorithms.

Adriano Nicola P. et all [6] obtained around AlSi10Mg of 67 g, which is a front tire housing of a trailer to be manufactured by selective laser sintering (SLS) process, since the starting weight of the studied part was around 148 g, it is reached a noticeable mass reduction of 54% with GD method.

Currently, 3D printing integrated with GD has been tested in the fields, such as the redesign of a seatbelt bracket by General Motors and the design of cabin partitions by the European Aeronautics, and Astronautics Corporation for Airbus [7]. From these works, it can be seen that GD can make full use of the design space provided by 3D printing technology, and 3D printing can ensure the manufacturability of generative results.

Bright et al. [8] performed GD of a helicopter frame and gained a derivative frame model with better fracture and deformation resistance. Wu et al. [9] has done optimization of the roller seat of a wind turbine blade turnover machine by GD process. The generative roller seat ensured strength, stiffness and also reduced the mass to 44.4% of the initial model. From the studies and applications of GD, it can be seen that it can automatically generate a large number of design models in a short period, which is convenient for designers as it allows them to choose the most appropriate model. Moreover, models generated by GD have a good mechanical property and light mass. Accordingly, in this article, it is aimed to generate the optimum design of the housing of a ball screw's nut, which is a part of the z axis of a woodworking cnc router by the GD tool, in terms of strength, weight, manufacturing process, manufacturing cost, and manufacturing duration with the Fused Deposition Modeling (FDM) process on Autodesk Fusion 360 software. The mechanical properties and manufacturing cost of the generated model have been compared to the one manufactured by a traditional method.

2. Material and Methods

In this study, structural optimization of the housing of a ball screw's nut, which is a part of z axis of woodworking cnc router was performed using the GD tool. Autodesk Fusion 360 software has been used as a GD design tool. The system components are given in Figure 1.
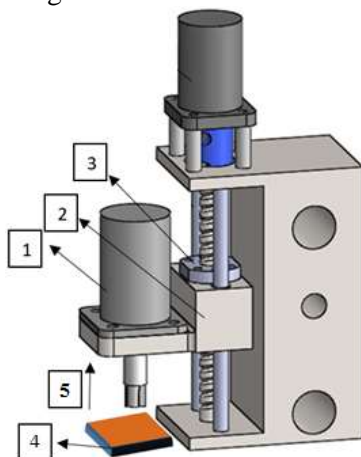

Figure 1*: Components of the system*

Definition of the system components in Figure 1:

1. Motor of the cutting head (Weight of 11 kg)

2. Housing of the ball screw's nut (Weight of 0,541 kg)

3. Ball screw's nut (Weight of 0.5 kg)

4. Workpiece

5. Cutting force of 500 N applied to the workpiece by cutting head (This force is reacted to the housing of the ball screw's nut.)

According to the GD parameters set up, the CAD model, on which GD to be performed is Fusion 360. Its dimensions are given in Figure 2. After designing CAD model of the housing, preserved and obstacle geometries are designed and set on the GD tool (Figure 3). In this study, GD process has been carried out with and without defining starting shape to observe the difference about the generation of GD model and their mechanical properties. Starting shape illustration is given in Figure 4.
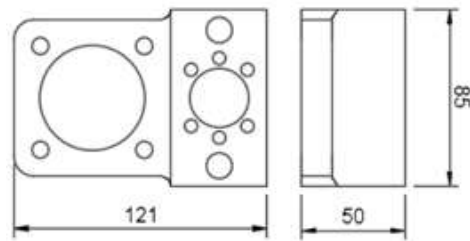

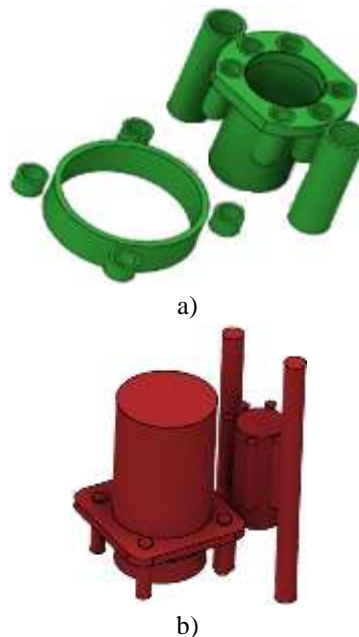***Figure 2****: Dimensions of body of ball screw's nut*

a)

b)

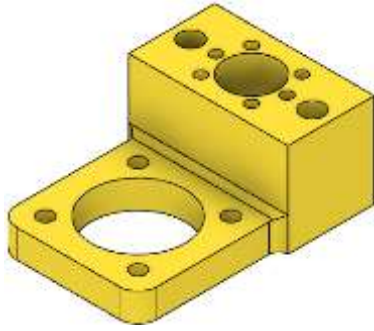***Figure 3****: a) Preserved geometry b) Obstacle Geometry*

Figure 4: Defining the starting shape
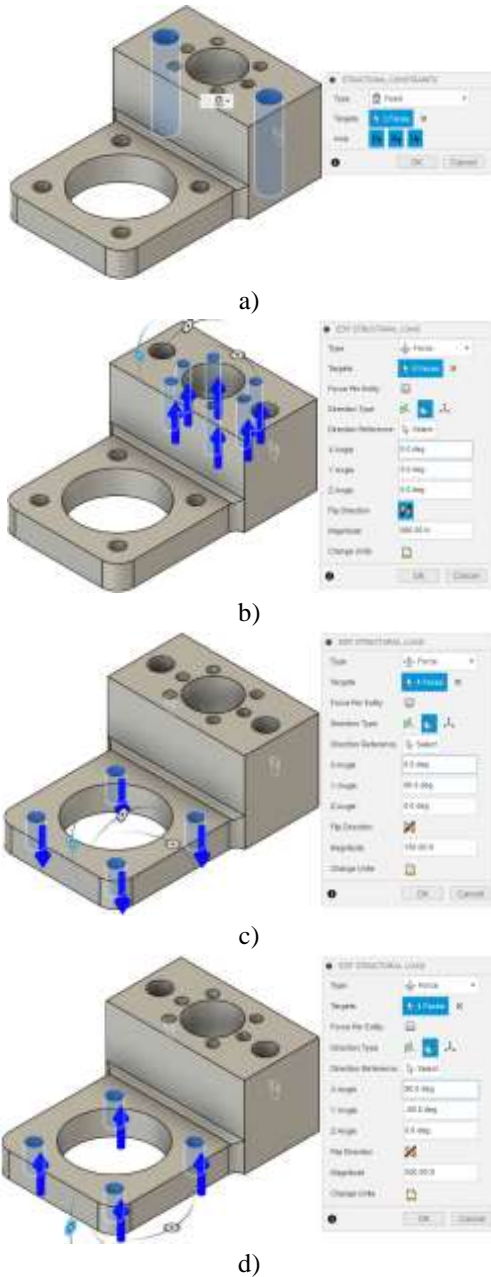

a)

b)

c)

d)

*Figure 5: a) Structural constraint, b) Load applied, c)
Load applied, d) Load applied*

In the objective and limits section, 2 of minimum safety factor (SF), lower mass than the original one and 1 mm of maximum displacement in global shape are set up for target GD model.

Load cases and structural constraints are defined with respect to the working configuration of the housing as shown in Figure 5.

The model has been fixed in Figure 5a, 980 N and 150 N of loads, which are applied to the housing during its movement upward have been set up as structural loads in Figure 5b and Figure 5c respectively. 500 N of load in Figure 5d, which is the cutting force acts to the workpiece during cutting process and reacts to the housing has been set up.

After setting up the load and constraint cases, manufacturing process and material were set up. Manufacturing process considered for the realization of the component is fused deposition modelling (FDM). Therefore, additive manufacturing has been set up as a manufacturing process and unrestricted manufacturing method also has been set up to see the other possible design models.

The housing material selected for FDM process is PA 603-CF. Its mechanical properties is given in Table 1.

Table 1: Mechanical properties of PA 603-CF.

Mechanical Properties	Value
Density	1.1 g/cm^3
Yield Strength	63 MPa
Tensile Strength	75 MPa
Young Modulus	4.7 GPa
Poisson Ratio	0.40

PA 603-CF has 1.1 g/cm^3 of density, 63 MPa of yield strength, 75 MPa of tensile strength, 4.7 GPa of young modulus, 0.4 of possion ratio.

3. Results and Discussions

After all parameters have been set up, GD models have been generated for starting shape and without starting shape definition with manufacturing processes of AM and unrestricted. Totally 4 different design models were generated by the GD tool.

GD design solutions and the mechanical properties of them obtained by the Fusion 360 GD Tool are
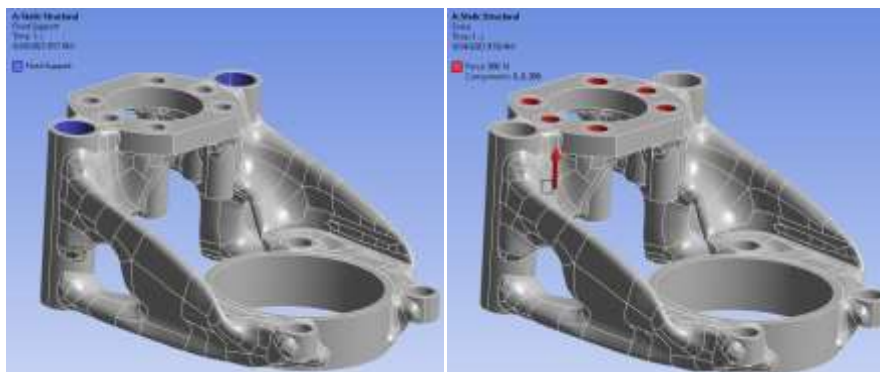
given in Table 2. As it is seen from design models in Table 2, there is not much design difference among starting shape and without starting shape solutions. Solution 3 designed for the additive manufacturing process with starting shape has been selected as the best design solution where its max von-Misses stress is the lowest, minimum safety factor is the highest compared to the other solutions. Its mass and maximum displacement are also satisfying. Mechanical properties of the part designed for solution 3 has been checked on Ansys software performing static analysis. Structural constraints with applied loads are given in Figure 6a. Maximum displacement and maximum von-Misses stress are given in Figure 6b and Figure 6c respectively.

According to the static analysis results on Ansys maximum displacement is 0.459 mm and maximum von-Misses stress is 17.374 MPa. Minimum safety factor is 3.63.

Maximum displacement analysis result given by the Fusion 360 GD Tool is 48% lower than the one given by Ansys. Maximum von-Misses stress analysis result given by the Fusion 360 GD Tool is 16% higher than the one given by Ansys. Minimum safety factor given by the Fusion 360 GD Tool is 15% lower than the one given by Ansys

Table 2: *Mechanical properties of the models generated by the GD tool.*

Mechanical Properties	Without Starting Shape		With Starting Shape	
	Additive Manufacturing	Unrestricted	Additive Manufacturing	Unrestricted
	Solution 1	Solution 2	Solution 3	Solution 4
Max von-Misses Stress	22.222 MPa	20.591 MPa	20.192 MPa	21.109 MPa
Min Factor of Safety Limit	2.835	3.060	3.120	2.984
Max Displacement	0.277 mm	0.226 mm	0.238 mm	0.233 mm
Mass	92 g	80 g	96 g	78 g

,   .

a)

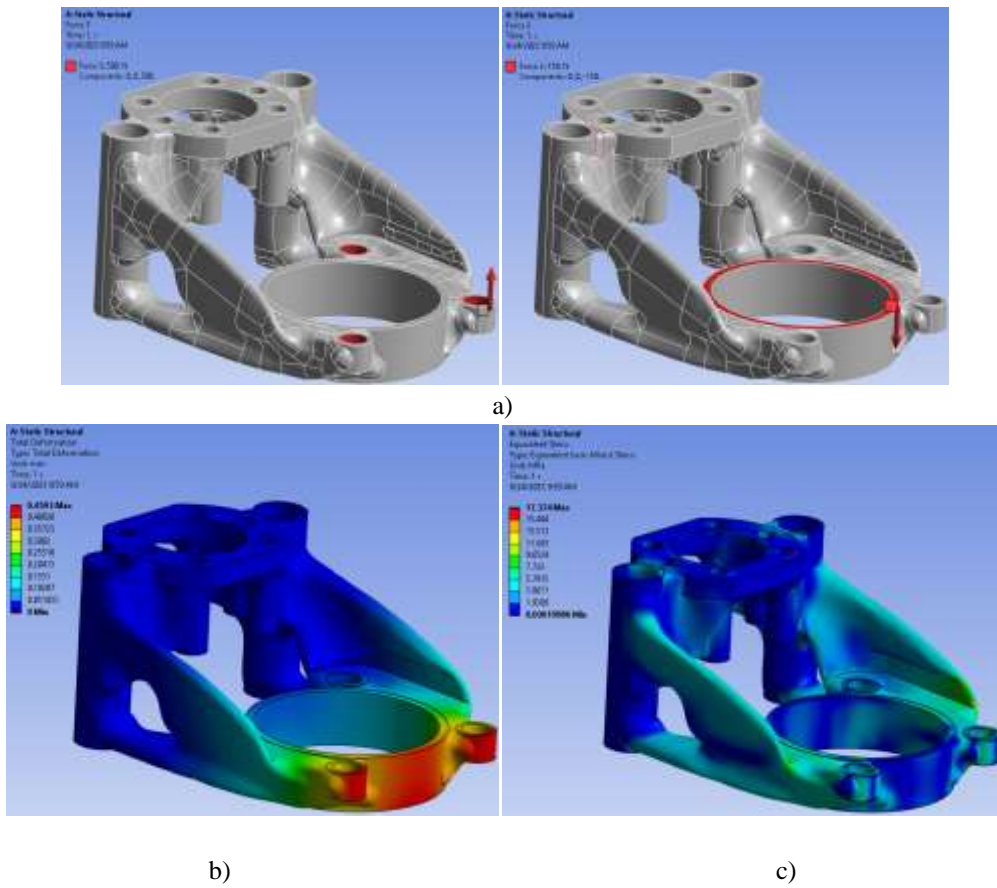b)   c)

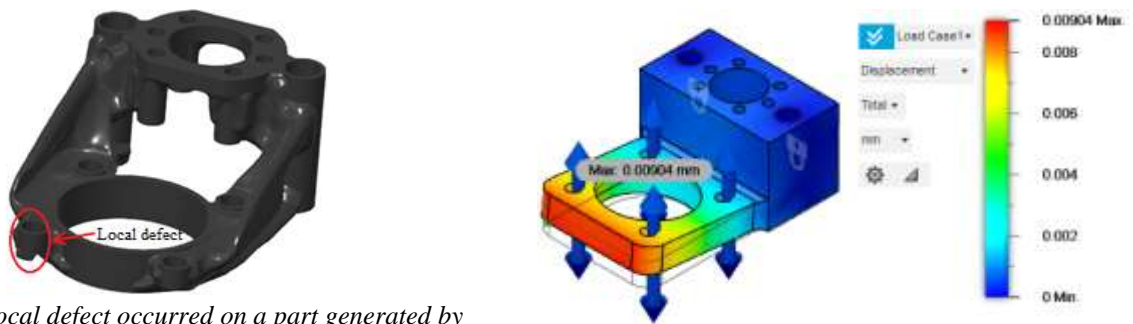***Figure 6****: a) Structural constraints b) Max displacement c) Max von Misses Stress analysis*

Figure 7: *Local defect occurred on a part generated by the GD tool.*

In solution 1, local design defect occurred on the model, which can be edited manually. It is shown in Figure 7.

Structural analysis of the housing was performed to be able to compare the GD model analysis results with the one of the housing model without optimization. Analysis results are illustrated in Figure 8. The material used as a housing without optimization is 3003-H16. Its mechanical properties are given in Table 3.

a)

b)
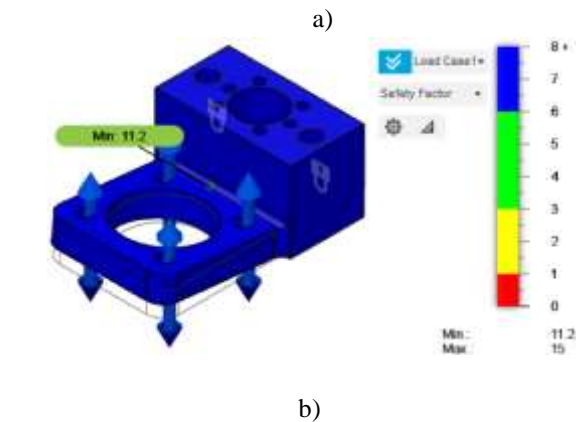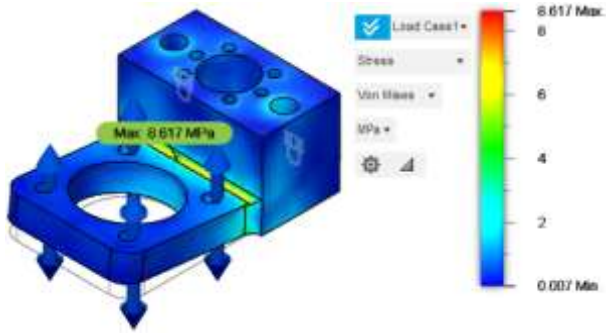
c)
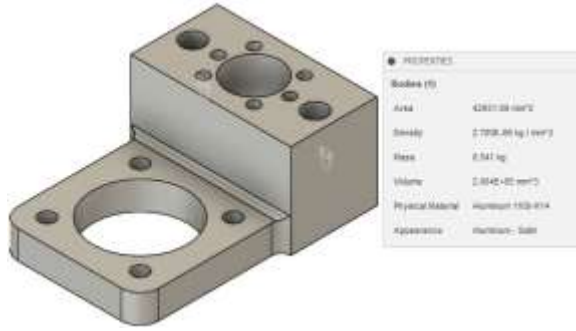
d)

***Figure 8:** a) Max displacement b) Minimum safety factor c) Max von-Misses Stress analysis results and d) 3003-H16 Material properties.*

***Table 3:** Mechanical properties of 3003-H16.*

Mechanical Properties	Value
Density	2.7 g/cm^3
Yield Strength	96.53 MPa
Tensile Strength	110.3 MPa
Young Modulus	69.64 GPa
Poisson Ratio	0.33

Additive manufacturing simulation has been created on the Fusion 360 software so that the design obtained with the GD tool for the solution 3 can be printed on a 3D printer. According to the simulation output, the printing time (6 hours, 4 minutes, 18 seconds), the amount of filament used (16.7 m), the number of printing layers (333), time and material consumption rates are given in print statistics in Figure 9a with FDM simulation model in Figure 9b. Analysis results and manufacturing cost of the housing of ball screw's nut designed by the GD tool is compared to the one without optimization given in Table 4. The housing with 3003-H16 material produced by cnc milling process has 8.6 MPa of maximum stress, 11.2 of minimum safety factor, 0.00904 mm of maximum displacement, weight of 541 g, 5 hours 40 minutes of manufacturing duration.

a)
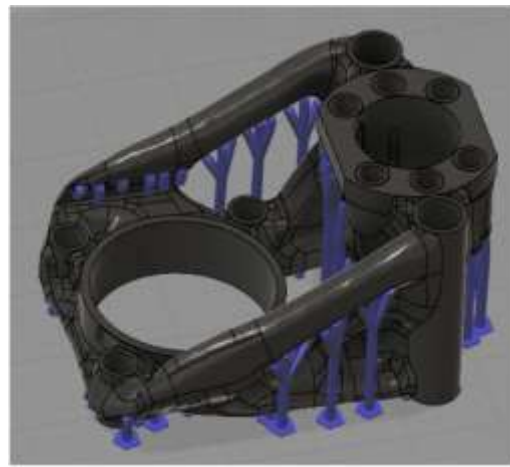
b)

*F**igure 9:** a) FDM simulation statistics, **b)** FDM simulation model.*

Manufacturing quotation for the housing was asked to three companies by sending 3D CAD file. The approximate manufacturing cost is 86 €. The housing with PA 603- CF material designed by the GD tool and to be manufactured by FDM process has 20.2 MPa, 3.12 of minimum safety factor, 0.238 mm of maximum displacement, weight of 96 g, 6 hours 4 minutes of manufacturing duration. Manufacturing quotation for the housing was asked to three companies by sending 3D CAD file. The approximate manufacturing cost is 13.50 €.

4. Conclusions

According to results, maximum displacement analysis result given by the Fusion 360 GD Tool is 48% lower than the one given by Ansys. Maximum von-Misses stress analysis result given by the Fusion 360 GD Tool is 16% higher than the one given by Ansys.

Table 4: *Comparison of cnc milling of 3003-H16 material with FDM process of PA603-CF material designed by GD.*

Material	3003-H16	PA 603-CF
Manufacturing Method	Cnc Milling	FDM
Maximum Stress (von-Misses)	8.6 MPa	20.2 MPa
Minimum Safety Factor	11.2	3.12
Maximum Displacement	0.00904 mm	0.238 mm
Weight	541 g	96 g
Manufacturing Duration	5 hours, 40 min	6 hours, 4 min
Manufacturing Cost	86 €	13.50 €

Minimum safety factor given by the Fusion 360 GD Tool is 15% lower than the one given by Ansys. Although there are differences in static analysis results in between the Fusion 360 GD Tool and Ansys, mechanical properties of PA 603-CF material designed with the GD tool is

satisfactory compared to that of 3003-H16 material designed without optimization.

PA 603-CF material weight is 82.3% less than 3003-H16 material weight. Manufacturing time is close to each other in both manufacturing methods. PA 603-CF material manufacturing cost with 3D printer is 84.3% less than the manufacturing cost of 3003-H16 material with cnc milling.

Lighter design with the GD tool and ease of 3D printing of complex shapes are of great importance in reducing costs. Models generated by the GD tool is easy to manufacture and aesthetically pleasing.

Author Statements:

- **Ethical approval:** The conducted research is not related to either human or animal use.
- **Conflict of interest:** The authors declare that they have no known competing financial interests or personal relationships that could have appeared to influence the work reported in this paper

References

[1] Krish, S. A. (2011). Practical generative design method. *Computer Aided Design, 43*, 88–100.

[2] Zhang, J., & Liu, N., & Wang, S. (2021). Generative Design and Performance Optimization of Residential Buildings based on Parametric Algorithm. *Energy Buildings, 244*, 111033.

[3] Bentley, P.J., & Wakefield, J.P. (1997). Conceptual Evolutionary Design by a Genetic Algorithm. *Engineering Design and Automation, 3*, 119–132.

[4] Jang, S., & Yoo, S., & Kang, N. (2022). Generative Design by Reinforcement Learning: Enhancing the Diversity of Topology Optimization Designs. *Computer Aided Design, 146*, 103225.

[5] Wang, H.Y., & Teng, R.M., & Yang, J., & Ren, L.Y. (2021). Lightweight analysis of truck crane turntable based on generative design. *J. Dalian Univversity Technology, 61*, 46–51.

[6] Pilagatti, A.N., & Vecchi G., & Atzeni E., & Iuliano L., & Salmi A. (2022). Generative Design and new designers' role in the manufacturing industry. *Procedia CIRP, 112*, 364-369 https://doi.org/10.1016/j.procir.2022.09.010.

[7] Wang, Y.Q., & Du, W.F., & Wang, H., & Zhao, Y.N. (2021). Intelligent Generation Method of Innovative Structures Based on Topology Optimization and Deep Learning. *Materials, 14*, 7680.

[8] Bright, J., & Suryaprakash, R., & Akash, S., & Giridharan, A. (2020). Optimization of quadcopter frame using generative design and comparison with DJI F450 drone frame. IOP Conference Series: *Materials Science and Engineering, 1012,* 012019.

[9] Wu, J., & Li, M., & Chen, Z., & Chen, W., & Xi, Y. (2020). Generative Design of the Roller Seat of the Wind Turbine Blade Turnover Machine Based on Cloud Computing. *In Proceedings of the 2020 11th International Conference on Mechanical and Aerospace Engineering ICMAE, Greece, Athens,* 14–17 July, pp. 212–217.

Research Article
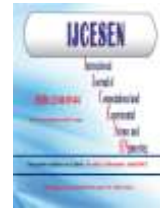
Transmission Rate of Fabric to Test Radiation Shielding Properties

Serpil EMİKÖNEL[1]*, Iskender AKKURT[2]

[1]Usak University, Vocational School of Health Services, Department of Medical Services and Techniques, Usak-Turkey
* **Corresponding Author Email:** serpil.emikonel@usak.edu.tr - **ORCID:** 0000-0002-4645-2454

[2]Suleyman Demirel University, Science and Arts Faculty, Physics Department, 32200, Isparta-Turkey
Email: iskenderakkurt@sdu.edu.tr - **ORCID:** 0000-0002-5247-7850

Abstract:

In parallel with the developments in technology, the use of radiation in many areas such as medicine, industry, agriculture and obtaining electrical energy through nuclear power plants has not only facilitated social life but also brought about many health problems due to exposure. It has become inevitable to be protected from the harmful effects of radiation because it poses a risk to human health. There are three basic rules in radiation protection: time, distance and shielding. The most effective method is armoring. Protective clothing is especially important for those working in radiation areas. In this study, thericoton fabric, which is widely used in daily life, was coated with different amounts of barite (0%, 40%, 50%, 60%) and its radiation absorption properties were examined. For this purpose, the transmission rate, which is an important parameter in terms of shielding properties, was investigated by using 511, 835 and 1275 keV gamma energies emitted from ^{22}Na and ^{54}Mn radioactive sources.

1. Introduction

Radiation has become a factor that significantly affects human health in daily life with the increase in its usage areas both from natural sources and with technological developments. The importance of protection from radiation increases because it poses a risk to human health in industry, agriculture, obtaining electrical energy through nuclear power plants, and especially in units such as radiology, where radiation is widely used in medical applications. Therefore, the three basic rules for protection from the harmful effects of radiation are time, distance and shielding. Shielding, the most effective method, is based on placing material between the radiation source and the system to be protected. Lead and heavy concrete are generally used to protect against radiation [1-3]. For this purpose, some of the studies on radiation protection are on ultraviolet (UV) protection of fabrics, while some are on fabrics produced for protection from electromagnetic radiation [4-7]. Protective clothing should be used especially by people working in

radiation areas [8-9]. In this respect, since lead, which is commonly used as radiation shielding material, is harmful to human health, it is very important to investigate the availability of new alternative materials that can absorb radiation. In this study carried out for this purpose, the use of barite mineral as shielding material against radiation was investigated by penetrating the fabric with different rates by coating method.

2. Material and Methods

The reason why tericoton fabric was preferred in this study is that it is widely used especially as aprons and shirts [10]. Barite was used as the coating material. In the study, the feature desired to be given to the fabric is the ability to absorb gamma rays by penetrating the barite mineral into the fabric [11]. For this purpose, the effect of barite addition at different rates by coating method, which is the most suitable method, on gamma ray retention was investigated. Measurements were carried out using the gamma spectroscopy system containing the

"3x3" sized NaI(Tl) detector located in the Suleyman Demirel University Gamma Spectroscopy Laboratory (Figure 1).
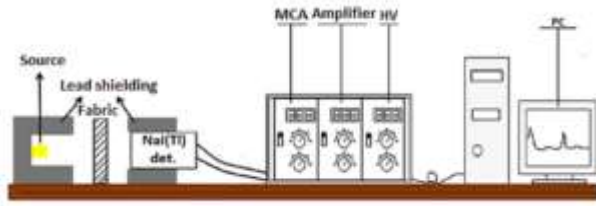

Figure 1. *Schematic view of the gamma spectroscopy system (Akkurt et al., 2015)*

Radiation measurements were made with [22]Na (511 and 1275 keV) and [54]Mn (835 keV) radioactive sources. An important parameter used in testing the radiation shielding property of a material is the transmission rate [12-13]. Transmission rate may also be used to for shielding properties and it is defined as equation 1.

$$Transmission = Ln\left(\frac{N}{No}\right) x \frac{1}{\mu_o} \qquad (1)$$

In the study, the transmission rate of fabric samples obtained by adding 0%, 40%, 50%, 60% barite to tericoton fabric was investigated at 511, 835 and 1275 keV gamma energies, depending on the change in barite ratio and energy.

3. Results and Discussions

As the transmission rate is the min length to stop gamma rays for specified rate, it is important to know. This is obtained and displayed in Figure 2, Figure 3, Figure 4 for 511,835 and 1275 keV gamma rays. It can be seen in this figure that small thickness of fabric is required for TCF60, TCF50, TCF40, TCF0 type fabric respectively for all energies. This is also another indication of the importance of barite coating on fabric to improve radiation shielding properties. According to Figure 1, Figure 2 and Figure 3, it is seen that the gamma rays can be stopped at shorter distances with the increase in the transmission rate with the increase in the barite ratio in the barite fabrics coded as TCF0, TCF40, TCF50, TCF60 obtained by using 0%, 40%, 50%, 60% barite.

4. Conclusions

In this study, in which the effect of barite mineral used on gamma ray trapping was investigated, it was
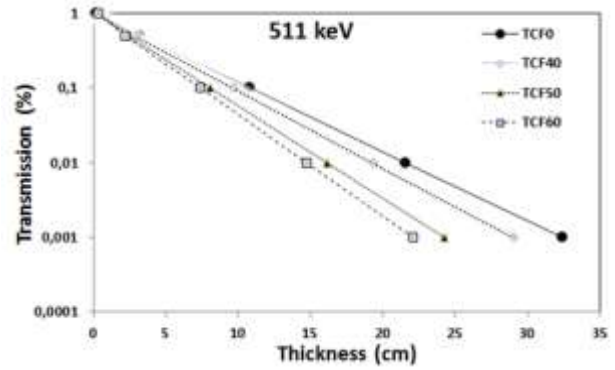
Figure 2. *The transmission rate as a function of thickness for all types of fabric for 511 keV.*
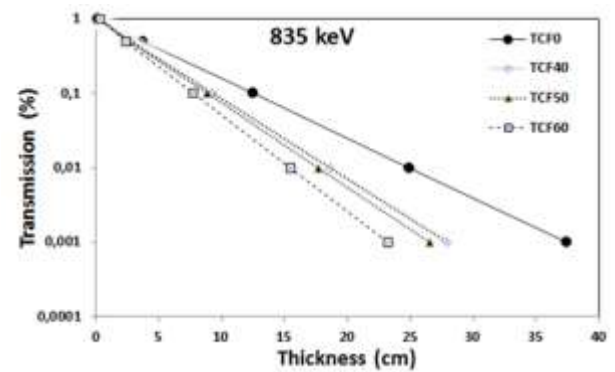
Figure 3. *The transmission rate as a function of thickness for all types of fabric for 835 keV.*

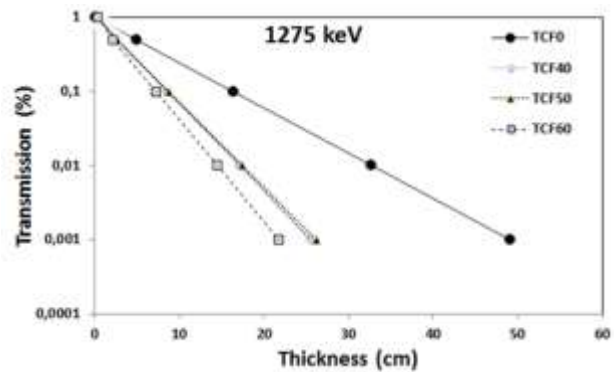**Figure 4.** *The transmission rate as a function of thickness for all types of fabric for 1275 keV.*

seen that the gamma ray absorption feature of the fabric coated with different ratios of barite increased, in other words, gamma rays could be stopped at shorter distances depending on the increase in barite ratio. Therefore, fabrics containing barite provide an important area of use as radiation shielding material.
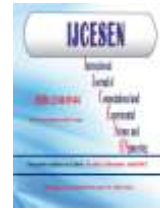
Author Statements:

References

[1] I. Akkurt vd (2004). The photon attenuation coefficients of barite, marble and limra. *Annals of Nuclear Energy* 31,577-582.

[2] I. Akkurt vd (2006). Radiation shielding of concretes containing different aggregates. *Cement and Concrete Composites*, 28(2),153-157.

[3] Çalık, A., Akkurt, İ., & Akyıldırım, H. (2009). Determınatıon Usıng as Radıatıon Armor of Boron Materıal" 5. Uluslararası İleri Teknolojiler Sempozyumu (IATS'09), 13-15 Mayıs 2009, Karabük, Türkiye.

[4] Akaydin, M., İkiz, Y., & Kurban, N. S. (2009). Measurement and evaluation of permeability of UV rays in cotton knitted fabrics. *Textile and Apparel*, 19(3), 212-217.

[5] Saravanan, D. (2007). UV protection textile materials. *AUTEX Research Journal*, 7(1), 53-62.

[6] Kilincarslan, S., Akkurt, I., Uncu, I., & Akarslan, F. (2016). Determination of radiation shielding properties of cotton polyester blend fabric coated with different barite rate. *Acta Physica Polonica A*, 129(4), 878-879.

[7] Akarslan, F., Molla, T., Akkurt, I., Kilinçarslan, Ş., & Üncü, I. (2014). Radiation protection by the barite coated fabrics via image processing methodology. *Acta Physica Polonica A*, 125(2), 316-318.

[8] I. Akkurt, F. Akarslan, K. Günoğlu, Ş. Kılınçarslan, I. Serkan Uncü, H. Demiralay, (2013). Bazı kumaş türlerinin nötron zırhlama özelliklerinin incelenmesi. *Süleyman Demirel Üniversitesi Fen Bilimleri Enstitüsü Dergis*i, 17(3),63-65

[9] Akkurt, İ., Emikönel, S., Günoğlu, K., Akarslan, F., Kılınçarslan, Ş., & Üncü, İ. S. (2015). Radiation shielding properties of barite coated tericoton fabric at 662 keV. *Avrupa Bilim ve Teknoloji Dergisi*, 3(6), 1-2.

[10] Emikönel, S. (2015). "Barit Kaplanmış Bazı Kumaş Türlerinin Radyasyon Soğurma Özelliklerinin Araştırılması". *Süleyman Demirel Üniversitesi*, *Fen Bilimleri Enstitüsü, Fizik Anabilim Dalı, Yüksek Lisans Tezi*, 71.

[11] İskender Akkurt, Serpil Emikönel, Feyza Akarslan, Kadir Günoğlu, Şemsettin Kilinçarslan, İ. Serkan Üncü. (2015). Barite Effect on Radiation Shielding Properties of Cotton-Polyester Fabric. *Acta Physıca Polonıca A*, 128,B-53.

[12] Akkurt, İ., Günoğlu, K., Başyiğit, C., & Akkaş, A. (2014). Hafif Betonların 511 ve 1275 Kev'deki Radyasyon Zayıflatma Katsayılarının Araştırılması. *Süleyman Demirel Üniversitesi Fen Bilimleri Enstitüsü Dergisi*, 16(3).

[13] Akkurt, I., Gunoglu, K., Kurtuluş, R., & Kavas, T. (2021). X- ray shielding parameters of lanthanum oxide added waste soda- lime glass. *X- Ray Spectrometry*, 50(3), 168-179.

Investigation of the mechanical behavior of recycled polypropylene-based composite materials filled with waste cotton and pine sawdust

İlyas KARTAL[1]*, Hilal SELİMOĞLU[2]

[1]Marmara University, Faculty of Technology, Metallurgical and Materials Engineering Dep., 34722, İstanbul-Turkey
* **Corresponding Author** : **Email:** ilyaskartal@marmara.edu.tr - **ORCID:** 0000-0001-9677-477X

[2]Marmara University, Institute of Pure and Applied Sciences, Polymer Science and Technology Dep., İstanbul-Turkey
Email: selimoglu.hillal@gmail.com - **ORCID:** 0000-0002-5344-7100

Abstract:

Composite materials are produced synthetically with a matrix material and a filler or reinforcement to provide the desired properties. In composites, synthetic fillers are often preferred. Natural fibers and fillers, on the other hand, are now preferred over synthetic fillers. These materials can be found in polymer matrices as reinforcement and fillers. Composite materials made from natural materials are replacing traditional materials in the industry for many reasons, including easy processing, lightness, and low cost.

In this study, the usability of pine wood sawdust and cotton together in polymer matrix composites was investigated. Pine sawdust is a product that emerges as waste, especially in the furniture industry. On the other hand, cotton has a wide area of use in the textile industry and is also obtained as a waste product. Recycled Polypropylene is used as a matrix material due to its intense use in industry. Pine sawdust was prepared using a sieve in the size of 0-250 microns. Since the waste cotton is in different sizes, it was cut to be 1 cm to have certain sizes. Composite materials were produced by adding pine sawdust and textile waste to recycled Polypropylene at different ratios. Composite samples were prepared by injection molding method. The physical properties of the samples such as tensile, impact, hardness and water absorption properties were investigated. SEM images of the fracture surfaces were analyzed. As a result of the study, it was evaluated that pine sawdust and waste cotton would be used in polypropylene-based composite applications.

1. Introduction

Composite materials are developed to meet the needs of the industry by changing the type, morphology, or amount of their components and improving their properties. It is quite common to use reinforcement and/or filler materials to modify the properties of composite materials [1-3]. Composite materials offer flexibility to both the manufacturer and the consumer by providing the desired properties in different environmental conditions. Since the composites are designed according to needs, they are used in each sector of the industry [2].

The use of polymer-based composites is rather common among composite types. Polymer matrix composite materials are at least two-phase materials consisting of polymer, which is the continuous phase, and filler or fiber, which is the dispersed phase. The continuous phase is responsible for filling the volume and carrying the charges to the dispersed phase. The dispersed phase improves one or more properties of the composite. Polymer matrix composites are widely used as special engineering materials in aerospace, civil engineering structures, and automotive applications due to their remarkable mechanical properties [3].

In general terms, the concept of reinforcement in composites is used to describe all additives that provide the highest tensile strength. Fillers, on the other hand, improve other properties while reducing these properties. In thermoplastic materials, fillers increase the density and hardness, decrease the thermal expansion, increase the thermal conductivity, and thus improve the balance in the final part, while reducing the cost. The form of the particle, the average particle diameter, and the particle size distribution all influence how the added filler changes a property in the plastic. [4-7].

Thermoplastic materials with widespread use in the industry are Polyethylene (PE), Polypropylene (PP),

Polyvinylchloride (PVC), and polyethylene terephthalate (PET) polymers. Cost and physical properties explain the widespread use of these polymers. Engineering plastics have been replaced by most metals in industrial products due to their properties such as high strength, heat resistance, and impact strength [3,8-10].

Polypropylene, which is used extensively in thermoplastic-based composites, is one of the plastics with a high production volume and a wide range of uses such as refrigerators, washing machines, and air conditioners. It has a very good balance between its physical and mechanical properties. Polypropylene-based products are economical compared to other polymer materials and can be easily recycled. Because it does not react with most materials, it is extensively used in the packaging industry. Polypropylene is used in automobile engineering instead of traditional materials because it is lightweight, has a high impact strength, and is resistant to relatively high temperatures [11,12].

Fillers are commonly used in composites. Environmental awareness, ecological concerns, and new regulations have caused organic fillers to replace inorganic fillers in polymer composites [13]. Renewability, low cost, non-toxicity, low density, and low abrasiveness during processing are the main reasons for the development of natural fillers in polymer composites [14].

The use of natural fibers or fillers in composites is also common, and some natural fibers used are cotton, banana, coconut, jute, kenaf, flax, bamboo, sisal, nutshell, rice, and wheat straw [15-18]. Polyolefin group polymers are often used in the production of composites with natural fibers. This requires the processing temperature to be below 200ºC. The degradation of the fibers was observed above this temperature [19-21]. In recent years, many studies have been conducted on the use of natural fillers and fibers [22-30]. The use of recycled plastic in such composites is also common. Thus, it offers a solution for some of the disposal problems in the waste of petroleum-based plastics [31-33].

In this study, waste cotton and pine wood sawdust were used as fillers. Millions of tons of waste are produced annually in the world, both in textile production and furniture production. The vast majority of these wastes go to waste collection areas. Although the textile industry has made efforts to reduce the amount of waste in recent years, only a small part of textile waste is recycled today. In 2050, the textile industry is expected to account for 26% of the world's carbon budget [34]. Synthetic fibers do not decompose in nature and are therefore harmful to living organisms. Moreover, the production and consumption of textiles have doubled in recent

years, and the presence of potential waste and groundwater pollution is also being considered [34-35]. These problems have become a necessity to introduce regulations to reduce waste and environmental impact in the textile industry [36-38]. For this reason, every step towards reducing the increasing textile industry waste is significant. It is imperative to improve the efficient use of all kinds of waste to create a sustainable ecosystem. A large percentage of textile waste consists of cotton and its blends with other synthetic fibers. [37]

In this study, the co-usability of pine wood sawdust and waste cotton in polymer matrix composites was investigated. Recycled Polypropylene material, which is used extensively in the industry, was used as the matrix material. It is expected that the use of the two wastes together will create synergy in the mechanical properties of recycled Polypropylene.

2. Materials and Method

2.1 Materials

Recycled Polypropylene was preferred as a composite matrix material due to its intense use in the industry and was obtained from local companies. Textile waste cotton and pine wood sawdust were used in the furniture sector as filler material. Filler materials were also obtained from local companies as waste. Since the waste cotton is in different sizes, it was cut to be 1 cm as seen in Figure 1 to have certain dimensions. Pine sawdust was prepared by using a 250-micron sieve.

Figure 1. *Image of waste cotton*

2.2 Sample preparation

Pots are produced from recycled Polypropylene used in this study. Pots were also produced from the

prepared mixture. The mixture contents are given in Table 1. Waste cotton and pine sawdust were added to Recycled Polypropylene in different weight ratios as seen in the table.

Table 1. Contents of samples (by weight, %)

Samples	Pine Sawdust	Waste Cotton	Recycled Polypropylene
rPP	0	0	100
5PS15C	5	15	80
10PS10C	10	10	80
15PS5C	15	5	80
20PS	20	0	80
20C	0	20	80

Abbreviations: rPP, recycled polypropylene; PS, pine sawdust; C, cotton

It is preferred to use a maximum of 20% filler addition to recycled Polypropylene by weight. Composite samples were homogenized using Haisi brand twin screw extrusion line. Tederic DT-200 branded injection machine was used to produce the samples.

Table 2. Injection conditions in composite production

Process	Injection Conditions
Temperature (ºC)	190-220
Pressure (bar)	100-110
Mold waiting time (s)	12

2.3 Tests and Analysis

For the tensile test of the composites, the sample was cut from the pots. The tensile test was performed on the Zwick brand Z010 universal type tensile tester at a tensile speed of 5 mm per minute. The hardness test was performed with a Zwick Shore D device, waiting for 10 seconds. The impact test was carried out on the Zwick B5113.30 brand test device with a 5.4 J hammer. For SEM analysis, samples were prepared from the fractured surfaces of the impact strength samples. For SEM analysis, the samples were coated with a 10 Å thick gold/palladium alloy. SEM test was performed with Polaron SC branded device. The samples were kept in water for 50 days to determine the water uptake ratio.

3. Results and Discussions

The strength value in filled polymer matrix composites varies depending on the active load transition between the matrix structure and the filler. Factors such as the filler ratio and size, and the bonding strength of the matrix layer between the filler also affect the strength.
The tensile strength and % strain values of the samples are given in table 3. The tensile strength of

the recycled Polypropylene sample without filler was determined as 21.30 MPa. According to the tensile test, it was observed that the highest tensile strength was in the sample coded 10PS10C (Figure 2). A slight increase in tensile strength was obtained compared to pure recycled Polypropylene. The tensile strength of the samples with a pine sawdust ratio of 20% was the lowest. The tensile strength of the samples decreased as expected after the sawdust ratio of 10%. Since cotton is based on cellulose, it has slightly reduced the tensile strength of pure recycled polypropylene.
The weak interfacial bond between the polymer matrix and the filler content reduces the tensile strength of the composite. It has been stated in different studies that the tendency to agglomerate with the increase of the filler amount or the insufficient hydrogen bond between the sawdust particles and the matrix causes a decrease in the tensile strength [39,40].

Table 3. Tensile strength properties depending on the filler ratios in the samples

Samples	Tensile Strength (MPa)	Max Strain (%)
rPP	21,30	7,40
5PS15C	20,71	6,26
10PS10C	21,40	5,30
15PS5C	18,15	4,54
20PS	17,11	4,18
20C	19,20	4,13
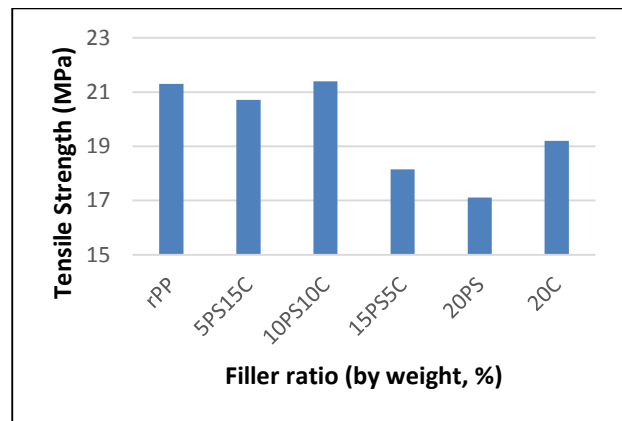
Figure 2. Tensile strength properties of composites materials

The values of Izod impact strength according to filler ratios is given in Figure 3. As a result of the impact test, it was observed that the impact strength of pure recycled Polypropylene was 23.15 kJ/m². As expected, the impact strength of recycled Polypropylene was the highest. The highest value in filler-added composite samples was measured as 19 kJ/m² with the sample coded 10PS10C. The lowest

impact strength was observed in the 20PS sample with a value of 8.85 kJ/m². The negative effects of natural fillers and fibers added to the polymer matrix on the impact strength of the composites are also seen in other studies in the literature [41].
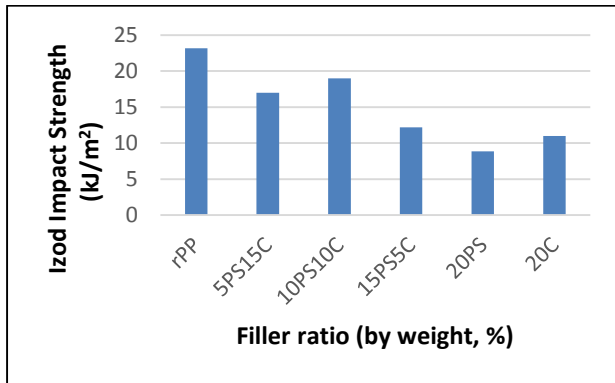

Figure 3. Izod impact strength properties composite samples

In Figure 4, the variation of the hardness values according to the filler ratios is given. The hardness of pure recycled Polypropylene was determined as 60 Shore D. The highest value was measured as 66 Shore D with the sample coded 10PS10C and showed an increase of around 10%. A decrease in the hardness value was observed in the subsequent filler ratios. With these results, it was determined that the hardness values of the natural filled composites added to the polymer matrix were compatible with the studies in the literature. [26,41].
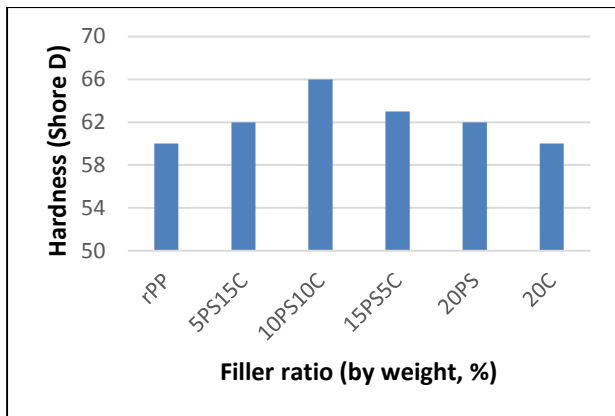

Figure 4. Hardness properties of composites materials

In Figure 5, the 50-day water absorption test results of the samples are given. At the end of 50 days, the highest water uptake was observed in the 20PS-coded sample. It is clearly seen that the water absorption rate increases as the sawdust content increases. An increase in water uptake was observed in all of the composite samples within 50 days. At the end of this period, the change in weight gains is around 1.6% and it has been determined that the curve tends to become flat.

In the literature, it is known that polypropylene has hydrophobic properties, while cellulose-based materials are hydrophilic. The increase in water absorption in composites with cellulose-based materials is clearly seen in the graph. Although the waste cotton filler is cellulose-based, it absorbs relatively less water than sawdust due to the dyed layer on its surface. The data obtained as a result of this study are following the literature [41].
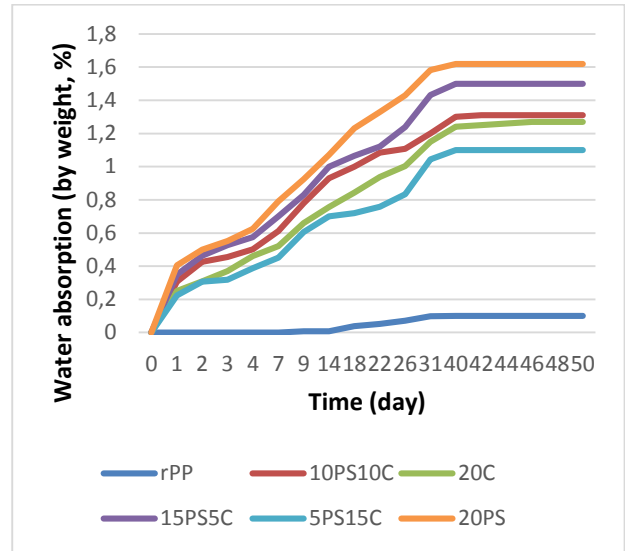
Figure 5. Water absorption properties of composites samples

SEM images of the fracture surfaces of the samples are given in Figure 6. Pure recycled PP showed high elongation as seen in SEM images (6a). This elongation value is also confirmed in the tensile test data. The sawdust in the 20% pine sawdust-filled sample is shown in Figure 6b. The length of the sawdust is over 150 microns, as predicted from the picture. According to the image, it can be said that there is not a very good adhesion between PP and sawdust. This situation can also be understood from the tensile and impact tests. The cotton fiber in polypropylene structure is seen in 6c and The fibrils were found to be around 10 microns in diameter. In 6d, sawdust and cotton are seen in the same image.

4. Conclusions

In this study, the effect of waste cotton and pine sawdust fillers on recycling polypropylene was investigated;

- The highest tensile value was seen in the 10PS10C coded sample among the composites. The tensile values of the following samples decreased compared to pure rPP.
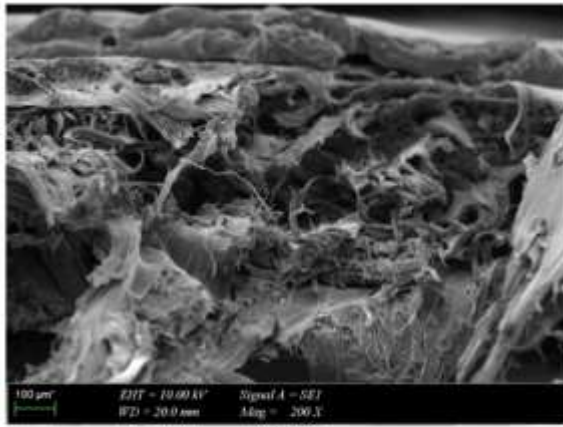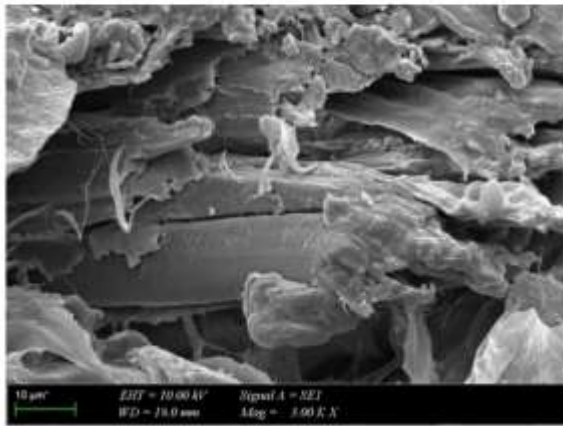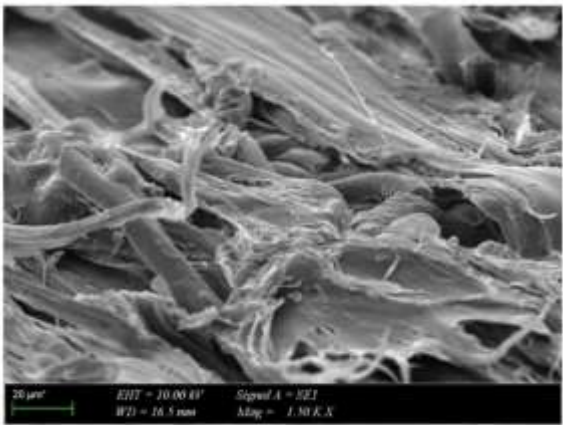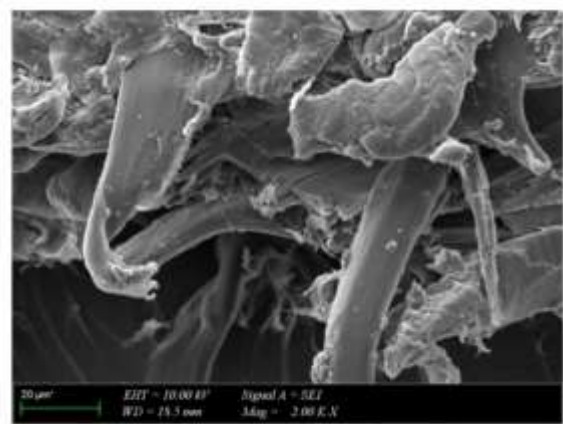
Figure 6. SEM images of samples a)rPP b)20PS c)20C d)15PS5C

- When we look at the water uptake data, it is seen that the composite samples absorb more water than pure rPP.
- Impact strength decreased in general composite samples compared to rPP, but this decrease was less in the 10PS10C-coded sample.
- It was determined that each composite sample had a partial increase in hardness values.
- The samples were prepared homogeneously as confirmed by SEM images. However, in certain samples, a strong bond between the matrix and the filler was not formed.

As a result of the study, it was evaluated that cotton and pine sawdust can be used together as filler in Polypropylene matrix composite materials, and the ideal ratio is 10% pine sawdust and 10% waste cotton (sample with code 10PS10C).

Author Statements:

- **Ethical approval:** The conducted research is not related to either human or animal use.
- **Conflict of interest:** The authors declare that they have no known competing financial interests or personal relationships that could have appeared to influence the work reported in this paper
- **Author contributions:** The authors declare that they have equal right on this paper.
- **Data availability statement:** The data that support the findings of this study are available on request from the corresponding author. The data are not publicly available due to privacy or ethical restrictions.

References

[1] Jose, J. P., & Joseph, K. (2012). Advances in Polymer Composites: Macro- and Microcomposites – State of the Art, New Challenges, and Opportunities. *In Polymer Composites* (pp. 1-16). https://doi.org/https://doi.org/10.1002/9783527645213.ch1

[2] Lubin, G. (1982). Handbook of Composites (1st ed.). Van Nostrand Reinhold Company Inc.

[3] Subramanian, M. N. (2017). Polymers. In Polymer Blends and Composites (pp. 7-55). Scrivener Publishing LLC.

https://doi.org/https://doi.org/10.1002/978111938358
1.ch2

[4] Ebnesajjad, S. (2016). Introduction to Plastics. In E. Baur, K. Ruhrberg, & W. Woishnis (Eds.), Chemical Resistance of Engineering Thermoplastics (pp. xiii-xxv). William Andrew Publishing. https://doi.org/https://doi.org/10.1016/B978-0-323-47357-6.00021-0

[5] Ramesh, M., Rajeshkumar, L. N., Srinivasan, N., Kumar, D. V., & Balaji, D. (2022). Influence of filler material on properties of fiber-reinforced polymer composites: A review. *e-Polymers,* 22(1), 898-916. https://doi.org/doi:10.1515/epoly-2022-0080

[6] Tcherdyntsev, V. V. (2021). Reinforced Polymer Composites. *Polymers,* 13(4), 564. https://www.mdpi.com/2073-4360/13/4/564

[7] Tegethoff, F. W. (2001). Calcium Carbonate: From the Cretaceous Period into the 21st Century (1st ed.). Birkhäuser

[8] Balasubramanian, M. (2013). Composite Materials and Processing (1st ed.). CRC Press. https://doi.org/https://doi.org/10.1201/b15551

[9] Chauhan, A. K., Singh, A., Kumar, D., & Mishra, K. (2021). Properties of Composite Materials. In Composite Materials (1st ed., pp. 61-78). CRC Press.

[10] Sachdeva, A., Singh, P. K., & Rhee, H. W. (2021). Composite Materials Properties, *Characterisation, and Applications* (1st ed.). CRC Press. https://doi.org/https://doi.org/10.1201/978100308063
3

[11] Ageyeva, T., Barany, T., & Karger-Kocsis, J. (2019). Composites. In J. Karger-Kocsis & T. Barany (Eds.), Polypropylene Handbook: Morphology, Blends and Composites (pp. 481-578). Springer International Publishing. https://doi.org/10.1007/978-3-030-12903-3_9

[12] Karian, H. (2003). Handbook of Polypropylene and Polypropylene Composites, Revised and Expanded (2nd ed.). CRC Press. https://doi.org/https://doi.org/10.1201/978020391180
8

[13] Joshi, S. V., Drzal, L. T., Mohanty, A. K., & Arora, S. (2004). Are natural fiber composites environmentally superior to glass fiber reinforced composites? *Composites Part A: Applied Science and Manufacturing,* 35(3), 371-376. https://doi.org/https://doi.org/10.1016/j.compositesa.
2003.09.016

[14] Kuram, E. (2022). Advances in development of green composites based on natural fibers: a review. Emergent Materials, 5(3), 811-831. https://doi.org/10.1007/s42247-021-00279-2

[15] Mesquita, R. G. d. A., César, A. A. d. S., Mendes, R. F., Mendes, L. M., Marconcini, J. M., Glenn, G., & Tonoli, G. H. D. (2017). Polyester Composites Reinforced with Corona-Treated Fibers from Pine, Eucalyptus and Sugarcane Bagasse. *Journal of Polymers and the Environment,* 25(3), 800-811. https://doi.org/10.1007/s10924-016-0864-6

[16] Murugu Nachippan, N., Alphonse, M., Bupesh Raja, V. K., Shasidhar, S., Varun Teja, G., & Harinath Reddy, R. (2021). Experimental investigation of hemp fiber hybrid composite material for automotive application. *Materials Today: Proceedings*, 44, 3666-3672. https://doi.org/https://doi.org/10.1016/j.matpr.2020.1
0.798

[17] Nneka Anosike-Francis, E., Ijeoma Obianyo, I., Wasiu Salami, O., Odochi Ihekweme, G., Ikpi Ofem, M., Olajide Olorunnisola, A., & Peter Onwualu, A. (2022). Physical-Mechanical properties of wood based composite reinforced with recycled polypropylene and cowpea (Vigna unguiculata Walp.) husk. *Cleaner Materials,* 5, 100101. https://doi.org/https://doi.org/10.1016/j.clema.2022.1
00101

[18] Raja, T., Vinayagam, M., Thanakodi, S., Seikh, A. H., Siddique, M. H., Subbiah, R., & Gebrekidan, A. M. (2022). Mechanical Properties of Banyan Fiber-Reinforced Sawdust Nanofiller Particulate Hybrid Polymer Composite. *Journal of Nanomaterials,* 2022, 9475468. https://doi.org/10.1155/2022/9475468

[19] Albinante, S. R., Platenik, G., & Batista, L. N. (2017). Composites of Olefin Polymer/Natural Fibers: The Surface Modifications on Natural Fibers. In Handbook of Composites from Renewable Materials (pp. 431-456). https://doi.org/https://doi.org/10.1002/978111944163
2.ch79

[20] Ichazo, M. N., Albano, C., González, J., Perera, R., & Candal, M. V. (2001). Polypropylene/wood flour composites: treatments and properties. *Composite Structures,* 54(2), 207-214. https://doi.org/https://doi.org/10.1016/S0263-
8223(01)00089-7

[21] Joseph, K., Thomas, S., & Pavithran, C. (1996). Effect of chemical treatment on the tensile properties of short sisal fibre-reinforced polyethylene composites. *Polymer,* 37(23), 5139-5149. https://doi.org/https://doi.org/10.1016/0032-
3861(96)00144-9

[22] Akil, H. M., Omar, M. F., Mazuki, A. A. M., Safiee, S., Ishak, Z. A. M., & Abu Bakar, A. (2011). Kenaf fiber reinforced composites: A review. *Materials & Design,* 32(8), 4107-4121. https://doi.org/https://doi.org/10.1016/j.matdes.2011.
04.008

[23] Demirer, H., Kartal, İ., Yıldırım, A., & Büyükkaya, K. (2018). The Utilisability of Ground Hazelnut Shell as Filler in Polypropylene Composites. *Acta Physica Polonica A*, 134, 254-256. https://doi.org/10.12693/APhysPolA.134.254

[24] Kartal, İ. (2020). Effect of Hornbeam Sawdust Size on the Mechanical Properties of Polyethylene Composites. *Emerging Materials Research*, 9(3), 979-984. https://doi.org/10.1680/jemmr.20.00164

[25] Kartal, İ., Naycı, G., & Demirer, H. (2019a). Cam ve Bambu Lifleriyle Takviyelendirilmiş Vinilester Kompozitlerinin Mekanik Özelliklerinin İncelenmesi. *International Journal of Multidisciplinary Studies and Innovative Technologies*

[26] Kartal, İ., Naycı, G., & Demirer, H. (2019b). Kestane/Gürgen Talaşı Dolgulu Vinilester Kompozitlerin Mekanik Özelliklerinin İncelenmesi. *European Journal of Science and Technology,* 723-728. https://doi.org/10.31590/ejosat.566756

[27] Kartal, İ., Naycı, G., & Demirer, H. (2020). The Effect of Chestnut Wood Flour Size on the Mechanical Properties of Chestnut Wood Flour Filled Vinylester Composites. *Emerging Materials Research*, 9, 1-6. https://doi.org/10.1680/jemmr.19.00179

[28] Kushwanth Theja, K., Bharathiraja, G., Sakthi Murugan, V., & Muniappan, A. (2023). Evaluation of mechanical properties of tea dust filler reinforced polymer composite. *Materials Today: Proceedings,* 80, 3208-3211. https://doi.org/https://doi.org/10.1016/j.matpr.2021.07.213

[29] Şengör, İ., Cesur, S., Kartal, İ., Oktar, F. N., Ekren, N., İnan, A. T., & Gündüz, O. (2018). Fabrication and Characterization of Hazelnut ShellPowder with Reinforced Polymer Composite Nanofibers ICNMA: 2018 20th International Conference on Nanostructured Materials and Applications, Zurich, Switzerland.

[30] Usman, M. A., Momohjimoh, I., & Usman, A. O. (2020). Mechanical, physical and biodegradability performances of treated and untreated groundnut shell powder recycled polypropylene composites. *Materials Research Express,* 7(3), 035302. https://doi.org/10.1088/2053-1591/ab750e

[31] Jan, P., Matkovič, S., Bek, M., Perse, L. S., & Kalin, M. (2023). Tribological behaviour of green wood-based unrecycled and recycled polypropylene composites. *Wear,* 524-525, 204826. https://doi.org/https://doi.org/10.1016/j.wear.2023.204826

[32] Shah, A. u. R., Imdad, A., Sadiq, A., Malik, R. A., Alrobei, H., & Badruddin, I. A. (2023). Mechanical, Thermal, and Fire Retardant Properties of Rice Husk Biochar Reinforced Recycled High-Density Polyethylene Composite Material. *Polymers,* 15(8), 1827. https://www.mdpi.com/2073-4360/15/8/1827

[33] Zănoagă, M., & Tanasă, F. (2011). Comparative Study On Performance Of Virgin And Recycled High Density Polyethylene-Wood Composites. Annals of the University Dunarea de Jos of Galati: Fascicle II, Mathematics, Physics, Theoretical Mechanics, 34.

[34] Shirvanimoghaddam, K., Motamed, B., Ramakrishna, S., & Naebe, M. (2020). Death by waste: Fashion and textile circular economy case. *Science of The Total Environment,* 718, 137317. https://doi.org/https://doi.org/10.1016/j.scitotenv.2020.137317

[35] Jha, M. K., Kumar, V., Maharaj, L., & Singh, R. J. (2004). Studies on Leaching and Recycling of Zinc from Rayon Waste Sludge. *Industrial & Engineering Chemistry Research,* 43(5), 1284-1295. https://doi.org/10.1021/ie020949p

[36] Hole, G., & Hole, A. S. (2020). Improving recycling of textiles based on lessons from policies for other recyclable materials: A minireview. *Sustainable Production and Consumption,* 23, 42-51. https://doi.org/https://doi.org/10.1016/j.spc.2020.04.005

[37] Mishra, R., Behera, B., & Militky, J. (2014). Recycling of textile waste into green composites: Performance characterization. *Polymer Composites*, 35(10), 1960-1967. https://doi.org/https://doi.org/10.1002/pc.22855

[38] Serra, A., Tarrés, Q., Llop, M., Reixach, R., Mutjé, P., & Espinach, F. X. (2019). Recycling dyed cotton textile byproduct fibers as polypropylene reinforcement. *Textile Research Journal,* 89(11), 2113-2125. https://doi.org/10.1177/0040517518786278

[39] Khan, M., Abas, M., Noor, S., Salah, B., Saleen, W., and Khan, R. (2021). "Experimental and statistical analysis of sawmill wood waste composite properties for practical applications," *Polymers* 13(4038), 1-19.

[40] Huda, M. S., Drzal, L. T., Misra, M., and Mohanty, A. K. (2006). "Wood-fiber-reinforced poly(lactic acid) composites: Evaluation of the physicomechanical and morphological properties," *J. Appl. Polym. Sci.* 102, 4856-4869.

[41] Kartal İ, Büyük B, (2023) Ağaç Talaşı Dolgulu Geri Dönüşüm Polipropilen Kompozitlerinin Mekanik Özelliklerinin İncelenmesi, 2nd International Materials Engineering and Advanced Manufacturing Technologies Congress (IMEAMTC'23) p. 156-162.

OTA 2.0: An Advanced and Secure Blockchain Steganography Algorithm

Mustafa TAKAOĞLU[1*], Adem ÖZYAVAŞ[2], Naim AJLOUNİ[3], Taner DURSUN[4], Faruk TAKAOĞLU[5], Selin DEMİR[6]

[1]TÜBİTAK, BİLGEM, UEKAE, Department of Blockchain Technologies (BZLAB), 41400, Kocaeli-Türkiye
* **Corresponding Author** : **Email:** mustafa.takaoglu@tubitak.gov.tr - **ORCID:** 0000-0002-1634-2705

[2]İstanbul Atlas University, Faculty of Engineering and Natural Sciences, 34413, İstanbul-Türkiye
Email: adem.ozyavas@atlas.edu.tr **- ORCID:** 0000-0001-5375-1826

[3]İstanbul Atlas University, Faculty of Engineering and Natural Sciences, 34413, İstanbul-Türkiye
Email: naim.ajlouni@atlas.edu.tr **- ORCID:** 0000-0002-5116-8933

[4]TÜBİTAK, BİLGEM, UEKAE, Department of Blockchain Technologies (BZLAB), 41400, Kocaeli-Türkiye
Email: taner.dursun@tubitak.gov.tr - **ORCID:** 0000-0001-5893-8219

[5] TÜBİTAK, BİLGEM, UEKAE, Department of Quantum Technologies, 41400, Kocaeli-Türkiye
Email: faruk.takaoglu@tubitak.gov.tr **- ORCID:** 0000-0003-0828-2017

[6]TÜBİTAK, BİLGEM, UEKAE, Department of Blockchain Technologies (BZLAB), 41400, Kocaeli-Türkiye
Email: selin.demir@tubitak.gov.tr **- ORCID:** 0009-0006-6331-6418

Abstract:

Blockchain technology, a disruptive force beyond Bitcoin, is finding applications across various fields, including scientific disciplines like steganography – the art of data hiding. Digital steganography has gained momentum with data digitization, especially in multimedia environments like images, text, audio, and videos. Blockchain's integration into steganography has led to interesting developments, like the OTA (Ozyavas-Takaoglu-Ajlouni) algorithm introduced in 2021. The OTA algorithm consists of two stages: the OTA-steganography algorithm and the OTA-chain algorithm (private blockchain). Developed using Java and JavaScript, the OTA platform utilises OTA-coins as its native currency. Previous versions allowed various file types as cover-multimedia, with the secret message encrypted using the Vernam Cipher symmetric encryption and hidden using OTA steganography. Unlike other steganography methods, OTA doesn't alter the cover-multimedia but uses bit-level data marking. In the OTA system, the marked data indices are stored in 1 KB arrays and transmitted to the receiver as transactions via OTA-chain, each incurring a fixed fee of 1 OTA-coin to prevent DDoS attacks. The OTA 2.0 algorithm improved on the previous version by switching to Hyperledger Fabric protocol, which offers open-source, permissioned blockchain solutions, decentralisation capabilities, and self-sovereign identity support. The new version also enhanced block creation time to 2 seconds, increased block size to 90 MB, and employed a 4-bit marking pattern while eliminating transaction fees. Thanks to its innovative key-sharing method and permissioned architecture, OTA 2.0 proves resistant to steganalysis methods commonly used in steganography studies.

1. Introduction

The confidentiality of information and its secure transmission between parties has been one of the most important topics of study throughout history. The art of data hiding, called steganography, is a very old subject of study. The science of steganography, the first examples of which were seen in the "Didim-Aydın" region of Turkey, has taken a digital form as a result of the emergence of computers and the digitalization of data. Today, data that is desired to be hidden for many different

purposes is shared between the parties by using steganography techniques. The most important basic rule in steganography is not to be noticed. For this reason, steganography is being attempted on many new mediums. Blockchain technology is one of the prominent innovations in this context [1-4].

To put it simply, blockchain technology is a secure, decentralised, and distributed database that stores digital transaction histories. It is based on cryptography and computer science principles. The first example of blockchain technology, which is believed to have started with Bitcoin, dates back to the 1990s, when cryptographers Stuart Haber and W Scott Stornetta introduced the concept of a chain of cryptographically secure blocks [5]. However, there were other attempts before Bitcoin with similar features, such as Digicash, Bitgold, Napster, Gnutella, BitTorrent, Hashcash, and B-money [6-12]. The success of Bitcoin can be attributed to factors like the announcement of its whitepaper [13] in 2008 and global events like economic crises and pandemics that followed. Although the Bitcoin protocol has been successful and contributed to the development of blockchain technology and distributed ledger technology on a broader scale, its single-purpose architecture as a payment system limits its realistic usability in other areas. As a result, the Ethereum protocol introduced the ability to develop smart contracts and the concept of the world state machine (Ethereum-Virtual-Machine, EVM), which paved the way for blockchain technology to be used in various fields [14]. Subsequently, other layer 0 and layer 1 protocols (Solana, Cosmos, Avalanche, Aptos, Algorand, etc.) proposed after Ethereum have provided capabilities for developing smart contracts while attempting to address scalability and interoperability challenges through different approaches [15-19].

In steganography research, the idea of using blockchain protocols or blockchain-based solutions as a medium is one of the explored topics. Suggestions have been made to perform steganography on transaction records or during the mining processes of existing permissionless blockchain protocols [20]. Traditional digital image steganography studies have been conducted using Non-Fungible Tokens (NFTs) and generative art [21]. Additionally, steganalysis methods have been applied to public blockchain transaction records to detect stego-multimedia. Another approach that led to the preparation of this study is the innovative concept known as "Blockchain Steganography," which proposes performing steganography in a blockchain environment. The OTA algorithm introduced in the article titled "A Novel and Robust Hybrid Blockchain and Steganography Scheme" offers a solution using a private blockchain for

steganography, rendering existing steganalysis methods ineffective and solving the hiding capacity problem with a unique data hiding method. The study describes an older protocol version called OTA 1.0, which has identified areas open to various improvements since its proposal in 2021, along with the advancement of capabilities in blockchain technology [20]. With the introduction of OTA 2.0, the new method addresses the identified shortcomings and proposes an innovative solution to enhance system security through the distribution of the One-Time-Pad (OTP), a.k.a. Vernam Cipher, symmetric encryption algorithm's key.

In the ongoing sections of the study, a literature review has been shared. The Preliminaries section covers steganography, blockchain technology, Hyperledger Fabric (HLF) blockchain protocol, InterPlanetary File System, OTP symmetric encryption algorithm (Vernam cipher), and the OTA 1.0 method. In the OTA 2.0 section, the proposed method is introduced. The Discussions section includes evaluations and comparisons. In the Conclusion section, the prominent aspects of the proposed method are examined, and the study's findings are discussed.

1.1 Literature Review

Chaudhary et al. [22] explored the combination of machine learning with Blockchain for secure and decentralised transactions. The integration of machine learning addresses constraints and enhances the potential of Blockchain. The study focused on using machine learning in Blockchain to develop a stego cryptography system for secure data communication. With the rapid growth of information and communication technology, communication systems face challenges in security, privacy, service delivery, and network management due to data volume and diverse endpoints. The proposed stego cryptography system offers a solution to achieve decentralised, secure, intelligent, and efficient network operation.

Torki et al. [23] discuss the advantages of using blockchain in steganography, combining its benefits for covert communication and data transmission. They review previous steganography schemes in blockchain, identifying their drawbacks. The authors propose two algorithms for steganography in blockchain: one with high capacity for key and steganography algorithm exchange, and the other with medium capacity for embedding hidden data. Their method is versatile and applicable to popular blockchains like Bitcoin and Ethereum. Experimental results demonstrate the efficiency and practicality of the proposed method in terms of execution time, latency, and steganography fee. The

paper also outlines the challenges of steganography in blockchain from both steganographers' and steganalyzers' perspectives.

Chaudhary et al. [24] introduced a comprehensive approach to enhance data security during communication over the network. Their study proposes utilising Blockchain, Deep Learning, and innovative steganography techniques. They employ hash functions to hide secret data, resulting in high embedding capacity and high-quality data input images. The combination of stego images, hash function-generated datasets, and Blockchain technology enhances data security efficiency. Deep learning algorithms are employed to further strengthen data security in the Blockchain, ensuring no null or duplicate values.

Jahavi et al [25]. proposed a model that uses steganography with neural networks, encryption, and hash functions to hide user identity information within images. These images are then stored on the Ethereum blockchain as NFTs, creating a secure and tamper-proof way to authenticate user identity across multiple platforms.

Sarkar et al. [26] proposed the Stego-chain method, combining Robert's edge detection for increased image embedding payload. Steganography was followed by AES encryption and blockchain transmission in small frames. Receiver retraces the steps with the key to recover information. However, details on blockchain transaction confirmation and reliability logic are lacking, and the study's blockchain content is insufficient.

Mohsin et al. [27] proposed modifications to the Particle Swarm Optimization (PSO) algorithm for secure transmission of COVID-19 data using blockchain. Multiple cover-images were used, and optimal storage locations were identified for each image. Hash values were added to stego-images for integrity. The blockchain system ensures tamper-proofing of stego-images with increased complexity. However, the information shared in the Claims and Limitations sections lacks accuracy and credibility.

Li and Kar [28] propose "B-Spot," a Steganography and Blockchain based photo transmission mechanism. It hides a secret photo within a cover photo using a 3-3-2 LSB image steganography algorithm. The stego-image is divided into blocks and connected by hash values to form a tamper-evident blockchain. A copy of the blockchain is stored in a hash table for recovery. The receiver verifies the blockchain's integrity and recovers lost or tampered blocks using the hash table. The mechanism demonstrates high data capacity, improved imperceptibility, reasonable computing time, and robustness to noise, adding an extra layer of security and robustness to existing schemes.

Basuki and Rosiyadi [29] developed a secure data transmission system using transaction steganography and image steganography methods. The traditional image steganography involved encrypting confidential data using the Ethereum system, creating information like partition number, image URL, and access time. Transaction steganography comprised three stages: transaction field selection, embedding method, and parsing method. Their unique work exemplifies blockchain steganography. The authors thoroughly examined steganography and blockchain systems and successfully applied them in their proposed system.

In the proposed research, Kandasamy and Ajay [30] advocate for the use of Blockchain technology in healthcare to securely exchange user data among hospitals, diagnostic laboratories, and pharmaceutical enterprises. Image-based diagnostics in the health sector are crucial, but securing medical images over public networks raises challenges in confidentiality and integrity. To address this, the researchers utilise steganography as a major tool to improve data security. They propose a system with two layers of security using the LSB (Least Significant Bit) method and encryption to insert medical images into cover images, creating stego images. The entire process is implemented using the MATLAB 2021 version, and simulation results demonstrate the effectiveness of the approach with a minimum mean square error of 0.5 for the extracted images.

Partala [31] proposed a robust system combining blockchain and Least Significant Bit (LSB) in cover communication. This system allows the sender to transmit information through a series of transactions, hiding 1 bit of data in each transaction. The blockchain system was well-designed, and steganography was successfully achieved. The only weakness lies in the time it takes to send data, as it requires more than an hour to transmit approximately 1 byte of data. Additionally, using one transaction for each bit can result in a high number of transactions for large data.

Horng et al. [32] used the RDHEI method with block permutation to encode cover images. They encrypted patient data using the histogram shifting method and concealed it within the cover image. The system operates on the blockchain, ensuring secure data transmission with an embedding rate of 0.8 bits per pixel (bpp). In environments like hospitals with a large amount of patient data, the hidden images have high resolution. However, for large datasets, the blockchain system, encryption processes, and steganography steps in this proposed system may take a long time to operate.

Xu et al. [33] proposed a steganography study utilising a method developed over public blockchain

transactions. It involves creating a new block by manipulating selected transactions and embedding steganographic information within it. However, the applicability of this method raises concerns because in many public blockchain systems, miners require significant processing power to create blocks.

Mazdutt et al. [34] discovered 1600 irregular transaction records in the Bitcoin Blockchain, which were different from the system-generated data. These entries can be easily identified, and efforts are ongoing to prevent such data anomalies. However, Xu et al. did not specify how to embed the stego-data they created into the block structure of a public blockchain without detection.

Giron et al. [35] proposed a steganalysis method to detect steganography techniques on the blockchain system. Despite their extensive research, they did not find any evidence of steganography on public blockchain systems. However, they observed some misuse of steganography in the suggested blockchain steganography studies in the literature. They applied Sequential analysis and Clustering analysis steganalysis methods on a large dataset consisting of Bitcoin and Ethereum blocks and bitcoin clusters. The study indicated that further work is needed in this area.

2. Prelimerities

In the Preliminaries section of this article, an in-depth exploration of essential concepts and technologies is undertaken to provide a solid foundation for subsequent discussions. The first subject of investigation is steganography, a discreet information transmission technique that conceals data within seemingly benign cover media, such as images, text, video or audio files. In the blockchain part of the article investigates the revolutionary domain of blockchain technology. This transformative innovation has disrupted diverse industries, enabling decentralised, secure, and tamper-resistant data storage and transactions. Specifically, the focus lies on the Hyperledger Fabric (HLF) blockchain protocol, distinguished for its permissioned and modular architecture, rendering it highly suited for enterprise blockchain applications. In addition, the examination extends to the InterPlanetary File System (IPFS), a peer-to-peer distributed file system offering an innovative approach to data storage and retrieval, ensuring content availability and resilience. Furthermore, the study delves into the OTP symmetric encryption algorithm, renowned for its exceptional security attributes. Based on the concept of a one-time pad, this algorithm achieves encryption and decryption of information, effectively precluding any potential cryptanalysis. Finally, a comprehensive explanation

of the OTA 1.0 blockchain steganography method is presented in this article.

2.1 Steganography

The term "steganography" is derived from the Greek words "steganos," meaning hidden, and "graphia," meaning writing. Steganography, an ancient subject of study, initially presented its early examples using physical techniques. Nowadays, with the transformation of information into data, steganography techniques are conducted in the computer environment and referred to as digital steganography. In a broader context, various techniques are employed to safeguard information/data from unauthorised parties, and these efforts are termed "information security." Information security encompasses two main aspects: cryptography and information hiding. Information hiding includes two subcategories: digital watermarking and digital steganography. Digital steganography further divides into linguistic and technical approaches [1-4].

Technical steganography is performed using various chosen methods on different covers such as images, text, videos, audios, and protocols. Among the methods, the most suitable one is selected for the specific cover. The selection is based on spatial domain and frequency domain techniques. Spatial domain methods involve the direct encoding of messages within pixel intensities, whereas transform domain techniques, also referred to as frequency domain images, entail a two-step process: transformation followed by message embedding within the image. Figure 1 presents the taxonomy of steganography [36].

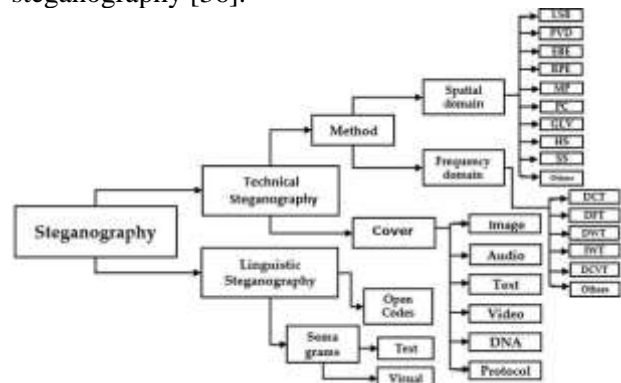***Figure 1.** Taxonomy of steganography [36].*

The application of the Least-Significant-Bit is an uncomplicated and rapid steganography method. To illustrate this in the context of an image cover, the process involves modifying the last 1 or 2 bits of each byte within the cover-image file at the byte level, resulting in a concealment operation. The visual outcome obtained by applying LSB to the

original image (cover-image), thereby hiding data, is termed the stego-image. Figure 2 depicts a visual representation explaining the 2-bit LSB technique applied to the utilised image [37].
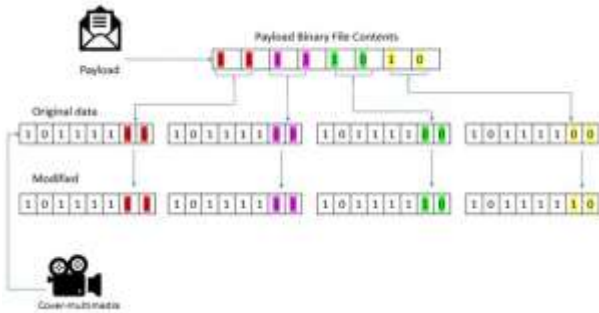

***Figure 2.** Least Significant Bit (2-Bit) [37].*

However, the LSB technique introduces visual distortions on the cover-image as changes are made on a bit-level, and these distortions can be detected using steganalysis methods. In the OTA 1.0 study, the proposed OTA-Steganography technique achieves data concealment on the cover-image at the bit level, similar to the LSB technique, but with a difference: instead of altering, it marks, ensuring data hiding without causing any modifications to the cover-image. During the marking process, the indices of matching bits are stored in arrays and are present on the blockchain. The utilised OTA-steganography method enables the concealment (marking) of vast amounts of information on the chosen cover-image without the concern of hiding capacity limitations. The goal of maintaining a high Peak-Signal-to-Noise Ratio (PSNR) value, indicating no alterations on the cover-image, is also achieved. Furthermore, the feasibility of steganalysis methods like Histogram analysis is eliminated [20].

2.2 Blockchain Technology

In 2008, an individual or organisation using the pseudonym Satoshi Nakamoto introduced Bitcoin, a decentralised, distributed, secure, and transparent solution that eliminates intermediaries, in the whitepaper titled "Bitcoin: A Peer-to-Peer Electronic Cash System." In the Bitcoin protocol, system security is ensured not through any encryption algorithm but solely through hash (Sha256) and the Elliptic Curve Digital Signature Algorithm (ECDSA). The Bitcoin protocol, developed in a public structure, allows anyone to participate as a miner, node, or user at any desired time and to exit as well. The system is fault-tolerant and remains unaffected by such developments. The protocol employs a proof-of-work (PoW) consensus algorithm, where miners solving a mathematical

puzzle earn the right to create a block and produce a new block. Additionally, the inclusion of currency into the system is carried out by miners within the protocol. However, a notable weakness of the Bitcoin protocol is its requirement for high computational power in the mining process, leading to substantial energy consumption. Another weakness lies in the relatively low transaction rate of 3-7 transactions per second (with a block creation time of 10 minutes). The monolithic nature of the Bitcoin protocol, developed solely as a payment system, has hindered its potential use in various technological domains. Despite recent efforts to develop Non-Fungible Tokens (NFTs) on the Bitcoin protocol, through solutions like Bitcoin Ordinals, it remains challenging to achieve universal applicability across all fields [13,21]. The architectural representation of the Bitcoin protocol is shared in Figure 3 [38].
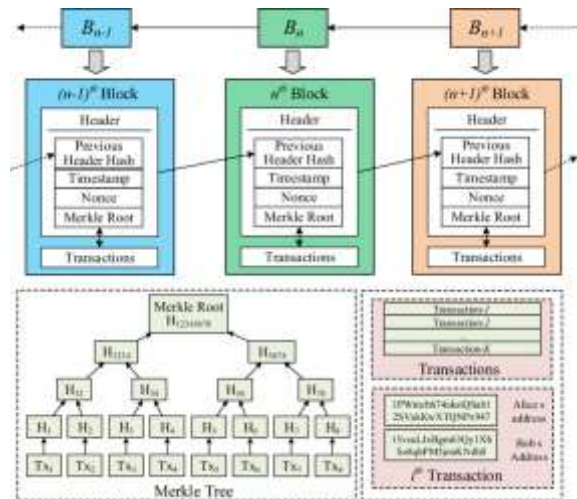
***Figure 3.** Bitcoin protocol architecture [38].*

The solution that emerged with the Ethereum protocol, proposed by Vitalik, has paved the way for the broader applicability of blockchain technology beyond the prominent payment systems of the Bitcoin protocol. The Ethereum protocol, introduced with its world state machine concept, Ethereum Virtual Machine, and smart contract features, has facilitated the decentralised, non-centralized, secure, and immutable nature of blockchain technology to be applied across various domains. Until the Merge fork that occurred on September 15, 2022, the Ethereum protocol utilised the Proof-of-Work (PoW) consensus algorithm, transitioning to Proof-of-Stake (PoS) after the Merge. Post-Merge, the Ethereum protocol has transformed into a Layer 1 blockchain protocol with significantly reduced energy consumption. However, similar to Bitcoin, the Ethereum protocol's transaction rate per second is not very high (between 14-110). Layer 2 architectures are being developed to address scalability issues in the Ethereum protocol. Yet,

future forks will play a significant role in introducing the high transaction capabilities seen in protocols like Solana to the Ethereum protocol. The concept of smart contracts, initially introduced with the Ethereum protocol, has opened the door for the applicability of blockchain technology in various fields. Smart contracts, developed to fulfil requirements in projects, execute on the Ethereum Virtual Machine (EVM). Users interacting with smart contracts pay transaction costs, and afterward, predefined conditions within the smart contract are triggered. Applications developed through smart contracts on the EVM are referred to as decentralised applications (DApps) [14].

The capability to develop smart contracts is not exclusive to the Ethereum protocol; nowadays, it is possible to develop smart contracts on various Layer 0 and Layer 1 protocols. Specifically, within Ethereum, smart contracts are developed using programming languages such as Solidity or Viper. In the Hyperledger Fabric (HLF) protocol, smart contracts are referred to as "chaincode," and in the Solana protocol, they are referred to as "programs." The ability to develop smart contracts also enables token creation, allowing for the tokenization of various assets today. Another significant advancement is the development of Decentralised Autonomous Organizations (DAOs) through smart contracts. For instance, utilising numerous smart contracts, it becomes feasible to autonomously and decentralise the entire range of services provided by an entity like a Notary Office on the blockchain network [14,15,39]. One of the innovations brought about by blockchain technology is the concept of new-generation digital identities and digital identity management systems. The concept of Decentralised Identifiers (DIDs) was standardised by the World Wide Web Consortium (W3C) in 2022. Verified identity information produced by an authorised Issuer (usually a government) is provided to users (Holders), and Verifiers can rapidly verify whether the Holder's possessed verifiable credential (VC) is accurate or not through the blockchain network. Thanks to this innovation, all competencies and credentials individuals possess and need to verify can become cryptographically shareable with counterparties without revealing sensitive information or with limited (selective disclosure) sharing. These and similar capabilities make blockchain technology one of the most applicable and effective alternatives in various fields today [40]. Protocols like Bitcoin, Ethereum, and Solana are entirely open to user access, known as permissionless solutions. In developed projects, it might be necessary to restrict system access and define interaction permissions, including write and read rights, at different levels for users in alignment

with specified requirements. In this context, permissioned blockchain protocols are used, which are favoured in the digital transformation projects of numerous private sector companies and public institutions. Both permissionless and permissioned blockchain protocols are almost entirely open source and are supported by the community [40].

2.3 Hyperledger Fabric Protocol

Hyperledger Fabric (HLF) protocol is a project within the Hyperledger Foundation family that is utilised in permissioned blockchain projects. HLF, an open-source blockchain protocol, is being developed by a community of developers. Presently, there are numerous software projects developed using HLF. The reason for HLF's widespread adoption can be attributed to its modular structure. Thanks to its modular design, various capabilities like consensus and membership services, decentralised identity plugins (Decentralised Identifiers), Hardware Security Module (HSM) integrations, and more can be added or removed from projects. The concept and capability of smart contracts introduced in the Ethereum protocol are presented in the HLF protocol as chaincode. HLF follows a container approach. Furthermore, transaction privacy, introduced as channels, ensures that only authorised nodes of a particular channel can access transactions. While the HLF protocol might not exhibit very high transaction per second (TPS) rates, its performance varies depending on the project's requirements, architecture, and complexity. Additionally, in HLF, the Membership Service Provider (MSP) specifies the rules for validating, authenticating identities, and granting access to the blockchain network. In HLF, clients initiate the creation of transactions. Within HLF, there are two types of peers: endorsing and committing peers. Peers are involved in the execution of chaincode. Furthermore, in the protocol, Orderer nodes play a role in achieving consensus. The transaction flow in the HLF protocol is illustrated in Figure 4 [41,42,43,44].
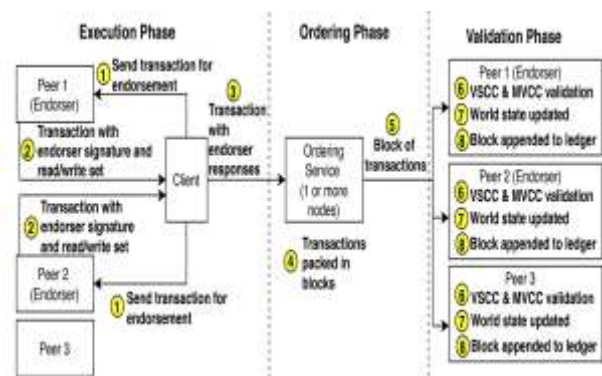

Figure 4. *Transaction flow in HLF protocol [41].*

Within the Hyperledger Fabric protocol, the creation of a new block prompts the need for its dissemination to other peers, which subsequently embark on the block's validation process. During this validation journey, peers initiate the verification by examining the ordering node's signature on the new block. This is followed by the block's deconstruction to unveil its embedded transactions. Moving forward, each transaction within the fresh block encounters two distinct validation phases: VSCC (Validation System Chaincode) validation and MVCC (Multi-Version Concurrency Control) validation. During the VSCC validation phase, peers undertake an assessment to ensure that the endorsements contained within the transaction align with the prescribed endorsement policy. Successful alignment results in verification success, thereby classifying the transaction as valid.

Conversely, misalignment designates the transaction as invalid. In the MVCC validation phase, peers delve into verifying whether the version of the key noted during the endorsement phase matches the version of the key stored within the current state database. A divergence in these versions signifies modification of a previous transaction, rendering it void. The data housed within the block is enveloped in a multi-layered structure. Accessing the data requiring verification necessitates multiple instances of deserialization of the block, a process characterised by substantial time consumption [39,43].

2.4 InterPlanetary File System (IPFS)

IPFS, denoting the InterPlanetary File System, signifies an intricate amalgamation of modular protocols poised to revolutionise extant conceptions of data organisation and transmission. Conceived with a confluence of content addressing and peer-to-peer networking principles, IPFS emblemizes a paradigmatic shift towards an unprecedented data regime. Within the open-source milieu, IPFS flourishes as a variegated tapestry of implementations, engendering a prolific ecosystem endowed with manifold possibilities. Paramount among its manifold applications is the pivotal function of effectuating decentralised data publication, thereby conferring agency over the dissemination of diverse data modalities such as files, directories, and comprehensive web entities, all within an inherently decentralised framework [45].

In its elemental configuration, IPFS assumes the character of a dynamic file system, underpinned by a meticulously architected distributed hash table (DHT) infrastructure. This construct, characterised by its capacity to facilitate seamless traversal and propagation of content-associated data units, demarcates IPFS from solutions confined by narrower storage methodologies or singularly purposed missions. Notably, Filecoin, intrinsically enmeshed within the IPFS fabric, harnesses its infrastructure for data archival and retrieval, culminating in a harmonious amalgamation that exudes the virtues of decentralised and highly efficient storage solutions. Subsequently, Hypercore, a prominent instantiation, emerges as a decentralised data-sharing paradigm, sustained by the very DHT substratum. Its vocation, however, veers towards fostering a milieu conducive to frictionless data interchange and dynamic collaborative endeavours. Swarm, an offspring of the Ethereum blockchain, ascends as a vanguard of decentralised purview. Orchestrating its ambitions through smart contracts and cryptographic artistry, it materialises as an impregnable repository of data integrity. It aspires to redress the exigencies of decentralised, immutable, and impermeable data custody, thus inaugurating an epoch of unwavering data stewardship[46].

In elucidating what IPFS does not signify, one is compelled to acknowledge its multi-dimensional essence. Resonating with the demeanour of a protocol, IPFS eschews the role of an autonomous storage proponent. Although symbiotic interludes transpire with storage providers, commonly referred to as "pinning services," IPFS maintains its quintessence as a symphonic architect rather than a custodian of data reservoirs. Similarly, in its interface with the cloud milieu, IPFS assumes the character of a gentle drizzle, complementing the overarching ambiance without masquerading as a preeminent cloud service provider [46,47].

2.5 Vernam Cipher

The Vernam Cipher, also known as the One-Time Pad (OTP), stands as one of the most intriguing and theoretically unbreakable encryption techniques. Its foundation lies in the concept of perfect secrecy, where an encrypted message provides no information about the original message, even to an adversary with unlimited computational power. This remarkable property stems from the fact that each character or bit in the plaintext is combined with a random character or bit from the key using the XOR operation. This results in an output that is seemingly random and offers no statistical patterns to exploit. One of the core challenges in utilising the OTP is the key management process. Each key used for encryption should be truly random and should be as long as the message itself, and produced for each encryption process uniquely. Key generation requires a trustworthy source of entropy, often derived from physical processes such as electronic

noise or radioactive decay. Additionally, securely distributing these lengthy keys to both the sender and receiver is paramount, as any compromise in the key exchange process could undermine the security of the entire system. The concept of the OTP has remains resilient even in the face of advancements in cryptography, including the advent of quantum computing. Unlike many other encryption methods that can potentially be broken by quantum computers due to their ability to efficiently factor large numbers, the OTP remains secure due to its unique properties and the fundamental principles on which it is built. To illustrate the OTP process, refer to Figure 5, which visually represents the steps involved in this encryption technique. This visualisation can help readers grasp the concept more easily and appreciate the elegance of the algorithm [48].
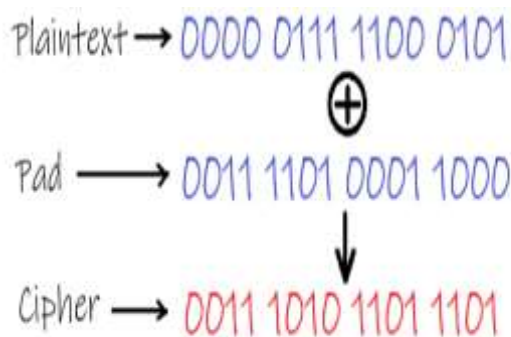

***Figure 5.** Steps of One-Time-Pad symmetric encryption.*

2.6 OTA 1.0

The OTA 1.0 algorithm is a private blockchain system formulated for covert communication through steganography. It has been constructed from the ground up using Java and JavaScript programming languages. As a private blockchain, entry into the OTA 1.0 system mandates authorization. Initially, 50 OTA tokens are apportioned to approved node wallets. The fixed cost for each transaction within the system is 1 OTA token. This proposed algorithm comprises two main phases: first, the steganography process, followed by the transmission of stego-data using the private OTA-chain blockchain system [20].

2.6.1 OTA 1.0 Steganography Algorithm

In the proposed OTA-steganography algorithm, the chosen multimedia items serving as covers are securely stored on a dedicated server. The URLs associated with these multimedia elements are then logged and saved within the OTA-chain blocks. This strategy enables the detection and rectification of inadvertent alterations that might occur during the

transmission of the cover multimedia through public channels. Unlike traditional steganography methods, the OTA-steganography algorithm abstains from concealing data within the cover multimedia image, rendering it impervious to steganalysis techniques. Thus, it stands apart from conventional approaches, boasting its own distinctive structure [20].

The process involves segmenting the plaintext data into varying numbers of bits, such as 2, 3, 4, and so forth, depending on the predetermined chunk size. Regardless of the chosen division, the algorithm undertakes systematic matches for bit patterns within the cover multimedia file to locate matching fragments of bits. Once a match is found, the algorithm records the starting bit position, or index, within the cover multimedia. Subsequent searches for remaining bit fragments continue from where the last successful search concluded, ensuring continuity [20].

If a search for a specific plaintext bit fragment traverses the entire cover multimedia without discovering the intended bit pattern, the search recommences from the file's inception, creating a cyclic process. As the algorithm successfully identifies all bit patterns from the plaintext data within the cover multimedia, the corresponding indices are compiled into an array known as the "address array." This array is further divided into kilobyte-sized segments, with each 1 kB of stego-data aligning with a single transaction within the OTA-chain. Figure 6 illustrates the architecture of the OTA-steganography algorithm [20].
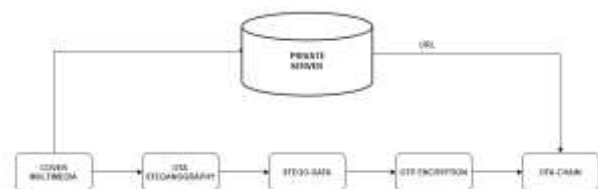
***Figure 6.** The architecture of OTA steganography [20].*

During the processing of the cover multimedia by the OTA-steganography algorithm, indices corresponding to 2, 3, and 4 bit fragments of the plaintext data are retained for the sake of performance assessment. Opting for larger fragments leads to a reduction in the size of the address array, yet it entails increased search time during the creation of this array. The stego-data, which in this context refers to the address array, generated by the OTA-steganography algorithm, undergoes encryption utilising the One-Time-Pad (OTP) algorithm. Sharing the OTP key can be executed through any means, as the OTA-chain's private blockchain structure mitigates any potential risks stemming from unauthorised possession of the key by malicious entities via public channels.

Despite the algorithm's initial design for smaller message sizes, its cyclic nature enables the transformation of data larger than the cover multimedia file into an address array [20].

The proposed OTA-steganography algorithm achieves an extensive payload capacity, courtesy of its unique approach involving precise marking and indexing of a single cover multimedia [20].

2.6.2 OTA(1.0)-Chain Algorithm

Crafted with a specific focus on meeting steganographic demands, the OTA-chain algorithm has been purposefully developed. Within the OTA-chain network, nodes harbouring steganographic information can establish secure intercommunication. Notably, conventional platforms like Bitcoin, and Ethereum blockchain platforms have been deliberately eschewed. This strategic choice is predicated on the objective of maintaining streamlined system costs, a rationale expounded upon earlier. Given the OTA-chain system's reliance on OTA coins, the transmission of an OTA coin alongside stego-data to the recipient serves a dual purpose. This OTA coin within the recipient's wallet acts as both a reminder and a cautionary message for the user. Effectively, the mechanism of sending the coin operates akin to a ring, functioning as a notifier for the recipient and also preventing DDoS attacks due to transaction costs [20].

Of paramount significance, the OTA coin is disbursed to eligible nodes without any associated cost, thereby constraining the system expenses solely to the processing capability offered by the participating nodes' hardware. Pioneering the development of the OTA-chain algorithm from the ground up facilitated the early integration of numerous essential functionalities into the system. The block framework of the proposed system, meticulously tailored to meet steganographic requisites, encompasses key components such as the sender address, receiver address, timestamp, last hash, hash, nonce, difficulty, URL, and data [20].

The OTA-chain algorithm introduces a concept of a private blockchain system, wherein unauthorised entities lacking access permissions are precluded from scrutinising transactions. The stego-data, once transmitted, undergoes OTP algorithm encryption and is subsequently inscribed into the system's blocks. This measure ensures that the system's nodes, which hold access privileges, remain inaccessible to malevolent entities and impervious to potential manipulations or insider attacks. Nodes exclusively possess the capability to review transactions confined within the OTA-chain system.

The proposed algorithm employs the Proof-of-Work consensus mechanism. The system's constituent nodes also serve as miners, and those bestowed with block writing authority are rewarded with 50 OTA coins. Moreover, a minimum transaction cost of 1 OTA coin has been established for activities on the OTA-chain. Each transaction, spanning up to 1 kB in size, corresponds precisely to 1 OTA coin. The stego-data integrated into the OTA-chain consists of 1 kB Ciphered Secret Data (CSD) encrypted arrays produced during the OTA-steganography phase. This arrangement segments encrypted data into 1 kB blocks, with the transaction count aligning with the quantity of these confidential data blocks [20].

The OTA-chain algorithm embodies an on-chain blockchain system. Information pertaining to the system's data is logged within OTA-chain blocks. Unlike analogous endeavours, the system blocks refrain from concealing image matrices, which optimises both time and processing efficiency. Notably, the proposed system sidesteps the costs associated with pre-existing platforms featured in prior literature studies. Within the OTA-chain framework, secure sharing of the URL address of the desired cover multimedia for purchasers is achieved, alongside encrypted stego-data. A schematic depiction of the OTA-steganography and OTA-chain architecture inherent to the OTA algorithm is presented in Figure 7 [20].
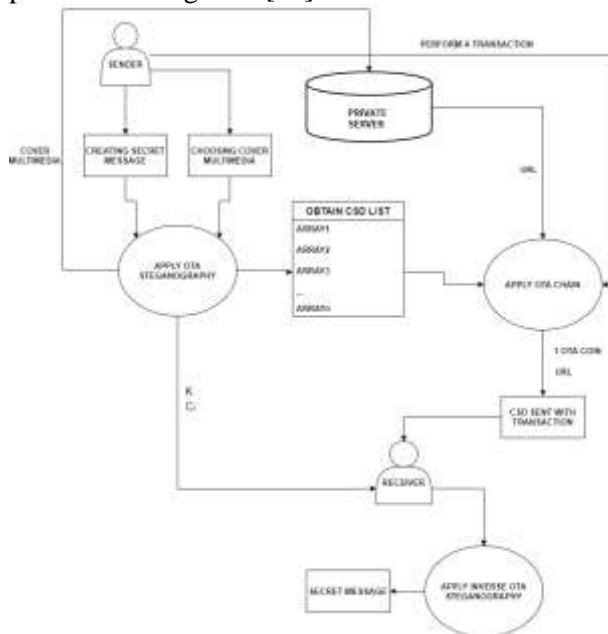

Figure 7. *Structure of OTA(1.0) algorithm [20].*

3. OTA 2.0

In the work, a new and improved system has been proposed with the aim of popularising and enhancing the applicability of the blockchain-steganography method recommended in OTA 1.0. In the proposed OTA 2.0 method, the Hyperledger Fabric protocol

has been used. Due to HLF being a permissioned platform, access permissions of users can be easily controlled. Furthermore, in OTA 2.0, access to the system can be achieved using Decentralised Identifiers (DID). The usage of TÜBİTAK BİLGEM's DID SDK (Indy) is envisaged in the proposed system. As HLF has a modular structure, it allows integration of various DID solutions. For the ease of use and widespread adoption of the proposed OTA 2.0, it is planned to be developed as a mobile application. Senders and recipients can transmit the desired types of files as steganographic cover-multimedia, embedding the secret message they want to convey in a way that does not cause any changes to the cover. The mobile application will be designed to have a simple and practical user interface. The OTA system will generate a DID for users registered in the system and associate it with their wallets. However, the verification and KYC processes of registered users have been kept out of scope in the study. Organisations wishing to implement the proposed method can make adjustments according to their needs and the scenarios they will use.

From a user perspective, using OTA 2.0 is quite simple. To send a secret message to the recipient's wallet address, they will select a file or take a photo from their phones and send it along with the message. There is no transaction cost associated with this process, and the recipient will receive an informational message (notification) indicating that they have received the information. The recipient must reach this message within 3 days; otherwise, access to the sent secret message will not be possible. This designated 3-day period can be changed up to 30 days. However, in the study, files are not planned to be pinned in IPFS, and as a result, files will be deleted from IPFS after a maximum of 30 days. Additionally, in steganographic processes, since the significance and validity of information are limited, it is crucial for the transmission of confidential data to be completed as quickly as possible in the process, leaving no meaningful trace behind. In addition to the deletion of non-pinned files in IPFS, due to the innovative key distribution method proposed in the study, the keypool creation seed used will be deleted from HLF after 3 days. As a result, accessing the key to the file encrypted with OTP will become impossible, rendering the received data unreadable by the recipient. Figure 8 illustrates the overall architecture of the proposed OTA 2.0 algorithm. Although OTA 2.0 is a permissioned system, and even though users granted access to the system are limited to sending data and reading incoming data only through mobile applications, the encrypted form of Secret Data using OTP is planned to be concealed through the OTA-steganography
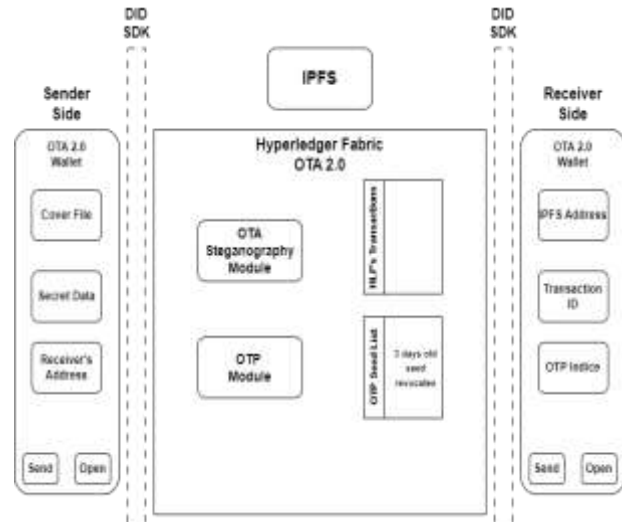

Figure 8. *Structure of OTA(2.0) algorithm.*

algorithm within HLF. This approach aims to prevent possible insider attacks by utilising the marked bit indices stored in HLF transactions. Furthermore, to counteract potential insider attacks, the cover-multimedia files stored in IPFS have been uploaded without pinning to ensure their deletion from IPFS after 30 days.

In the proposed OTA 2.0 study, an innovative key generation and distribution method for OTP has been suggested. The keypool is created on HLF using a randomly selected seed value. The chosen seed values are generated on an hourly basis, and the seed value generated for each hour is kept in the OTP Seed List. Seed values stored in the OTP seed list are removed from the list if they exceed 72 hours. To start from a randomly chosen point in the created keypool and cover the size of the data to be concealed, a key is selected, and the secret data is XORed. The index information of the selected key point is recorded for communication to the recipient. With this proposed method, the encryption process occurs within HLF's chaincode, and the key distribution process is carried out without sharing the key itself. If the receiver attempts an insider attack on the system, they cannot access the HLF transaction data, and since they cannot generate the keypool's seed value from the received key selection point index without the seed, they cannot use it to execute a successful attack. This lack of usability prevents any potential risks. Due to the deletion of the seed value after 72 hours, the key cannot be obtained, ensuring security against any type of attack that might be directed at the system. Figure 9 illustrates the encryption architecture of the OTP module, while Figure 10 shares the decryption architecture of the OTP module. The OTA-Steganography algorithm introduced in OTA 1.0 has been utilised in OTA 2.0 with slight differences.
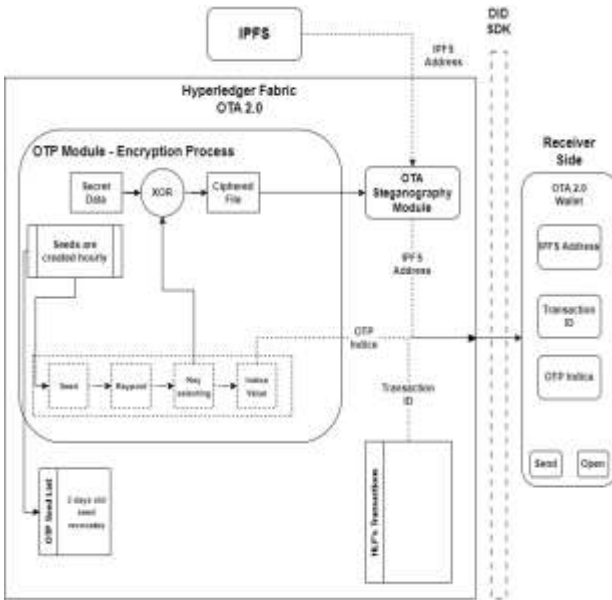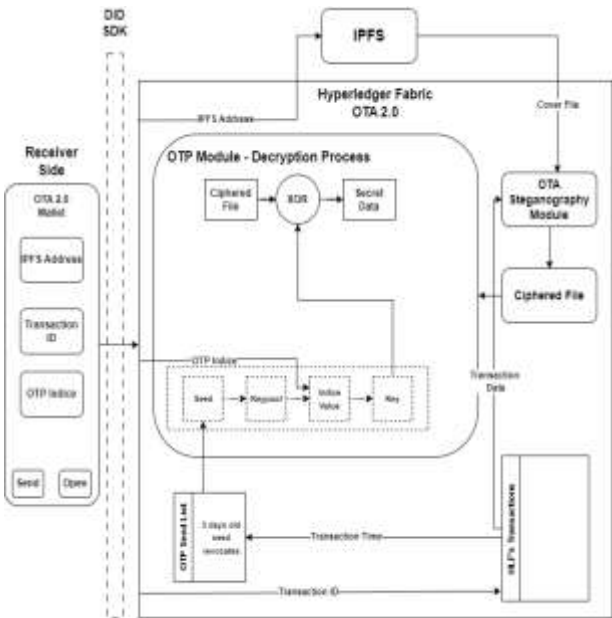
Figure 9. *Structure of encryption process.*

Figure 10. *Structure of decryption process.*

Table 1. *The likelihood of discovering an n-bit pattern within an m-bit cover multimedia.*

	128 Byte	**256 Byte**	**512 Byte**	**1 kB**	**4 kB**
4-bit	~100%	~100%	~100%	~100%	~100%
6-bit	99.99%	~100%	~100%	~100%	~100%
8-bit	98.35%	99.98%	99.99%	~100%	~100%
10-bit	64.10%	85.45%	98.81%	99.91%	~100%

1. **User Registration in OTA 2.0:** After installing the OTA 2.0 mobile application, users complete their KYC processes and are provided with verifiable credentials for their wallets.
2. **Cover-Multimedia Selection:** Users can select files of various types. The chosen file is uploaded to IPFS through the mobile application, and the IPFS link is sent to OTA 2.0.
3. **Entering Secret Data:** The confidential data intended for transmission is input at this stage. While there is no specific limitation on the size of Secret Data, its size is expected to be relatively small due to the nature of steganographic processes.
4. **Entering Receiver Address:** The recipient's wallet information needs to be provided to the mobile application.
5. **Initiation of Sending Process:** Once cover-multimedia, secret data, and receiver address data are entered, the sender requests the transmission to the recipient through OTA 2.0 using APIs.
6. **Identity Verification:** Whenever OTA 2.0 interacts with users, it first verifies the verifiable credential (VC) of the requesting sender. This step may increase processing time but is crucial for security. The system ensures the validity of the user's access permission. Upon validation, the user's request is processed.
7. **IPFS Interaction:** The cover-multimedia IPFS link from the received transaction request is used to access the file. The cover-multimedia is sent to the OTA-Steganography module.
8. **KeyPool Creation:** A new random seed is generated every hour, and random numbers are generated and used as keys using these seed values. The seed value generated for each hour is written to the OTP Seed List. Seed values exceeding 72 hours are removed from this list.

In the previous version, data embedding was performed with 4-bit, 6-bit, 8-bit, and 10-bit patterns. However, in OTA 2.0, it was decided to use only a 4-bit data embedding.

The calculation of the likelihood of not encountering a bit pattern of size n within cover multimedia of length m, where m is greater than n, is achieved through Markov chains. Specifics regarding bit patterns of varying lengths, cover multimedia length, and their associated probabilities are outlined in Table 1. As seen in the table, it is seen that the data embedding performed using 4-bit patterns yields quite successful results. The process of a blockchain-steganography operation in OTA 2.0 follows these steps:

9. **Encryption of Secret Data:** The secret data provided by the sender is XORed with a key selected from the keypool created using the Vernam Cipher. The size of the key matches the size of the secret data. A random point is selected from the keypool to read the key. The index of the selected point is recorded for the recipient, completing the encryption process.

10. **OTA-Steganography Process:** The cover-multimedia retrieved from IPFS and the encrypted secret data from the OTP module are concealed using 4-bit patterns. The indices of matching bits are recorded, and this information is written in the data block of the sent transaction. Only one transaction's data is allowed to be recorded in each block. The block creation time in HLF is set at 2 seconds, which can be adjusted if needed. The block size is set to 90 MB, which is sufficient for steganographic processes.

11. **Sending Notification to Receiver:** After completing its operation, the OTA-Steganography module triggers a transaction in HLF, creating a block. Subsequently, the OTP index value, transaction ID, and IPFS address are sent to the recipient, and a notification is sent to their mobile wallet.

12. **Receiver's Request for Accessing the Secret Data:** Upon receiving the notification, the recipient requests to access the received secret message. The recipient's VC is checked, as there is a possibility they could be added to the revocation list during the time that has passed. If the recipient has a valid VC, HLF processes the incoming request.

13. **Accessing Cover-Multimedia from IPFS:** Using the IPFS link in the recipient's digital wallet, the cover-multimedia is accessed and sent to the OTA-Steganography module.

14. **Utilising Transaction ID:** Using the Transaction ID provided by the recipient, information about the bit indices marked with 4-bit patterns is retrieved from the ledger. Additionally, the date and time information of the transaction indicated by the Transaction ID is used to check the OTP Seed List. If less than 72 hours have passed, the seed value is sent to the OTP decryption module.

15. **Locating the Ciphered File:** After providing the cover-multimedia and the indices marked with patterns to the OTA-Steganography module, the encrypted secret data file is obtained from the cover-multimedia using the bit indices. This ciphered file is then sent to the OTP module.

16. **Locating the Secret Data:** To unlock the ciphered file provided to the OTP module, the key needs to be re-generated. To achieve this, the keypool used at the time of file encryption is reconstructed using the seed value. The key is read from the keypool based on the index of the selected point, which is then used to perform an XOR operation and access the secret data. The retrieved Secret Data is then sent to the receiver.

Another advantage of implementing the OTA 2.0 algorithm within the Hyperledger Fabric protocol is the ease with which suspicious or unwanted users can be added to the revocation list. Furthermore, the MVCC mechanism inherent in the HLF protocol prevents DDoS attacks. The OTA 2.0 architecture is highly secure: All steganalysis methods are unable to detect blockchain steganography carried out through chaincodes. All types of files can be used as cover-multimedia, and data can be concealed without making any modifications to the files, without any issue of hiding capacity.

Neither Secret Data nor Cover-Multimedia are stored in HLF-ledger blocks. HLF-ledger blocks solely contain the indices of marked bits, which by themselves hold no meaningful information. After 72 hours (this duration can be extended or reduced), the transaction records registered in the system lose their utility. Files stored in IPFS, due to not being pinned, are deleted from the system within a maximum of 30 days, leaving behind no trace that can be detected.

Although the likelihood is extremely low, even if an attacker were to possess cover-multimedia, block data, and the OTA-Steganography algorithm simultaneously, they would be unable to acquire the same keypool without having the seed value (they lack direct access to the Seed list), and even if they had the seed value, they would not be able to obtain the same keypool without access to the same random number generator library used in the OTP module's chaincode, which is highly improbable. While this scenario is highly unlikely, user interactions with OTA 2.0 are restricted through mobile wallets, ensuring limited access to HLF block records. They cannot view other users' information beyond what is shown in their notifications. Moreover, all access to the system is managed through DID control, and user access is monitored.

The OTA 2.0 algorithm is designed within a permissioned architecture, which makes its distribution quality lower compared to a public blockchain project and somewhat centralised.

However, it provides a structure that perfectly addresses the needs of parties requiring blockchain steganography. The fact that HLF is an open-source platform and is regularly developed by an open-source community greatly facilitates the sustainability and improvement of the system. Additionally, HLF's modular structure, as demonstrated in the TÜBİTAK's DID SDK example, allows for the use of your own SDKs. In this context, for future cryptographic designs that may be required, they can be integrated into OTA 2.0 through HLF.

4. Discussions

The proposed OTA 2.0 Blockchain Steganography method aims to enhance the approach suggested in OTA 1.0. OTA 1.0 is significant for being the first method to propose steganography on a blockchain, thus contributing to the literature. OTA 1.0 consisted of two parts: OTA-Steganography and OTA-Chain. OTA-Chain was a newly developed private blockchain solution. In the OTA-Steganography phase, secret message data was matched to cover-multimedia data at the bit level using different bit patterns (4, 6, 8, 10), and the indices of the matching bits were stored in arrays that did not exceed 1 KB. These 1 KB arrays were sent to the recipient's wallet in OTA-Chain, with a fixed fee of 1 OTA-coin for the transaction. Upon registration, all users were provided with 50 OTA-coins, and the purpose of introducing a utilisation token was to prevent DDoS attacks. However, OTA 1.0 displayed weaknesses due to its lack of open-source nature, absence of support from an open-source committee, and therefore, its inability to create a usage example.

Additionally, OTA-Chain couldn't be developed further in terms of software after it was proposed, and monitoring and benchmarking tools couldn't be prepared. For all these reasons, the aim was to implement the blockchain steganography method from OTA 1.0 on a different platform and overcome the encountered issues. In this context, in this prepared study, the OTA-Steganography and OTA-Chain approach has been restructured using the Hyperledger Fabric protocol. Moreover, innovations such as the decentralised identifier extension and OTP key generation and distribution have been added to the system.

In OTA 2.0, OTA-Chain has been replaced with Hyperledger Fabric. In this context, the use of OTA-Coin has been discontinued, and a new model has been introduced that has no transaction fees and utilises the internal mechanism of HLF (MVCC) to guard against DDoS attacks. OTA-Steganography, on the other hand, is proposed as a chaincode (OTA-Steganography Module) within HLF, and

simultaneously, marking using a 4-bit pattern is suggested. The selection of the 4-bit pattern, as seen in Table 1, has proven to be effective in achieving almost 100% probability of marking for nearly all file sizes.

All file types are compatible with the OTA-Steganography module. This is because all file types are read at the bit level, enabling blockchain steganography to be carried out by marking these bits. Additionally, the cover-multimedia chosen by the user comes from IPFS, and cover-multimedia files are not stored in HLF. This approach aims to enhance steganographic security and system scalability. Files stored in IPFS are not pinned, limiting the duration of cover-multimedia retention on IPFS to a maximum of 30 days. Given the importance of quickly transmitting data to the recipient in steganographic processes, long-term data storage is unnecessary. Therefore, in the process of creating the OTP keypool, which is another important development in the system, the seed values used are irreversibly deleted from the system after 72 hours, aligning with the spirit of steganography.

Similarly, the size of the hidden data sent to the recipient is generally very small, adhering to the essence of steganography. However, in the system, a significant improvement has been made by allocating a 90 MB block size for each transaction, enabling the transmission of larger hidden data sizes. The block creation time in HLF is set to 2 seconds, and the block size is set at 90 MB. As a result, the use of a 1 KB array is no longer necessary. Just like in OTA 1.0, OTA 2.0 ensures that no degradation occurs in the cover-multimedia. Subjecting the cover-multimedia stored in IPFS to steganalysis methods doesn't pose any security vulnerability and remains undetectable.

The OTP encryption algorithm, being a highly secure symmetric encryption method, has been utilized in OTA 2.0, just as it was in OTA 1.0. A different approach has been taken in generating the key that needs to be chosen for the size of the file to be encrypted. In the OTP module, a seed value is generated every hour to create a changing keypool. This keypool is accessible only at the chaincode level of HLF. The generated seed values are stored in the OTP-Seed List for 72 hours before being deleted. From these created keypools, a random starting point is selected, and key selection is performed for the size of the file. The secret data is encrypted using this key, and the index value of the key selection is recorded to be transmitted to the recipient. This proposed solution deviates from conventional key distribution methods, aiming to mitigate security vulnerabilities that might arise in traditional key distribution processes.

If the recipient wishes to access the data sent after receiving the notification within 3 days, they provide the OTP index, transaction ID, and IPFS address to OTA 2.0 to access the secret data. In this process, the seed value used at the time of the transaction is employed to recreate the keypool, and using the OTP index information, the key is obtained. By applying reverse OTA-Steganography, the ciphered document is obtained, decrypted using the key, and then conveyed to the user. Throughout this process, the user merely needs to possess a valid verifiable credential and make requests through OTA 2.0's APIs via their mobile wallet.

The Hyperledger Fabric protocol is not particularly efficient in terms of speed. The proposed DID integration and the necessity for DID verification in every transaction, along with the communication between the Mobile Wallet and OTA 2.0 and IPFS through APIs, will lead to lower TPS (transactions per second) rates in the system. However, OTA 2.0 does not require the high TPS typically needed in financial solutions. The fact that transaction processing times are not very short is not considered a significant issue. The system's performance can be monitored through benchmarking and monitoring tools. The proposed OTA 2.0 algorithm in this study possesses a significantly superior infrastructure and security features compared to its predecessor, OTA 1.0. The integration of the Mobile Wallet extension also paves the way for OTA 2.0 blockchain steganography to be easily accessible to end-users. The user base for the OTA 2.0 algorithm is highly specific and limited. Therefore, the realisation and maintenance of OTA 2.0 would require a considerable investment from an organisation. The OTA 2.0 algorithm, as suggested by the expert teams at TÜBİTAK BİLGEM UEKAE BZLAB, and professors from Istanbul Atlas University is being developed for testing purposes and in a secure environment as part of BZLAB's R&D activities. However, there are no plans to offer it as a final product to users. The implementation of the proposed OTA 2.0 algorithm in this study has not been fully completed. Therefore, tests and analyses, including system speed and cybersecurity analysis, are not currently available for sharing.

4. Conclusion

In essence, OTA 2.0 signifies a notable leap ahead of its precursor, tapping into the capabilities of the Hyperledger Fabric protocol. This evolution ushers in a spectrum of benefits, encompassing open-source availability, permissioned blockchain solutions, decentralization, and endorsement of self-sovereign identity. Furthermore, the algorithm's enhancements, including quicker block creation,

expanded block size, and integration of a 4-bit marking pattern, amplify its effectiveness. Through the removal of transaction fees and the introduction of an inventive key-sharing methodology within its permissioned framework, OTA 2.0 adeptly thwarts conventional steganalysis techniques. This pioneering technology empowers the seamless and secure embedding of confidential messages across diverse multimedia formats.

Author Statements:

- **Ethical approval:** The conducted research is not related to either human or animal use.
- **Conflict of interest:** The authors declare that they have no known competing financial interests or personal relationships that could have appeared to influence the work reported in this paper
- **Acknowledgement:** The authors declare their acknowledgment to the TÜBİTAK-BİLGEM-UEKAE-Blockchain Technologies Department (BZLAB).
- **Author contributions:** The authors declare that they have equal right on this paper.
- **Funding information:** The authors declare that there is no funding to be acknowledged.
- **Data availability statement:** The data that support the findings of this study are available on request from the corresponding author. The data are not publicly available due to privacy or ethical restrictions.

References

[1] Takaoğlu, M., Özyavaş, A., Ajlouni, N. & Takaoğlu, F. (2023). Highly Secured Hybrid Image Steganography with an Improved Key Generation and Exchange for One-Time-Pad Encryption Method. *Afyon Kocatepe Üniversitesi Fen Ve Mühendislik Bilimleri Dergisi.* 23(1):101-114. DOI:10.35414/akufemubid.1128075

[2] Şahin, F., Çevik, T. & Takaoğlu, M. (2021). Review of the Literature on the Steganography Concept. *International Journal of Computer Applications.* 183(2):38-46. DOI:10.5120/ijca2021921298

[3] Takaoğlu, F. & Takaoğlu, M. (2020). Hiding Image and Text Data with DCT and DWT Techniques. *Journal of İstanbul Aydın University.* 12(3):189-200. DOI:10.17932/IAU.IAUD.2009.002/iaud_v12i3001

[4] Takaoğlu, F. & Takaoğlu, M. (2020). Today's Validity of Printer Steganography and Yellow Dot Analysis. *e-Journal of New Media / Yeni Medya Elektronik Dergi-eJNM.* 4(3):186-194. DOI:10.17932/IAU.EJNM.25480200.2020/ejnm_v4i3004

[5] Takaoğlu, M., Özer, Ç. & Parlak, E. (2019). Blockchain Technology and Possible Application Areas in Turkey. *International Journal of Eastern Anatolia Science Engineering and Design.* 1(2):260-295.

[6] Chaum, D. (1983). Blind signatures for untraceable payments. *Advances in Cryptology Proceedings of Crypto.* 82(3):199-203. DOI:10.1007/978-1-4757-0602-4_18

[7] Szabo, N. (2008). *Bit Gold.* http://unenumerated.blogspot.com/2005/12/bit-gold.html

[8] Fanning, S., Parker, S. & Contreras, H. S. (1999). *Nabster.* https://en.wikipedia.org/wiki/Napster_(streaming_service)

[9] Frankel, J. & Pepper , T. (2000). *Gnutella.* https://www.gnutellaforums.com/

[10] Cohen, B. (2001). *BitTorrent.* https://www.bittorrent.org/

[11] Back, A. (1997). *Hashcash.* http://www.hashcash.org/

[12] Dai, W. (1998). *Bmoney.* http://www.weidai.com/bmoney.txt

[13] Nakamoto, S. (2008). *Bitcoin: A Peer-to-Peer Electronic Cash System.* https://bitcoin.org/bitcoin.pdf

[14] Buterin, V. (2014). *Ethereum.* https://ethereum.org/en/whitepaper/

[15] Yakovenko, A. (2018). *Solana: A new architecture for a high performance blockchain v0.8.13.* https://solana.com/solana-whitepaper.pdf

[16] Kwon, J. (2014). *Tendermint: Consensus without Mining.* https://tendermint.com/static/docs/tendermint.pdf

[17] Sekniqi, K., Laine, D., Buttolph, S. & Sirer, E. G. (2020). *Avalanche Platform.* https://assets.website-files.com/5d80307810123f5ffbb34d6e/6008d7bbf8b10d1eb01e7e16_Avalanche%20Platform%20Whitepaper.pdf

[18] Ching, A. & Shaikh, M. (2022). *The Aptos Blockchain: Safe, Scalable, and Upgradeable Web3 Infrastructure.* https://aptos.dev/assets/files/Aptos-Whitepaper-47099b4b907b432f81fc0effd34f3b6a.pdf

[19] Chen, J. & Micali, S. (2017). *Algorand Theoretical Paper.* https://algorandcom.cdn.prismic.io/algorandcom%2Fece77f38-75b3-44de-bc7f-805f0e53a8d9_theoretical.pdf

[20] Takaoğlu, M., Özyavaş, A., Ajlouni, N., Alshahrani, A. & Alkasasbeh, B. (2021). A Novel and Robust Hybrid Blockchain and Steganography Scheme. *Appl. Sci.* 11:10698. DOI:10.3390/app112210698

[21] Takaoğlu, M., Takaoğlu, F. & Dursun, T. (2023, July 20-21). *NBS: An NFT-Based Blockchain Steganography Method.* Conference: the 2nd International Conference on Computing, IoT, and Data Analytics (ICCIDA), La Mancha-Spain. https://iccida.net/

[22] Chaudhary, A., Sharma, A. & Gupta, N. (2023). Designing A Secured Framework for the Steganography Process Using Blockchain and Machine Learning Technology. *International Journal of Intelligent Systems and Applications in Engineering*, 11(2s):96–103.

[23] Torki, O., Ashouri-Talouki, M. & Mahdavi, M. (2023). Hierarchical Deterministic Wallets for Secure Steganography in Blockchain. *The ISC International Journal of Information Security.* 15(1):73-81. DOI: 10.22042/isecure.2022.319074.729

[24] Chaudhary, A., Sharma, A. & Gupta, N. (2023). A Novel Approach to Blockchain and Deep Learning in the field of Steganography. *International Journal of Intelligent Systems and Applications in Engineering.* 11(2s):104–115.

[25] Jahnavi, S., Pradeep, S., Navtej, P., Medini, H.S. & Mamisha. (2023). Blockchain Technology Based Image Steganography. *International Journal of Innovative Research in Technology.* 9(12):637-642.

[26] Sarkar, P.; Ghosal, S.K.; Sarkar, M. (2020). Stego-Chain: A Framework to Mine Encoded Stego-Block in a Decentralized Network. *J. King Saud Univ. Comput. Inf. Sci.* 2020, 16, 25–29.

[27] Mohsin, A.H.; Zaidan, A.A.; Zaidan, B.B.; Mohammed, K.I.; Albahri, O.S.; Albahri, A.S.; Alsalem, M.A. (2021). PSO–Blockchain-Based Image Steganography: Towards a New Method to Secure Updating and Sharing COVID-19 Data in Decentralised Hospitals Intelligence Architecture. *Multimed. Tools Appl.* 2021, 80, 14137–14161.

[28] Li, D., & Kar, P. (2022). B-Spot: Blockchain and Steganography based Robust and Secure Photo Transmission Mechanism. *Journal of Mobile Multimedia.* 18(06):1677–1708. DOI:10.13052/jmm1550-4646.18610

[29] Basuki, A.I.; Rosiyadi, D. (2019). *Joint Transaction-Image Steganography for High Capacity Covert Communication.* In Proceedings of the 2019 International Conference on Computer, Control, Informatics and its Applications (IC3INA), Tangerang, Indonesia, 23–24 October 2019; pp. 41–46.

[30] Kandasamy, L. & Ajay, A. (2023). *Implementation of Blockchain Technology for Secure Image Sharing Using Double Layer Steganography.* In: Hu, Z., Wang, Y., He, M. (eds) Advances in Intelligent Systems, Computer Science and Digital Economics IV. CSDEIS 2022. Lecture Notes on Data Engineering and Communications Technologies, vol 158. Springer, Cham. DOI:10.1007/978-3-031-24475-9_16

[31] Partala, J. (2018). Provably Secure Covert Communication on Blockchain. *Cryptography.* 2(3):18. DOI:10.3390/cryptography2030018

[32] Horng, J. H., Chang, C. C., Li, G. L., Lee, W. K. & Hwang, S.O. (2021). Blockchain-Based Reversible Data Hiding for Securing Medical Images. *J. Healthc. Eng.* DOI:10.1155/2021/9943402

[33] Xu, M., Wu, H., Geng, G., Zhang, X. & Ding, F. (2019). *Broadcasting steganography in the blockchain.* In International Workshop on Digital Watermarking; Springer: Berlin-Heidelberg, Germany, 2019; pp. 256–267.

[34] Matzutt, R., Hiller, J., Henze, M., Ziegeldorf, J. H., Müllmann, D., Hohlfeld, O. & Wehrle, K. (2018). *A*

Quantitative Analysis of the Impact of Arbitrary Blockchain Content on Bitcoin. In Financial Cryptography and Data Security; Meiklejohn, S., Sako, K., Eds.; Springer: Berlin-Heidelberg, Germany, 2018; pp. 420–438.

[35] Giron, A. A., Martina, J. E. & Custódio, R. (2021). Steganographic Analysis of Blockchains. *Sensors.* 21(12): 4078. DOI:10.3390/s21124078

[36] Hashim, M. M., Rahim, M. S. M., Johi, F. A., Taha, M. S. & Hamad, H. S. (2018). Performance evaluation measurement of image steganography techniques with analysis of LSB based on variation image formats. *International Journal of Engineering & Technology.* 7(4):3505-3514. DOI:10.14419/ijet.v7i4.17294

[37] Al-Refai, S. & Al-Jarrah, M. M. (2020). *Secure Data Hiding Technique Using Batch Video Steganography.* In Proceedings of the 2019 2nd International Conference on Information Hiding and Image Processing (IHIP 2019). Association for Computing Machinery, New York, NY, USA, 1–4. DOI:10.1145/3383913.3383914

[38] Pinchen Cui, P., Guin, U., Skjellum, A. & Umphress, D. (2019). Blockchain in IoT: Current Trends, Challenges, and Future Roadmap. *Journal of Hardware and Systems Security.* 3(4):338-364. DOI:10.1007/s41635-019-00079-5

[39] Yan, T., Chen, W., Zhao, P. & et al. (2021). Handling conditional queries and data storage on Hyperledger Fabric efficiently. *World Wide Web.* 24:441–461. DOI:10.1007/s11280-020-00844-5

[40] Takaoğlu, M., Dursun, T., Doğan, A., Er, H., Bozkurt Günay, B., Emeç, C., Kumru, A., Demir, S., Kurt Toplu, S. & Özcandan, N. (2023). *The Impact of Self-Sovereign Identities on CyberSecurity.* IST-186-RSM, Specialist Meeting, Blockchain Technology for Coalition Operations. https://bilgem.tubitak.gov.tr/uekae-yayinlar/

[41] Khan, D., Jung, L. T., Hashmani, M. A. & Cheong, M. K. (2022). Empirical Performance Analysis of Hyperledger LTS for Small and Medium Enterprises. *Sensors.* 22(3):915. DOI:10.3390/s22030915

[42] Chacko, J. A., Mayer, R. & Jacobsen, H. A. (2021). *Why Do My Blockchain Transactions Fail? A Study of Hyperledger Fabric.* In Proceedings of the 2021 International Conference on Management of Data (SIGMOD '21). Association for Computing Machinery, New York, NY, USA, 221–234. DOI:10.1145/3448016.3452823

[43] Zhou, E., Sun, H., Pi, B., Sun, j., Yamashita, K. & Nomura, Y. (2019). *Ledgerdata Refiner: A Powerful Ledger Data Query Platform for Hyperledger Fabric.* Sixth International Conference on Internet of Things: Systems, Management and Security (IOTSMS), Granada, Spain, 433-440. DOI: 10.1109/IOTSMS48152.2019.8939212

[44] Ke, Z. & Park, N. (2022). Performance modeling and analysis of Hyperledger Fabric. *Cluster Comput.* DOI:10.1007/s10586-022-03800-2

[45] Song, M., Han, J., Eom, H. & Son, Y. (2022). *IPFSz: An Efficient Data Compression Scheme in InterPlanetary File System.* in IEEE Access. 10:122601-122611. DOI:10.1109/ACCESS.2022.3223107

[46] Benet, J. (2014). I*PFS documentation.* https://docs.ipfs.tech/

[47] Muralidharan, S. & Ko, H. (2019). *An InterPlanetary File System (IPFS) based IoT framework.* 2019 IEEE International Conference on Consumer Electronics (ICCE), Las Vegas, NV, USA, 2019, pp. 1-2. DOI:10.1109/ICCE.2019.8662002

[48] Bennett, C. H., Brassard, G. & Breidbart, S. (2014). Quantum Cryptography II: How to re-use a one-time pad safely even if P=NP. *Nat Comput.* 13(4):453-458. DOI:10.1007/s11047-014-9453-6
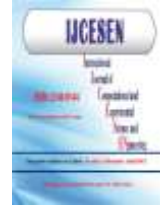
Investigation of Mechanical Properties of Domestic Black Tea Waste Filled Vinylester Composites

İlyas KARTAL[1]*, Kübra KASAP[2], Halil DEMİRER[3]

[1]*Marmara University, Technology Faculty, Metallurgy and Materials Engineering, 34722, Istanbul-Turkey
* **Corresponding Author** : **Email:** ilyaskartal@marmara.edu.tr - **ORCID:** 0000-0001-9677-477X

[2]Marmara University, Institute of Pure and Applied Sciences, 34779, Istanbul-Turkey
Email: kubrakasap@marun.edu.tr - **ORCID:** 0000-0001-7807-5078

[3]Marmara University, Technology Faculty, Metallurgy and Materials Engineering, 34779, Istanbul-Turkey
Email: hdemirer@marmara.edu.tr – **ORCID:** 0000-0001-7870-5797

Abstract:

Recently, green composites have been produced by using renewable resources in order to find a solution to problems such as increasing environmental concerns and decreasing reserves. It is a sustainable composite with its ability to adapt to nature and the environment, to use waste, to show a certain strength, to be processed in a simple way, and which does not require new production techniques, can be processed on micro or nano scale, can be recycled, have the quality of being renewed. is highly preferred. In this study, domestic black tea waste was used as a filler. As the matrix material, vinylester resin is preferred because it can be easily processed at room conditions and is less costly. Waste tea was added to the matrix as a filler in an open mould at the rates of 0%, 5%, 10%, 15%, 20% and 25%. Tensile, impact and hardness tests were performed on composite samples. Fractured surface examinations of the samples were also examined by SEM. When the results are compared, it can be said that the 10% domestic black tea waste filled vinylester composite has slightly better mechanical properties than the other samples. Thus, it was evaluated that domestic black tea waste could be used as a filler in composite applications.

1. Introduction

Composites are materials obtained as a result of combining more than one material or phase with a suitable method in order to combine the appropriate properties of two or more materials in a single material and to obtain superior new properties. It is a highly preferred material class with its positive features such as adaptability to different situations, serving specific purposes, exhibiting desired properties, resistance to chemicals and corrosion, high durability/density ratio, high modulus/weight ratio, and lightness. It is used in a wide and diverse field such as aviation, space and defence industry, land and sea vehicles, sports equipment, construction, infrastructure and energy sector [1-3]. Conventional petroleum-based composites have many advantages, but are not biodegradable due to their toxic effect. Conventional composite materials that have reached the end of their useful life are

difficult and expensive to recycle, and are sometimes destroyed by burial and sometimes by incineration. The pollution caused by the destroyed materials and the rapidly decreasing natural resources pose a great problem for the future. For this reason, the interest in environmentally friendly, sustainable raw materials has increased in recent years with environmental concerns and demands of legal authorities. The use of natural fibers as reinforcement material and wood materials as filler material in composites in engineering applications has become increasingly widespread, and the concept of green composites has come to the fore [4-5].

A composite material consists of the combination of two or more materials in macro dimensions and without mixing with each other, and one or more of these materials is named as reinforcement/filler material, while the other structure surrounding the

reinforcement/filler material is defined as matrix. [6].

The most basic feature that distinguishes composite materials from the molecular structure called mixture; The two main components (matrix and reinforcement phase) appear prominently in the inner region of the composite materials and do not dissolve in each other [7].

Today, the use of composite materials in areas such as automotive, aviation, health, sports and maritime is increasing. One of the most important and most frequently produced and developed types of composite materials is polymer matrix composites. While epoxy, vinylester and polyester are used as matrix material intensively in composites, fibers such as glass, carbon and aramid are preferred as reinforcement materials. Due to many advantages such as corrosion resistance, lightness, good mechanical properties, this group of composite materials is in demand today [8].

In composites, the matrix material transmits and distributes the applied force to the reinforcement phase through the interface. The mechanical properties of the matrix material are very important for the load transfer reinforcing element to function in the composite material. The interface, which acts as the adhesive between the matrix structure and the reinforcement element, transmits the force to the reinforcement phase. This region is the most important place that affects the elastic modulus of the material. Thus, it can be said that the most important factor determining the strength of composites is good interfacial bonding [9].

Composite materials cause more than one beneficial properties to emerge in the material itself. At the same time, it is a very popular material group with its ability to comply with different conditions, to work for special purposes, to exhibit good behaviour against expected features, to be light with its high strength/density ratio, high modulus/weight ratio [10-13].

Green composites are materials that one or more of their components originate from natural origins and are in demand. Biodegradability offers alternatives to traditional composites in terms of finding alternatives to environmental problems and decreasing resources, ease of use, not harming the skin, low cost, and soundproofing and recycling. Green composites are believed to have a major impact on ecosystem problems, as they are derived from structures found in nature, and have a promising effect on shrinking oil resources. With all these positive properties, green composites, developed as a new nature-friendly polymeric composite material, show technical and low-cost benefits in commercial and engineering

applications and have a dragging effect in the global market [14-15].

In this study, green composite was prepared, vinylester polymer was used as matrix material and domestic black tea waste was used as reinforcement element.

Vinylester resins are a type of resin that is produced by the reaction of epoxy resin and unsaturated acid. It is the most used version obtained by the reaction of methacrylic acid dissolved in the styrene monomer structure and bisphenol A (BPA) epoxy resin. It has high resistance to ambient conditions. Although vinylester resins are thermoset based, their simple processability and rapid curing properties have been improved with epoxy resins compared to unsaturated polyester resins. However, it shows good strength and corrosion resistance [16-17].

Numerous studies have been conducted on green composites in the literature. Some of the studies carried out are thermoset composite materials reinforced with hazelnut, paddy shells and wood shavings [18], chestnut/hornwood sawdust filled vinylester composites [19], bamboo and glass fiber reinforced vinylester composites [20], hazelnut shell filled polypropylene matrix composites [21], chestnut wood flour filled vinylester composites [22], hornbeam sawdust filled polyethylene composites [23] are just a few of these studies.

2. Material and Methods

2.1 Materials

Bisphenol-A based vinylester resin (E-275-Erco Boya, İstanbul), which is ideal for hand casting, was chosen as the matrix material. 50% active methyl ethyl ketone peroxide (Erco Ece Boya, İstanbul) was used as a reaction initiator. Cobalt naphthalate used as accelerator was used as 1% of the weight of the resin. Domestic black tea waste used as a filler was obtained from tea grown in Rize province in the Eastern Black Sea Region. After drinking Çaykur Tiryaki branded black tea, the remaining pulp was collected as waste, dried and ground (figure 1 and figure 2).

In addition, Teflon mould was used to prepare standard tensile, impact and hardness samples.

2.2 Methods

Composite samples prepared are a combination of domestic black tea waste and vinylester resin. Composite mixtures were formed by adding domestic black tea waste at different rates (0%, 5%, 10%, 15%, 20%, 25% by weight) to vinylester. 2%

by weight of methyl ethyl ketone peroxide (Erco Boya, İstanbul) was added to the resin as a hardener and 1% by weight of cobalt naphthalate (Erco Boya, İstanbul) as accelerator. The mixtures were poured into an open Teflon mold and solidified. Mold release agent has been applied in order to remove the composite material from the mold more easily.

The tensile test was applied to the samples in the Zwick brand Z010 universal type tensile test device according to the ISO 527 standard at a tensile speed of 5 mm per minute. The impact strength of the unnotched test specimens was used with a 5.4 J Izod hammer on the Zwick brand B5113.30 impact tester. Hardness test measurements were made on the Zwick brand Shore D tester. For SEM analysis, the samples were coated with a 10 Å thick gold/palladium alloy. The SEM test was performed with the Polaron SC branded device located in the Marmara University Faculty of Technology Laboratory.

Figure 1. Grinding Tea in a Blender

Figure 2. Image of Ground Domestic Black Tea Waste

3. Results and Discussions

The tensile strength value of a particle reinforced polymer matrix in the composite varies depending on the active charge transfer between the matrix structure and the particle reinforcements. Factors such as particle additive ratio, size, surface properties also directly affect the strength.

According to the tensile test data (figure 3), the highest tensile strength was observed in the 10% tea waste filled vinylester based composite. An increase of approximately 15% in tensile strength was obtained compared to the pure vinylester sample. A decrease in tensile strength was observed as the tea waste ratio increased (15% and later). Irregular shaped black tea waste particles in the composite structure also had a notch effect and had a positive effect on the strength of the composite structure during the tensile test.
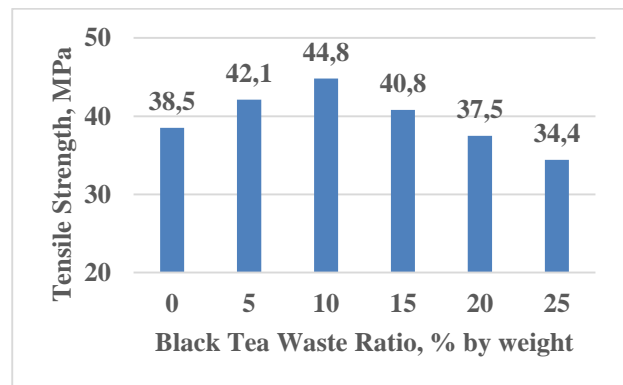

Figure 3. Variation of Tensile Strength with Black Tea Waste Ratio

The modulus value of the particle-reinforced polymer matrix composite can be increased by adding high-hardness particles to the polymer matrix structure. The modulus of elasticity value is dependent on the total charge present in the fiber or filler and is independent of the particle size size and interfacial adhesion ability.

As the amount of waste tea waste increased in the blends, the modulus value increased slightly (figure 4). Again, the highest value was seen in the mixtures with 10% filling ratio. In the following ratios, the module value decreased. When the variation of Izod impact strength of with the ratio of black tea waste was examined, it was observed that the impact resistance of the composite decreased

slightly with the increase of the tea waste ratio. Waste tea reduced the impact strength (figure 5).
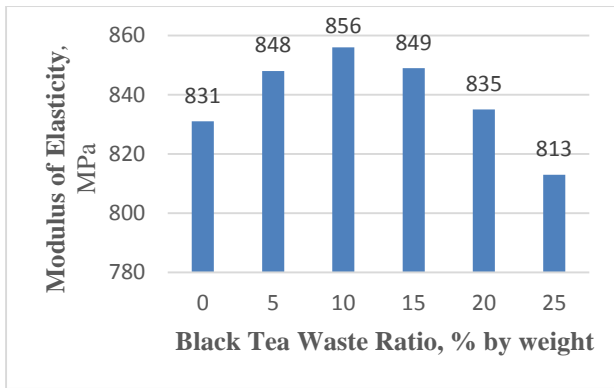

Figure 4. *Variation of Modulus of Elasticity with Black Tea Waste Rate*
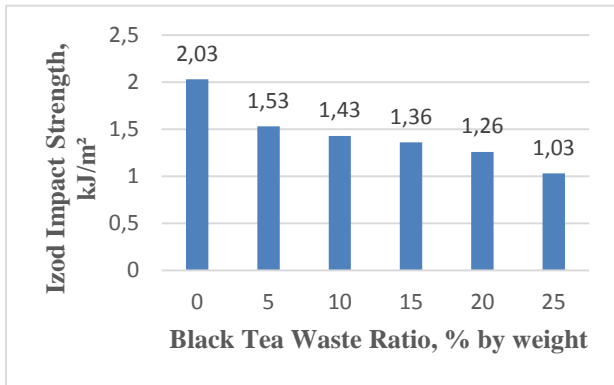

Figure 5. *Variation of Izod Impact Strength with Black Tea Waste Rate*

The reason for this is thought to be the reason that tea wastes are found in many different sizes. When the Shore D hardness test results were examined, it was determined that there was no obvious change in the hardness test values with the addition of domestic tea waste (figure 6).
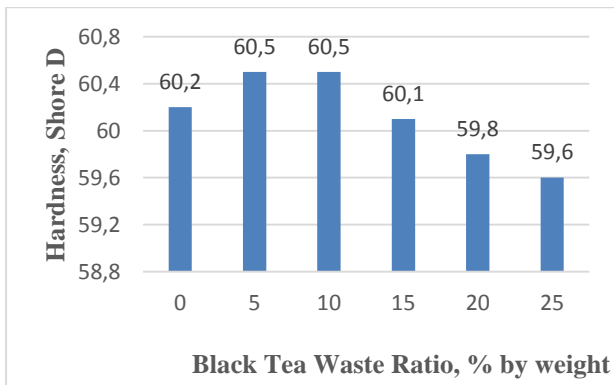

Figure 6. *Variation of Shore D Hardness Value with Black Tea Waste Ratio*

SEM images of the samples are given in Figure 7. In Figure 7a, damage lines are seen on the surface of the pure vinylester and it is understood that there is a brittle fracture. As can be seen from other SEM images, tea wastes have very different sizes and structures. After the grinding process, no size separation was made, and the wastes were used as they were. As can be seen from the images, it is seen that there is tea waste in the size of 10 microns, as well as tea waste in the size of 500 microns.
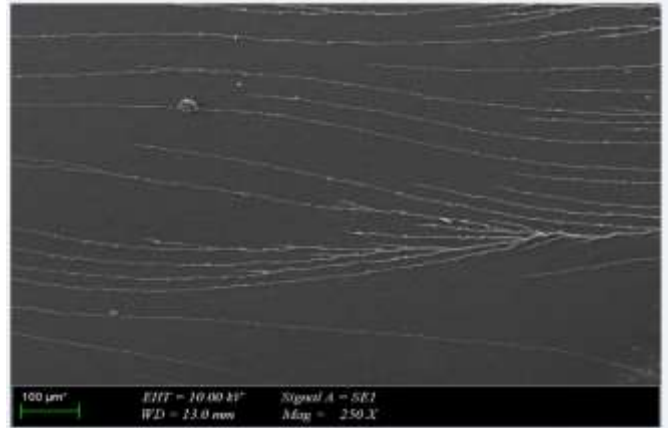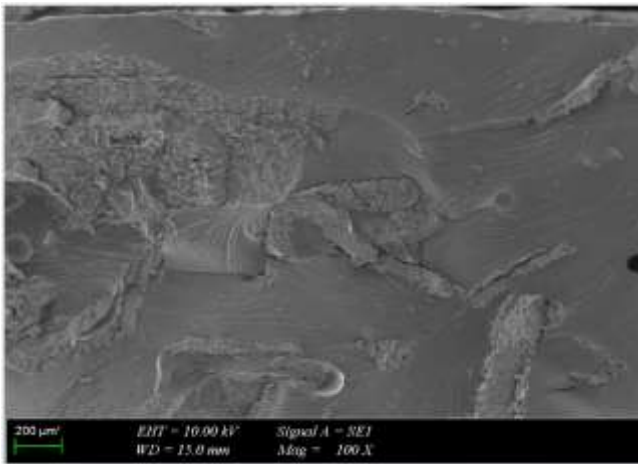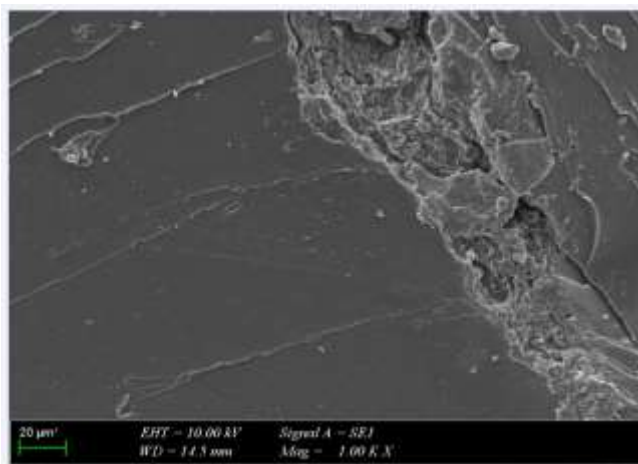

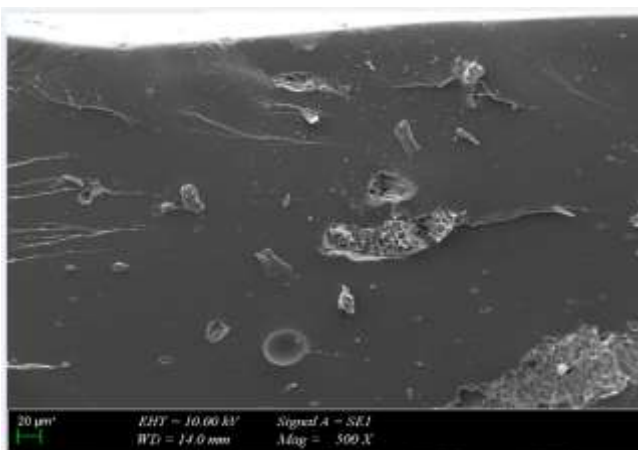*(a) Pure Vinylester*
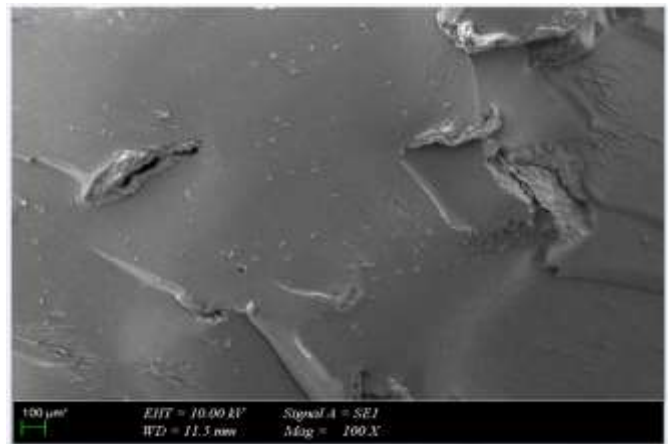
(b) 5% black tea waste filler composite

438
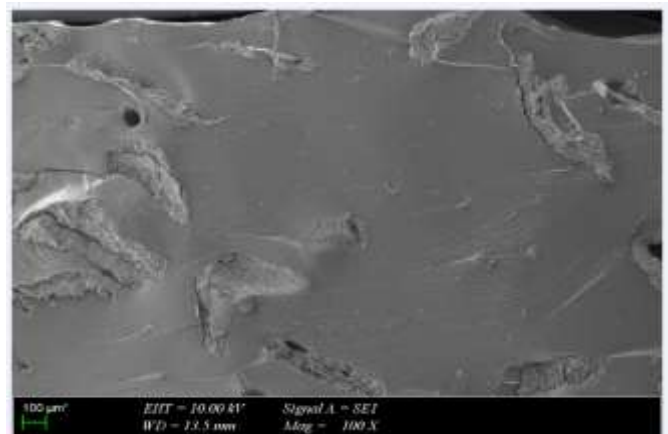
(c) 10 % black tea waste filler composite

(d) 15 % black tea waste filler composite

(e) 20 % black tea waste filler composite

(f) 25% black tea waste filler composite

Figure 7. *SEM images of pure vinylester and black tea waste filler composites*

4. Conclusions

In this study, the use of domestic black tea waste as a filler in composite material was examined. A slight improvement in mechanical properties was observed as the filler ratio increased in vinylester based composite materials. According to the tensile test data, it was observed that 10% domestic black tea waste filler showed better strength. It was determined that the modulus of elasticity value was also high at this 10% filler rate. Impact test values have decreased due to different sizes of filler in the structure. The hardness values remained almost the same.

At the end of this study, it was concluded that in addition to contributing to the solution of environmental problems, it even allows for improvement in some mechanical and physical properties, and the use of such fillings in composite materials may be a suitable decision.

Author Statements:

- **Ethical approval:** The conducted research is not related to either human or animal use.
- **Conflict of interest:** The authors declare that they have no known competing financial interests or personal relationships that could have appeared to influence the work reported in this paper
- **Acknowledgement:** The authors declare that they have nobody or no-company to acknowledge.
- **Author contributions:** The authors declare that they have equal right on this paper.
- **Funding information:** The authors declare that there is no funding to be acknowledged.
- **Data availability statement:** The data that support the findings of this study are available on request from the corresponding author. The data are not publicly available due to privacy or ethical restrictions.

References

[1] Jose A.M., Kim Y.A., Leal-Ekman S., Hunter C.P. (2012). *Conserved tyrosine kinase promotes the import of silencing RNA into Caenorhabditis elegans cells*, Proc. Natl. Acad. Sci. USA., 109: 14520–14525.

[2] Sabu, T., Kuruvilla J.; Kumar, M., Goda, K., Sreekala M. S. (2012*). Introduction to Polymer Composites, Polymer Composites*, Volume 1, First Edition, Wiley-VCH Verlag GmbH & Co 209.

[3] Kandpal, B.C., Chaurasia, R., Khurana, V. (2015). Recent Advances in Green Composites – A Review, *International Journal For Technological Research In Engineering (IJTRE)* 2(7)

[4] Santulli, C., Sarasini, F., Tirillò, J., Valente, T., Valente, M., Caruso, A.P., Infantino, M., Nisini, E., Minak, G. (2013). Mechanical Behaviour of Jute

Cloth/Wool Felts Hybrid Laminates, *Materials and Design*, 50,309–321.

[5] Yan, L., Chouw, N., Jayaraman, K. (2014). *Flax Fibre and Its Composites*, Composites: Part B Engineering (Compos Part B- Eng), vol. 56, pp. 296-317.

[6] Sanjay, M. R., G. R. Arpitha, and B. Yogesha. (2015). Study on mechanical properties of naturalglass fibre reinforced polymer hybrid composites: A review. *Materials today proceedings*. 2(4-5), 2959-2967.

[7] Sabu, T., Kuruvilla, J., Kumar, M., Goda, K., Sreekala M. S. (2012) *Introduction to Polymer Composites*, Polymer Composites, 1st Edition., Springer, Boston, MA.

[8] Post, W., et al. (2017), Healing of a glass fibre reinforced composite with a disulphide containing organic-inorganic epoxy matrix. *Composites Science and Technology* 152, 85-93.

[9] Qu, J. (1993). The effect of slightly weakened interfaces on the overall elastic properties of composite materials. *Mechanics of Materials,* 14(4), 269-281.

[10] Chou, T. ve Ko, F. (1989) *Textile Structural Composites*, Elsevier Science Publishers, Amsterdam.

[11] Kandpal, B.C., Chaurasia, R., Khurana, V. (2015) Recent Advances in Green Composites – A Review, *International Journal For Technological Research In Engineering (IJTRE),* 2, 742-747.

[12] William D. Callister, J. D. (2014). *Composites. J. D. William D. Callister içinde*, Materials Science and Engineering an Introduction (s. 636). United States America: Wiley.

[13] Qu, J. (1993). The effect of slightly weakened interfaces on the overall elastic properties of composite materials. *Mechanics of Materials*, 14(4), 269-281.

[14] Thakur, V. K., Thakur, M.K., Gupta, R.K. (2014). Review: Raw Natural Fiber–Based Polymer Composites, *International Journal of Polymer Anal. Charact. (IJPAC)*, 19,256–271.

[15] Paul, W., Jan, I., Ignaas, V. (2003). Natural Fibers: Can They Replace Glass in Fiber Reinforced Plastics, *Comput Sci Technol,* 63,1259–1264.

[16] Blankenship, L.T., White, M.N., Puckett, P.M. (1989). *Vinyl Ester Resins: For Composites*, Dow Chemical U.S.A, Freeport, Texas, pp. 1-36.

[17] Astrom, B.T. (1997). *Manufacturing of Polymer Composites*, Department of Aeronautics, Royal Insitute of Technology, Chapman & Hall, pp. 1-175.

[18] Kartal, İ., (2018). Kord bezi ile takviye edilmiş polyester kompozitlerin kırılma özelliklerinin incelenmesi. *BAUN Fen Bilimleri Enstitüsü Dergisi*, 20 (2), 396-400.

[19] Boriaa S., Pavlovicb A., Fragassab C., ve Santullic C. (2016) Modeling of Falling Weight Impact Behavior of Hybrid Basalt/Flax Vinylester Composites, *Prodecia Engineering*, 167, 223-230.

[20] Kartal İ., Naycı G., Demirer H., (2019) Cam ve Bambu Lifleriyle Takviyelendirilmiş Vinilester Kompozitlerin Mekanik Özelliklerinin İncelenmesi, *International Journal of Multidisciplinary Studies and Innovative Technologies*, 3(1),34-37.

[21] Demirer H., Kartal İ., Yıldırım A., Büyükkaya K., (2018) The Utilisability of Ground Hazelnut Shell as Filler in Polypropylene Composites, *Acta Phys. Pol. A* 134, 254-256.

[22] Kartal İ., Naycı G., Demirer H., (2020*)* The effect of chestnut wood flour size on the mechanical properties of vinyl ester composites, *Emerging Materials Research*, 9(3), 960-965.

[23] Kartal İ., (2020), Effect of hornbeam sawdust size on the mechanical properties of polyethylene composites, *Emerging Materials Research* 9(3): 979–984.